The Medical Applications of Hyperpolarized Xe and Non-proton Magnetic Resonance Imaging

by

Vira Grynko

Faculty of Science & Environmental Studies

Lakehead University, Thunder Bay, Ontario

October 2023

A dissertation submitted in partial fulfillment

of the requirements of the degree of Doctor of Philosophy

Chemistry and Materials Science Program

Thunder Bay, Ontario, Canada 2023

Vira Grynko 2023 ©

To my grandmother Alla and father Sergey.

The Medical Applications of Hyperpolarized Xe and Non-proton Magnetic Resonance Imaging

Vira Grynko
Doctor of Philosophy, 2023
Chemistry and Materials Science Program
Lakehead University

Abstract

Hyperpolarized ^{129}Xe (HP ^{129}Xe) magnetic resonance imaging (MRI) is a relatively young field which is experiencing significant advancements each year. Conventional proton MRI is widely used in clinical practice as an anatomical medical imaging due to its superb soft tissue contrast. HP ^{129}Xe MRI, on the other hand, may provide valuable information about internal organs functions and structure. HP ^{129}Xe MRI has been recently clinically approved for lung imaging in the United Kingdom and the United States. It allows quantitative assessment of the lung function in addition to structural imaging. HP ^{129}Xe has unique properties of anaesthetic, and may transfer to the blood stream and be further carried to the highly perfused organs. This gives the opportunity to assess brain perfusion with HP ^{129}Xe and perform molecular imaging. However, the further progression of the HP ^{129}Xe utilization for brain perfusion quantification and molecular imaging implementation is limited by the absence of certain crucial milestones.

This thesis focused on providing important stepping stones for the further development of HP ^{129}Xe molecular imaging and brain imaging. The effect of glycation on the spectroscopic characteristics of HP ^{129}Xe was studied in whole sheep blood with magnetic resonance spectroscopy. An additional peak of HP ^{129}Xe bound to glycated hemoglobin was observed. This finding should be implemented in the spectroscopic HP ^{129}Xe studies in patients with diabetes. The optimization of cucurbit[6]uril hyperpolarized chemical exchange saturation transfer

(HyperCEST) performance will allow a significant reduction in the dose of injected biosensors for molecular imaging. The possibility of obtaining higher HyperCEST performance with lower molecular cage concentrations is possible with the utilization of the most effective pulse sequences for various molecular biosensors. The optimal pulse sequence for the cucurbit[6]uril molecule was identified, resulting in a 2.5-fold reduction in the detection limit. Multi-slice brain images acquired for the first time with HP ^{129}Xe using gradient echo imaging open new capabilities for spatially accurate HP ^{129}Xe brain perfusion evaluation. The feasibility of multi-slice imaging has been demonstrated for HP ^{129}Xe, paving the way for advancements in all currently investigated techniques utilizing HP ^{129}Xe.

This groundbreaking research not only marks a significant milestone, but also paves an entirely new and promising avenue for the progression and enhancement of MRI techniques employing HP ^{129}Xe. The findings of this study create a foundation for novel approaches and methodologies, fostering the potential for substantial improvements in the field of HP ^{129}Xe MRI.

Acknowledgements

I would like to express my sincere gratitude to my supervisor Dr. Mitchell Albert for the opportunity to conduct research under his guidance. Due to Dr. Albert's experienced supervision, continuous support and regular check-ups of my progress I was able to successfully finish my PhD journey. I would also like to thank the members of my supervisory committee, Dr. Alla Reznik,Dr. Michael Campbell, and Dr. Robert Mawhinney who helped me and provided continued support through the past years. I am extremely grateful to Dr. Alla Reznik for her invaluable patience and feedback. I want to convey my appreciation to Dr. Robert Mawhinney for his meticulous editing of my thesis. In conclusion, my sincere appreciation goes to Dr. Tomanek for graciously agreeing to serve as my external reviewer and for thoughtfully examining my thesis.

I am deeply indebted to Dr. Yurii Shepelytskyi, whose help was invaluable in all possible ways at each step of research. I could not have survived this journey without his meticulous guidance, patient explanations and numerous facts about history.

I would like to thank the present members of the Albert group Dr. Viktoriia Batarchuk, Ruba Aldossary, Tanu Talwar and Karla Rodriguez for creating such a friendly and positive work environment. The amount of effort invested by this team in the regulatory paperwork and numerous grants can not be expressed.

I am extremely grateful to Tanu Talwar for all her help with any possible questions and immerse patience. I am thankful for the amount of time and nerves that she invests into the daily life of the lab.

I would like to thank Karla Rodriguez for all her positive affirmations that actually work and make impossible things real.

I would like to acknowledge every present and past member of Dr. Albert's lab for their contribution to my research. My endless gratitude goes to Tao Li, Martina Agostino, Vincent Knight, Nikka Stoger, and Francis Hane for their work on managing an infinite amount of regulatory paperwork required for the successful conduction of human experiments. Also, I would like to thank them for proofreading and grammar editing my papers, and conference abstracts.

I am grateful for the financial support that made this work possible. All of the studies in this thesis were partially supported by the Thunder Bay Regional Health Research Institute. I am thankful for the scholarships that allowed me to conduct these studies. I was supported by the Ontario Trillium Scholarship from 2018 to 2022 and the Mathematics of Information Technology and Complex Systems (Mitacs) Elevate Grant for 2022-2023.

I would like to thank Dr. Oleksandr Grynko for his support, patience and help over these years. I would not have reached this point in my life without him. I am grateful to my mother Nadiia Popova for all her love and courage during this journey. Without her support, this work would never have been possible. I would like to thank all my friends especially Tasya Kovalenko for their endless enquiries about the status of my PhD.

Finally, I would like to thank Graeme Edward Nuttall for being there in the moments of my disbelief.

Statement of Contributions

Chapter 2 “Hyperpolarized 129Xe imaging of the brain” consists of the published review paper “Hyperpolarized 129Xe imaging of the brain: Achievements and Future Challenges” Shepelytskyi Y., **Grynko V.,** Rao M.R., Li T., Agostino M., Wild J.M., Albert M.S in *Magnetic Resonance in Medicine*, volume 86, issue 6, pages 3175-3181 (2021). Vira Grynko shares the first authorship with Yurii Shepelytskyi for it.

Authors Contributions: Vira Grynko has performed a literature search, analyzed literature sources, and written the next sections of the paper: Introduction, HP 129Xe spectroscopy and Chemical Shift Imaging (CSI) of the brain, Relaxation time measurements, HP 129Xe uptake models, and Brain disease detection with HP 129Xe. Yurii Shepelytskyi has written Structural brain imaging with HP 129Xe, Perfusion imaging with HP 129Xe, Functional MRI with HP 129Xe, and Discussion sections. Text editing and corrections were done by Tao Li and Martina Agostino. The design, strategy and planning of the manuscript were performed by Mitchell Albert, Vira Grynko, and Yurii Shepelytskyi. The final manuscript proofreading was done by Madhwesha Rao, Jim Wild, and Mitchell Albert. Madhwesha Rao also contributed to writing Perfusion imaging with HP 129Xe section.

Chapter 3 “Effect of blood glycation on 129Xe spectroscopic parameters” consists of the published article “Revealing a Third Dissolved-Phase Xenon-129 Resonance in Blood Caused by Hemoglobin Glycation” Mikowska, L.; **Grynko, V**.; Shepelytskyi, Y.; Ruset, I.C.; Deschamps, J.; Aalto, H.; Targosz-Korecka, M.; Balamore, D.; Harańczyk, H.; Albert, M.S. in *International Journal of Molecular Sciences,* volume 24. Issue 14, article number 11311 (2023). Vira Grynko shares the first authorship with Lutoslava Mikowska. Author Contributions: Conceptualization, Lutosława Mikowska, Vira Grynko, Yurii Shepelytskyi, Marta Targosz-Korecka, and Mitchell

Albert; methodology, Lutosława Mikowska, Vira Grynko; software, Vira Grynko, Yurii Shepelytskyi; validation, Lutosława Mikowska, Vira Grynko, Yurii Shepelytskyi; formal analysis, Vira Grynko, Yurii Shepelytskyi; investigation, Lutosława Mikowska, Vira Grynko, Yurii Shepelytskyi, Joseph Deschamps, Hannah Aalto; writing—original draft preparation, Vira Grynko, Yurii Shepelytskyi; writing—review and editing, Lutosława Mikowska, Vira Grynko, Yurii Shepelytskyi, Iullian C. Ruset, Dilip Balamore, Mitchell Albert; supervision, Hubert Harańczyk, and Mitchell Albert; project administration, Vira Grynko, Yurii Shepelytskyi, and Mitchell Albert; All authors have read and agreed to the published version of the manuscript.

Chapter 4 "Multi-slice brain imaging with hyperpolarized ^{129}Xe" includes the published article "Hyperpolarized 129Xe multi-slice imaging of the human brain using a 3D gradient echo pulse sequence" **Grynko V.**, Shepelytskyi Y., Li T., Hassan A., Granberg K., Albert M.S in *Magnetic Resonance in Medicine*, volume 86, issue 6, pages: 3175-3186 (2021).

Authors contributions: Vira Grynko, and Yurii Shepelytskyi conceptualized the idea and designed the analysis methods. Vira Grynko, Yurii Shepelytskyi, and Tao Li collected the data. Vira Grynko performed the analysis. Vira Grynko wrote the original manuscript. Vira Grynko and Yurii Shepelytskyi, Mitchell Albert edited and reviewed the manuscript. Ayman Hassan, Karl Granberg and Mitchell Albert supervised the project. Yurii Shepelytskyi, and Mitchell Albert did the project administration. All authors have read and agreed to the published version of the manuscript.

Chapter 5 "Optimization of Hyperpolarized Chemical Exchange Saturation Transfer Performance" was published as an article "Cucurbit[6]uril Hyperpolarized Chemical Exchange Saturation Transfer Pulse Sequence Parameter Optimization and Detectability Limit Assessment

at 3.0T” **Grynko, V**.; Shepelytskyi, Y.; Batarchuk, V., Aalto, H.; Li, T., Ruset, I.C.; DeBoef, B., Albert, M.S. in *ChemPhysChem,* article number e202300346 (2023).

Authors contributions: Vira Grynko, and Yurii Shepelytskyi conceptualized and designed the study. Vira Grynko, Yurii Shepelytskyi, Viktoriia Batarchuk, Hannah Aalto and Tao Li collected the data. Vira Grynko, Yurii Shepelytskyi, and Viktoriia Batarchuk performed data analysis. Vira Grynko designed the set-up for HyperCEST studies in blood samples. Vira Grynko and Yurii Shepelytskyi wrote the original manuscript. Vira Grynko, Yurii Shepelytskyi, Viktoriia Batarchuk, Iulian C. Ruset, and Mitchell Albert edited and reviewed the manuscript. Brenton DeBoef and Mitchell Albert supervised the project. Yurii Shepelytskyi, Viktoriia Batarchuk, and Mitchell Albert did the project administration. All authors have read and agreed to the published version of the manuscript.

List of Abbreviations

Acquisition - ACQ

Apparent Diffusion Coefficient – ADC

Arterial Spin Labeling – ASL

Bandwidth – BW

Blood Oxygenation Level Dependent – BOLD

Cerebral Blood Flow – CBF

Cerebrospinal Fluid -– SCF

Chemical Exchange Saturation Transfer – CEST

Chemical Shift Imaging – CSI

Chemical Shift Saturation Recovery – CSSR

Computed tomography – CT

Cryptophane-A – CryA

Cucurbit[6]uril – CB6

Cyclodextrins – CDs

Cyclotriveratrylene Units – CTV

Data Acquisition – ACQ

Diffusion Tensor Imaging - DTI

Diffusion-Weighted Imaging – DWI

Dynamic Nuclear Polarization – DNP

Dynamic Susceptibility Contrast - DSC

Echo Time – TE

Electrical Impedance Tomography – EIT

Electrical Source Imaging – ESI

Electrocardiography – ECG

Electroencephalography – EEG

Field-of-View – FOV

Flip Angle – FA

Fluid-attenuated Inversion Recovery – FLAIR

Free Induction Decay – FID

Functional MRI – fMRI

Gadolinium-based Contrast Agents – GBCA

Gradient Echo Pulse Sequence – GRE

Hemodynamic Response – HDR

Hounsfield Units – HU

Hyperpolarized – HP

Iterative Decomposition with Echo Asymmetry and Least Squares Estimation – IDEAL

Magnetic Resonance Imaging – MRI

Magnetic Resonance Spectroscopy – MRS

Magnetic Source Imaging – MSI

Magnetoencephalography – MEG

Metal Organic Polyhedrals – MOPs

Metastable Exchange Optical Pumping – MEOP

Nuclear Magnetic Resonance – NMR

Number of Signal Averages – NSA

Octafluorocyclobutane – OFCB

Perfluorooctyl Bromide – PFOB

Perfluoropropane – PFP

Positron Emission Tomography – PET

Pseudo-continuous ASL – pCASL

Pulse Sequence Diagram – PSD

Radiofrequency – RF

Red Blood Cells – RBC

Region of Interest – ROI

Repetition Time – TR

Signal-to-Noise Ratio – SNR

Single-Photon Emission Computed Tomography - SPECT

Spin Echo – SE

Spin Exchange Optical Pumping – SEOP

Tesla – T

Time-of-Flight – TOF

Ultrashort Echo Time – UTE

Ventilation Defect Percentage – VDP

Ventilation Volume – VV

Ventilation/Perfusion Ratio – V/Q

Xenon - Xe

Xenon Transfer Contrast – XTC

List of Tables

List of Figures

Table of Contents

Chapter 1: Introduction

1.1 Medical Diagnostic Imaging

Medical imaging modalities are key components of accurate diagnoses in certain medical conditions[1,2]. Typically, they involve the visual representation of the structure or functions of organs or tissues in the body[3]. Medical imaging techniques can provide valuable information about biological processes and anatomical details, along with abnormalities and processes of various diseases[4]. Medical imaging can be considered a part of biological imaging, which also involves the detection of biological processes that can be a sign of pathological changes[5].

The main modalities used in medical imaging can be divided into two groups, those which utilize ionizing radiation and those which do not. The imaging modalities that involve ionizing radiation are X-ray radiography, X-ray computed tomography (CT), positron emission tomography (PET), digital mammography, and single-photon emission computed tomography (SPECT). Medical imaging modalities that do not involve any ionizing radiation are endoscopy, thermography, medical photography, medical optical imaging, electrical source imaging (ESI), tactile imaging, ultrasonic and electrical impedance tomography (EIT), magnetic resonance imaging (MRI), magnetic resonance spectroscopy (MRS), and magnetic source imaging (MSI). Moreover, there are recording and measurement techniques such as electroencephalography (EEG), magnetoencephalography (MEG), and electrocardiography (ECG), which do not produce images but represent data as a parameter graph vs. time or maps[3,5]. These methods have less accuracy as compared to others. Most commonly in clinical practice X-ray imaging, CT, MRI, ultrasound, and PET[6] are used. All of the aforementioned modalities provide structural or anatomical imaging, with the exception of PET, SPECT, and MEG, which only provide functional

imaging. MRI is unique as it can provide both structural/anatomical and functional imaging with superb contrast.

X-ray imaging is one of the most popular techniques when it comes to imaging the fine details of bones due to its high resolution[7]. It is based on the difference in attenuation coefficients of the tissues. The tissues' attenuation coefficients depend on density and atomic composition, specifically they are influenced by the number of electroni. The higher the attenuation coefficient, the more radiation energy will be absorbed, hence the tissue will have a higher signal-to-noise ratio (SNR)[8]. It is a quick and non-invasive procedure which makes it cost-effective and widely accessible in the medical field. It has several limitations, however, such as overlapping structures when complex anatomical regions are imaged, and exposure limits. The ionizing radiation which always accompanies X-ray imaging severely limits its utilization as a repetitive method of imaging, since cumulative radiation exposure may increase the risk of radiation-related health problems[9]. Also, radiation makes X-ray undesirable for imaging during pregnancy. X-ray provides limited information about soft tissue contrast due to the low difference in the attenuation coefficients, hence it is ineffective for the detection of certain soft tissue pathologies[10].

CT also utilizes X-ray beams. It has the ability to produce 3D images of both bones and soft tissues through the back-projection of the sinogram created from multiple X-ray attenuation data[8]. It captures the entire area within the scanner's field-of-view (FOV) and provides a more detailed evaluation of a wide range of medical conditions compared to x-ray imaging[5]. CT has higher contrast and higher spatial resolution (~0.5-0.625 mm) than X-ray, however, it involves higher doses of radiation (10-20 mSv)[11]. Despite having the same disadvantages as X-ray and having the highest dose of ionizing radiation among all other medical imaging modalities, CT has

a tendency to be overused or ordered without medical necessity when other imaging methods would suffice due to the high spatial resolution (about 30 μm) of internal structures[12,13].

PET is a medical imaging modality that provides information on metabolic activity. It relies on the β^+-decay of injected radiolabelled tracers whose accumulation depends on the tissue's properties. The commonly used isotopes for the radiolabeled tracers are ^{11}C, ^{18}F, ^{13}N, and ^{15}O. PET has the highest sensitivity among all imaging techniques due to the absence of the natural sources of the radiation emitted by the radiotracer's gamma-rays within the human body. Though a very small dose of radiopharmaceuticals is required for image acquisition ($\sim 10^{-6}$g)[14], the patient is still subjected to ionizing radiation. Another limitation of PET is lower spatial resolution as compared to MRI and CT[15,16], which is caused by relatively high positron spread range and strong time limitations due to the short half-life of the used isotopes[17]. The half-life of the radiolabeled compounds also contributes to the high cost of PET scans.

Another imaging modality that is widely used for diagnoses of soft tissue abnormalities is ultrasound. It involves the detection of elastic waves with frequencies from 1 MHz to 20 MHz reflected from organs and internal structures[8]. Each wave must travel from the emitter to the area of investigation and back to the transducer, passing through multiple tissues in its path. Interaction with various tissues leads to high distortion of the sound waves and significant noise creation. The result is a relatively low SNR as compared to other imaging techniques[18]. Moreover, the ultrasound spatial resolution is also limited and is usually higher than 300 μm[8]. Other important limitations of this modality are image artifacts and challenges associated with visualizing anatomical structures located beyond the bony structures within the human body[5]. Nevertheless, these limitations are compensated for by the affordability of this imaging method and the convenience of transporting ultrasound imaging systems.

MRI is able to provide both anatomical and functional imaging and is widely used for imaging of soft tissues due to the high contrast and reasonable spatial resolution (~100 μm)[19]. MRI relies on the nuclear magnetic resonance (NMR) signal originating from the difference in spin populations on the Zeeman energy levels created by the application of a strong magnetic field. Since the spin population excess is ~10^{-5}, conventional clinical MRI sensitivity is relatively low[20]. Clinical proton (^{1}H) MRI typically utilizes magnetic field strength in the range from 1.5 to 7 Tesla (T) and detects the signal from water protons[21]. The main advantage of MRI is that a wide range of medical conditions including neurological, musculoskeletal, and cardiovascular disorders can be detected without utilizing ionizing radiation. However, MRI has poor sensitivity and a high cost of operation. MRI is commonly used for imaging the brain[22], spinal cord, joints, and organs like the heart and abdomen, among other applications in healthcare[1]. Functional imaging with conventional MRI may be performed with diffusion-weighted imaging (DWI), blood oxygenation level dependent (BOLD) functional MRI, oxygen-enhanced MRI, and other techniques. Multinuclear MRI techniques open possibilities of molecular imaging for the detection of abnormal processes within the body.

1.2 ^{1}H Magnetic Resonance Imaging

The history of MRI should be told from the development of NMR in 1937 by Isidor Rabi for which he received a Nobel Prize in 1944. His method was mainly used for chemical structures until the 1960s when Raymond Damadian proposed that this method could be used on living organisms. Paul Lauterbur published images of glass capillaries filled with water in 1973 and received a Nobel Prize together with Peter Mansfield (who developed the whole-body MRI scanner) in 2003[23]. It's not surprising that each stage of MRI's development has been recognized

by the Nobel committee, considering how MRI has transformed the field of medical imaging by offering excellent soft tissue contrast and high resolution without the use of ionizing radiation.

MRI technique is based on the imaging of nuclei with an odd number of protons and/or neutrons since they have differences in populations on the energy levels in the constant external magnetic field, also known as Zeeman splitting[24]. The most widely used nucleus in MRI is the ^{1}H proton due to its presence in water molecules, which are highly prevalent in the human body. The generated signal is directly proportional to the concentration of atoms, as well as the difference in populations on Zeeman's energy levels (which is $\sim 10^{-5}$ for thermally polarized nuclei). Therefore, in order to receive an adequate signal, MRI requires a sufficient number of nuclei within the voxel.

The most important feature of MRI is superior soft tissue contrast. The density of specific tissues causes different energy dissipation rates following energy transmission by radiofrequency (RF) pulse. Numerous techniques are available for selectively imaging specific tissues by leveraging the physical properties of the nuclei within those tissues[25–27].

While conventional proton MRI is a widely available clinical imaging method, it still faces several challenges that restrict its range of applications. The primary constraint lies in imaging regions lacking protons, such as the human lungs. The areas with low proton density also create image artifacts due to high differences in the magnetic susceptibility with surrounding tissues. Human lungs provide a good illustration of how disparities in tissue/air susceptibility result in signal voids on MRI images[28–30]. In addition to the abovementioned, MRI is highly susceptible to physiological motion which creates numerous image artifacts. Therefore, special techniques have been developed to eliminate artifacts caused by respiratory and cardiac motion. MRI signal is limited with the number of nuclei withing the region of interest. Additionally, in order to receive images with high resolution, techniques with long scan times have to be utilized.

1.3 Physics of Magnetic Resonance Imaging.

In order to facilitate the investigation of the MRI imaging techniques developed in this thesis and offer a clearer comprehension of the underlying theory, this section offers insight into the essential principles of NMR. Readers who are interested in further details of basic MRI principles may check the "Basics of Magnetic Resonance Imaging" by Oldendorf et al[19]. Those who want to explore the complex details of MRI may find interesting "Magnetic Resonance Imaging: Physical Principles and Pulse Sequence Design" by Haacke et. al[31].

1.3.1 Angular Momentum, Nuclear Magnetic Moment and Magnetization in an external static magnetic field.

Magnetic dipole moment $\vec{\mu}$ can be imagined as a pair of equal magnetic charges but with opposite signs, as an analogue of the electric dipole. However, this analogue is not perfect as the magnetic charges do not exist.

In the constant magnetic field ($\vec{B}$), it will experience torque $\vec{N}$:

$$\vec{N} = \vec{\mu} \times \vec{B}, \qquad [1-1]$$

where $\vec{\mu}$ is a magnetic moment. Non-zero torque on the system leads to the changing of the system's total angular momentum $\vec{J}$:

$$\frac{d\vec{J}}{dt} = \vec{N} \qquad [1-2]$$

A combination of the two abovementioned equations will provide the change in angular momentum over time:

$$\frac{d}{dt}\vec{J}(t) = \vec{\mu}(t) \times \overrightarrow{B_0}(t) \qquad [1-3]$$

However, the intrinsic angular momentum of nuclei can also be derived from the quantum side:

$$\vec{J} = \hbar I, \qquad [1-4]$$

where $\hbar$ represents the Dirac constant and I is the nuclear spin. These nuclei will have a magnetic moment $\vec{\mu}$ which will result from the multiplication of angular momentum with gyromagnetic ratio γ:

$$\vec{\mu} = \gamma \vec{J} \qquad [1-5]$$

The gyromagnetic ratio is unique for each nucleus constant which represents the ratio of spin magnetic momentum $\vec{\mu}$ and the angular momentum $\vec{J}$. Below in Table 1-1 can be found the gyromagnetic ratios of the most widely used nuclei in MRI diagnostic and research. Typically, only nuclei with a spin of $\frac{1}{2}$ are used in MRI due to the complexity of NMR spectra of nuclei with higher spins and their reduced signal.

Table 1-1: Gyromagnetic ratios of widely used atoms in MRI[32].

Nucleus	$\gamma, MHz/T$
^{1}H	42.58
^{19}F	40.06
^{31}P	17.24
^{13}C	10.71
^{3}He	-32.43
^{129}Xe	-11.78

Up to this moment, all discussion was about one nucleus. However, it is useful to generalize our consideration of multinuclear systems. The magnetic properties of a multinuclear system can be described by magnetization. Magnetization of the spin system is the density of the spin magnetic moments in it:

$$\vec{M} = \frac{1}{V} \sum_{protons\ in\ V} \overrightarrow{\mu_i}\ , \qquad [1-6]$$

where the volume V is small enough that the external magnetic field is constant over it in approximation.

Taking into account equations [1-3] and [1-5], the equation [1-6] may be rearranged for the equation of the net magnetization in volume V:

$$\frac{1}{V}\sum_{i=1}^{N}\frac{d\overrightarrow{\mu_i}}{dt} = \frac{\gamma}{V}\sum_{i=1}^{N}\overrightarrow{\mu_i} \times \overrightarrow{B_0} \qquad [1-7]$$

Or

$$\frac{d\vec{M}(t)}{dt} = \gamma\vec{M}(t) \times \vec{B}_0(t) \qquad [1-8]$$

The equation above can be resolved using a determinant form:

$$\frac{d\vec{M}}{dt} = \gamma \begin{vmatrix} \vec{\imath} & \vec{\jmath} & \vec{k} \\ M_x & M_y & M_z \\ B_x & B_y & B_z \end{vmatrix} \qquad [1-9]$$

Where $\vec{\imath}, \vec{\jmath}, \vec{k}$ are unit vectors, and x, y, z are directions.

The determinant can be expended as a system of scalar differential equations, also known as Bloch equations:

$$\begin{cases} \frac{dM_x(t)}{dt} = \gamma\left(M_y(t)\cdot B_z(t) - M_z(t)\cdot B_y(t)\right) \\ \frac{dM_y(t)}{dt} = \gamma\left(M_x(t)\cdot B_z(t) - M_z(t)\cdot B_x(t)\right) \\ \frac{dM_z(t)}{dt} = \gamma\left(M_x(t)\cdot B_z(t) - M_y(t)\cdot B_x(t)\right) \end{cases} \quad [1-10]$$

The assumption that vector $\overrightarrow{B_0}$ is placed along +z direction allows the solving of equation [1-10] to illustrate the component's behaviour of net magnetization:

$$M_z = M_0 cos\theta\,, \quad [1-11]$$

$$M_{xy} = (M_0 sin\theta)\cdot e^{-i\omega_0 t}. \quad [1-12]$$

Where M_{xy} is a rotating vector in the xy plane which was presented as a complex variable $M_{xy} = M_x + iM_y$ and M_z is the component of the magnetization vector along the +z axis. θ is a polar angle.

The equations discussed above suggest that the net magnetization vector precesses about the magnetic field lines with the calculated frequency:

$$\omega_0 = \gamma B_0 \quad [1-13]$$

ω_0 is known as a Larmor frequency, where the sign of the gyromagnetic ratio γ determines the direction of the unique precession of each nucleus. If $\gamma > 0,$ the direction of the precession is clockwise and if $\gamma < 0$ it is counterclockwise.

1.3.2 Zeeman effect and Polarization

The potential energy of the nuclear magnetic moment placed into an external magnetic field can be determined through the magnetic dipole moment and the external magnetic field induction vector $\overrightarrow{B_0}$:

$$E = -\vec{\mu}\cdot\overrightarrow{B_0} \quad [1-14]$$

Considering the definition of the magnetic dipole moment stated in equations [1-4] and [1-5]:

$$E = -\gamma\hbar I B_0 \qquad [1-15]$$

The nuclear spin of the proton has two opposite values of $I = +\frac{1}{2}$ and $I = -\frac{1}{2}$, which correspond to the "spin-up" and "spin-down" energy states. In the presence of an external magnetic field, the "spin-up" state where the spin magnetic moment is aligned with the direction of the magnetic field will have lower energy and will be considered the "ground" state. While the spin magnetic moment which is antiparallel to the external magnetic field will have higher energy and can be considered an "excited" or "spin-down" state (Figure 1-1). In the absence of an external magnetic field, these two energy levels deteriorate. However, in the presence of a magnetic field, this phenomenon also recognized as Zeeman energy level splitting or simply Zeeman effect[24] will create an energy gap between two energy states:

$$E = -\left(-\frac{1}{2}\right)\gamma\hbar B_0 - \left(-\frac{1}{2}\gamma\hbar B_0\right) = \gamma\hbar B_0 \qquad [1-16]$$

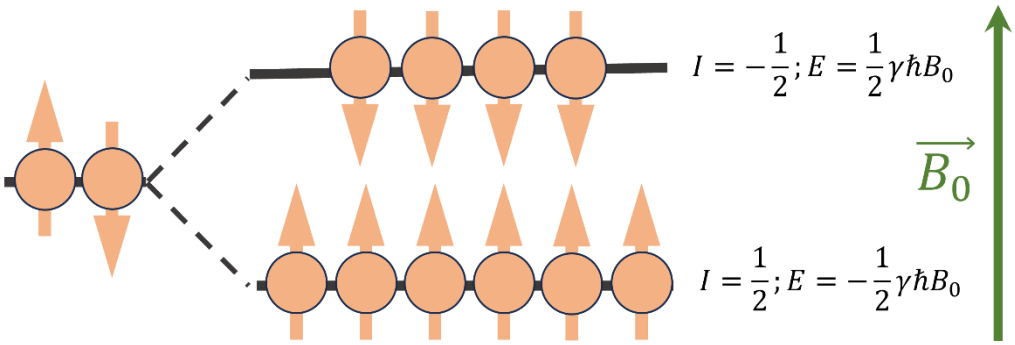

Figure 1-1 Thermally polarized nuclear spins in the presence of an external magnetic field

The number of spins on each energy level can be determined by Boltzman's distribution:

$$N_i = N_0 e^{\frac{-E_i}{kT}}, \qquad [1-17]$$

where i is the number of the level, E_i is the energy of the level, and k is Bolzman constant ($k = 1.38 \times 10^{-23}, \frac{J}{K}$), T is the absolute temperature.

Considering that the "ground" energy state has lower potential energy, it will be more populated than the "excited" state. This difference in the population can be determined by nuclear spin polarization:

$$P = \frac{N_\uparrow - N_\downarrow}{N_\uparrow + N_\downarrow}, \qquad [1-18]$$

where $N_\uparrow$ is the number of spins in the "ground" state aligned with the magnetic field and $N_\downarrow$ is the number of spins in the "excited" state aligned against the magnetic field. Taking into account the Boltzman equation [1-17] and equation [1-14]:

$$P = \frac{e^{\frac{\mu B_0}{kT}} - e^{-\frac{\mu B_0}{kT}}}{e^{\frac{\mu B_0}{kT}} + e^{-\frac{\mu B_0}{kT}}} = \tanh\left(\frac{\mu B_0}{kT}\right) = \tanh\left(\frac{\hbar\gamma B_0}{2kT}\right), \qquad [1-19]$$

Since $2kT \gg \hbar\gamma B_0$,

$$P \cong \frac{\hbar\gamma B_0}{kT} \qquad [1-20]$$

Considering a clinical MRI magnetic field strength of 3T and a patient with nominal body temperature, the polarization of the proton atoms within the body will be approximately 9.9×10^{-6}. Due to this small polarization, the image voxel should have a large enough quantity of ^{1}H nuclei to conduct imaging.

To express the net magnetization in thermal equilibrium via polarization, the equation [1-6] should be noted, along with equations [1-4] and [1-5]. If the spin $I = -\frac{1}{2}$:

$$\vec{M} = N_V \vec{\mu} P = N_V \left(\frac{\hbar\gamma}{2}\right)\left(\frac{\hbar\gamma\overrightarrow{B_0}}{2kT}\right) = \frac{N_V \hbar^2 \gamma^2 \overrightarrow{B_0}}{4kT}, \qquad [1-21]$$

Where N_V is the number of magnetic dipole moments in volume V.

1.3.3 Magnetization precession in Time-Varying Magnetic Field.

In the sections above we discussed the effect of a static magnetic field on nuclear magnetization. However, in order to obtain an NMR signal, an RF pulse should be applied to the system to disturb its thermal equilibrium. The RF pulse will create an additional time-varying magnetic field $\overrightarrow{B_1}$ in the direction perpendicular to the static external magnetic field $\overrightarrow{B_0}$. $\overrightarrow{B_1}$ can also be described as a rotating vector in the xy-plane:

$$\overrightarrow{B_1}(t) = \left|\overrightarrow{B_1}\right| \cdot e^{-i\omega t}, \qquad [1-22]$$

where ω is the angular frequency of an RF pulse. In order to further simplify the calculations, it would be prudent to transfer from a laboratory frame of reference (where $\overrightarrow{B_1}(t)$ rotates), to the rotating reference frame (which rotates about the z-axis with the same frequency ω as $\overrightarrow{B_1}(t)$). The vector $\overrightarrow{B_1}(t)$ will remain still in this reference frame. The effective magnetic field which will affect the net magnetization can be calculated considering the application of B_1:

$$\overrightarrow{B_{eff}} = B_1\hat{\imath} + \gamma\left(B_0 - \frac{\omega}{\gamma}\right)\hat{k}. \qquad [1-23]$$

In the equation above, the component $B_1\hat{\imath}$ is static along the x-axis and the longitudinal component is reduced by $\frac{\omega}{\gamma}$.

If the frequency of radiation of the RF pulse ($\overrightarrow{B_1}(t)$ field) is equal to the Larmor frequency of the system, only the time-varying component will determine the effective magnetic field:

$$\overrightarrow{B_{eff}} = B_1\hat{\imath}. \qquad [1-24]$$

The behaviour of the net magnetization vector described in the previous section with equation [1-8] should be modified with consideration of the effective magnetic field:

$$\frac{d\vec{M}(t)}{dt} = \vec{M}(t) \times \gamma\overrightarrow{B_{eff}} = \vec{M}(t) \times \gamma B_1 \hat{\imath}. \qquad [1-25]$$

Using the previous solution for the equation of an external magnetic field, the rotation of the magnetization vector with the application of $\overrightarrow{B_1}$ may be calculated:

$$\omega_1 = \gamma B_1. \qquad [1-26]$$

The flip angle at which the RF pulse will rotate the net magnetization during the applied time τ can be calculated as a magnitude of the ω_1 integrated with respect to time:

$$\theta = \int_0^\tau |\omega_1|\, dt = \gamma \int_0^\tau B_1(t) dt\,. \qquad [1-27]$$

When the RF pulse with flip angle (FA) θ is applied to the system, the position of the magnetization vector may be calculated through the next matrix:

$$\begin{pmatrix} M_x{}' \\ M_y{}' \\ M_z{}' \end{pmatrix} = \begin{pmatrix} 1 & 0 & 0 \\ 0 & cos\theta & sin\theta \\ 0 & -sin\theta & cos\theta \end{pmatrix} \cdot \begin{pmatrix} M_x \\ M_y \\ M_z \end{pmatrix}. \qquad [1-28]$$

The magnitudes of the components of the magnetization vector will be determined by:

$$\left|M_{xy}\right| = M_0 sin\theta;\ \ |M_z| = M_0 cos\theta, \qquad [1-29]$$

where M_0 is the initial magnitude of the magnetization vector before the application of an RF pulse.

If the frequency of the RF pulse is equal to the Larmor frequency of the system, the electromagnetic energy of the pulse will be absorbed by the nuclei in the "ground" state since the amount of provided energy will be equal to the energy gap between the "ground" and "excited" states. However, if the RF pulse is turned off, the nuclei will dissipate the excess of energy through the emission of electromagnetic waves with Larmour frequency. The excited nuclei will return from the "excited" state to the "ground" state.

After termination of the RF pulse, the net magnetization vector will continue to precess about the external magnetic field, even though the magnetization rotation around the x-axis is gone. The magnetization precession around the external magnetic field creates a changing magnetic flux through the coil placed perpendicular to the xy-plane. The magnetic flux, Φ, creates the measurable signal which is also referred to as free induction decay (FID). It is worth mentioning that only the transverse magnetization component will have an effect on the signal since it is perpendicular to the coil, while the longitudinal component which is parallel to the coil will not induce magnetic flux.

The detected signal can be calculated with the help of the Faraday's law of induction:

$$S(t) = -\frac{d\Phi(t)}{dt} = -\int_{V_s} \overrightarrow{B_1}(\vec{r}) \cdot dV \left(\frac{d\vec{M}(\vec{r},t)}{dt}\right), \qquad [1-30]$$

where $S(t)$ is the detected signal measured in volts, V_s the volume of the sample, $\overrightarrow{B_1}(\vec{r})$ – magnetic field produced by RF pulse, $\vec{M}(\vec{r},t)$ – magnetization density in the transverse plane at the position determined by the radius vector $\vec{r}$.

Considering that $\vec{M}(\vec{r},t) = \vec{M}(\vec{r})e^{-i\omega_0 t}$, since it is a rotating vector the equation [1-30] may be modified:

$$S(t) = i\omega_0 e^{-i\omega_0 t} \int_{V_s} \vec{M}(\vec{r}) \cdot \overrightarrow{B_1}(\vec{r}) \cdot dV. \qquad [1-31]$$

However, the energy transferred to the net magnetization is dissipated by two different mechanisms. The longitudinal component of magnetization regrows, and the system returns to thermal equilibrium due to the interaction of the spins with surrounding molecules (spin-lattice relaxation), while the transverse component of magnetization decays due to interactions of spins (spin-spin relaxation). These mechanisms add more complexity to the equation [1-31].

1.3.4 Spin-lattice Relaxation

After the application of an RF pulse, the system was excited due to transferred energy as discussed in the previous section. The process that brings the system back to thermal equilibrium is called spin lattice relaxation. It is responsible for regrowth of the net magnetization along the longitudinal direction. This process, also referred to as longitudinal or T_1 relaxation, occurs via interaction with the rapidly fluctuating magnetic fields caused by movements of surrounding magnetic moments. In order to facilitate the transitions between energy states, the frequencies of the rapid magnetic fields should be reasonably close to γB_0. The T_1 longitudinal relaxation, after the termination of the RF pulse in the rotating frame of reference, is described by a differential equation:

$$\frac{d}{dt}M_z = -\frac{M_z - M_0}{T_1}. \qquad [1-32]$$

Where M_0 is the initial magnetization at thermal equilibrium, T_1 is the longitudinal (spin-lattice) time constant, and M_z is the longitudinal component of the magnetization.

Considering the longitudinal relaxation process, the dynamic of the net magnetization is:

$$\frac{d}{dt}\vec{M}(t) = \gamma\left(\vec{M}(t) \times \overrightarrow{B_0}(t)\right) - \frac{M_z(t) - M_0}{T_1}\hat{k}\,. \qquad [1-33]$$

The general solution of the equation [1-32] describes the changes in longitudinal relaxation with respect to time:

$$M_z(t) = M(0)e^{-\frac{t}{T_1}} + M_0\left(1 - e^{-\frac{t}{T_1}}\right). \qquad [1-34]$$

If we consider that there is no longitudinal magnetization immediately after the application of a 90° RF pulse, M(0), longitudinal magnetization at t=0 is also 0. Hence,

$$M_z(t) = M_0\left(1 - e^{-\frac{t}{T_1}}\right). \qquad [1-35]$$

It can be observed from the equation above, that the longitudinal magnetization is regrowing exponentially with time and the rate of regrowth is determined by T_1. Figure 1-2 illustrates the behaviour of longitudinal magnetization for a range of T_1 values after the application of a 90° RF pulse.

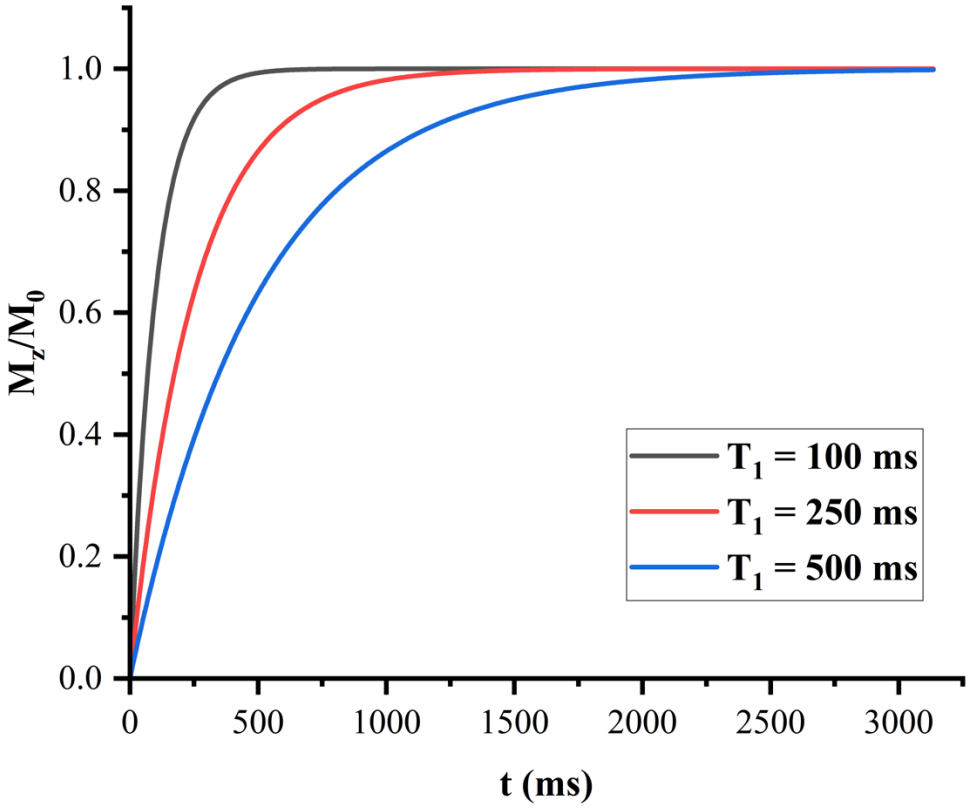

Figure 1-2 Longitudinal magnetization change following the application of a 90° RF pulse for T1 values of 100ms, 250ms, and 500ms.

If we consider the RF pulses with FA θ different from 90°, the spin-lattice relaxation equation will be:

$$M_z(t) = M_0\left(1 - (1 - cos\theta)\cdot e^{-\frac{t}{T_1}}\right). \qquad [1-36]$$

Additionally, the equation [1-31] which describes signal evolution should be changed to reflect spin-lattice relaxation effect:

$$S(t) = i\omega_0 e^{-i\omega_0 t} \cdot \int_{V_s} \overrightarrow{B_1}(\vec{r})\, \vec{M}(\vec{r}) \left(1 - (1 - cos\theta) e^{-\frac{t}{T_1(\vec{r})}}\right) dV. \qquad [1-37]$$

Since tissues in the human body have various T_1 relaxation times, they will have different signal intensities at the same moment of time if signal readout happens before longitudinal magnetization has fully regrown. This property is used widely for obtaining MRI contrast images. Full regrowth of the longitudinal magnetization will provide the maximum signal. It was experimentally found that it happens approximately at $5T_1$ after the application of a 90° RF pulse.

1.3.5 Spin-Spin Relaxation

As mentioned previously, there are two components of magnetization: longitudinal and transverse. In the previous section, the behaviour of the longitudinal magnetization was discussed after the application of an RF pulse. However, the transverse magnetization also experiences changes. The interactions of the neighbouring spins' magnetic moments will cause the loss of their coherence and dephasing and, hence, the decay of transverse magnetization. This effect is called spin-spin (transverse or T_2) relaxation. It can be represented by the following differential equation in a rotating frame of reference where T_2 is the spin-spin relaxation constant:

$$\frac{dM_{xy}}{dt} = -\frac{M_{xy}}{T_2}. \qquad [1-38]$$

This equation can be solved for transverse magnetization M_{xy} to illustrate its behaviour:

$$M_{xy} = M(0) e^{-\frac{t}{T_2}}, \qquad [1-39]$$

where M(0) is the transverse magnetization at the t=0 after the RF pulse ending.

It should be noted that T_2 values are always less than or equal to the T_1 value of the nuclei. The behaviour of the transverse magnetization after application of the 90° RF pulse is shown in Figure 1-3 for three different T_2 values.

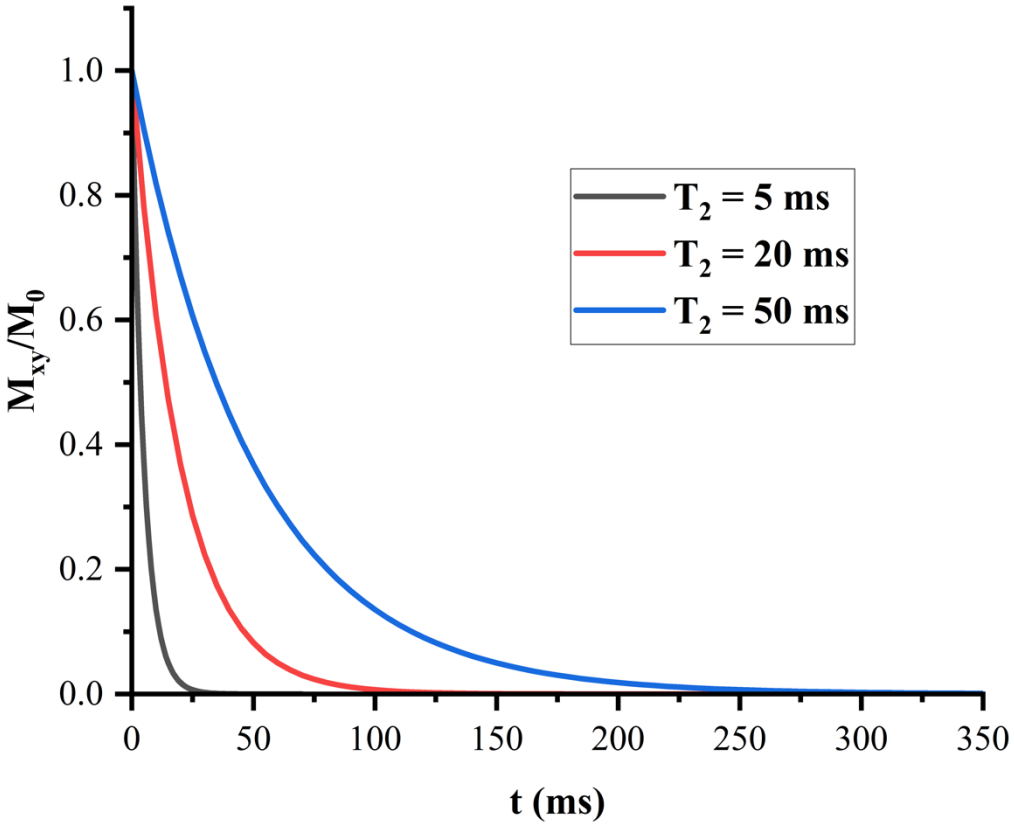

Figure 1-3 Transverse relaxation after application of 90° FA RF pulse for T_2 values of 5ms, 20ms, and 50ms.

In addition to the direct spin-spin interactions, spins can feel surrounding inhomogeneities of the external magnetic field and differences in local magnetic susceptibility. This will also contribute to the speed of spins dephasing and transverse magnetization decay. The relaxation time which includes the aforementioned factors is effective or apparent spin-spin relaxation time (T_2^*), which is even shorter than T_2 since it accounts for T_2^i- the contribution from magnetic field

inhomogeneities and T_2^s – the effect of local susceptibility differences in the sample. The equation for T_2^* is:

$$\frac{1}{T_2^*} = \frac{1}{T_2} + \frac{1}{T_2^i} + \frac{1}{T_2^s}. \qquad [1-40]$$

The equation of the signal [1-37] should be modified to reflect the T_2^* effect:

$$S(t) = i\omega_0 e^{-i\omega_0 t} \cdot \int_{V_s} \vec{M}(\vec{r}) \cdot \overrightarrow{B_1}(\vec{r}) \cdot e^{-\frac{t}{T_2^*(\vec{r})}} \cdot \left(1 - (1 - cos\theta) e^{-\frac{t}{T_1(\vec{r})}}\right) dV. \qquad [1-41]$$

We have shown that spin-spin relaxation affects the signal, making it unique for each tissue at the same point in time. This is used for the generation of MRI contrast for tissues in which T_2 values are notably different.

The longitudinal and transverse relaxation will alter the net magnetization behaviourdescribed in equation [1-25]:

$$\frac{d\vec{M}}{dt} = \gamma \cdot \left(\vec{M} \times \overrightarrow{B_{eff}}\right) - \frac{M_x\hat{\imath} + M_y\hat{\jmath}}{T_2} - \frac{M_z - M_0}{T_1}\hat{k}. \qquad [1-42]$$

1.3.6 Spatial localization of the MRI signal.

In the preceding sections, the primary emphasis was placed on the process of generating the MRI signal. However, to make MRI truly imaging modality, the signal must be localized. The signal from each voxel should be placed spatially in order to generate the image. This localization is achieved through the linear magnetic field gradients applied in addition to the external magnetic field B_0. These gradients are superimposed over the external magnetic field, hence the Larmor frequencies defined by equation [1-13] will be altered differently for specific points of the imaged sample. This will create a unique frequency and phase for each spatial position. Typically, three linear gradients are applied:

$$G_x = \frac{dB_z}{dx}; G_y = \frac{dB_z}{dy}; G_z = \frac{dB_z}{dz}. \quad [1-43]$$

The magnetic field gradient vector can be expressed by the following:

$$\vec{G}(\vec{r},t) = \frac{dB_z(t)}{dx}\hat{\imath} + \frac{dB_z(t)}{dy}\hat{\jmath} + \frac{dB_z(t)}{dz}\hat{k}. \quad [1-44]$$

Although three additional magnetic fields are applied, the net magnetic field will still point along the z-direction:

$$\vec{B}(x,y,z) = B_0\hat{k} + \left(G_x x + G_y y + G_z z\right)\hat{k}. \quad [1-45]$$

The phase of the nuclei rotation is also spatially distributed by linear magnetic fields:

$$\Delta\varphi(\vec{r},t) = \gamma \int_0^t G\,(\vec{r},t)\cdot\vec{r}dt. \quad [1-46]$$

Information about the MRI signal is stored in the k-space – a space of spatial frequencies. Let us assume that:

$$\vec{k}(t) = \frac{\gamma}{2\pi}\int_0^t \vec{G}\,(t)dt. \quad [1-47]$$

Therefore equation [1-46] changes to:

$$\Delta\varphi(\vec{r},t) = 2\pi\left(\vec{k}(t)\cdot\vec{r}\right). \quad [1-48]$$

The position in k-space characterizes the amount of phase gained during the magnetic field gradients application. The information from k-space can be transformed into an image by doing the inverse Fourier transform which converts the signal from the frequency domain into the time domain.

In doing so, the application of the magnetic field gradients will add an additional linear phase factor into the signal equation:

$$S(t) = i\omega_0 e^{-i\omega_0 t} \int_{V_s} \vec{M}(\vec{r}) \cdot \overrightarrow{B_1}(\vec{r}) \cdot \left(1 - e^{-\frac{t}{T_1(\vec{r})}}\right) \cdot e^{-\frac{t}{T_2^*(\vec{r})}} \cdot e^{-i\Delta\varphi(\vec{r},t)} dV. \qquad [1-49]$$

And taking into account equation [1-48] we get:

$$S(\vec{k}) = i\omega_0 e^{-i\omega_0 t} \int_{V_s} \vec{M}(\vec{r}) \cdot \overrightarrow{B_1}(\vec{r}) \cdot \left(1 - e^{-\frac{t}{T_1(\vec{r})}}\right) \cdot e^{-\frac{t}{T_2^*(\vec{r})}} \cdot e^{-i2\pi(\vec{k}\cdot\vec{r})} dV. \qquad [1-50]$$

For simplification of the equation above, the effective magnetization density that incorporates the relaxation effects, phase effects, and $\overrightarrow{B_1}$, will be introduced:

$$M_{eff}(r) = i\omega_0 e^{(-i\omega_0 t)} \cdot \vec{M}(\vec{r}) \cdot \overrightarrow{B_1}(\vec{r}) \cdot \left(1 - e^{-\frac{t}{T_1(\vec{r})}}\right) \cdot e^{-\frac{t}{T_2^*(\vec{r})}}. \qquad [1-51]$$

Therefore equation [1-50] is modified to:

$$S(\vec{k}) = \int_{V_s} M_{eff}(\vec{r}) \cdot e^{-i2\pi(\vec{k}\cdot\vec{r})} dV. \qquad [1-52]$$

It may be observed that the signal is a function of the position in k-space and integrated over all image space. The effective magnetization density may be calculated using the inverse Fourier transform of equation [1-52]:

$$M_{eff}(\vec{r}) = \int_{k_s} S(\vec{k}) \cdot e^{i2\pi(\vec{k}\cdot\vec{r})}\, dk. \qquad [1-53]$$

Now effective magnetization is the function of the position in the image space and integrated over k-space.

To have an MRI image with sufficient contrast and resolution, the k-space should have enough data. This data is acquired through the application of unique sequences of RF pulses, magnetic field gradient waveforms, and timing parameters.

1.3.7 Pulse sequence parameters

The parameters of the pulse sequences determine the contrast, SNR, and resolution of the acquired image. Each pulse sequence can be separated into four main steps: RF pulse, slice-selection, phase encoding, and frequency encoding.

1.3.7.1 RF pulse

The RF excitation pulse is the first step for nearly all pulse sequences (with the exemption of those where pre-pulses are applied). It tips the longitudinal magnetization into the transverse or xy-plane and makes it discoverable by the coils. The RF pulse may be of any angle as long as it creates a projection on the xy-plane. Intuitively, the closer FA is to 90°, the higher the acquired signal will be. However, the spin-lattice relaxation effect, which recovers the longitudinal magnetization, will affect the recovery time in the next way: the higher be FA, the longer time it will take for magnetization to recover. Therefore, the time between two subsequent excitation pulses, necessary for magnetization to recover, is called repetition time or TR. Richard Ernst was awarded the Nobel Prize for his development of the optimal FA for SNR maximization for a particular TR[33]. This so-called Ernst angle is expressed by:

$$\theta = \cos^{-1}\left(e^{-\frac{TR}{T_1}}\right). \qquad [1-54]$$

One of the fundamental characteristics of the RF pulse is the associated bandwidth (BW) which determines the range of the precessional frequencies that will be excited. If the FA of the RF pulse is less than 30°, the small FA approximation may be used for BW calculation: a Fourier transform of the RF pulse shape may be performed. However, if the RF pulse has an infinite spectrum, the BW is determined by the frequency range containing ~95% of the RF power. This is typical for rectangular RF pulses.

1.3.7.2 Slice selection gradient

The application of an RF pulse is necessary to excite the spins within the sample, however, the excitation of the whole sample is not desirable. Therefore, it must be localized. This localization is achieved through the application of a slice-selective magnetic field gradient applied simultaneously with the RF excitation pulse. This gradient also can be referred to as z-gradient since it is conventionally aligned with the external magnetic field $\overrightarrow{B_0}$. It allows the excitation of a specific slice of magnetization. There are three conventionally accepted orientations of the slices, which depend on the orientation of the slice-selecting gradient: axial orientation, coronal orientation, and sagittal orientation.

The thickness of the 2D excited slice is determined by the BW_{RF} – bandwidth of excitation pulse and G_z – the strength of the slice-selection magnetic field gradient:

$$\Delta z = 2\pi \cdot \frac{BW_{RF}}{\gamma G_z}. \qquad [1-55]$$

It should be mentioned that transverse magnetization accumulates the phase during the application of the slice-selecting gradient, henceforth an additional gradient is applied in the opposite direction to destroy the accumulated phase.

1.3.7.3 Phase Encoding Gradient

In order to arrange the data acquisition in 2D space the phase and frequency encoding gradients are applied. Their directions are interchangeable, but typically phase encoding gradients are applied along the ordinate or y-axis. The applied gradient makes the spins precess a frequency which is a function of the position:

$$\omega(y) = \gamma G_y y. \qquad [1-56]$$

After termination of the gradient, the frequency of the spins returns to the original value, but the phase accumulated during the gradient application remains.

The position of the k-space after the phase encoding gradient is:

$$k_y = \frac{\gamma}{4\pi} \cdot \left(T_{PE} + t_f - t_s\right) G_y, \qquad [1-57]$$

where T_{PE} – the duration of the phase encoding gradient, t_f – time when the current in the gradient coil is terminated, and t_s – a time when the gradient strength gets to the G_y value. This equation was derived for the trapezoidal gradient form, which is the most widely utilized in practice.

1.3.7.4 Frequency Encoding and Acquisition

Frequency encoding gradients are applied after phase encoding happens or simultaneously with it. The filling of the k-space or data acquisition (ACQ) is happening at the same time as frequency encoding. Typically, frequency encoding gradients are applied along the abscissa or x-axis.

The duration and signs of the phase and frequency encoding gradients determine the trajectory of the k-space filling with data.

1.3.8 Imaging Pulse Sequences

There are numerous pulse sequences developed for MRI imaging. Conventionally the MRI signal is acquired after an echo of the excited signal is generated. There are two main techniques for it: spin echo and gradient echo.

1.3.8.1 Spin Echo Imaging Pulse Sequence

Considering section 1.3.5 where the transverse relaxation was discussed, there are T_2 and T_2^* decays. While T_2 is irreversible and caused by microscopic magnetic field fluctuations, T_2^*

decay is caused by local differences in the external magnetic field in addition to T_2 decay. The dephasing caused by the local dissimilarities of the external magnetic field can be eliminated by the application of the refocusing RF pulse. The basic spin echo (SE) technique relies on the application of a 180° refocusing RF pulse which rotates magnetization vectors around the application axis of the refocusing pulse. It may be observed in Figure 1-4, that the 90° excitation pulse rotates the longitudinal magnetization vector into the transverse plane. The dephasing of the different magnetic moments' vectors occurs over time. The refocusing 180° RF pulse is applied to result in the generation of the signal echo, which happens at echo time (TE). It should be mentioned that slice selective gradients are applied during the excitation and refocusing RF pulses, phase encoding gradient is applied before refocusing pulse and frequency encoding gradient is applied for echo readout.

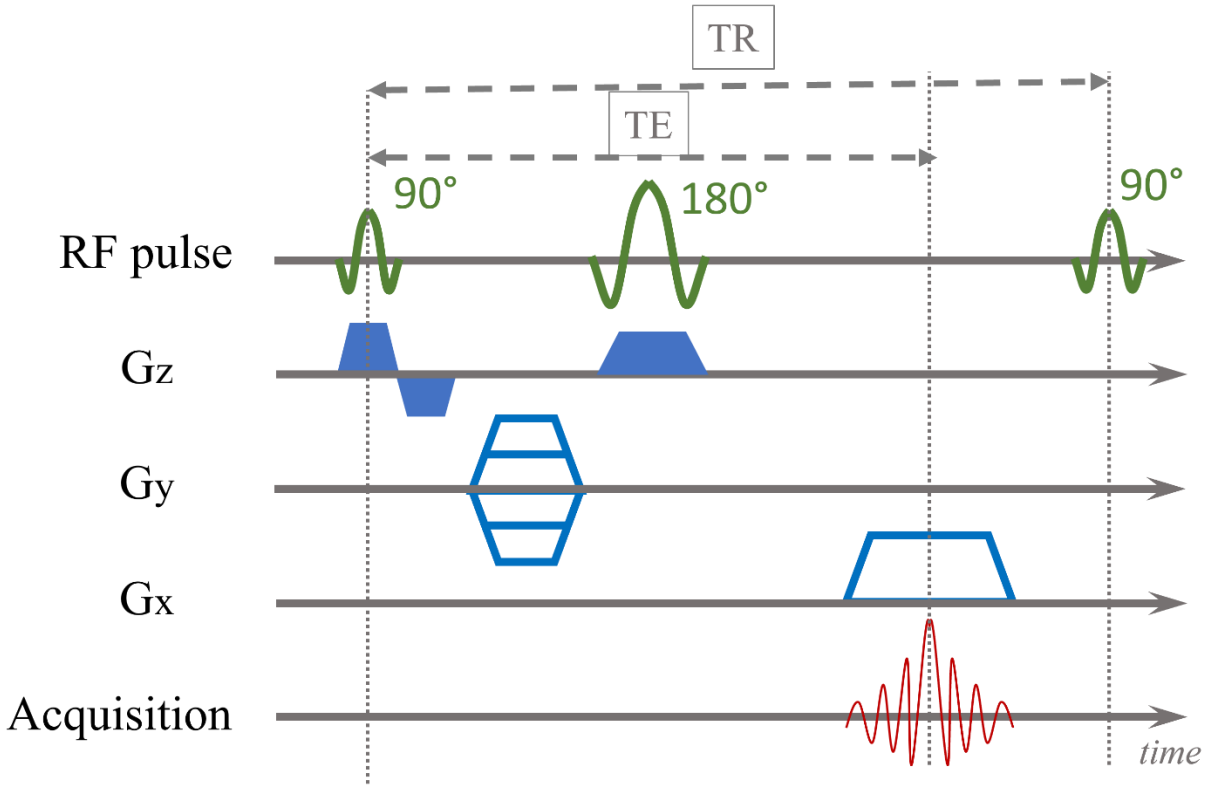

Figure 1-4 Basic spin echo pulse sequence.

1.3.8.2 Gradient Echo Imaging Pulse Sequence

The first step of the SE pulse sequence and gradient echo (GRE) sequence is the same: application of excitation pulse together with slice selective gradient. However, the signal echo is created by the application of gradients, not by additional RF pulse. Firstly, a negative frequency gradient is applied which dephases magnetic moment vectors and after the refocusing positive frequency gradient is applied and an echo is created.

Conventional 2D GRE utilizes Cartesian trajectories with k-space filled line-by-line (Figure 1-5). The pulse sequence should be repeated multiple times to fill all lines of k-space.

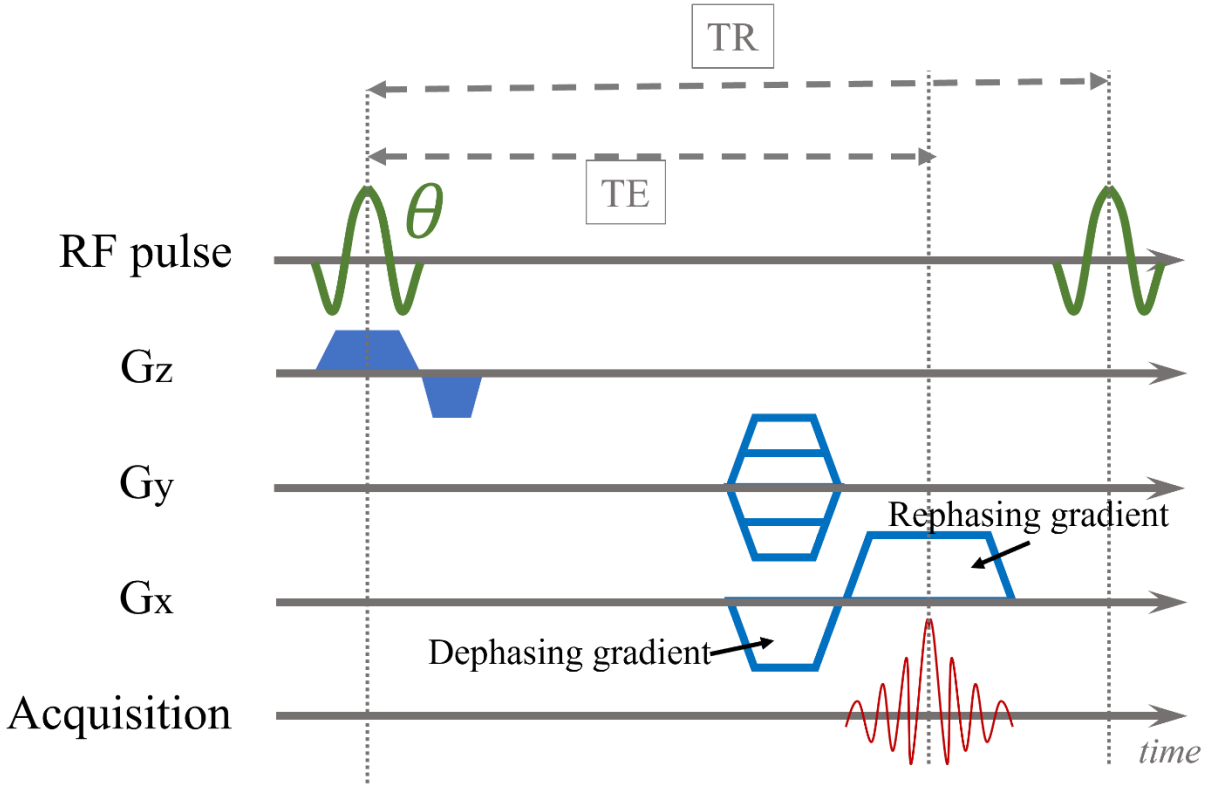

Figure 1-5 Pulse sequence diagram of the 2D gradient echo.

1.3.8.3 3D Gradient Echo Imaging

The conversion from 2D to 3D GRE requires some modifications. RF pulses typically used for 3D imaging have a short duration and a broad excitation profile in the frequency domain, they

are also considered "hard" pulses. 3D imaging requires the excitation of the whole imaged volume; therefore, the magnitude of the slice-selection gradient is reduced to excite a thick slice of magnetization or slice selective gradient is absent at all. When the k-space filling happens the phase encoding gradients are simultaneously applied in two directions G_y and G_z; they are followed by a frequency encoding gradient (Figure 1-6). The 3D k-space dataset is sampled and then the Fourier transform is used to recreate the final 3D image.

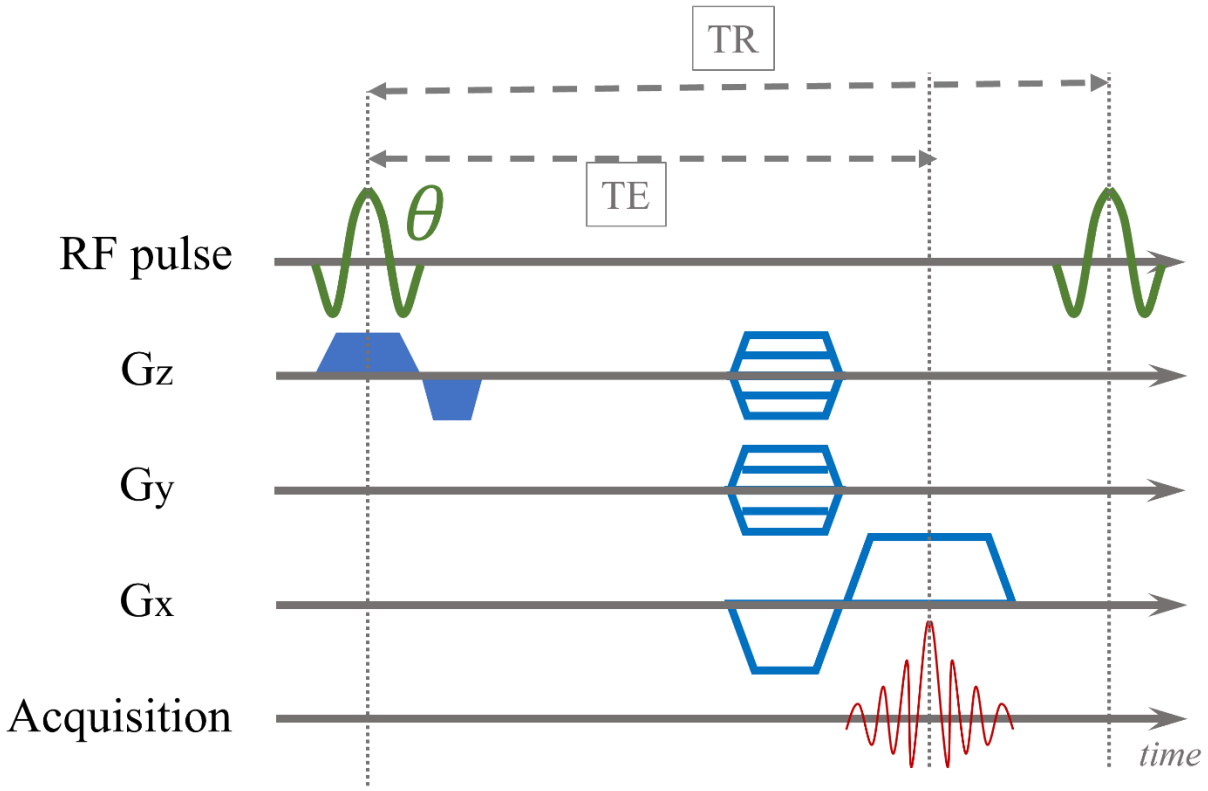

Figure 1-6 Pulse sequence diagram for a 3D GRE imaging acquisition.

1.3.9 Image parameters

Each image can be characterized by a field of view (FOV) which is calculated from the k-space:

$$FOV_x = \Delta k_x^{-1}; FOV_x = \frac{2\pi}{\gamma \cdot G_x \cdot T_s}, \qquad [1-58]$$

where Δk_x- the distance between two k-space points in x-direction, T_s – signal sampling time.

$$FOV_y = \Delta k_y;\ \ FOV_y = \frac{2\pi}{\gamma \cdot \Delta G_y \cdot T_p}, \qquad [1-59]$$

where Δk_y – the distance between two k-space points in y direction, ΔG_y – the difference of the G_y magnitude, T_{PE} – duration of the phase encoding gradient.

The image resolution is determined by the k-space coverage in both directions:

$$\Delta x, y = \frac{1}{2k_{x,y}^{\max}}\ . \qquad [1-60]$$

One of the main and most important characteristics of an image is SNR, which also determines image quality. It is calculated by dividing the mean signal value by the standard deviation of the noise. The Brownian motion of electrons within the sample causes the MRI noise which can be described in the next equation:

$$noise = \sqrt{(4kTR_s\Delta f)}, \qquad [1-61]$$

where R_s – the real part of the input impedance, Δf - frequency BW, T – sample temperature.

Considering the equation [1-50] for the signal and the equation discussed above:

$$SNR = \frac{i\omega_0}{\sqrt{4kTR_s\Delta f}} e^{-i\omega_0 t} \int_{V_s} \vec{M}(\vec{r}) \cdot \overrightarrow{B_1} \cdot \left(1 - e^{-\frac{t}{T_1(\vec{r})}}\right) \cdot e^{-\frac{t}{T_2^*(\vec{r})}} \cdot e^{-i2\pi(\vec{k}\cdot\vec{r})} dV. \qquad [1-62]$$

Image SNR is determined by the available magnetization, T_1, T_2^*, TR, TE. It can be calculated by the next equation for the applied FA θ:

$$SNR \propto \frac{\left(1 - e^{-\frac{TR}{T_1}}\right) e^{-\frac{TE}{T_2^*}}}{1 - cos\theta e^{-\frac{TR}{T_1}}} \cdot sin\theta. \qquad [1-63]$$

If $\theta = 90°$:

$$SNR \propto \left(1 - e^{-\frac{TR}{T_1}}\right) e^{-\frac{TE}{T_2^*}}. \quad [1-64]$$

Additionally, SNR depends on the voxel size and acquisition time:

$$SNR \propto (voxel\ size) \cdot \sqrt{readout\ time}; \quad [1-65]$$

$$SNR \propto \Delta x \cdot \Delta y \cdot \Delta z \cdot \sqrt{\frac{NSA \cdot N_x \cdot N_y \cdot N_z}{BW}}, \quad [1-66]$$

where NSA is the number of signal averages, $\Delta x, \Delta y, \Delta z$ – dimensions of the voxel, N_x, N_y, N_z – number of readout points in x-, y-, and z-directions.

Another important characteristic of the image is contras-to-noise ratio (CNR), it is calculated as a difference in signals of the region-of-interest (ROI) (S_{ROI}) and background ($S_{background}$) divided by noise value from equation [1-61]:

$$CNR = \frac{S_{ROI} - S_{background}}{noise} \quad [1-67]$$

1.4 Brain Proton Imaging

As it is very clear by now from the information discussed above conventional ^{1}H MRI has superior soft-tissue contrast. Hence, it is widely used for the diagnostic of brain diseases and abnormalities. The commonly acquired images for the clinical examinations are 3D T_1- and T_2-weighted images (T1WI and T2WI)[34,35]. The basic principles of T1WI are the utilization of short TE and short TR, while T2WI is acquired with intermediate TE and long TR.

3D T1WI images have high grey-white matter contrast and good spatial resolution, it is the most commonly used sequence for structural analysis and allows easy annotation of healthy tissues[34,36–38]. Moreover, T1WI provides a thorough assessment of cerebral atrophy[39].

T2WI is ideal for scoring the gray matter, subcortical lesions, and infratentorial lesion categories[34].

T_2-weighted fluid-attenuated inversion recovery (T2-FLAIR) is used to distinguish cerebrospinal fluid (CSF) and subtle lesions[40]. It utilizes the 180° pre-pulse at the inversion time prior to the excitation pulse, which nulls the signal from CSF on the images[25]. It is used for vascular damage detection and can indicate metabolic, inflammatory, infective, and toxic processes[36]. It is considered best for changes in deep white matter lesions.

T_2^*-weighted (susceptibility-weighted) gradient echo sequence (T2*GRE) is used to detect microhemorrhages and cerebral microbleeds[41], which is helpful for Alzheimer's disease diagnosis[34,42].

Diffusion weighted imaging (DWI) contrast is created by microscopic water motion. It provides information which is absent in the standard T1WI and T2WI. It is mostly used for acute stroke assessment but also can be used for brain tumours. It is characterized by the apparent diffusion coefficient (ADC) and images are usually represented as ADC maps. Lesions with restricted diffusion are bright on the DWI images and dark on the ADC maps[43]. Additionally, DWI can differentiate between necrotic lesions and abscesses and it is particularly useful for detecting recent infarct[44].

As an example, the basic protocol used for clinical assessment of cognitive impairment includes the next sequences: 3D T1WI, T2WI, FLAIR, T2*GRE, and DWI (ADC map)[36]. Vascular brain injuries can be diagnosed by using routine MRI scans: white matter hypointensities are seen

on the FLAIR images, cerebral microbleeds are visible on GRE MRI sequences and T_2-weighted MRI[45].

More advanced imaging techniques utilized in medical diagnosis include arterial spin labelling (ASL), magnetic resonance spectroscopy (MRS), dynamic susceptibility contrast (DSC), diffusion tensor imaging (DTI), and many others.

ASL uses magnetically labelled blood as a flow tracer delivering the cerebral blood flow (CBF) images. The perfusion characteristics of brain and brain lesions may provide specific diagnosis[46]. It also provides valuable information about tumours tissue perfusion which is used for operation planning[43].

MRS or chemical shift imaging (CSI) is a multivoxel technique, which acquires signals from different metabolites in the brain. Typically, MRS acquisition starts with anatomic images, which are used for further localization, and then the spatial distribution of metabolites is acquired. The result of 2D MRS is a matrix of metabolites spectra. The concentration of metabolites is very important information, which can tell about abnormal processes[47]. For example, the main metabolites of interest in brain tumours are choline, creatine, N-acetylaspartate, myoinositol, lipids and lactate.

DSC MRI is mostly used for measuring relative cerebral blood volume, cerebral blood flow, mean transit time and other parameters[38]. Typically, the gadolinium-based contrast agents (GBCA) are utilized for the injection. They further spread through the body and brain tissue specifically and alter the signal of the surrounding protons. The diffusion of the GBCA is monitored by a dynamic series of T_2 or T_2^*-weighed MR images[48].

1.5 Hyperpolarized ^{129}Xe MRI

Conventional MRI relies on the signal detection from the excited spins, however, as it was discussed in section number 1.3.2, only a small number of spins with lower energy can accept the energy. This number of spins is determined by population difference, which is also referred to as polarization. Indeed, the extremely low thermal polarization of almost all nuclei poses a challenge, requiring a combination of factors such as high natural abundance, high gyromagnetic ratio, and most importantly – high concentrations of the nuclei in the imaged sample or area. However, when imaging the areas which by default do not have a high proton concentration, for example, lungs, the only solution is to use gaseous agents visible in MRI. The effectiveness of this solution was for the first time demonstrated by Albert et al in 1994, when the imaging of the excised mouse lungs was performed using hyperpolarized ^{129}Xe (HP ^{129}Xe) at 9.4 T[49]. Utilization of HP gases allowed to visualize the distribution of the inhaled gas within the lungs[50].

This section is dedicated to the basic concepts of the HP MRI and its utilization. There are three main techniques that allow transferring nuclei into the hyperpolarized state: spin exchange optical pumping (SEOP), dynamic nuclear polarization (DNP), and metastable exchange optical pumping (MEOP). DNP is mostly used for hyperpolarization of ^{13}C atoms[51], but also can be utilized for non-conducting solids, while MEOP may only be used for ^{3}He hyperpolarization[52].

To gain a deeper understanding of the fundamental concepts behind HP noble gas MRI, readers are encouraged to consult the book titled "Hyperpolarized and Inert Gas MRI: From Technology to Application in Research and Medicine" authored by Albert and Hane[53].

1.5.1 Spin Exchange Optical Pumping

Since the main focus of this work is HP ^{129}Xe, only its hyperpolarization process will be discussed in detail. Spin Exchange Optical Pumping (SEOP) may be used for hyperpolarization

only gases, but with high levels of polarization[54]. The process involves the initial polarization of the alkali atom's electrons by circularly polarized light and further transfers the polarization to the noble gas nuclei. Alkali metals are used for SEOP due to having one valence electron on the outer shell, the most widely utilized alkali metal is rubidium (Rb). Rb has a comparably big atom radius and, a low melting point, its D_1 transition is possible using commercially available lasers, and the spin-exchange cross-section between Rb and noble gas is high.

The first step is optical pumping during which the Rb vapour is created and illuminated by circularly polarized light (Figure 1-7A). It will cause the polarization of the electrons on the s-shell, specifically, the transition from the ground state $^2S_{1/2}$ to the excited state $^2P_{1/2}$ (of course, different alkali metal transitions will occur from the $S_{1/2}$ to $P_{1/2}$ on correcsponding energy level). The allowed change of the magnetic quantum number determined by electronic selection rules is $\Delta m = \pm 1$. Hence the allowed transitions for Rb are $m_s = -1/2 \rightarrow m_p = +1/2$ and $m_s = +1/2 \rightarrow m_p = -1/2$, these transitions are induced by left circularly polarized light (red wavy arrow) and right circularly polarized light respectively. The excited electrons will tend to lose the gained energy and relax back to the ground state, this transition will also occur by selection rule. Additionally, atoms with electrons in the excited state may collide with noble gas atoms, which will equalize the population of $m_p = -1/2$ and $m_p = +1/2$ sublevels. In order to fully polarize the Rb vapour, the quenching gas N_2 is present in the chamber. The collisions of the excited electrons with N_2 molecules allows the transition $\Delta m = 0$: $5P(m_p = -1/2) \rightarrow 5S(m_s = -1/2)$ and $5P(m_p = +1/2) \rightarrow 5S(m_s = +1/2)$. As a result of these collisions, the process will continue until the complete polarization of the Rb vapour. It should be noted that buffer gases such as helium

are present in the chamber for pressure broadening of the Rb absorption cross section to enable a large fraction of laser light to be productively absorbed.

The next step of the SEOP is spin exchange, which is initiated by flowing the mixture of noble gas, ^4He, and N_2 through the optical cell. The interaction of the noble gas and polarized s-shell Rb electrons allows the transfer of angular momentum through hyperfine Fermi interaction. The transfer may occur through either binary non-elastic collisions or the formation of transient Van der Waals complexes. Binary collisions (Figure 1-7B) involve only Rb and noble gas atoms, they are dominant for noble gases with high pressure (~760 Torr). For heavier noble gases like ^{129}Xe, which polarized at low pressures (~10-100 Torr), the contribution of van der Waals complexes to the spin exchange greatly exceeds the contribution of binary interactions. Atoms of Rb and noble gas create van der Waals complex (Figure 1-7C), which is destroyed by the collision with N_2 molecules, however, the time of interaction is enough for orbital moment transfer.

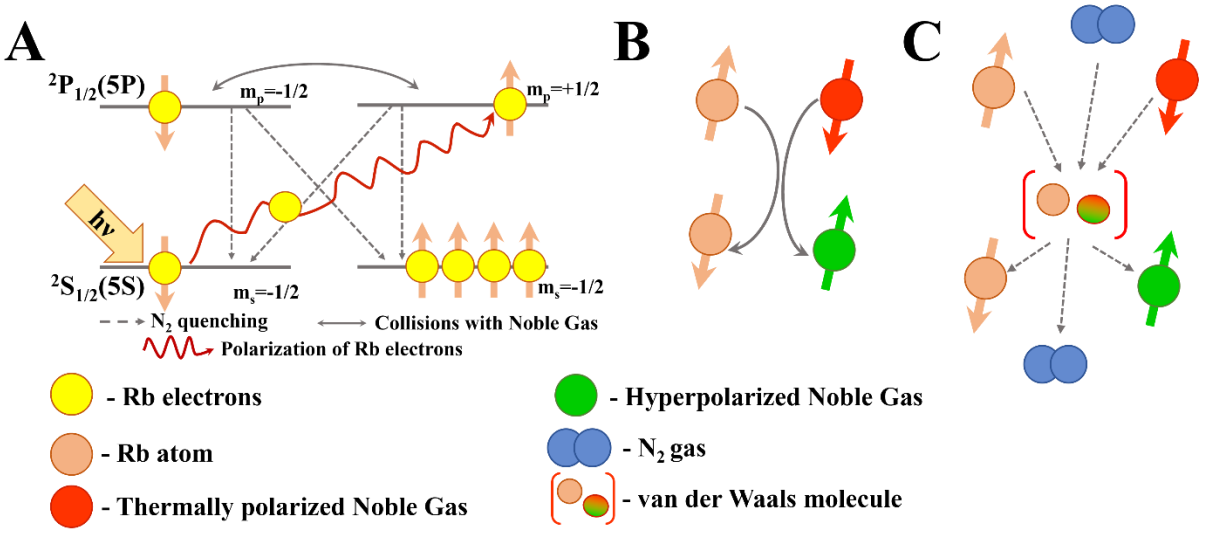

Figure 1-7 A) Optical pumping process of alkali metal electronic spins. B) Two-body spin-exchange collisions. C) Three-body spin-exchange collisions.

The HP noble gas has then to be separated from the mixture. The mixture is accumulated in the cold finger immersed in liquid N_2, noble gases typically have a higher freezing point, hence they are frozen out and separated from ^4He and N_2.

Of course, not all interactions lead to successful spin-exchange transfer, however, the Rb vapour can be "reused" and polarized again with optical pumping. This will allow to achieve high polarization of the noble gases over time.

1.5.2 Imaging considerations for HP nuclei

The hyperpolarized state is an artificially induced metastable state, hence it does not exist in thermal equilibrium and trying to reach it. That causes different nuclear magnetic properties of the HP nuclei compared to thermally polarized nuclei discussed in sections 1.3.4 and 1.3.5.

The main difference in the HP nuclei properties is the absence of longitudinal magnetization regrowth. Spin-lattice relaxation brings the net magnetization to the thermal equilibrium state, however, in this state the excess in the spin population between the energy levels is much lower than in the hyperpolarized state. The hyperpolarized state has a large population excess on one of the Zeeman levels and T_1 relaxation will destroy this excess, and the energy will dissipate. This property changes the equation for longitudinal magnetization [1-35] since $M(0) \gg M_o$:

$$M_z(t) = M(0)e^{-\frac{t}{T_1}}. \qquad [1-68]$$

The inability of HP nuclei to restore net magnetization after imaging sequences causes conventional MRI imaging techniques to be unsuitable for HP imaging.

In order to create MRI images with decent quality as many as possible data points should be stored in k-space, this requires longitudinal magnetization to last sufficiently long. This can be

achieved with the utilization of low FA for excitation pulses to encode the lines of k-space. However, loss of magnetization will happen over k-space encoding, resulting in image blurring if the outer areas of k-space are encoded last. If constant FA is used it is possible to correct the k-space trajectory to compensate for signal loss. The other solution is using variable FA, which will account for magnetization loss.

Another approach for HP imaging is returning the longitudinal magnetization by rewinding pulses. Basically, the initial 90° excitation pulse and the first k-space trajectory are acquired, then another pulse is applied to tip back magnetization to the z-axis and the sequence is repeated. This technique requires a long enough spin relaxation time of the HP nuclei in the media. Additionally, there is a high possibility of image artifact due to local and external magnetic field inhomogeneities[55].

Yet, there is an advantage of using HP nuclei due to the absence of need in long TR times. Therefore, the scan times for HP nuclei are very low compared to ^{1}H MRI.

1.5.3 Imaging with HP ^{129}Xe

The HP MRI was initially invented to address the challenges of the conventional MRI in lung imaging. The main "go-to" HP gases are ^{3}He and ^{129}Xe, however, ^{129}Xe slowly wins over ^{3}He due to its lower cost. It is used in research and preclinical imaging, moreover, it was approved for clinical lung imaging in the UK in 2021[56] and by US FDA in 2022[57].

Xenon is a well-known general anesthetic agent, hence it is safe for inhalation if the total concentration of it in the lungs stays below 50% and the patient's oxygen saturation is monitored[58]. Typically, the single breath-hold inhalation of 1L of HP ^{129}Xe is done for lung imaging as this allows to keep the ^{129}Xe concentration at a safe level without any adverse effects[59–61]. Lung imaging with HP ^{129}Xe allows for visualization of well-ventilated lung areas and areas with

ventilation defects determined by the ^{129}Xe signal intensity. The important biomarkers for pulmonary disorders such as ventilation volume (VV) and ventilation defect percentage (VDP) may be estimated from the images. Diffusion weighted imaging with HP ^{129}Xe allows to calculation of ADC values which provides information about the alveolar size and lung microstructure[62,63]. Moreover, HP ^{129}Xe lung imaging was recently used to understand the consequences of COVID-19[64–66]. The ventilation abnormalities were clearly detected in the lungs impacted by COVID-19.

Another important application of HP ^{129}Xe is assessment of the brain perfusion. It is possible due to sufficient ^{129}Xe solubility in the blood (Oswald coefficient is 0.17, L)[30] and further distribution to the highly perfused organs like the brain and kidneys. The utilization of HP ^{129}Xe for brain imaging is elaborated in Chapter 2 of this thesis.

1.5.4 HP ^{129}Xe in blood

As it was mentioned before HP ^{129}Xe has good solubility in blood[67] and other tissues. Furthermore, the chemical structure of ^{129}Xe comprises a relatively big atom and large electron cloud which is very stable due to the complete outer valence shell. The presence of a large electron cloud makes HP ^{129}Xe very sensitive to the local magnetic fields resulting in a unique chemical shift of ^{129}Xe in each media. For example, in the whole blood, HP ^{129}Xe has two distinct peaks: ^{129}Xe bound to RBC and ^{129}Xe dissolved in plasma[68]. Additionally, the other spectroscopic parameters are also changing with the altering of the media properties. Albert et al proved that HP ^{129}Xe T_1 is affected by the oxygenation of the whole blood[69].

The discussed HP ^{129}Xe properties were efficiently used for the gas transfer study in the human lungs. The first-ever results were demonstrated by Mugler et al in 1997 with inhalation of 0.5 L of HP ^{129}Xe and signal observation over time[70]. Over the time, the techniques for gas transfer

were refined and currently, there are two main approaches: chemical shift saturation transfer (CSSR) and xenon transfer contrast (XTC).

CSSR technique utilizes a narrow BW 90° saturation pulse for dissolved ^{129}Xe signal destruction and further monitors its recovery over time[71]. It should be mentioned that only the MR spectroscopy spectra are acquired. It calculates the average gas time which can be used as a biomarker for various lung diseases[72–74] and correlates with lung parenchyma thickness[72].

XTC relays on the acquisition of time-resolved depolarization maps of the HP ^{129}Xe gas phase[75,76]. Depolarization pulses in this case applied multiple times to the ^{129}Xe dissolved in blood and lung tissue. Of course, signals in the blood and lung tissue will regrow due to exchange, which will result in gas phase signal depletion which gets mapped by XTC imaging.

However, for both of these approaches, the exact value of the ^{129}Xe chemical shift in the blood and lung tissue is required. But, as it was already proven, chemical shift can be altered by the presence of molecules with local magnetic fields, hence it is feasible to study the effects of metabolites such as oxygen and glucose on the chemical shift of the dissolved HP ^{129}Xe.

1.5.5 Chemical Exchange Saturation Transfer

Chemical Exchange Saturation Transfer (CEST) involves saturation of the bound pool with RF pulses applied over a time period longer than the presence of a molecule, whose signal is saturated, in the host. This results in the destruction of the signal from the bound pool. However, due to chemical exchange, the signal from the bulk pool will be also saturated by the accumulation of the thousands of molecules affected by the saturation pulse from the bound pool. The saturation may be evaluated quantitively by the next formula:

$$CEST = \frac{SNR_{ref} - SNR_{sat}}{SNR_{ref}} \cdot 100, \qquad [1-69]$$

Where $CEST$ is the saturation of the bulk pool in %, SNR_{ref} – signal-to-noise ratio of the bulk pool without application of saturation pulses, SNR_{sat} – signal-to-noise ratio of the bulk pool after application saturation pulses to the bound pool. The results of the CEST approach may be illustrated by z-spectrum, which shows the remaining z-magnetizations after saturation pulses application over the range of frequencies.

1.5.6 Hyperpolarized Chemical Exchange Saturation Transfer

The decent solubility of HP ^{129}Xe in aqueous solutions makes it a good candidate for multiple molecular studies[77–79]. Additionally, HP ^{129}Xe's large electron cloud provides it with a broad chemical shift range (about 300 ppm) in different chemical environments. If a host structure is present in the solution, HP ^{129}Xe may undergo transient binding with it. In addition, if the exchange time is relatively slow compared to the NMR time scale, two different HP ^{129}Xe NMR resonances may be detected: one from the bulk pool or dissolved ^{129}Xe and another from the bound pool or ^{129}Xe inside of the host. In cases, when these two resonances are well-separated, the selective RF pulses may be applied to one of them (typically the bound pool). Another ^{129}Xe pool will also "feel" these RF pulses due to constant ^{129}Xe exchange. This may be used for the detection of one of the pools by NMR.

If the CEST effect is combined with HP nuclei, a new method Hyperpolarized Chemical Exchange Saturation Transfer (HyperCEST) is created. The HyperCEST scheme is shown in Figure 1-8 on the example of cucurbit[6]uril molecule (CB6). HP ^{129}Xe atom enters CB6 from the dissolved pool and the depolarization RF pulse applied at the frequency of ^{129}Xe bound to CB6. This leads to the destruction of HP ^{129}Xe polarization inside the CB6 molecule. Depolarized ^{129}Xe leaves the CB6 molecule and transfers to the dissolved pool. Depolarized ^{129}Xe accumulated in

the dissolved pool over time of saturation pulse application due to constant exchange, which makes the signal from the dissolved ^{129}Xe significantly drop or disappear at all. It should be noted, that in the whole blood dissolved ^{129}Xe exists in two forms: ^{129}Xe bound to red blood cells (RBC) and ^{129}Xe dissolved in plasma, this makes the HyperCEST experiment more complicated.

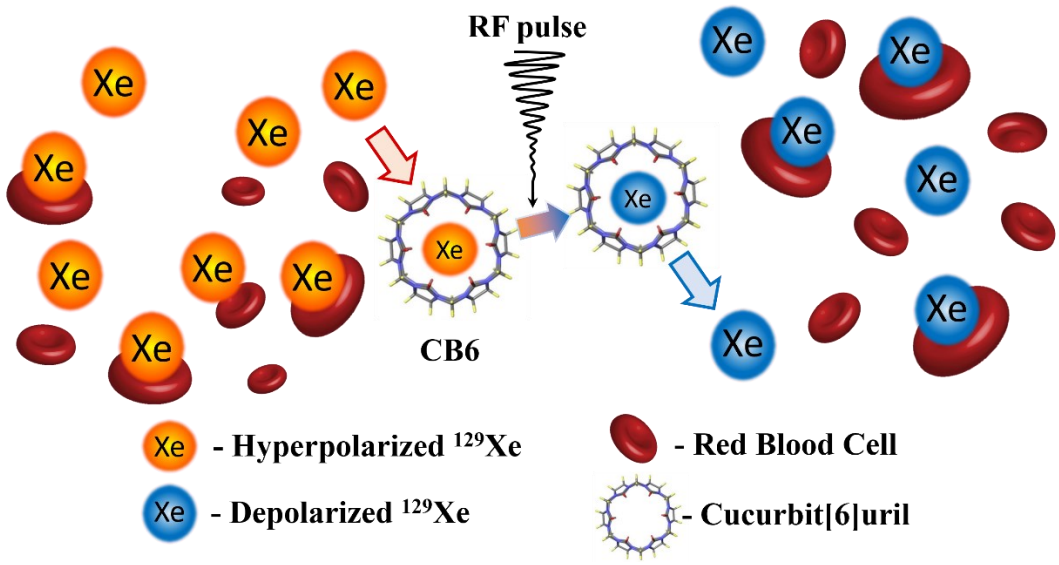

Figure 1-8 HyperCEST scheme with cucurbit[6]uril as a host molecule.

Over the span of the HyperCEST experiment RF depolarization pulse is applied to the range of frequencies and NMR spectra are recorded after each RF depolarization pulse. The results of HyperCEST are displayed in z-spectra the same as for CEST. The typical z-spectra is shown in Figure 1-9, there is only one dissolved pool of HP ^{129}Xe for simplicity.

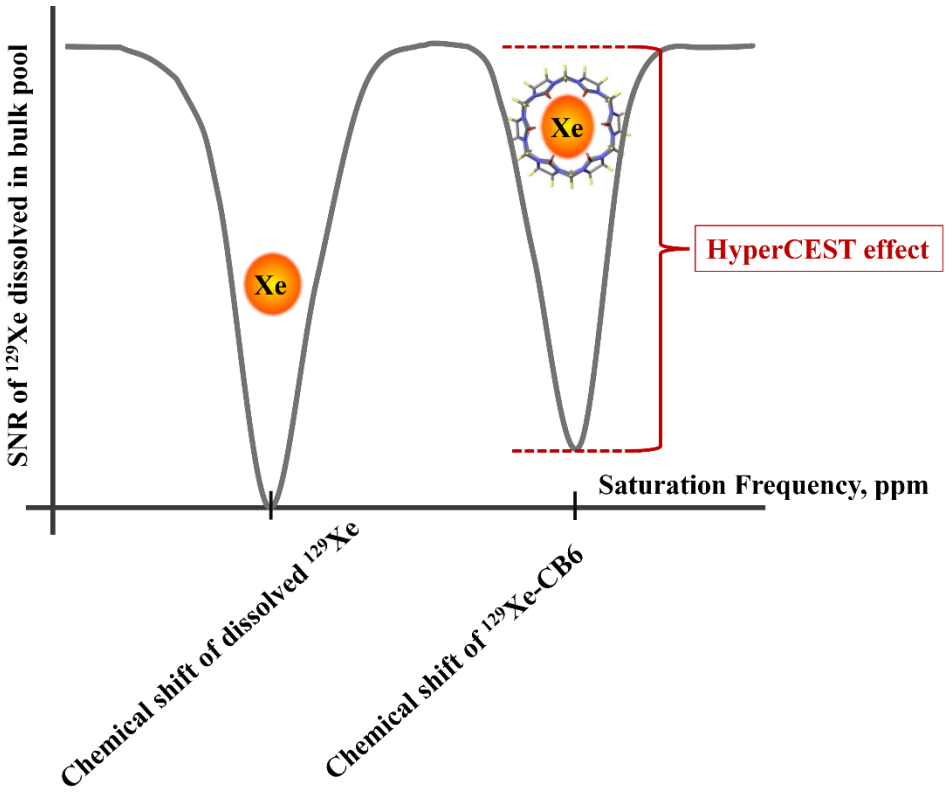

Figure 1-9 HyperCEST z-spectrum for HP ^{129}Xe with one ^{129}Xe dissolved pool.

HyperCEST has some advantages compared to other CEST techniques[80]. The first one is the large chemical shift between pools, which allows full depolarization of one of the pools. Second is the relatively long exchange times, hence excessively large B_1 pulse (depolarization pulse) powers are not required for good saturation response. The third advantage is the relatively long T_1 values of HP ^{129}Xe in the dissolved pool, hence the decay of the hyperpolarized signal does not affect HyperCEST values considerably.

1.5.7 HyperCEST agents

There are a lot of important properties of HP ^{129}Xe host agents that have to be considered for high HyperCEST performance such as biocompatibility of solvent which is capable of dissolving the agent, chemical shift of ^{129}xe within the agent and binding constant. Currently, only

these effective host agents are known for HP ^{129}Xe: cryptophanes, cucurbit[6]urils, pillar[5]arenes, cyclodextrins, metal organic polyhedrals (MOPs), micelles and liposomes, viral capsids and bacteriophages, gas binding proteins, nanoemulsions and gas vesicles.

Cryptophanes are one of the most well-studied supramolecular hosts for HP ^{129}Xe. They provide a hydrophobic cavity formed by two hydrophobic cyclotriveratrylene units (CTV) connected by three linkers[81]. Cryptophane-A (CryA) has been shown as the most efficient HyperCEST agent among cryptophanes. It is formed by three ethoxy alkyl linkers connecting two CTV caps and can host one ^{129}Xe atom. It provides a good chemical shift of encapsulated ^{129}Xe: ~62 ppm and ~193 ppm for ^{129}Xe-CryA and free ^{129}Xe in solution respectively[79]. The main advantages of cryptophanes are a high ^{129}xe binding constant and medium to fast exchange rate, nM sensitivity as HyperCEST agents, functionalizable, and water-soluble. Conversely, there are some disadvantages: a complicated synthesis with low yields, commercial unavailability, having some isomers, that are not easy to isolate, and which does not provide HyperCEST[82].

Cucurbit[n]urils are also hydrophobic hosts which are synthetized by condensation of glycoluril and formaldehyde/paraformaldehyde under acidic conditions[83]. Depending on the number of glycoluril units in the molecule, “n” in the cucurbit[n]urils may be equal to 5,6,7,8,10. Cucurbit[6]uril (CB6) was shown as the most efficient HyperCEST agent for HP ^{129}Xe[84]. It is the only supramolecular cage in which HyperCEST was demonstrated in-vivo by Hane et al[85]. Cucurbit[n]urils have several benefits over other hosts. They are non-toxic and have been studied in-vivo, easily synthesizable and commercially available, enable fast ^{129}Xe exchange and gas turnover, they are water-soluble in the presence of ions. On the other hand, they are not easily functionalizable due to high stability, the presence of other biological molecules may reduce their HyperCEST performance. CB6 was utilized for the creation of chemically activated CB6-rotaxane

molecular biosensors[86]. Rotaxane was used as a blocker of the CB6 cavity, while its "dumbbell" part was used as a stopper. The activation of the HyperCEST is performed by creating the conditions for rotaxane cleavage from CB6. For example, CB6-rotaxane was utilized for sensing the extracellular H_2O_2 at low physiological levels[87,88].

Pillar[n]arenes is another family of the supramolecular cages, where typically n=5. They have a rigid cylindrical pillar-like structure consisting of repeating phenyl units connected by methylene bridges at the para position[89,90]. Pillar[5]arene has electron-rich groups which help encapsulate electron-deficient and neutral molecules. Recently, Fernando et al synthesized a water-soluble decacationic pillar[5]arene, which can be easily functionalized and showed 23% of HyperCEST depletion[91]. The main advantages of the pilla[5]arenes are the ability to "tune" HP ^{129}Xe exchange and chemical shift by introducing co-guests, good yields of synthesis, and potentially low toxicity. The disadvantages are unavailability from commercial sources, fast ^{129}Xe exchange, and the need for the co-guest for decent ^{129}Xe binding.

Cyclodextrins (CDs) are cyclic oligosaccharides built from glucose subunits connected by α-1,4 glycosidic bonds[92,93]. There are three main CDs that have six, seven and eight glucose subunits, α-, β- and γ- cyclodextrins respectively. These supramolecules are cone-shaped and contain hydrophobic interior and polar exterior surface[94]. All three types of CDs combined with pseudorotaxanes complexes are exploited for HyperCEST studies, with HyperCEST depletion of 30% for α-CD[95], and 47.5% for γ-CD[86], unfortunately β-CD complex did not show any HyperCEST. The biggest advantage of CDs over all other agents is the easy synthesis and relatively easy functionalization of pseudorotaxanes[96].

MOPs are self-assembling supramolecular metal complexes consisting of metal cations and organic sub-components. They have hydrophobic cavities of different sizes and can encapsulate

hydrophobic guest[97]. Recently Du et al reported metal organic tetrahedral capsules $[Co_4L_6]^{4-}$, where L is 4,4′-bis[(2-pyridinylmethylene)amino][1,1′-biphenyl]-2,2′-disulfonate, which showed the HyperCEST depletion of 85%[98]. Similar results were observed when Co was replaced by Fe atoms, however, four different HyperCEST depletions were observed[99]. The advantages of MOPs are weak ^{129}Xe binding and relatively slow exchange, good water solubility, straightforward synthesis, and bound ^{129}Xe peak position may be altered by temperature and pH. However, the cation present in MOPs may alter the T_1 of HP ^{129}Xe which is not desirable. Also, the monofunctionalization of MOPs may be difficult to accomplish.

Liposomes also are self-assembling entities which have a spherical form and contain phospholipids. They usually are combined with CryA as an HP ^{129}Xe host for utilization in HyperCEST. Capsids and bacteriophages also utilize CryA for being able to perform HyperCEST detection[100–102].

Proteins on the other hand can reversibly bind gas molecules due to their unique structure. A good example of such proteins is TEM-1 β-lactamase which is engineered from E.coli. It showed 23% HyperCEST depletion at 0.1 μM protein concentration[103]. The greatest advantage of proteins is that they are non-toxic, however, they may exhibit non-specific binding which makes them less desirable as HyperCEST hosts.

Another gas carriers that may act as a ^{129}Xe hosts are perfluorooctyl bromide (PFOB) nanodroplets[104]. ^{129}Xe has a broad peak when placed inside of PFOB with the chemical shift from the dissolved phase of -80 ppm[105]. Similar to the nanodroplets bacterial gas vesicles also may encapsulate ^{129}Xe. They are gas-filled protein-shelled intracellular nano compartments that provide buoyancy to cells once the fraction of the cell volume is occupied by gas[106–109]. The structure of gas vesicles had to be tuned to produce strong enough interactions with HP ^{129}Xe, as a result, the

HyperCEST depletion of 33% was observed[110]. Potentially, the utilization of nanodroplets and gas vesicles may lead to the detection of HP ^{129}Xe with picomolar sensitivity, they can easily be combined with targeting moiety and enable stable HyperCEST due to physical partitioning instead of chemical affinity. Still, nanoemulsions may be unstable over time and gas vesicles may collapse under pressure, which may affect their in-vivo applications.

Overall, the ^{129}Xe HyperCEST approach is still under development and further investigation of all possible supramolecular and other hosts is crucial for the creation of efficient molecular biosensors with HP ^{129}Xe.

1.6 Thesis Outline

Chapter 1 has described the theoretical basics of ^{1}H MRI, the background of HP ^{129}Xe MRI its advantages over clinically available MRI and its challenges. The main advantages and disadvantages of widely used imaging modalities were discussed. The current utilization of HP ^{129}Xe in research studies was presented. HyperCEST technique background and its utilization for molecular imaging were presented.

Chapter 2 introduces the overview of the HP ^{129}Xe brain imaging current state, its achievements, and future directions. This work was published in *Magnetic Resonance in Medicine* (a peer-reviewed journal) in 2022.

Chapter 3 describes the effect of the glucose concentration changes on the HP ^{129}Xe chemical shift and spin-spin relaxation in whole sheep blood. The changes in T_2 relaxation were observed with the increase of glucose concentration. Two different peaks of HP ^{129}Xe were identified. The red blood cells glycation was assumed to be the origin of the additional to typical HP ^{129}Xe bound to normal hemoglobin peak. Consequently, the second peak was attributed to HP

^{129}Xe bound to glycated hemoglobin. This work was published in *International Journal of Molecular Sciences* (a peer-reviewed journal) in 2023.

Chapter 4 demonstrates the application of HP ^{129}Xe for multi-slice brain imaging done for the first time. Five slices of the human brain were successfully acquired in axial and sagittal orientations. The intensity of the HP ^{129}Xe signal was correlated with the different brain tissues. This work was published in *Magnetic Resonance in Medicine* (a peer-reviewed journal) in 2021.

Chapter 5 describes the maximization of HyperCEST performance for cucurbit[6]uril. Four different hyperpolarization saturation pulses were studied: sinusoidal, block, sinc, and hyperbolic secant. In addition, the effect of the pulse flip angle on the HyperCEST depletion was evaluated. The best performance was demonstrated by sinusoidal and sinc pulses. The highest HyperCEST values were observed at the maximum angles. This allowed for a decrease in the detectability limit of cucurbit[6]uril in phosphate-buffered saline and whole bovine blood. This work was published in *ChemPhysChem* (a peer-reviewed journal) in 2023.

Chapter 6 provides a brief overall summary of my thesis work and discusses possible future research directions.

1.7 References

1. Doi K. Diagnostic imaging over the last 50 years: Research and development in medical imaging science and technology. *Phys Med Biol*. 2006;51:R5-R27. doi:10.1088/0031-9155/51/13/R02
2. Barentsz J, Takahashi S, Oyen W, Mus R, De Mulder P, Reznek R, Oudkerk M, Mali W. Commonly used imaging techniques for diagnosis and staging. *Journal of Clinical Oncology*. 2006;24(20):3234-3244. doi:10.1200/JCO.2006.06.5946

3. Atabo SM, Umar AA. A review of imaging techniques in scientific research/clinical diagnosis. *MOJ Anat Physiol*. 2019;6(5). doi:10.15406/mojap.2019.06.00269

4. Bercovich E, Javitt MC. Medical Imaging: From Roentgen to the Digital Revolution, and Beyond. *Rambam Maimonides Med J*. 2018;9(4):e0034. doi:10.5041/rmmj.10355

5. Hussain S, Mubeen I, Ullah N, Shah SSUD, Khan BA, Zahoor M, Ullah R, Khan FA, Sultan MA. Modern Diagnostic Imaging Technique Applications and Risk Factors in the Medical Field: A Review. *Biomed Res Int*. Published online 2022:5164970. doi:10.1155/2022/5164970

6. Smith-Bindman R, Miglioretti DL, Larson EB. Rising use of diagnostic medical imaging in a large integrated health system. *Health Aff*. 2008;27(6):1491-1502. doi:10.1377/hlthaff.27.6.1491

7. Huda W, Brad Abrahams R. X-ray-based medical imaging and resolution. *American Journal of Roentgenology*. 2015;204(4):W393-W397. doi:10.2214/AJR.14.13126

8. Bushberg JT, Seibert JA, Leidholdt EM, Boone JM. *The Essential Physics of Medical Imaging 2nd Edition*. Lippincott Williams & Wilkins; 2002.

9. Lin EC. Radiation risk from medical imaging. *Mayo Clin Proc*. 2010;85(12):1142-1146. doi:10.4065/mcp.2010.0260

10. Shung KK, Smith MB, Tsui BMW. *Principles of Medical Imaging*. Academic Press; 1992.

11. Smith-Bindman R, Lipson J, Marcus R, Kim KP, Mahesh M, Gould R, Berrington De González A, Miglioretti DL. Radiation dose associated with common computed tomography examinations and the associated lifetime attributable risk of cancer. *Arch Intern Med*. 2009;169(22):2078-2086. doi:10.1001/archinternmed.2009.427

12. Onishi H, Hori M, Ota T, Nakamoto A, Osuga K, Tatsumi M, Fukui H, Tsukagoshi S, Uranishi A, Saito Y, Taniguchi A, Enchi Y, Sato K, Tomiyama N. Phantom study of in-stent restenosis at high-spatial-resolution CT. *Radiology*. 2018;289(1):255-260. doi:10.1148/radiol.2018180188

13. Behzadi A, Ung Y, Lowe V, Deschamps C. The role of positron emission tomography in the managment of non-small cell lung cancer. *Can J Surg*. 2009;52(3):235-242.

14. Chiotis K, Stenkrona P, Almkvist O, Stepanov V, Ferreira D, Arakawa R, Takano A, Westman E, Varrone A, Okamura N, Shimada H, Higuchi M, Halldin C, Nordberg A. Dual tracer tau PET imaging reveals different molecular targets for 11C-THK5351 and 11C-PBB3 in the Alzheimer brain. *Eur J Nucl Med Mol Imaging*. 2018;45(9):1605-1617. doi:10.1007/s00259-018-4012-5

15. Yeo SK, Shepelytskyi Y, Grynko V, Albert MS. Molecular imaging of fluorinated probes for tau protein and amyloid-β detection. *Molecules*. 2020;25(15). doi:10.3390/molecules25153413

16. Hane FT, Robinson M, Lee BY, Bai O, Leonenko Z, Albert MS. Recent Progress in Alzheimer's Disease Research, Part 3: Diagnosis and Treatment. *Journal of Alzheimer's Disease*. 2017;57:645-655. doi:10.3233/JAD-160907

17. Duncan K. Radiopharmaceuticals in PET Imaging. *J Nucl Med Technol*. 1998;26:228-234.

18. Contreras Ortiz SH, Chiu T, Fox MD. Ultrasound image enhancement: A review. *Biomed Signal Process Control*. 2012;7(5):419-428. doi:10.1016/j.bspc.2012.02.002

19. Oldendorf W, Oldendorf W. *Basics of Magnetic Resonance Imaging*. Springer US; 1988. doi:10.1007/978-1-4613-2081-4

20. Dance DR, Christofides S, Maidment ADA, Mclean ID, Ng KH. *Diagnostic Radiology Physics A Handbook for Teachers and Students*. International Atomic Energy Agency; 2014.

21. Moser E, Laistler E, Schmitt F, Kontaxis G. Ultra-high field NMR and MRI-the role of magnet technology to increase sensitivity and specificity. *Front Phys*. 2017;5(AUG). doi:10.3389/fphy.2017.00033

22. Andreasen NC. Brain Imaging: Applications in Psychiatry. *Science (1979)*. 1988;239:1381-1388.

23. Lauterbur PC. Image Formation by Induced Local Interactions: Examples Employing Nuclear Magnetic Resonance. *Nature*. 1973;242:190-191. doi:10.1038/242190a0

24. Zeeman P. The effect of magnetization on nature of light emitted by a substance. *Nature*. 1897;55(1424):347.

25. Hajnal J V., Bryant DJ, Kasubovski L, Pattany PM, De Coene B, Lewis PD, Pennock JM, Oatridge A, Young IR, Bydder GM. Use of Fluid Attenuated Inversion Recovery (FLAIR) Pulse Sequences in MRI of the Brain. *J Comput Assist Tomogr*. 1992;16(6):841-844.

26. Reeder SB, Pineda AR, Wen Z, Shimakawa A, Yu H, Brittain JH, Gold GE, Beaulieu CH, Pelc NT. Iterative decomposition of water and fat with echo asymmetry and least-squares estimation (IDEAL): Application with fast spin-echo imaging. *Magn Reson Med*. 2005;54(3):636-644. doi:10.1002/mrm.20624

27. Hoh HB, Laitt RD, Wakeley C, Kabala J, Goddard P, Potts MJ, Harrad RA. The STIR sequence MRI in the assessment of extraocular muscles in thyroid disease. *Eye*. 1994;8:506-510.

28. Obert AJ, Gutberlet M, Kern AL, Kaireit TF, Grimm R, Wacker F, Vogel-Claussen J. 1H-guided reconstruction of 19F gas MRI in COPD patients. *Magn Reson Med*. 2020;84(3):1336-1346. doi:10.1002/mrm.28209

29. Couch MJ, Ball IK, Li T, Fox MS, Littlefield SL, Biman B, Albert MS. Pulmonary ultrashort echo time 19F MR imaging with inhaled fluorinated gas mixtures in healthy volunteers: Feasibility. *Radiology*. 2013;269(3):903-909. doi:10.1148/radiol.13130609

30. Couch MJ, Ball IK, Li T, Fox MS, Ouriadov A V., Biman B, Albert MS. Inert fluorinated gas MRI: a new pulmonary imaging modality. *NMR Biomed*. 2014;27(12):1525-1534. doi:10.1002/nbm.3165

31. Haacke E, Brown R, Thompson M, Venkatesan R. *Magnetic Resonance Imaging: Physical Principles and Pulse Sequence Design.* Wiley-Liss; 1999.

32. Herb K. Gyromagnetic ratio table. Published 2023. Accessed October 9, 2023. https://www.kherb.io/docs/nmr_table.html

33. Shampo MA, Kyle RA, Steensma DP. Richard ernst-nobel prize for nuclear magnetic resonance spectroscopy. *Mayo Clin Proc*. 2012;87(12). doi:10.1016/j.mayocp.2012.01.023

34. Guo H, Siu W, D'Arcy RCN, Black SE, Grajauskas LA, Singh S, Zhang Y, Rockwood K, Song X. MRI assessment of whole-brain structural changes in aging. *Clin Interv Aging*. 2017;12:1251-1270. doi:10.2147/CIA.S139515

35. Lu H, Nagae-Poetscher LM, Golay X, Lin D, Pomper M, Van Zijl PCM. Routine clinical brain MRI sequences for use at 3.0 tesla. *Journal of Magnetic Resonance Imaging*. 2005;22(1):13-22. doi:10.1002/jmri.20356

36. Harper L. *Maximising the Diagnostic Value of Structural MRI in the Diagnosis of Dementia*. 2015.

37. Bauer S, Wiest R, Nolte LP, Reyes M. A survey of MRI-based medical image analysis for brain tumor studies. *Phys Med Biol*. 2013;58(13). doi:10.1088/0031-9155/58/13/R97

38. Derks SHAE, van der Veldt AAM, Smits M. Brain metastases: the role of clinical imaging. *British Journal of Radiology*. 2022;95(1130). doi:10.1259/BJR.20210944

39. Jack CR, Bernstein MA, Fox NC, Thompson P, Alexander G, Harvey D, Borowski B, Britson PJ, Whitwell JL, Ward C, Dale AM, Felmlee JP, Gunter JL, Hill DLG, Killiany R, Schuff N, Fox-Bosetti S, Lin C, Studholme C, DeCarli CS, Krueger G, Ward HA, Metzger GJ, Scott KT, Mallozzi R, Blezek D, Levy J, Debbins JP, Fleisher AS, Albert M, Green R, Bartzokis G, Glover G, Mugler J, Weiner MW. The Alzheimer's Disease Neuroimaging Initiative (ADNI): MRI methods. *Journal of Magnetic Resonance Imaging*. 2008;27(4):685-691. doi:10.1002/jmri.21049

40. De Coene B, Hajnal J V, Gatehouse P, Longmore DB, White SJ, Oatridge A, Pennock JM, Young ian R, Bydder GM. MR of the Brain Using Fluid-Attenuated Inversion Recovery (FLAIR) Pulse Sequences. *AJNR*. 1992;13(November/December):1555-1564.

41. Tang MY, Chen TW, Zhang XM, Huang XH. GRE T2* -weighted MRI: Principles and clinical applications. *Biomed Res Int*. Published online 2014:312142. doi:10.1155/2014/312142

42. Greenberg SM, Vernooij MW, Cordonnier C, Viswanathan A, Al-Shahi Salman R, Warach S, Launer LJ, Van Buchem MA, Breteler MM. Cerebral microbleeds: a guide to detection and interpretation. *Lancet Neurol*. 2009;8(2):165-174. doi:10.1016/S1474-4422(09)70013-4

43. Rees J. Advances in magnetic resonance imaging of brain tumours. *Curr Opin Neurol*. 2003;16:643-650. doi:10.1097/01.wco.0000102626.38669.b9

44. Gass A, Ay H, Szabo K, Koroshetz WJ. Diffusion-weighted MRI fir the “small stuff”: the details of acute cerebral ischaemia. *The Lancet*. 2004;3:39-45.

45. Debette S, Schilling S, Duperron MG, Larsson SC, Markus HS. Clinical Significance of Magnetic Resonance Imaging Markers of Vascular Brain Injury: A Systematic Review and Meta-analysis. *JAMA Neurol*. 2019;76(1):81-94. doi:10.1001/jamaneurol.2018.3122

46. Telischak NA, Detre JA, Zaharchuk G. Arterial spin labeling MRI: Clinical applications in the brain. *Journal of Magnetic Resonance Imaging*. 2015;41(5):1165-1180. doi:10.1002/jmri.24751

47. Bertholdo D, Watcharakorn A, Castillo M. Brain Proton Magnetic Resonance Spectroscopy: Introduction and Overview. *Neuroimaging Clin N Am*. 2013;23(3):359-380. doi:10.1016/j.nic.2012.10.002

48. Welker K, Boxerman J, Kalnin A, Kaufmann T, Shiroishi M, Wintermark M. ASFNR recommendations for clinical performance of MR dynamic susceptibility contrast perfusion imaging of the brain. *American Journal of Neuroradiology*. 2015;36(6):E41-E51. doi:10.3174/ajnr.A4341

49. Albert MS, Cates GD, Driehuys B, Happer W, Saam B, Springer C.S, Wishnia A. Biological magnetic resonance imaging using laser-polarized 129Xe. *Nature*. 1994;370:199-201.

50. Couch MJ, Blasiak B, Tomanek B, Ouriadov A V., Fox MS, Dowhos KM, Albert MS. Hyperpolarized and Inert Gas MRI: The Future. *Mol Imaging Biol*. 2015;17(2):149-162. doi:10.1007/s11307-014-0788-2

51. Comment A, Jannin S, Hyacinthe JN, Miéville P, Sarkar R, Ahuja P, Vasos PR, Montet X, Lazeyras F, Vallée JP, Hautle P, Konter JA, Van Den Brandt B, Ansermet JP, Gruetter R,

Bodenhausen G. Hyperpolarizing gases via dynamic nuclear polarization and sublimation. *Phys Rev Lett*. 2010;105(1). doi:10.1103/PhysRevLett.105.018104

52. Suchanek K, Cieślar K, Olejniczak Z, Pałasz T, Suchanek M, Dohnalik T. Hyperpolarized 3 He gas production by metastability exchange optical pumping for magnetic resonance imaging. *Optica Applicata*. 2005;XXXV(2).

53. Albert MS, Hane FT. *Hyperpolarized and Inert Gas MRI From Technology To Application In Research And Medicine*. Elsevier; 2017.

54. Happer W. Optical pumping. *Rev Mod Phys*. 1972;44(2):169-249.

55. Shepelytskyi Y. *Medical Applications of Fluorine-19 and Hyperpolarized Xenon-129 Magnetic Resonance Imaging*. 2020.

56. Wild J. Hyperpolarized Gas Lung Imaging. *GE Signapulse*. Published online 2019. https://www.gesignapulse.com/signapulse/spring_2019/MobilePagedArticle.action?articleId=1488828#articleId1488828

57. FDA approves Hyperpolarized Xenon for MRI. Applied Radiology. Published 2023. Accessed October 4, 2023. https://appliedradiology.com/articles/fda-approves-hyperpolarized-xenon-for-mri#

58. Luttropp HH, Thomasson R, Dahm S, Persson J. Clinical experience with minimal flow xenon anesthesia. *Acla Anaesihessiol Scand*. 1994;38:121-125.

59. Rao MR, Norquay G, Stewart NJ, Hoggard N, Griffiths PD, Wild JM. Assessment of brain perfusion using hyperpolarized 129Xe MRI in a subject with established stroke. *Journal of Magnetic Resonance Imaging*. 2019;50(3):1002-1004. doi:10.1002/jmri.26686

60. Hane F, Li T, Plata JA, Hassan A, Granberg K, Albert M. Inhaled Xenon Washout as a Biomarker of Alzheimer's Disease. *Diagnostics*. 2018;8:41. doi:10.3390/diagnostics8020041

61. Shepelytskyi Y, Hane FT, Grynko V, Li T, Hassan A, Albert MS. Hyperpolarized 129Xe Time-of-Flight MR Imaging of Perfusion and Brain Function. *Diagnostics*. 2020;10:630. doi:10.3390/diagnostics10090630

62. Ouriadov A, Farag A, Kirby M, McCormack DG, Parraga G, Santyr GE. Lung morphometry using hyperpolarized 129Xe apparent diffusion coefficient anisotropy in chronic obstructive pulmonary disease. *Magn Reson Med*. 2013;70(6):1699-1706. doi:10.1002/mrm.24595

63. Kirby M, Heydarian M, Svenningsen S, Wheatley A, McCormack DG, Etemad-Rezai R, Parraga G. Hyperpolarized 3He Magnetic Resonance Functional Imaging Semiautomated Segmentation. *Acad Radiol*. 2012;19(2):141-152. doi:10.1016/j.acra.2011.10.007

64. Matheson Bsc AM, Mcintosh Bsc MJ, Kooner Bsc HK, Lee J, Desaigoudar V, Bier E, Driehuys Phd B, Svenningsen S, Santyr GE, Kirby Phd M, Albert MS, Shepelytskyi Phd Y, Grynko Msc V, Ouriadov A, Abdelrazek M, Dhaliwal I, Nicholson JM, Parraga G. Persistent 129 Xe MRI Pulmonary and CT Vascular Abnormalities in Symptomatic Individuals with Post-Acute COVID-19 Syndrome. *Radiology* . 2022;305(2):466-476. https://apilab.ca/our_code.html

65. Zhou Q, Rao Q, Li H, Zhang M, Zhao X, Shi L, Ye C, Zhou X. Evaluation of Injuries Caused by Coronavirus Disease 2019 Using Multi-Nuclei Magnetic Resonance Imaging. *Magnetic Resonance Letters*. 2021;August; 1(1):2-10. doi:10.1016/j.mrl.2021.100009

66. Li H, Zhao X, Wang Y, Lou X, Chen S, Deng H, Shi L, Xie J, Tang D, Zhao J, Bouchard LS, Xia L, Zhou X. Damaged lung gas exchange function of discharged COVID-19 patients

detected by hyperpolarized 129Xe MRI. *Sci Adv*. 2021;7(1):1-9. doi:10.1126/sciadv.abc8180

67. Chang Y V. MOXE: A model of gas exchange for hyperpolarized 129Xe magnetic resonance of the lung. *Magn Reson Med*. 2013;69(3):884-890. doi:10.1002/mrm.24304

68. Norquay G, Leung G, Stewart NJ, Tozer GM, Wolber J, Wild JM. Relaxation and exchange dynamics of hyperpolarized 129Xe in human blood. *Magn Reson Med*. 2015;74(2):303-311. doi:10.1002/mrm.25417

69. Albert MS, Kacher DF, Balamore D, Venkatesh AK, Jolesz FA. T1 of 129Xe in Blood and the Role of Oxygenation. *Journal of Magnetic Resonance*. 1999;140(1):264-273. doi:10.1006/jmre.1999.1836

70. Mugler JP, Driehuys B, Brookeman JR, Cates GD, Berr SS, Bryant RG, Daniel TM, De Lange EE, Downs JH, Erickson CJ, Happer W, Hinton DP, Kassel NF, Maier T, Phillips CD, Saam BT, Sauer KL, Wagshul ME. MR imaging and spectroscopy using hyperpolarized 129Xe gas: Preliminary human results. *Magn Reson Med*. 1997;37(6):809-815. doi:10.1002/mrm.1910370602

71. Driehuys B, Cofer GP, Pollaro J, Mackel JB, Hedlund LW, Johnson GA. Imaging alveolar-capillary gas transfer using hyperpolarized 129Xe MRI. *Proceedings of the National Academy of Sciences*. 2006;103(48):18278-18283. doi: 10.1073/pnas.0608458103

72. Qing K, Mugler JP, Altes TA, Jiang Y, Mata JF, Miller GW, Ruset IC, Hersman FW, Ruppert K. Assessment of lung function in asthma and COPD using hyperpolarized 129Xe chemical shift saturation recovery spectroscopy and dissolved-phase MRI. *NMR Biomed*. 2014;27(12):1490-1501. doi:10.1002/nbm.3179

73. Kern AL, Gutberlet M, Qing K, Voskrebenzev A, Klimeš F, Kaireit TF, Czerner C, Biller H, Wacker F, Ruppert K, Hohlfeld JM, Vogel-Claussen J. Regional investigation of lung function and microstructure parameters by localized 129Xe chemical shift saturation recovery and dissolved-phase imaging: A reproducibility study. *Magn Reson Med*. 2019;81(1):13-24. doi:10.1002/mrm.27407

74. Fox MS, Ouriadov A, Thind K, Hegarty E, Wong E, Hope A, Santyr GE. Detection of radiation induced lung injury in rats using dynamic hyperpolarized ^{129} Xe magnetic resonance spectroscopy. *Med Phys*. 2014;41(7):072302. doi:10.1118/1.4881523

75. Ruppert K, Brookeman JR, Hagspiel KD, Mugler JP. Probing lung physiology with xenon polarization transfer contrast (XTC). *Magn Reson Med*. 2000;44(3):349-357. doi:10.1002/1522-2594(200009)44:3<349::AID-MRM2>3.0.CO;2-J

76. Dregely I, Ruset IC, Mata JF, Ketel J, Ketel S, Distelbrink J, Altes TA, Mugler JP, Miller GW, Hersman FW, Ruppert K. Multiple-exchange-time xenon polarization transfer contrast (MXTC) MRI: Initial results in animals and healthy volunteers. *Magn Reson Med*. 2012;67(4):943-953. doi:10.1002/mrm.23066

77. Tilton RF, Kuntz ID. *Photoluminescence of Solutions*. Vol 21. Academic Press; 1982. https://pubs.acs.org/sharingguidelines

78. Goodson BM. Advances in magnetic resonance: Nuclear magnetic resonance of laser-polarized noble gases in molecules, materials, and organisms. *Journal of Magnetic Resonance*. 2002;155(2):157-216. doi:10.1006/jmre.2001.2341

79. Schröder L. Xenon for NMR biosensing - Inert but alert. *Physica Medica*. 2013;29(1):3-16. doi:10.1016/j.ejmp.2011.11.001

80. Harel E, Schröder L, Xu S. Novel detection schemes of nuclear magnetic resonance and magnetic resonance imaging: Applications from analytical chemistry to molecular sensors. *Annual Review of Analytical Chemistry*. 2008;1:133-163. doi:10.1146/annurev.anchem.1.031207.113018

81. Brotin T, Dutasta JP. Cryptophanes and their complexes - Present and future. *Chem Rev*. 2009;109(1):88-130. doi:10.1021/cr0680437

82. Jayapaul J, Schröder L. Molecular sensing with host systems for hyperpolarized 129Xe. *Molecules*. 2020;25(20). doi:10.3390/molecules25204627

83. Lagona J, Mukhopadhyay P, Chakrabarti S, Isaacs L. The cucurbit[n]uril family. *Angewandte Chemie - International Edition*. 2005;44(31):4844-4870. doi:10.1002/anie.200460675

84. Hane FT, Smylie PS, Li T, Ruberto J, Dowhos K, Ball I, Tomanek B, DeBoef B, Albert MS. HyperCEST detection of cucurbit[6]uril in whole blood using an ultrashort saturation Pre-pulse train. *Contrast Media Mol Imaging*. 2016;11(4):285-290. doi:10.1002/cmmi.1690

85. Hane FT, Li T, Smylie P, Pellizzari RM, Plata JA, Deboef B, Albert MS. In vivo detection of cucurbit[6]uril, a hyperpolarized xenon contrast agent for a xenon magnetic resonance imaging biosensor. *Sci Rep*. 2017;(3):41027. doi:10.1038/srep41027

86. Finbloom JA, Slack CC, Bruns CJ, Jeong K, Wemmer DE, Pines A, Francis MB. Rotaxane-mediated suppression and activation of cucurbit[6]uril for molecular detection by 129Xe hyperCEST NMR. *Chemical Communications*. 2016;52(15):3119-3122. doi:10.1039/c5cc10410f

87. Niethammer P, Grabher C, Look AT, Mitchison TJ. A tissue-scale gradient of hydrogen peroxide mediates rapid wound detection in zebrafish. *Nature*. 2009;459(7249):996-999. doi:10.1038/nature08119

88. Weinstain R, Savariar EN, Felsen CN, Tsien RY. In vivo targeting of hydrogen peroxide by activatable cell-penetrating peptides. *J Am Chem Soc*. 2014;136(3):874-877. doi:10.1021/ja411547j

89. Ogoshi T, Kanai S, Fujinami S, Yamagishi TA, Nakamoto Y. para-bridged symmetrical pillar[5]arenes: Their Lewis acid catalyzed synthesis and host-guest property. *J Am Chem Soc*. 2008;130(15):5022-5023. doi:10.1021/ja711260m

90. Xue M, Yang Y, Chi X, Zhang Z, Huang F. Pillararenes, a new class of macrocycles for supramolecular chemistry. *Acc Chem Res*. 2012;45(8):1294-1308. doi:10.1021/ar2003418

91. Fernando PUAI, Shepelytskyi Y, Cesana PT, Wade A, Grynko V, Mendieta AM, Seveney LE, Brown JD, Hane FT, Albert MS, Deboef B. Decacationic pillar[5]arene: A new scaffold for the development of 129Xe MRI imaging agents. *ACS Omega*. 2020;5(43):27783-27788. doi:10.1021/acsomega.0c02565

92. Stella VJ, he Q. Cyclodextrins. *Toxicol Pathol*. 2008;36(1):30-42. doi:10.1177/0192623307310945

93. Jansook P, Ogawa N, Loftsson T. Cyclodextrins: structure, physicochemical properties and pharmaceutical applications. *Int J Pharm*. 2018;535(1-2):272-284. doi:10.1016/j.ijpharm.2017.11.018

94. Del Valle EMM. Cyclodextrins and their uses: A review. *Process Biochemistry*. 2004;39(9):1033-1046. doi:10.1016/S0032-9592(03)00258-9

95. Wang Y, Dmochowski IJ. An Expanded Palette of Xenon-129 NMR Biosensors. *Acc Chem Res*. 2016;49(10):2179-2187. doi:10.1021/acs.accounts.6b00309

96. Shepelytskyi Y, Newman CJ, Grynko V, Seveney LE, Deboef B, Hane FT, Albert MS. Cyclodextrin-based contrast agents for medical imaging. *Molecules*. 2020;25(23):13-17. doi:10.3390/molecules25235576

97. Mal P, Schultz D, Beyeh K, Rissanen K, Nitschke JR. An unlockable-relockable iron cage by subcomponent self-assembly. *Angewandte Chemie - International Edition*. 2008;47(43):8297-8301. doi:10.1002/anie.200803066

98. Du K, Zemerov SD, Hurtado Parra S, Kikkawa JM, Dmochowski IJ. Paramagnetic Organocobalt Capsule Revealing Xenon Host-Guest Chemistry. *Inorg Chem*. 2020;59(19):13831-13844. doi:10.1021/acs.inorgchem.9b03634

99. Du K, Zemerov SD, Carroll PJ, Dmochowski IJ. Paramagnetic Shifts and Guest Exchange Kinetics in ConFe4- nMetal-Organic Capsules. *Inorg Chem*. 2020;59(17):12758-12767. doi:10.1021/acs.inorgchem.0c01816

100. Meldrum T, Schröder L, Denger P, Wemmer DE, Pines A. Xenon-based molecular sensors in lipid suspensions. *Journal of Magnetic Resonance*. 2010;205(2):242-246. doi:10.1016/j.jmr.2010.05.005

101. Meldrum T, Seim KL, Bajaj VS, Palaniappan KK, Wu W, Francis MB, Wemmer DE, Pines A. A xenon-based molecular sensor assembled on an MS2 viral capsid scaffold. *J Am Chem Soc*. 2010;132(17):5936-5937. doi:10.1021/ja100319f

102. Stevens TK, Palaniappan KK, Ramirez RM, Francis MB, Wemmer DE, Pines A. HyperCEST detection of a 129Xe-based contrast agent composed of cryptophane-A

molecular cages on a bacteriophage scaffold. *Magn Reson Med*. 2013;69(5):1245-1252. doi:10.1002/mrm.24371

103. Wang Y, Roose BW, Palovcak EJ, Carnevale V, Dmochowski IJ. A Genetically Encoded β-Lactamase Reporter for Ultrasensitive129Xe NMR in Mammalian Cells. *Angewandte Chemie - International Edition*. 2016;55(31):8984-8987. doi:10.1002/anie.201604055

104. Wolber J, Rowland IJ, Leach MO, Bifone A. Perfluorocarbon emulsions as intravenous delivery media for hyperpolarized xenon. *Magn Reson Med*. 1999;41(3):442-449. doi:10.1002/(SICI)1522-2594(199903)41:3<442::AID-MRM3>3.0.CO;2-7

105. Stevens TK, Ramirez RM, Pines A. Nanoemulsion contrast agents with sub-picomolar sensitivity for xenon NMR. *J Am Chem Soc*. 2013;135(26):9576-9579. doi:10.1021/ja402885q

106. Walsby AE. Gas Vesicles. *Microbiol Rev*. 1994;58(1):94-144.

107. Walsby AE. The permeability of blue-green algal gas-vacuole membranes to gas. *Proc R Soc Lond B Biol Sci*. 1969;173(1031):235-255. doi:10.1098/rspb.1969.0049

108. Oliver RL, Walsby AE. Direct evidence for the role of light-mediated gas vesicle collapse in the buoyancy regulation of Anabaena flos-aquae (cyanobacteria)'. *Limnol Oceanogr*. 1984;29(4):879-886.

109. Thomas A N RH, Walsby DAE. Buoyancy Regulation in a Strain of Microcystis. *J Gen Microbiol*. 1985;131:799-809.

110. Lakshmanan A, Lu GJ, Farhadi A, Nety SP, Kunth M, Lee-Gosselin A, Maresca D, Bourdeau RW, Yin M, Yan J, Witte C, Malounda D, Foster FS, Schröder L, Shapiro MG. Preparation of biogenic gas vesicle nanostructures for use as contrast agents for ultrasound and MRI. *Nat Protoc*. 2017;12(10):2050-2080. doi:10.1038/nprot.2017.081

Chapter 2: Hyperpolarized ^{129}Xe imaging of the brain

This topic has been elaborated in the following publication: Shepelytskyi Y., **Grynko V.,** Rao M.R., Li T., Agostino M., Wild J.M., Albert M.S "**Hyperpolarized 129Xe imaging of the brain: Achievements and Future Challenges**" published in *Magnetic Resonance in Medicine*, volume 86, issue 6, pages 3175-3181 (2021). The publication text is listed below, it was published under CC BY 4.0 DEED licence.

Hyperpolarized ^{129}Xe imaging of the brain: Achievements and Future Challenges

Yurii Shepelytskyi[1,2,‡], Vira Grynko[2,3,‡], Madhwesha R. Rao[4], Tao Li[1], Martina Agostino[1], Jim M. Wild[4,5], and Mitchell S. Albert[1,2,6]

1. Chemistry Department, Lakehead University, Thunder Bay, ON, CA;
2. Thunder Bay Regional Health Research Institute, Thunder Bay, ON, CA;
3. Chemistry and Materials Science Program, Lakehead University, Thunder Bay, ON, CA;
4. POLARIS, Unit of Academic Radiology, Department of IICD, University of Sheffield, Sheffield, United Kingdom;
5. Insigneo Institute for in silico medicine, Sheffield, United Kingdom;
6. Northern Ontario School of Medicine, Thunder Bay, ON, CA.

[‡]Yurii Shepelytskyi and Vira Grynko share the first authorship for this publication

Correspondence: Mitchell S. Albert, Lakehead University, 955 Oliver Road, Thunder Bay, Ontario P7B 5E1, Canada. E-mail: malbert1@lakeheadu.ca

Abstract:

Hyperpolarized (HP) xenon-129 (^{129}Xe) brain MRI is a promising imaging modality currently under extensive development. HP ^{129}Xe is nontoxic, capable of dissolving in pulmonary blood, and it is extremely sensitive to the local environment. After dissolution in the pulmonary blood, HP ^{129}Xe travels with the blood flow to the brain and can be used for functional imaging such as perfusion imaging, hemodynamic response detection, and blood-brain barrier permeability assessment. HP ^{129}Xe MRI imaging of the brain has been performed in animals, healthy human subjects, and in patients with Alzheimer's disease and stroke. In this review, the overall progress in the field of HP ^{129}Xe brain imaging is discussed, along with various imaging approaches and pulse sequences used to optimize HP ^{129}Xe brain MRI. In addition, current challenges and limitations of HP ^{129}Xe brain imaging are discussed, as well as possible methods for their mitigation. Finally, potential pathways for further development are discussed as well. HP ^{129}Xe MRI of the brain has the potential to become a valuable novel perfusion imaging technique and has the potential to be utilized in the clinical setting in the future.

2-1. Introduction

There are multiple brain imaging modalities currently available for clinical diagnostic use, including ultrasound, computed tomography (CT), single-photon emission computed tomography (SPECT), positron emission tomography (PET), and magnetic resonance imaging (MRI). MRI is a non-invasive technique that utilizes no ionizing radiation and can produce images with high spatial resolution and contrast-to-noise ratio (CNR). Despite numerous developments and discoveries since MRI was invented in 1973[1], the main limitation of MRI remains the same – low sensitivity[2,3]. The MRI signal originates from the net magnetization of the sample due to the small population difference between the Zeeman energy levels of nuclei with typically a ½ spin number.

Conventional MRI utilizes the nuclear magnetic resonance (NMR) signal from water protons (^{1}H); numerous contrast agents are being developed to enhance the ^{1}H MRI signal and provide the ability to localize the area of interest[4–6]. Many of these agents, such as gadolinium chelated contrast agents, are focused on decreasing the spin-lattice (T_1) and effective spin-spin (T_2*) relaxation of ^{1}H nuclei, which increases the MR contrast in T_1- and T_2*-weighted images. Despite the wide use of ^{1}H contrast agents, this approach is limited due to the presence of the background signal from surrounding tissues, which limits any increase in CNR. Additionally, there are a variety of techniques, such as Blood Oxygen Level Dependent (BOLD) functional MRI, Arterial Spin Labeling (ASL), and MR angiography, which require multiple image acquisitions and complicated image postprocessing procedures for accurate data interpretation[7,8].

Another fundamentally different method for enhancing the MRI signal involves creating a hyperpolarized (HP) nuclear state[9]. The HP state is a metastable state which can achieve up to a 10^5 times larger spin population excess, compared to the thermal equilibrium state. Traditional HP MRI techniques work with non-proton MRI sensitive nuclei such as xenon-129 (^{129}Xe), helium-3 (^{3}He), and carbon-13 (^{13}C)[10–13]. The signal from HP nuclei can be enhanced by up to 10^5 times, and MRI images of HP agents can be acquired with almost no background signal. Due to this signal boost, imaging of low concentration HP agents becomes possible. Currently, the main application of HP gas MRI is for lung imaging of healthy individuals and individuals with lung disorders[2,13]. HP ^{129}Xe undergoes gas exchange in the lungs[14–16], it easily dissolves in pulmonary blood[13,16,17], and it then distributes throughout the body. Since HP ^{129}Xe has a sufficiently long T_1 relaxation time in the blood (T_1 in a range of 3.4 -7.8 s)[18–21], HP ^{129}Xe MRI has the potential to produce functional images of highly perfused organs[9,22–24]. Although this idea was originally formulated at

the end of the 20th century[9], HP ^{129}Xe imaging in the brain is only recently under extensive development, and HP ^{129}Xe imaging of the kidneys has just been demonstrated about a year ago.

Despite the intensive development of dissolved-phase HP ^{129}Xe imaging in brain tissues over the past decade, there have been no dedicated comprehensive reviews for the advances in this area. This review article aims to highlight the current progress and development in the field of HP ^{129}Xe brain imaging, as well as to discuss the technical challenges associated with this technology. The imaging approaches currently used are also reviewed and discussed. It is anticipated that insights into the challenges and opportunities of this field can be highlighted and aid in further advancements in the methodology and technique development of this technology with subsequent clinical translation.

2-2. HP ^{129}Xe spectroscopy and Chemical Shift Imaging (CSI) of the brain

Historically, xenon was utilized in medicine as an anesthetic due to its ability to dissolve in brain tissue[25–29]. In addition to its anesthetic applications, xenon-129 was widely employed for cerebral blood flow evaluation using Xenon Computed Tomography (Xe-CT)[30–32]. Implementation of the hyperpolarization process for boosting the ^{129}Xe MRI signal established an entirely new field of brain imaging and investigations with HP ^{129}Xe[9]. One of the properties that is most important for brain research with HP ^{129}Xe dissolved in various brain tissues is its chemical shift. The first *in vivo* ^{129}Xe brain magnetic resonance spectrum was obtained by Swanson et al. in 1997 from the rat brain[33]. A single blood-tissue resonance peak was identified and used to produce an HP ^{129}Xe 2D chemical shift MRI image of the rat brain (Figure 2-1). Later that year, Mugler et al. performed the first ^{129}Xe magnetic resonance spectroscopy (MRS) study of the human head[34]. In that study, volunteers inhaled between 300 mL and 500 mL of HP ^{129}Xe in one breath; fifteen consecutive spectra of the head were subsequently acquired during and after a 15 s breath-hold

period. The spectra showed one peak from the gas phase and one peak from the dissolved phase that was shifted 196 ppm from the gas peak. The dissolved phase peak appeared at the end of the inhalation period at approximately 5 s and disappeared 40 s after the start of the breath-hold. The main limitation for the acquisition of human brain images at that time was the extremely low polarization of HP ^{129}Xe achievable, approximately 2%[34].

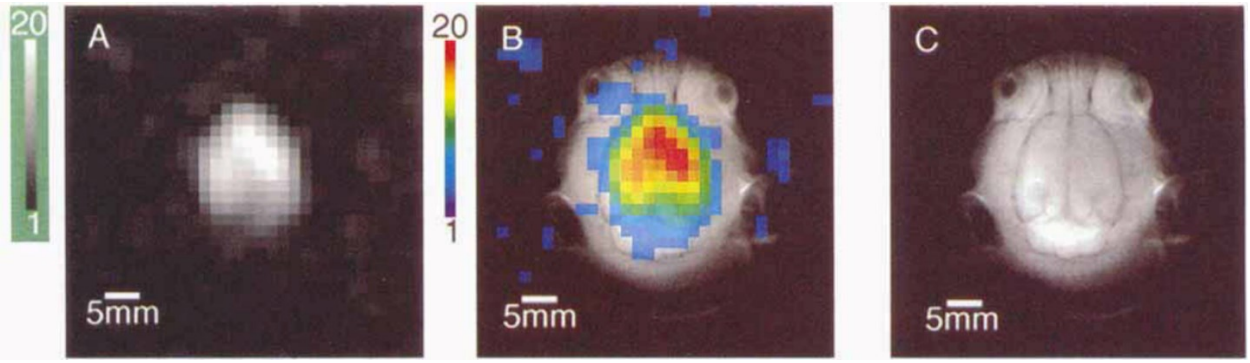

Figure 2-1 (A) HP ^{129}Xe axial 2D chemical shift images of the rat brain in greyscale; (B) Color-coded overlay onto a high-resolution proton image. The signal-to-noise ratio of the HP ^{129}Xe image was equal to 20. (C) High-resolution proton spin-echo MRI image used for brain localization. Images are reprinted with permission from the publisher[33].

Obtaining a spectral peak from HP ^{129}Xe dissolved in the brain allowed the conduction of a dynamic study of the distribution of xenon in the rat brain using 1D and 2D CSI[35]. Swanson et al. detected a signal from the rat brain using 1D CSI with a low flip angle and investigated the time evolution of this signal. The polarization of ^{129}Xe in this study, however, was still low (5-8%); the study was performed mainly to observe the signal evolution within the body of the rat.

Duhamel et al. used a different approach for observation of the HP ^{129}Xe solubility in the rat brain at 2.35 T[36]. They injected naturally abundant HP ^{129}Xe dissolved in a lipid emulsion, into the carotid artery, and observed two peaks at 199 and 194 ppm. These peaks were identified as ^{129}Xe dissolved in the tissue and the intravascular compartment, respectively[36]. It was clear that the signal intensity was too small to observe peaks from all brain tissues. Therefore, a final

conclusion regarding the specific resonance frequencies of all ^{129}Xe compartments, rather than merely just their frequency ranges, was not possible. Wakai et al. was able to observe all the individual ^{129}Xe resonances by averaging 60 acquisitions during continuous breathing of an enriched HP ^{129}Xe gas mixture. They observed five ^{129}Xe spectral peaks in the rat brain that ranged between 189 ppm and 210 ppm[37]. Following this work, Nakamura et al. assigned a spectral peak at 195 ppm to the brain tissue, one at 210 ppm to HP ^{129}Xe dissolved in the blood, and one at 189 ppm to non-brain tissues (assumed to be muscle)[38]. Their conclusions on the resonance frequencies of HP ^{129}Xe in the brain were aided by employing a rat model involving an arterial ligation. Kershaw et al. found the peaks at 195 ppm and 192 ppm originated from grey and white matter, respectively[39]. Additionally, the peaks at 189 ppm and 198 ppm were interpreted as signals from the jaw muscle and fat tissue[39].

The ability to distinguish the HP ^{129}Xe peaks in the human brain has become possible with the availability of increased xenon polarization. 1D CSI spectra of the human brain with ^{129}Xe polarized up to 8%, and a 2D CSI image using 14% polarized ^{129}Xe dissolved in brain tissue superimposed on a ^{1}H image, were obtained by Kilian et al in 2002[40]. Two additional peaks at 198 ppm and 195 ppm were observed on the 1D CSI spectra beside an already identified peak at 196 ppm from Mugler et al.'s results[34]. The 2D CSI measurements (Figure 2-2) revealed at least three additional peaks at 185 ppm, 193 ppm, and 200 ppm after spectral averaging, in addition to a peak previously observed at 197 ppm[40]. Following their initial study, Kilian et al. performed an additional 2D CSI using isotopically enriched HP ^{129}Xe to determine the origin of ^{129}Xe peaks in the tissue compartment[41]. The authors observed two dominant peaks from HP ^{129}Xe in the brain region at 196 ppm and 193 ppm, and two additional minor peaks from HP ^{129}Xe in non-brain

tissues located below the brain at 190 ppm and 201 ppm. The origins of the dominant peaks at 196 ppm and 193 ppm were proposed to come from the grey and white matter, respectively.

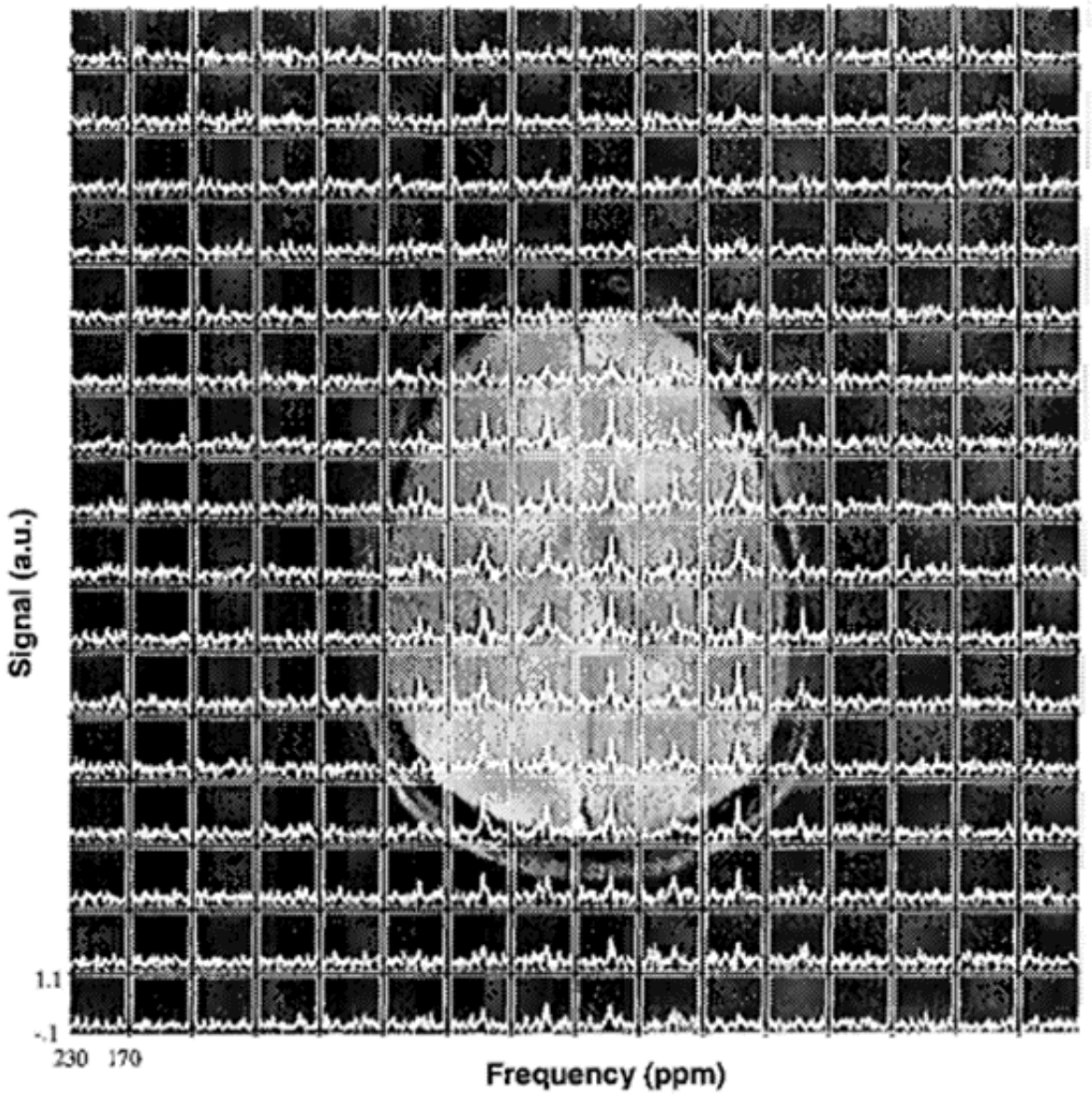

Figure 2-2 2D CSI spectra of HP ^{129}Xe dissolved in brain tissue superimposed onto a ^{1}H image. The image was reprinted with permission from the publisher[40].

After more than 10 years since these animal studies, during which time the polarization of HP ^{129}Xe was significantly improved, Rao et al. demonstrated the first HP ^{129}Xe human brain CSI, with detailed spectroscopy, at 1.5 T in 2015, where a red blood cell (RBC) ^{129}Xe peak was observed for the first time[42]. During the following year, they published a detailed study on the assignments of all the observed HP ^{129}Xe brain peaks, which was based on high-resolution spectroscopy and CSI measurements[43]. In the latter study, three healthy volunteers each inhaled 1 L of HP ^{129}Xe, followed by a 20 s breath-hold, during which the acquisition was performed. CSI was conducted to assign the HP ^{129}Xe peaks obtained from the spectroscopy results (Figure 2-3d) to various tissue compartments within the head. An HP ^{129}Xe peak at 188 ppm (Figure 2-3a) was assigned to HP ^{129}Xe dissolved in soft muscular tissue in the cheek and ^{129}Xe in the midbrain. The peak at 192 ppm (Figure 2-3b) corresponded to HP ^{129}Xe dissolved in white matter, the peak at 196 ppm (Figure 2-3c) corresponded to HP ^{129}Xe dissolved in grey matter, and the peak at 200 ppm (Figure 2-3e) was assigned to HP ^{129}Xe dissolved in the plasma, fat tissue outside of the brain, and cerebrospinal fluid. The final peak observed at 217 ppm (Figure 2-3f) showed high signal intensity at the location of the Circle of Willis and corresponded to HP ^{129}Xe dissolved in RBCs. The results of this study mostly agreed with the results obtained from previous studies using animal models. One difference, however, was in frequency of the RBC peak, which was reported at 210 ppm in rats, and at 217 ppm in humans.

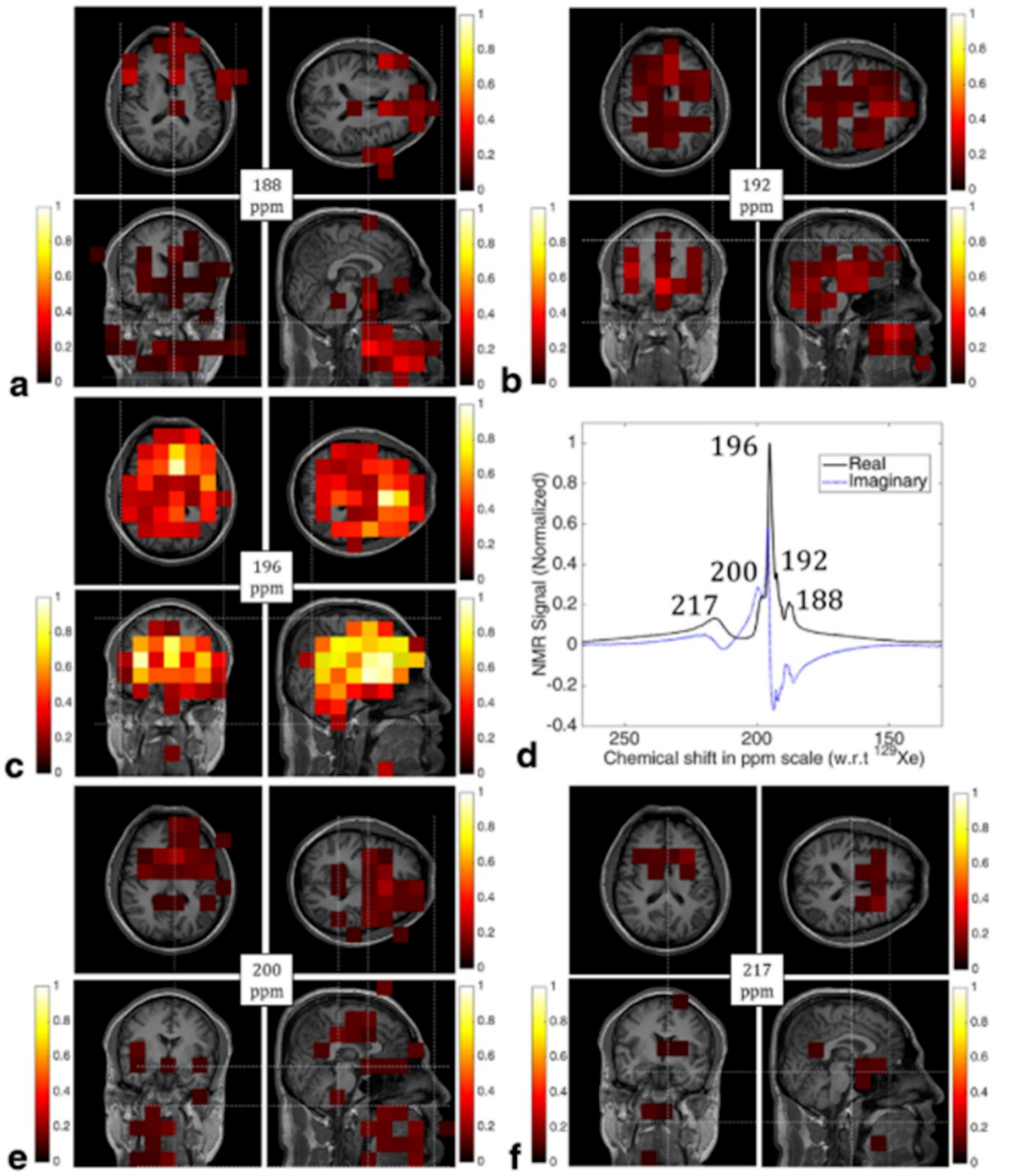

Figure 2-3 2D CSI of spatially resolved peaks from ^{129}Xe in the human head superimposed onto ^{1}H images. (a) Tissue in the cheek muscle and the midbrain/brainstem (b) White matter and cartilaginous soft tissue (c) Gray matter (d) Spectra of the whole brain with a bandwidth of 136.0 9 ppm and a spectral resolution of 0.33 ppm (e) Body interstitial fluid/plasma, fat tissue outside of the brain and cerebrospinal fluid (f) RBC. The figure was reprinted with permission from the publisher[43].

A spectroscopic study by Li et al.[44] evaluated the influence of the pulmonary oxygen concentration on the HP ^{129}Xe brain signal. The authors proposed an "apparent relaxation time" as a parameter that reflects the dependence of the HP ^{129}Xe brain signal on the pulmonary oxygen concentration. The optimal pulmonary oxygen concentration range for maximizing the SNR of ^{129}Xe brain images was reported to be between 25% and 35%, which agrees with previous experimental and theoretical findings[45].

Antonacci et al. raised an important question of the effect of the macroscopic susceptibility gradients upon the dissolved-phase HP ^{129}Xe chemical shift[46]. They pointed out the lack of consistency of the HP ^{129}Xe chemical shift dissolved in the same tissues in the different studies. To solve this problem, they proposed a novel method for mitigation of the effects of the macroscopic susceptibility gradients by referencing the dissolved ^{129}Xe resonances with the chemical shifts of the nearby ^{1}H water protons. This allows the comparison of the chemical shift values from different studies and aids in the correct identification of the origin of the peaks.

2-3. Relaxation time measurements

Another important characteristic of HP ^{129}Xe are the spin-lattice or longitudinal (T_1) and spin-spin or transverse (T_2) relaxation times. The image quality depends on the repetition time and echo time, which are set based on the longitudinal and transverse relaxation time values respectively. The first measurement of the longitudinal relaxation was performed *ex vivo* in rat brain tissue at 9.4 T by Wilson et al.[47] T_1 relaxation times were determined at varying oxygenation levels and were reported to be 18±1 sec in the oxygenated state and 22±2 sec in the deoxygenated state. Following this *ex vivo* study, Duhamel et al. measured the longitudinal and transverse magnetization *in vivo* at 2.35 T[48]. The T_1 of HP ^{129}Xe dissolved in brain tissue was calculated to be 14±1 sec and the T_2^* was measured to be 8.0±1.2 ms[49]. Spin-lattice relaxation for the white

matter was also derived from human brain dynamic spectra by Kilian et al. to be 8 s[50]. The next measurement of T_1 relaxation was performed *in vivo* in the rat brain by Wakai et al, who proposed a method for measuring the longitudinal relaxation without the need for an estimation of the flip angle[51]. Using this approach, the longitudinal relaxation time of ^{129}Xe in the rat brain was found to be 26 ± 4 s. Due to the large discrepancies reported for T_1 in the above studies, in 2008, Zhou et al. reinvestigated the longitudinal relaxation time of ^{129}Xe dissolved in the rat brain by developing a mathematical description of the HP ^{129}Xe wash-out process from the brain[52]. The authors determined the longitudinal relaxation time of ^{129}Xe dissolved in the rat brain using a two pulse method (T_1 = 15.3 ± 1.2 s) and also a multi-pulse protocol (T_1 = 16.2 ± 0.9 s)[52].

The effective spin-spin relaxation (T_2^*) for the ^{129}Xe grey matter peak in the rat brain was estimated mainly from the linewidth at half-height of the peak by Mazzanti et al. to be 5.42±0.3 ms at 4.7 T (observed at 194.7 ppm)[53], and by Rao et al. in the human brain at 1.5 T to be 8.8 ms[43].

In summary, there is a lack of consistency among the measured relaxation values (Table 2-1). Furthermore, there were no T_1 measurements performed for HP ^{129}Xe dissolved in the grey matter in humans. An accurate assessment of HP ^{129}Xe T_1 in the grey matter at different magnetic field strengths is vital for the practical implementation of HP ^{129}Xe brain imaging. Indeed, one of the main potential applications of HP ^{129}Xe brain imaging is rapid quantification of cerebral perfusion, as well as blood-brain barrier permeability. According to multiple mathematical models that were developed[50,54–56], however, the HP ^{129}Xe signal dynamics depend equally on both tissue perfusion and the T_1 relaxation time. Therefore, until T_1 is quantified with high accuracy in healthy individuals as well as in patients with neurodegenerative or cerebrovascular diseases, brain perfusion imaging using HP ^{129}Xe MRI will remain mostly qualitative.

Surprisingly, there were no T_2* measurements conducted for HP ^{129}Xe dissolved in human brain white matter, cerebral blood plasma and RBCs, and soft muscle tissue. These measurements are essential for further HP ^{129}Xe brain imaging pulse sequence development because they will allow proper optimization of the imaging TEs.

Table 2-1: Chemical shift, longitudinal and transverse relaxation of HP ^{129}Xe dissolved in the different brain tissues

	Chemical shift relative to gas peak (ppm)		T_1(s)	T_2^*(ms)
Rat brain studies	Tissue	194.5 (2.0 T)[33] 199 (2.35 T)[36] 195 (4.7 T)[38] 198 (4.7 T)[39]	14.0±1.0 (2.35 T)[48] 3.6±2.1 (2.35 T)[57] 26±4 (4.7 T)[51] 15.3-16.2 (4.7 T)[52]	8.0±1.2 (2.35 T)[48] 5.42±0.3 (4.7 T)[53]
	Muscle	189 (4.7 T)[38] 189 (4.7 T)[39]		
	Blood	210 (4.7 T)[38]		
	Gray matter	195 (4.7 T)[39]		
	White matter	192 (4.7 T)[39]		
Arterial blood			18±1 (oxygenated 9.4T)[47] 22±2 (deoxygenated 9.4T)[47] 13.7±1.6 (4.7 T)[18]	

			13-16 (1.5 T)[20]	
Human brain studies	Grey matter	196.5 (2.94 T)[50] 196 (3 T)[41] 196 (1.5 T)[43]		8.8 (1.5 T)[43]
	White matter	193 (3 T)[41] 192 (1.5 T)[43]	8 (2.94 T)[50]	
	Red Blood Cells	222 (1.5 T)[20] 224 (4.7 T)[18] 217 (1.5 T)[43]		
	Blood plasma	197 (1.5 T)[20] 198 (4.7 T)[18] 200 (1.5 T)[43]		
	Muscle tissue	188 (1.5 T)[43]		

2-4. Structural brain imaging with HP ^{129}Xe.

At the end of the 20st century, the initial discovery of boosting the ^{129}Xe signal with hyperpolarization for structural imaging of the brain using HP ^{129}Xe was extremely promising[9]. After signal intensity measurements at the beginning of the 21st century, however, it became clear that the polarization of HP ^{129}Xe needed to be significantly higher than what was possible at that time. Swanson et al. measured an SNR of 20 in the rat brain with 3.1x3.1x10 mm^3 voxels[33]. Due

to the limited concentration of HP ^{129}Xe dissolved in brain tissue, CSI was employed as the main imaging approach for HP ^{129}Xe brain studies. To address the limitation of relying upon CSI for HP ^{129}Xe brain imaging, Nouls et al. developed a fast 3D radial gradient echo acquisition approach for HP ^{129}Xe brain imaging[58]. They acquired high-resolution 3D images of the HP ^{129}Xe distribution in the rat brain with an isotropic 32 x 32 x 32 matrix and a voxel size of 3.65 x 3.65 x 3.65 mm^3. (Figure 2-4).

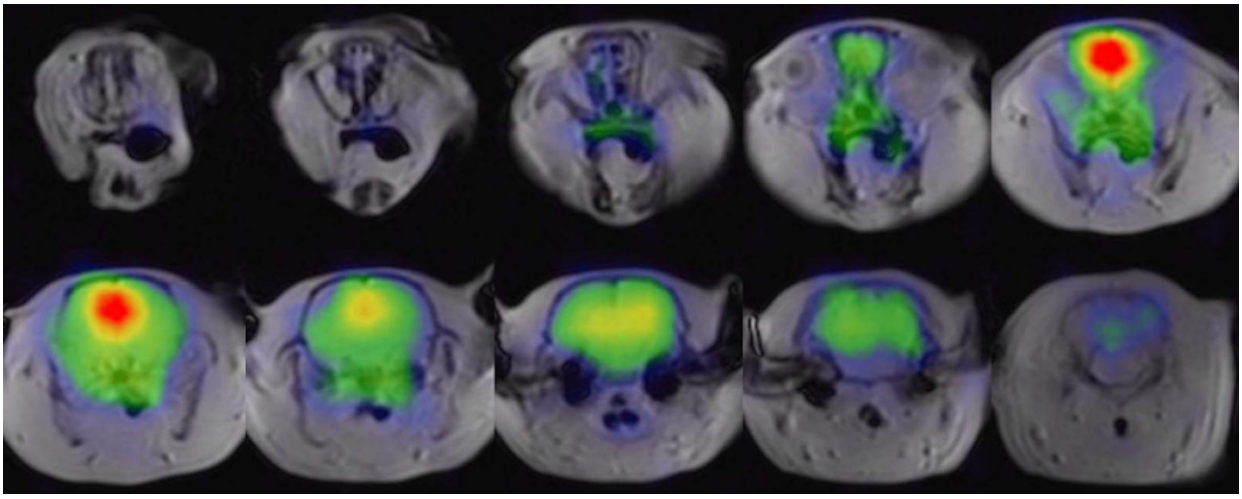

Figure 2-4 3D HP ^{129}Xe MR images of rat brains. The dissolved HP ^{129}Xe image (color) is overlaid onto a ^{1}H anatomical image (grayscale). The ^{129}Xe signal largely matches the brain tissue. The ^{129}Xe signal was notably intense in the olfactory bulb and mid-brain regions and was largely absent from the cerebellum. The images are reprinted with permission from the publisher[58].

Recently, Friedlander et al. demonstrated spectrally resolved HP ^{129}Xe imaging of the rat brain using iterative decomposition with echo asymmetry and least-square estimation (IDEAL) using a spiral readout at 3.0 T[59,60]. Using this approach, images of ^{129}Xe dissolved in brain tissue and red blood cells (RBCs) were acquired with an SNR of 31±4 and 16±2, respectively, and a resolution of 0.5x0.5 cm^2.[59] Utilizing time-resolved dynamic spiral IDEAL imaging, Friedlander et. al. was able to perform, for the first time, ^{129}Xe local blood-brain barrier (BBB) permeability assessment in hypercapnic and normocapnic rats during continuous breathing of HP ^{129}Xe[60].

Successful IDEAL decomposition of the dissolved-phase HP ^{129}Xe signal will likely be of interest for human brain imaging in future studies.

The first HP ^{129}Xe structural human brain image was acquired at 1.5 T by Rao et. al. in 2015, once the process of polarization was improved[42]. The image was acquired in an axial projection using a 2D spoiled gradient-echo sequence with a voxel size of 6.88 x 6.88 x 50 mm^3. The HP ^{129}Xe brain image correlated with the corresponding anatomical ^{1}H MR image.

Rao et al. recently went on to perform 3D isotropic spectroscopic imaging of HP ^{129}Xe in the human brain[61]. The acquisition matrix was 10 x 10 x 10, yielding a slice thickness of 2 cm and an acquisition voxel size of 8 cm^3. The acquired images were interpolated to a voxel size of 0.24 cm^3 and a slice thickness of 0.625 cm. This novel approach for HP ^{129}Xe spectroscopic imaging cold be potentially implemented in further brain oxygenation mapping.

The most recent contribution to HP ^{129}Xe structural brain imaging was achieved by Grynko et. al. by acquiring 3D multi-slice images of the human brain at 3.0 T (Figure 2-5)[62]. Five slices of the human brain were imaged with a slice thickness of 20 mm and an acquisition voxel volume of 1.22 cm^3 which is the smallest acquisition voxel volume of HP ^{129}Xe human brain imaging currently achieved. The highest SNR was reported to be 18.76±4.95 from the inhalation of 1 L of HP ^{129}Xe polarized to ~50%.

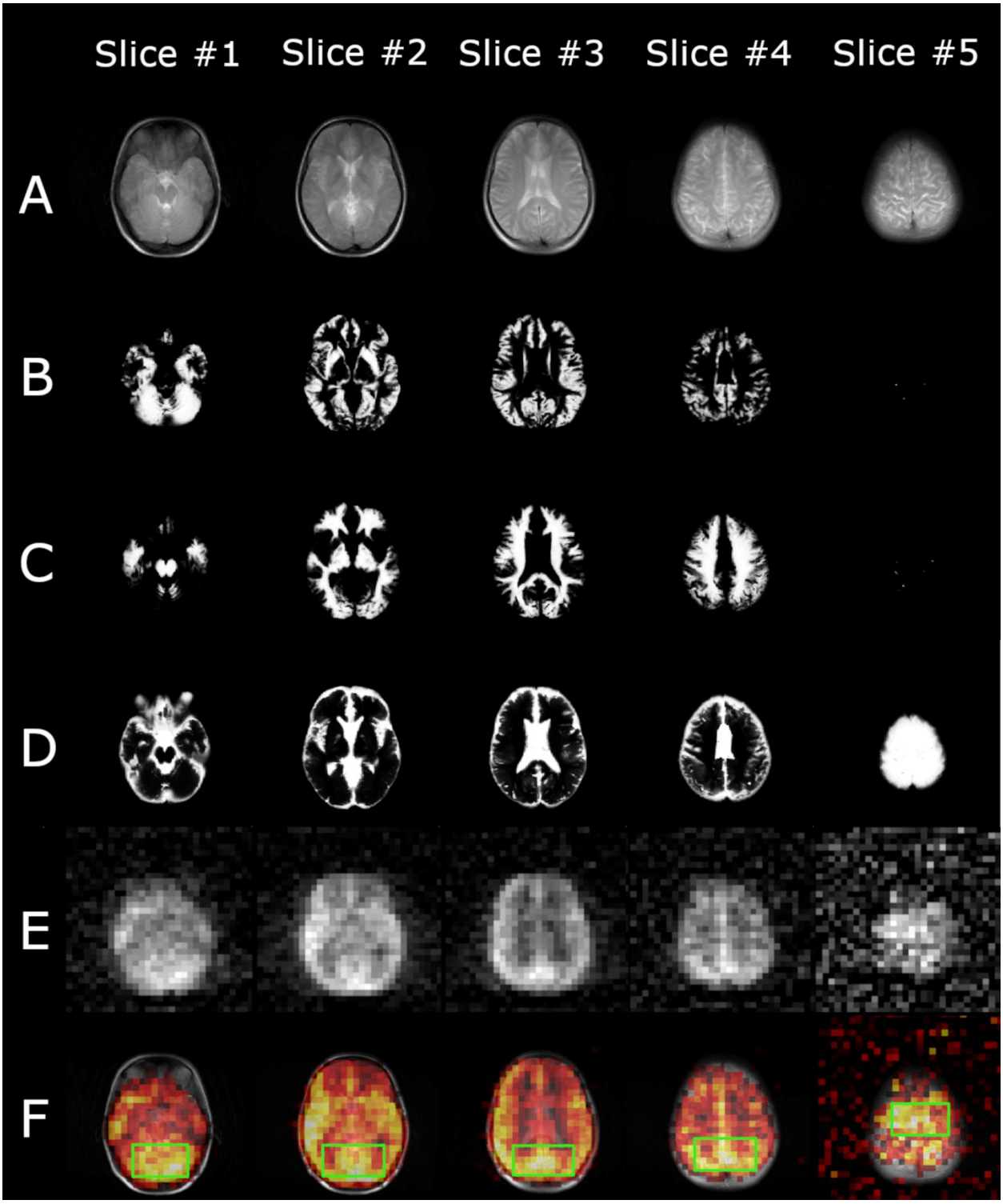

Figure 2-5 The first HP ^{129}Xe 3D GRE multi-slice image of the human brain. (A) ^{1}H T_2-weighted anatomical axial turbo spin-echo (TSE) images of a representative healthy volunteer, (B-D) Axial anatomical images of grey matter (B), white matter (C), and cerebrospinal fluid (CSF) (D) segmented using high-resolution TSE ^{1}H T_2- -weighted images of a representative healthy volunteer. (E) 3D GRE HP ^{129}Xe

axial brain slices acquired 10 s into the breath-hold. (F) Thresholded HP ^{129}Xe axial brain slice images superimposed on top of the corresponding ^{1}H anatomical images from row (A). It can be seen, that the HP ^{129}Xe signal corresponds well to the grey matter distribution in the brain. In addition, a partial correlation has been observed between the white matter images and the HP ^{129}Xe images. The image was reprinted with permission from the publisher[60].

These two recent studies provided a significant step forward, demonstrating the ability of HP ^{129}Xe brain imaging to produce multiple slices, which will allow the accurate and precise anatomical localization of HP ^{129}Xe dissolved in the human brain.

Despite these recent achievements in structural HP ^{129}Xe imaging of the brain, the imaging voxel size remains approximately two orders in magnitude larger compared to that of conventional anatomical proton MRI (^{1}H voxel size ~ 10 mm^{3}). The low concentration of ^{129}Xe dissolved in the brain tends to significantly restrict the spatial resolution achievable for imaging. Based upon previous uptake models[50,63] (detailed in the next section) and the Oswald solubility of ^{129}Xe in pulmonary blood[64], it is estimated that only about 1-2% percent of the amount of inhaled ^{129}Xe actually dissolves in the brain tissues. In spite of the low concentrations of ^{129}Xe achievable in brain tissue, however, it will be seen in the following sections that there is great value for employing HP ^{129}Xe for perfusion and other functional studies of the brain.

2-5. HP ^{129}Xe uptake models

The dynamics of HP ^{129}Xe uptake in the brain and its wash-out are complex and require careful consideration of multiple factors. Therefore, an accurate mathematical model of HP ^{129}Xe signal dynamics is required for appropriate experimental design.

The first attempt to model ^{129}Xe uptake in brain tissues was performed by Peled et al. in 1996[63]. They proposed an uptake model which calculated the time-dependent build-up of polarized ^{129}Xe in brain tissue compartments based on estimates of the ^{129}Xe relaxation times in tissue, perfusion rates, arterial transmit time, and partition coefficients. The authors considered

continuous breathing a dose of 70% enriched HP ^{129}Xe mixed with 30% O_2. The model predicted a maximum concentration of ^{129}Xe of 27 uM for grey matter and 8 uM for white matter and myelin, reached at 60 s after inhalation. Martin et al. extended Peled's model by accounting for different breathing protocols and estimated the ^{129}Xe concentration in the brain for a wide range of T_1 values for the gas and tissue phases[65]. The key ^{129}Xe T_1 parameters used in the model were as follows: 1000 s in the polarizer cell, 6 s in the arterial blood and in the tissue, and 12 s in the mouth and lungs. In this model, the polarization of ^{129}Xe was assumed to be equal to 100%. The lung to brain transit time was estimated to be 5 s. Three different breathing protocols were investigated: continuous breathing, hyperventilation followed by a breath-hold, and hyperventilation followed by continuous breathing. The maximum HP ^{129}Xe concentration in the grey matter was calculated to be 0.09 mM at 15 s post inhalation for both the hyperventilation with a breath-hold, and the continuous breathing, methods. The ^{129}Xe concentration in the brain was predicted to be 0.04 mM at 50 s after inhalation for the continuous breathing protocol[65]. Although both of these initially proposed models did not account for such factors as chemical shift effects, HP ^{129}Xe passage through biological membranes, and ^{129}Xe exchange between brain compartments, they provided useful information for conducting further research. Kilian et al. went on to propose an improved ^{129}Xe uptake model based on spectroscopic MR measurements at various time points after ^{129}Xe inhalation[50]. The model was in agreement with the quantitative ^{129}Xe spectroscopy experimental data. Kilian also reported that the longitudinal ^{129}Xe relaxation in grey matter was slower than that in white matter ($T_{1g}>T_{1w}$)[50]. This model, however, also had drawbacks. It did not account for the gradient of ^{129}Xe solubility in grey and white matter or the exchange of ^{129}Xe between the tissues and the bloodstream. Following this, Shepelytskyi et. al. expanded upon Kilian's model for the case of HP ^{129}Xe dynamic imaging, and implemented it for perfusion imaging of the human brain[54]

An additional mathematical description of the HP ^{129}Xe wash-out process was developed by Zhou et al. for better estimation of the longitudinal relaxation time of ^{129}Xe dissolved in the brain tissues[52]. Following this, Kimura et al. developed an HP ^{129}Xe uptake model and investigated ^{129}Xe uptake using Chemical Shift Saturation Recovery (CSSR) spectroscopy in the mouse brain[66]. This model allowed improvements to the estimation accuracy of the HP ^{129}Xe longitudinal relaxation time in the mouse brain. Imai et al. also developed a theoretical model of the ^{129}Xe signal dynamics in the mouse brain, and suggested a method for its quantitative measurement under continuous ^{129}Xe ventilation conditions[67].

The most recent kinetic model of HP ^{129}Xe uptake was developed by Rao et al. for the determination of the transfer rate of inhaled xenon from cerebral blood to the grey matter in the human brain[55,68]. Using the time course of the HP ^{129}Xe spectroscopic signal, the authors introduced a tracer kinetic model that explains the exchange of ^{129}Xe between these compartments[55]. In this model, the transient ratio of the HP ^{129}Xe concentration from grey matter to the blood was calculated from single-voxel MRS spectra. The slope of the transient ratio over time was proposed as a physiological marker of BBB permeability. The main advantage of Rao et al.'s model compared to other uptake models is that it considers the forward exchange of ^{129}Xe between the cerebral blood and grey matter tissue. It considers, however, only the forward transfer of HP ^{129}Xe, and also neglects the gradient of the HP ^{129}Xe concentration in the grey mater.

The further development of more complex mathematical models is required to accurately describe the concentration of HP ^{129}Xe in the brain, and consequently, its signal dynamics. Future models must also make a special effort to describe the HP ^{129}Xe diffusion processes in brain tissues. They must consider both forward and retrograde transfer of HP ^{129}Xe as well as properly describe the HP ^{129}Xe concentration gradient within the brain tissues. The diffusion coefficients of HP ^{129}Xe

in the cerebral blood and brain tissues currently remains unknown, which reduces the accuracy of the previously established models since they often utilize the value of the ^{129}Xe diffusion coefficient in aqueous solutions as a substitute for that in the brain. Dedicated measurements of these important physical parameters for HP ^{129}Xe are required in order to make further progress on HP ^{129}Xe uptake modelling.

2-6. Perfusion imaging with HP ^{129}Xe

Perfusion imaging is widely used in the clinic for the assessment of cerebrovascular physiology in order to diagnose brain pathologies such as brain tumours and stroke. Hyperpolarized ^{129}Xe is an exogenous agent which can act as an imaging agent for the evaluation of brain perfusion. This application was first predicted by Duhamel et al. in 2002, but the low polarization values of HP ^{129}Xe (18-20%) at that time did not permit the researchers to obtain high-quality results for perfusion assessment in the rat brain[49]. The next attempt for perfusion evaluation was performed by Rao et al. in the human brain in 2018, with HP ^{129}Xe polarized to 35% at 1.5 T[68–70]. Three healthy volunteers inhaled 1 L of 87% enriched ^{129}Xe for a 24 s breathhold duration. The HP ^{129}Xe uptake images were acquired with time intervals of 8 s, 16 s, 24 s, 32s, 40 s, and 48 s after inhalation (Figures 2-6a-f). The volunteers resumed breathing at 24 s. The resulting images were zero-padded up to an 80x80 in-plane resolution from 7.81x7.81x130 mm^3 voxels with a 32x32 resolution. The first four images were signal averaged for further comparison to arterial spin labeling (ASL) imaging. The signal averaged HP ^{129}Xe images exhibited certain advantages over ASL perfusion imaging in that they did not require averaging over a period of several minutes and they further lacked any undesired signals from blood vessels (Figure 2-6h). The SNR from the averaged images (Figure 2-6g) was 31±9, 24±4 and 23±2 from the three healthy volunteers[70]. Although this technique is limited by the quantity of ^{129}Xe that is delivered to the brain and also

by the loss of ^{129}Xe polarization during transport from the lungs to the brain, it can be utilized for qualitative perfusion estimates in the human brain.

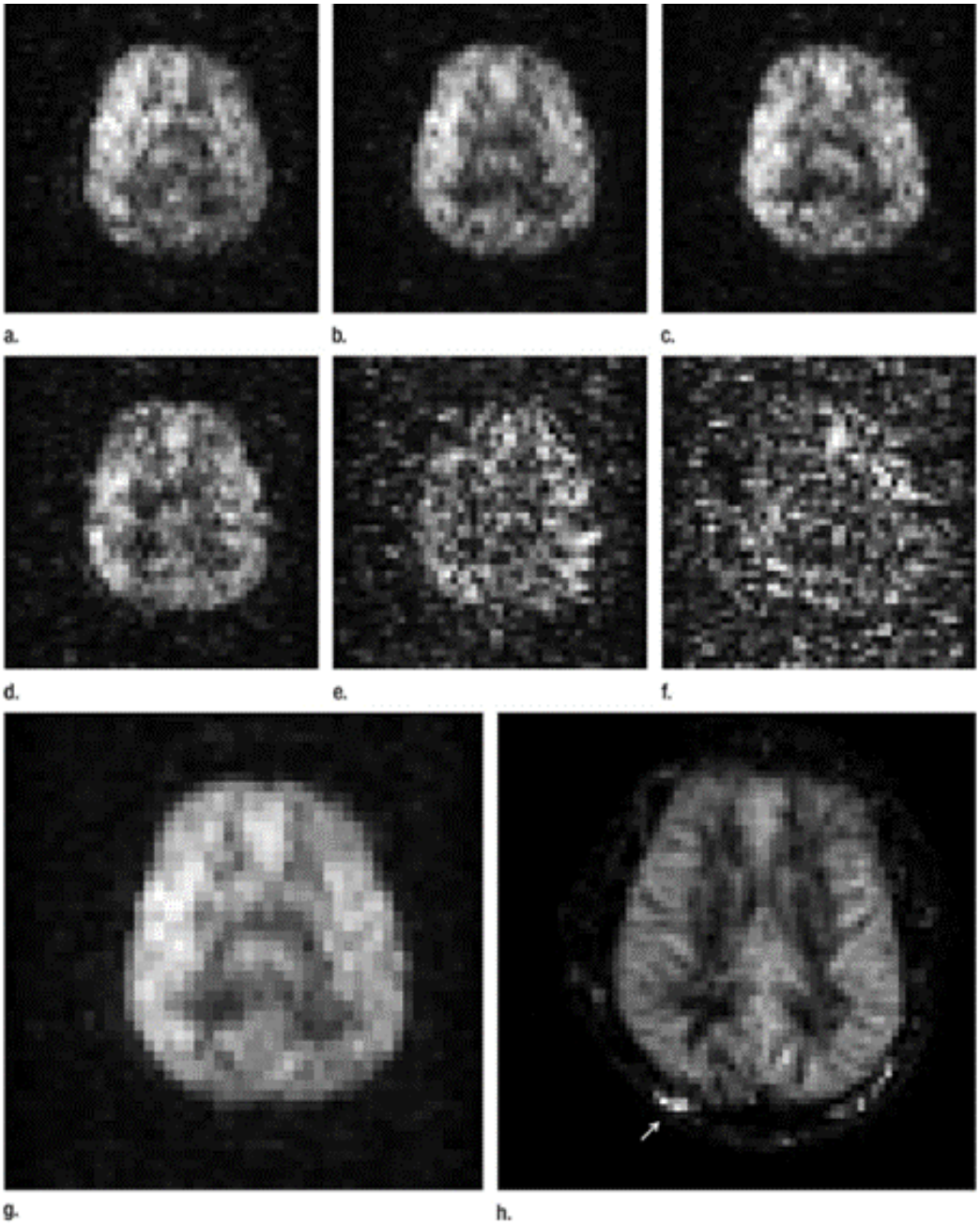

Figure 2-6 Brain perfusion in vivo images of a healthy volunteer. (a-f) HP ^{120}Xe imaging at 1.5 T at (a)8 s, (b) 16 s, (c) 24 s after inhalation during a breath-hold, (d) 32 s, (e) 40 s, (f) 48 s after continuing breathing. (g) average of the first four images (a-d) with 33 s total imaging time. (h) Pseudocontinuous arterial spin-labeling image at 3.0 T; summation of seven contiguous sections with total imaging time of 10 minutes. Images are reprinted with permission from the publisher[70].

Recently, Rao et al. demonstrated a moderate correlation between the cerebral perfusion values as measured by ASL and the ^{129}Xe uptake in the human brain[71]. In order to investigate this correlation, the ASL perfusion images were corrected for any depolarization that ^{129}Xe would experience using two exponential terms to account for the T_1 polarization decay of HP ^{129}Xe in the blood and during its residency time in grey matter. The authors reported a moderate positive correlation (correlation coefficient range of 0.34 - 0.63) between the corrected perfusion images obtained using ASL and the HP ^{129}Xe brain images.

The most recent study on HP ^{129}Xe perfusion imaging was conducted by Shepelytskyi et al. in 2020[54]. They demonstrated a novel ^{129}Xe Time-of-Flight (TOF) MR imaging technique capable of quantitative perfusion measurements. It was a different approach compared to that employed by Rao et al[70]. It was based on the time-resolved depolarization of dissolved HP ^{129}Xe in the brain and the acquisition of dynamic images after subsequent TOF wash-in delays. It fostered the absence of any background signal and isolated the HP ^{129}Xe delivered by the cerebral blood flow. Cerebral perfusion was recalculated from the dynamic HP ^{129}Xe TOF images using a modified version of Kilian's HP ^{129}Xe uptake model[50]. Three dynamic TOF images were acquired using incremental TOF delay times: 2.5 s, 6.7 s, and 7.1 s for axial projections; and 1 s, 6.5 s, and 7.1 s for sagittal projections. The images were acquired using a 20x20 acquisition matrix with a 12.5x12.5x70 mm^3 voxel volume, and zero-padded to a 32x32 matrix. Figure 2-7 shows the dynamic HP ^{129}Xe images and resulting perfusion map, overlaid on T_2-weighted ^{1}H brain images.

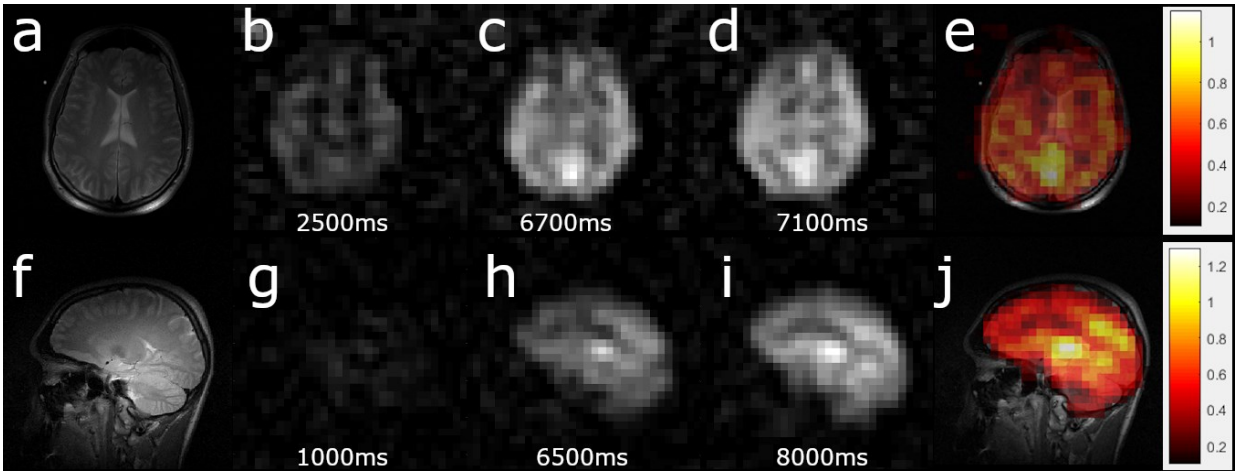

Figure 2-7 Example of perfusion map acquisition. (a,f) High-resolution, T_2-weighted ^{1}H scans for brain localization. (b-d) Three dynamic HP ^{129}Xe TOF images acquired 2.5 s, 6.8 s, and 7.1 s after the application of a depolarization radiofrequency pulse in the axial projection. The gradual SNR increase can be observed with increasing wash-in time. (e) The perfusion map created by the pixel-by-pixel recalculation of the TOF slope was used to calculate the sum of the perfusion rates of gray and white matter superimposed on top of a high-resolution proton brain image. Three dynamic TOF images acquired after 1 s, 6.5 s, and 8 s in the sagittal view (g-i). (j) Perfusion map in the sagittal view. Similar to (e), the intensity values were the net sum of the white and gray matter perfusion rates. Images are reprinted with permission from the publisher[54].

In spite of the fact that several major advances have been made in the development of HP ^{129}Xe perfusion imaging, this methodology remains largely in its infancy. There are numerous technical challenges associated with these approaches that originate from the issues highlighted in the sections above. Most applications of HP ^{129}Xe MRI for cerebral perfusion imaging remain to a large extent qualitative due to the fact that there have not been any imaging techniques developed which allow an accurate implementation of the existing HP ^{129}Xe dynamic models. Shepelytskyi et. al. carried out a quantitative estimation of cerebral perfusion[54], however, they utilized several significant simplifications which somewhat reduce the accuracy of their estimations.

2-7. Functional MRI with HP ^{129}Xe

Since HP ^{129}Xe acts as a natural cerebral blood flow tracer, it was suggested that HP ^{129}Xe brain imaging should be capable of detecting physiological activity in the brain via changes in the

local hyperpolarized ^{129}Xe density contrast[9]. The fundamental principles behind this mechanism are quite simple compared to the conventional Blood Oxygen Level Dependence (BOLD) technique for functional brain MR imaging (fMRI): blood flow to areas of the brain that respond to stimulation is higher, and consequently, the local concentration of HP ^{129}Xe in these regions will also be higher. Brain activation maps can therefore be created after subtraction of an HP ^{129}Xe reference image acquired during a resting state. This approach was utilized by Mazzanti et al. in 2011, who first demonstrated the ability of HP ^{129}Xe brain MRI to detect and map sensory stimulation of the rat brain[53]. Two-dimensional HP ^{129}Xe CSI images were acquired pre- and post-stimulation (Figure 2-8b-d) from injection of capsaicin into the fore-paw. The authors observed an increase of the HP ^{129}Xe signal in the somatosensory brain regions responsible for pain processing[53].

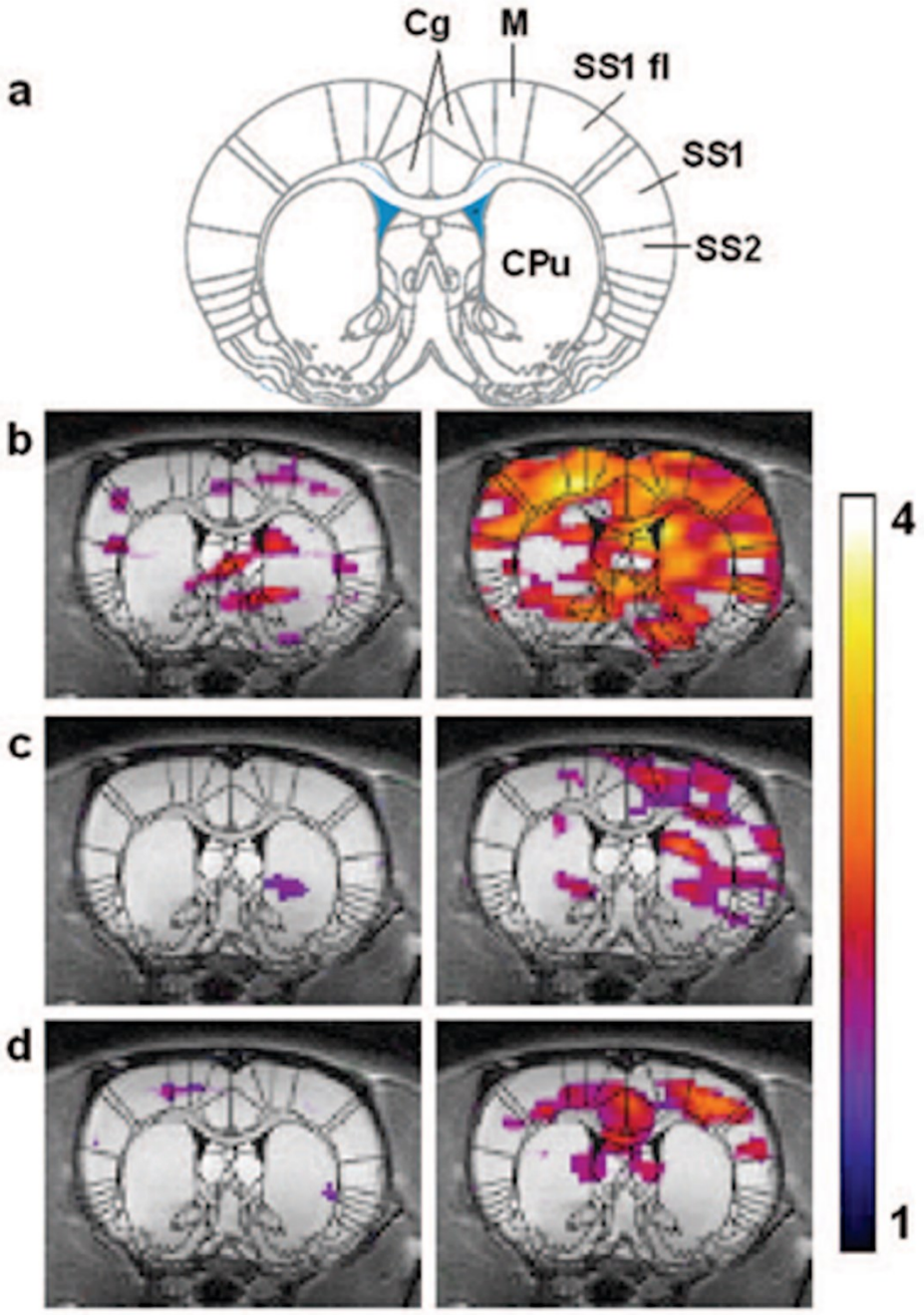

Figure 2-8 HP ^{129}Xe fMRI data from three animals. The HP 129Xe signal is shown as a false-color overlay on the corresponding 1 mm thick coronal proton reference image taken from the same animal. The left panel shows the HP ^{129}Xe signal intensity during baseline, and the right panel shows HP ^{129}Xe signal intensity after injection of capsaicin 20 ul (3 mg/ml) into the right forepaw. The color scale represents SNR, and only signal with SNR above two are shown. Superimposition of a rat brain atlas (18) shows specific areas of the brain: cingulate cortex (Cg), the motor cortex (M), primary somatosensory cortex, SS1 forelimb region (SS1 and SS1 fl), the secondary somatosensory cortex (SS2), and striatum (CPu). The images were reprinted with permission from the publisher[53].

Although these early results seemed promising, this methodology was fraught with inherent errors and limitations. The direct subtraction approach for two HP ^{129}Xe brain images is associated with a high level of potential errors caused by the interbreath-hold variability of the HP ^{129}Xe signal. This signal variability has been estimated to be ~ 30%, which can cause a large potential for false-positive and false-negative results during hemodynamic response mapping. This challenge was overcome by Shepelytskyi et al. who performed functional MRI of the human brain using the novel HP ^{129}Xe TOF imaging technique, which had been developed for perfusion assessment[54]. The HP ^{129}Xe TOF pulse sequence substantially reduced the interbreath-hold signal variability[72] and functioned well for an accurate assessment of the hemodynamic response (HDR)[54]. The HDR to visual and motor stimuli (Figure 2-9) was investigated. The resulting functional brain HDR maps (Figure 2-9b) correlated well with conventional ^{1}H BOLD functional MRI (Figure 2-9d).

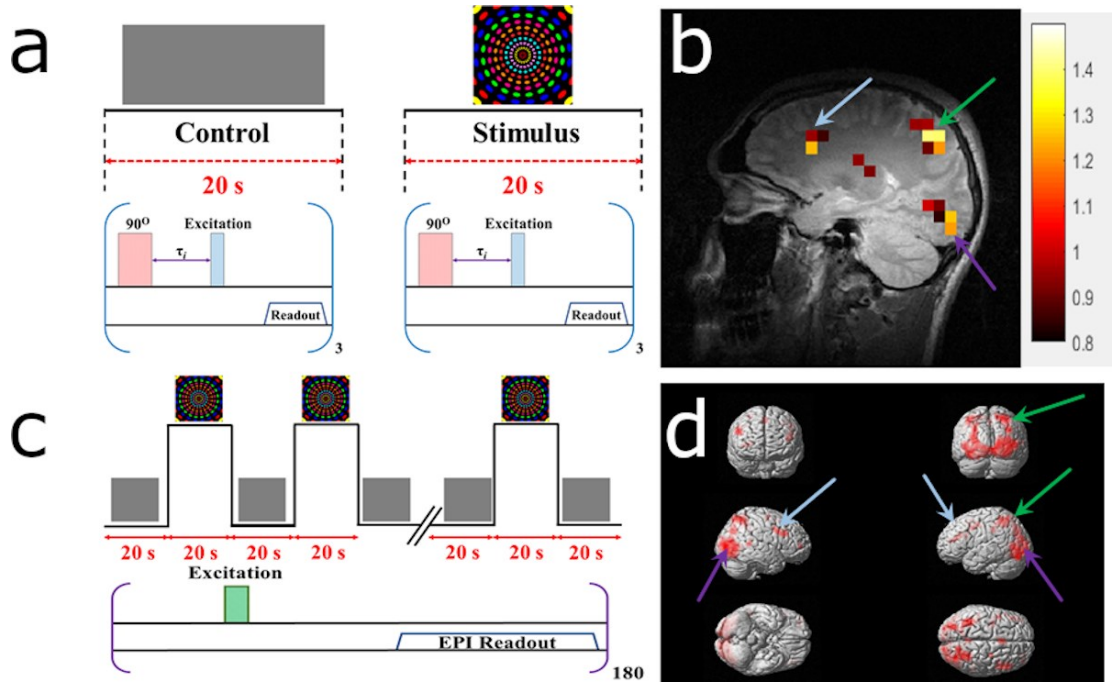

Figure 2-9 Detection of a hemodynamic response from a colorful visual stimulus using HP 129Xe perfusion mapping validated by blood oxygenation level-dependent (BOLD) brain functional MRI (fMRI).

(a) Experimental design used for hemodynamic response detection. Two separate perfusion maps were acquired during the control (gray screen) and visual stimulation. (b) Hemodynamic response map created by subtracting the control perfusion map from the stimulated perfusion map and overlaid on top of a high-resolution proton scan. Activation of the occipital lobe, superior parietal lobe, and frontal gyrus was observed. (c) BOLD fMRI experimental design for validation of the HP ^{129}Xe technique. (d) BOLD fMRI 3D activation maps demonstrate a correlation with a ^{129}Xe hemodynamic response map. The activated areas are indicated by colored arrows. Images are reprinted with permission from the publisher[54].

Although a spatial correlation between the HP ^{129}Xe HDR maps and conventional ^{1}H fMRI images was observed, the HP ^{129}Xe HDR maps had a substantially lower spatial resolution. The HDR maps had a single slice thickness of ~70 mm and 300 mm for axial and sagittal orientation respectively and an in-plane pixel size of 7.81 mm^2, whereas the conventional proton fMRI images were acquired with a 4 mm slice thickness and 3.91 mm^2 in-plane spatial resolution. Despite the significant limitations in spatial resolution, HP ^{129}Xe HDR mapping outperformed conventional fMRI in terms of temporal resolution as the whole brain was mapped in less than in 20 s.

2-8. Brain disease detection with HP ^{129}Xe

Despite the low signal intensity of HP ^{129}Xe dissolved in the human brain, it is possible to evaluate various differences in xenon physical properties between healthy subjects and subjects with brain-related diseases. Zhou et al. demonstrated the first application of HP ^{129}Xe brain CSI for *in vivo* ischemic stroke imaging[73] in a rat model. The large hypointense region corresponding to the ischemic core (Figure 2-10c) was observed in an HP ^{129}Xe image (Figure 2-10b)[73]. These results were corroborated by conventional ^{1}H diffusion-weighted imaging as well as by histology (Figure 2-10a).

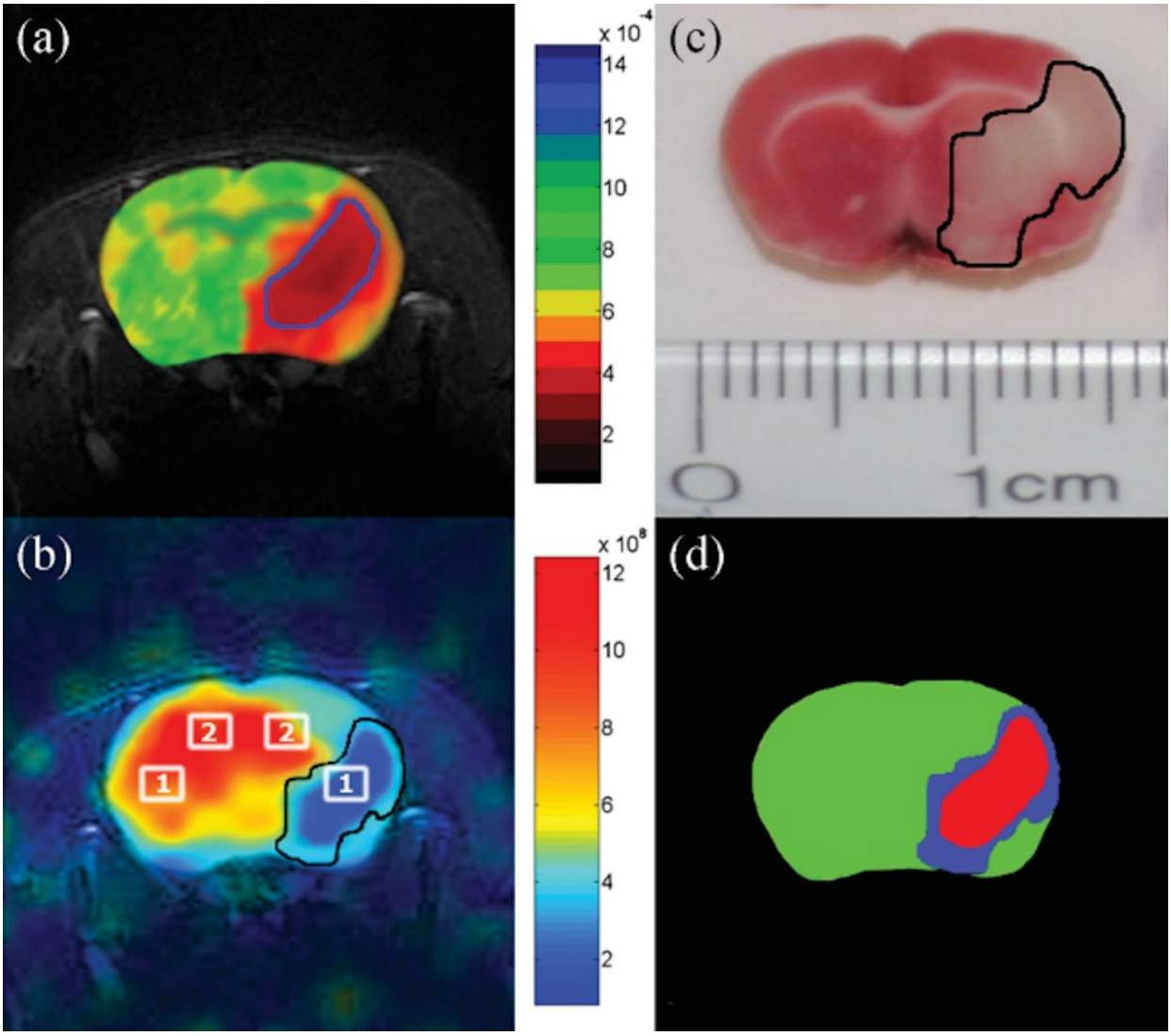

Figure 2-10 In vivo evaluation of stroke using 2D ^{129}Xe CSI. (a) Representative ^{1}H apparent diffusion coefficient map image obtained after a right middle cerebral artery occlusion. (b) Corresponding HP ^{129}Xe 2D CSI indicating the large signal void corresponding to the ipsilesional hemisphere. (c) Corresponding 2,3,5-triphenyltetrazolium chloride (TTC)-stained brain section of the same animal. (d) Tricolor map based on the ADC and TTC images shown in (a) and (c). Green, red and blue represent non- ischemic stroke. The images were reprinted with permission from the publisher[73].

Following this initial study in animal models, Rao et al. conducted HP ^{129}Xe brain perfusion imaging in a 52-year old volunteer who had a stroke two years and three months before imaging with HP ^{129}Xe[74]. The conventional proton MRI revealed intracranial arterial occlusion with collateralization (Figure 2-11a). To evaluate perfusion using HP ^{129}Xe, three 32 x 32 images were

acquired during a breath-hold at 8 s, 16 s and 24 s after inhalation of 1 L of HP ^{129}Xe with 35% polarization. The images were reconstructed up to an 80 x 80 in-plane resolution with subsequent averaging from a 32 x 32 matrix with voxel size 6.875 x 6.875 x 50 mm^3. The final image (Figure 2-11d) revealed a region of signal hypointensity, which indicated poor ^{129}Xe uptake in the stroke area. The regional cerebral blood flow (CBF; Figure 2-11c) calculated from pseudo-continuous arterial spin labelling (pASL) (Figure 2-11b), however, was higher in the same area, which indicated a delayed hyper-perfusion. The lower ^{129}Xe signal can be explained by a shorter mean transit time due to a higher CBF. This reduces the transfer of ^{129}Xe to the tissue and delays the delivery of ^{129}Xe to that area, which affects the magnetization because of its T_1 decay. Overall, this pioneering study demonstrated proof-of-principle contrast for using HP ^{129}Xe imaging for stroke imaging in human subjects.

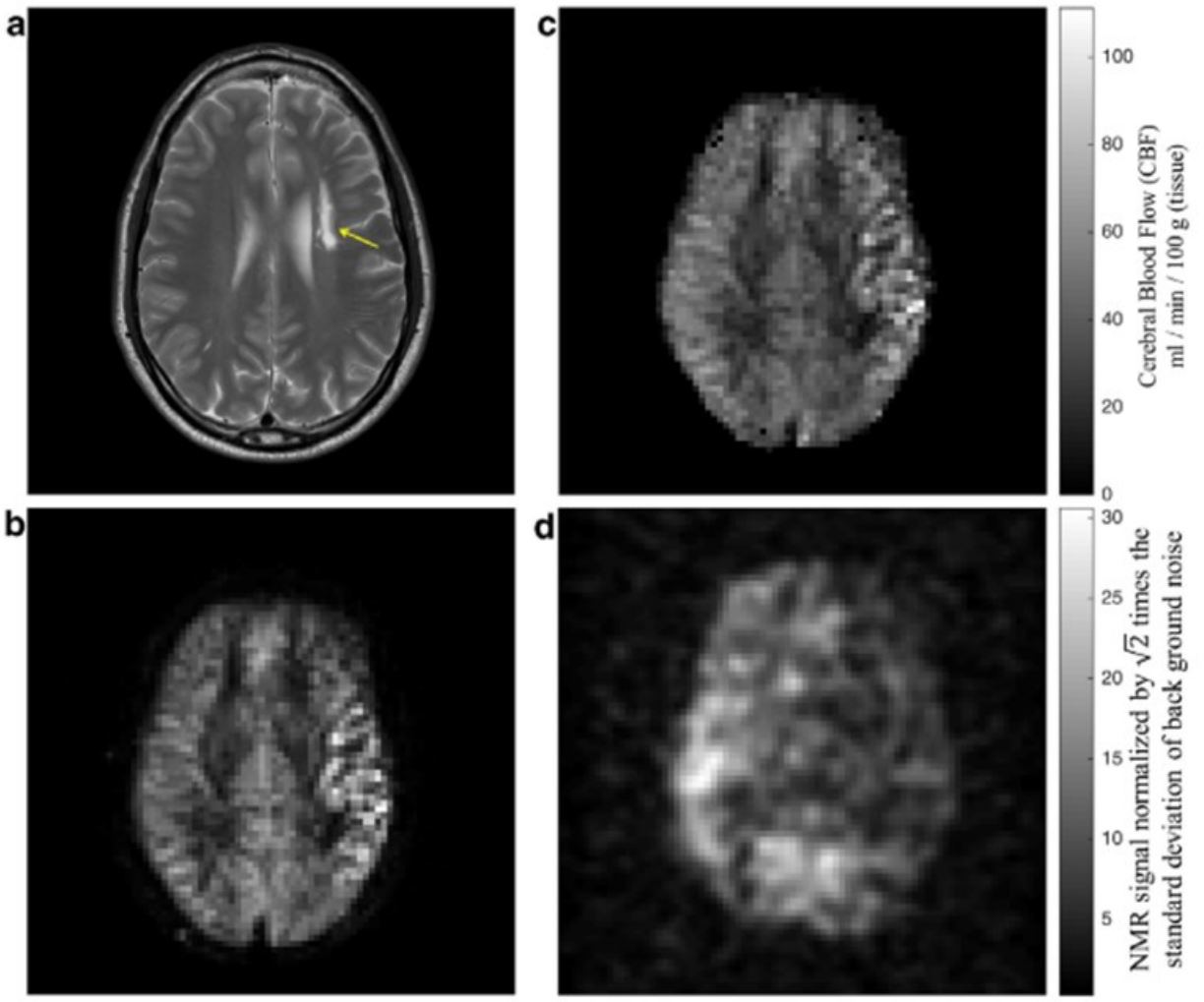

Figure 2-11 Brain MR images acquired in the same session from a subject with established stroke. (a) axial T_1-wighted image showing infarct in the centrum semiovale of the left cerebral hemisphere (arrow). (b) An axial image from pseudocontinuous ASL shows hyperintensity in the cerebral cortex adjacent to infarction. (c) Map of CBF estimated from ASL in (b) shows increased perfusion. (d) Hyperpolarized ^{129}Xe brain image shows reduced uptake in the brain tissue supplied by the left internal carotid artery. The ^{129}Xe signal in the region of hypointensity in (d) was 60% lower when compared with the average signal in the healthy region. Images are reprinted with permission from the publisher[74].

Another neurological disorder that affects the cerebral blood flow and the brain tissues is Alzheimer's disease (AD). To investigate the possibility of using HP ^{129}Xe imaging for AD detection, Hane et al. conducted an HP ^{129}Xe washout study in 2018[56]. Four participants diagnosed with mild to moderate AD and four age-matched healthy volunteers underwent HP ^{129}Xe gas MRS and MRI during a 20 s breath-hold. Sixty dynamic MRS scans were acquired every 2 s starting

from initialization of the breath-hold. Three dynamic balanced steady state free precession (SSFP) MRI images were acquired at 10 s, 20 s, and 30 s after gas inhalation. Five different peaks were observed using MRS that agreed with the spectroscopy results from Rao et al. in 2016[43]. Interestingly, however, in this study, the ^{129}Xe signal from grey matter was 43% lower in AD participants compared to healthy volunteers, and the white matter peaks were not statistically different between the two subject cohorts. This reduction in HP ^{129}Xe signal resulted in a decrease in the SNR of images acquired from the AD subjects (Figure 2-12a). The white and grey matter spectral peaks were monitored over time: the ^{129}Xe washout half-life for healthy participants was 20 s and 16 s for white and grey matter, respectively, while the ^{129}Xe washout half-life for participants with AD was 42 s and 43 s in white (Figure 2-12c) and grey matter (Figure 2-12d), respectively. The analysis of the dynamic ^{129}Xe MR images (Figure 2-12b) revealed that the Xe washout parameters were similar in the caudal brain regions for both cohorts of participants, whereas the prefrontal regions showed a reduction of the localized ^{129}Xe washout parameter in AD volunteers. Therefore, a ^{129}Xe retention parameter was proposed as a potential biomarker for AD detection.

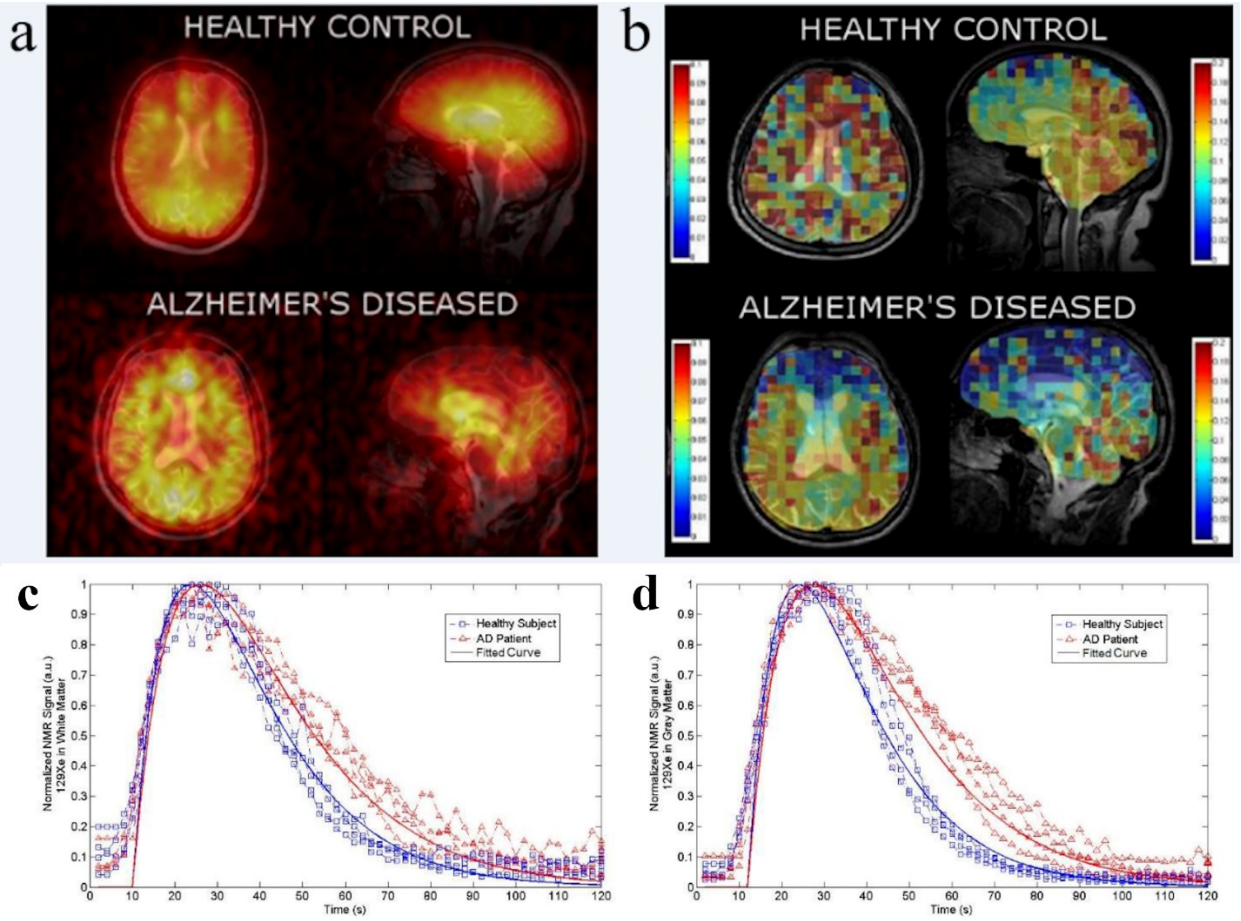

Figure 2-12 Axial and sagittal 129Xe MRI of healthy controls and Alzheimer's Disease (AD) participants. (b) Xenon washout parameter maps of healthy controls age-matched to AD patients overlaid onto T2W anatomical images. MRS SNR of 129Xe-WM (C) and 129Xe-GM (D) spectral peaks as a function of time for healthy controls (blue) and AD participants (red). The participants inhaled 500 mL of HP 129Xe and held their breath for 20 s. 129Xe MRS from the brain region was acquired every 2 s. An increase in 129Xe signal after approximately 10 s was noticed as the 129Xe reached the brain. At 20 s, the participant exhaled and the 129Xe signal began to decrease at different rates for AD participants compared to healthy controls for WM and GM. Images are reprinted with permission from the publisher[54].

2-9. Discussion

HP ^{129}Xe MR imaging of the brain is a promising medical imaging modality that is currently under extensive development. Thirteen articles on HP ^{129}Xe brain imaging were published between the period of the invention of HP ^{129}Xe MRI in 1994, and 2008, while 26 articles were published between 2008 to the present. Furthermore, the number of papers published in the

HP ^{129}Xe brain imaging field grew steadily over the past decade. The most prominent practical application of HP ^{129}Xe brain imaging so far has been its utilization for cerebral perfusion imaging[54,56,70,74]. The free dissolution of HP ^{129}Xe in the pulmonary blood renders ^{129}Xe an exogeneous blood-flow contrast agent. The signal intensity of HP ^{129}Xe brain images is determined mainly by the tissue perfusion, but further regulated by the level of polarization, the amount of Xe that is inhaled, and the concentration of xenon that is transferred to the brain (Xe solubility are 0.17 in the blood, 0.135 in grey matter, and 0.224 in white matter[50]). Furthermore, HP ^{129}Xe is an exogeneous perfusion inhalation contrast agent that does not provide any undesired background signal.

Unlike ^{1}H arterial spin labelling (ASL) perfusion imaging, the lack of background signal and need for intensive signal averaging both provide some of the main advantages of HP ^{129}Xe brain perfusion imaging. With this in mind, the acquisition protocol for HP ^{129}Xe MRI can potentially be simpler compared to that required for ASL MRI for future implementation in the clinic. Since no signal averaging is required, the specific absorption rate of HP ^{129}Xe perfusion imaging scans can also potentially be lower compared to ASL proton scans. Also, in contrast to ASL MRI, HP ^{129}Xe brain perfusion imaging can be performed at low field, due to both the exogeneous nature of HP ^{129}Xe and the fact that its signal has a weak dependence of the Bo magnetic field strength[75–77]. While ASL perfusion imaging is already well developed for clinical use, HP ^{129}Xe perfusion imaging is still in its infancy; further improvements to its method of signal acquisition, and increases to the ^{129}Xe polarization level, will be required in order to render HP ^{129}Xe perfusion imaging competitive with ASL MRI.

Another advantage of HP ^{129}Xe brain perfusion imaging is its ability for extremely rapid image acquisition. This fact–originates from the non-recoverable nature of the hyperpolarized

longitudinal magnetization. Since the HP state is a metastable non-equilibrium state, spin-lattice relaxation destroys the longitudinal component of its net magnetization over time. Therefore, the utilization of a short TR is highly beneficial, which also results in a short scan time. HP ^{129}Xe brain image acquisition times are typically on the order of seconds[56,74] (Table 2), albeit, further shortening of the scan time is usually possible. Such short image acquisition times also reduce the sensitivity of HP ^{129}Xe cerebral perfusion imaging to motion artifacts. In contrast, ASL perfusion imaging scans usually require several minutes due to the need for multiple signal averages, which makes conventional ASL MRI techniques very sensitive to motion artifacts[78–80].

Despite the aforementioned advantages of HP ^{129}Xe cerebral perfusion imaging, this methodology currently has several limitations. First, in order to perform HP ^{129}Xe MR imaging, the research center or clinical site must possess an MRI scanner capable of performing multinuclear imaging. In addition, is the need for a high yield ^{129}Xe polarizer (which is an expensive piece of equipment), and dedicated MRI coils tuned to the resonance frequency of ^{129}Xe. It is desirable to utilize a dual-tuned ^{1}H/^{129}Xe RF head coil since initial ^{1}H brain localization is required prior to HP ^{129}Xe brain imaging. Additionally, the use of isotopically enriched ^{129}Xe is often required to achieve acceptable SNR levels since the concentration of HP ^{129}Xe is relatively low in the brain tissues. The necessity of specialized equipment and isotopically enriched ^{129}Xe gas renders HP ^{129}Xe brain perfusion imaging much more expensive than conventional clinical ^{1}H perfusion MRI techniques.

As previously mentioned, another challenge for HP ^{129}Xe brain imaging is the relatively low concentration of ^{129}Xe dissolved in brain tissues (on the order of uM[50]). Therefore, the overall HP ^{129}Xe signal level originating from the brain is quite low, resulting in relatively low image SNR, which significantly limits the utilization of HP ^{129}Xe for anatomical brain imaging. In

common practice, in order to optimize the HP ^{129}Xe brain image SNR, the acquisition matrix is typically kept at a low resolution, and a single slice image is commonly acquired. The most commonly used acquisition matrix is 32 x 32, which is two times smaller compared to the most frequently used acquisition matrix for ASL imaging. In addition, ASL-based perfusion imaging techniques can acquire images with a slice thickness ~3-4 mm, whereas the minimum slice thickness achieved so far for HP ^{129}Xe imaging is 20 mm. This yields an HP ^{129}Xe voxel size that is at least 20 times larger compared to typical ASL voxel sizes. Recent advances in 3D GRE HP ^{129}Xe brain imaging can help to increase the spatial resolution of HP ^{129}Xe cerebral perfusion images and potentially render them comparable to modern clinical ASL standards. Further increases to the HP ^{129}Xe polarization (ideally up to the theoretical limit of 86%[81]) could potentially facilitate the enhancement in the signal required for utilization of an acquisition matrix of 64 x 64, which would meet current clinical standards for perfusion imaging. Even if this is accomplished, a 64 x 64 acquisition matrix will not be sufficient for structural brain imaging with HP ^{129}Xe, since conventional ^{1}H MRI is capable of much higher resolution. Therefore, it can be foreseen that HP ^{129}Xe brain MRI does not bode well as a new anatomical MRI imaging modality, but has great potential for applications in the fields of functional imaging, such as perfusion imaging, blood flow detection, and BBB permeability imaging.

Extensive development of both hardware and MR pulse sequences is required to increase the SNR and spatial resolution of HP ^{129}Xe brain MRI. The highest reported level of ^{129}Xe polarization utilized for brain imaging so far was ~ 50%[54,62,72], which is a significant advancement compared to polarization values used for earlier experiments[41,50]. An increase in the polarization level will produce a linear increase in the ^{129}Xe signal level. In addition, an increase in the isotopic enrichment of ^{129}Xe gas used for imaging will also give a linear increase in the image SNR. Finally,

the development and implementation of a multi-channel phased-array receiver RF coil could also increase the SNR of HP ^{129}Xe brain imaging. Although preliminary results have been reported using a 6-channel phased array ^{129}Xe brain coil for *in vivo* single-voxel spectroscopy[82], further implementation of the parallel imaging approach for imaging purposes is essential to advance HP ^{129}Xe imaging of the human brain.

Alongside hardware development, future work must also be focused on imaging pulse sequence development and breathing protocol optimization. Due to the short TR requirements, HP ^{129}Xe brain imaging mostly utilizes gradient echo (GRE) imaging pulse sequences. Until recently, the most commonly used MR protocol for ^{129}Xe brain imaging was a thick single-slice 2D GRE image acquisition with standard sequential k-space filling[54,56,70,74]. The use of non-Cartesian k-space trajectories, which oversample the center of a k-space (such as radial trajectories), can further increase the image SNR, and may allow the acquisition of thinner slices and higher spatial resolution in HP ^{129}Xe brain images. The downside of using non-Cartesian k-space trajectories is that they undersample the outer edges of k-space, which results in blurriness of the image.

Recent development by Rao et. al. allowed progression to 3D multi-slice isotropic ^{129}Xe brain MRI spectroscopic imaging, which could be further implemented for brain oxygenation mapping and for voxel-wise quantification of HP ^{129}Xe dissolved in different brain compartments[61].

Another pulse sequence approach worth pursuing is translation from 2D GRE to 3D GRE imaging. 3D GRE imaging will allow the image SNR to increase through additional phase encoding in the slice-selection direction and will allow multi-slice image acquisition. A proof-of-concept demonstration of 3D GRE HP ^{129}Xe imaging in humans was recently demonstrated by Grynko et. al[62]. In this study, utilization of a 3D GRE sequence allowed reduction of the voxel size

by 93% compared to the 2D GRE imaging approach. Since all the spins in the volume of interest get excited simultaneously, 3D GRE multi-slice imaging better utilizes the hyperpolarized magnetization, compared to 2D GRE multi-slice imaging. Combining 3D GRE pulse sequences with non-Cartesian k-space trajectories has the potential to further improve the quality of HP ^{129}Xe brain images.

The breathing protocol is another vital factor that should be carefully considered. The most commonly used breathing protocol for HP ^{129}Xe human brain imaging is the inhalation of 1L of HP gas followed by a subsequent breath-hold[54,56,70,74,83,84]. This approach, however, is associated with a high level of signal variability (~30%)[72,84]. This signal variability can be caused by numerous factors, such as the exact quantity of HP ^{129}Xe gas dispensed in the bag each time, the T_1 relaxation during gas storage before being administered, different concentrations of HP ^{129}Xe in the lungs, cerebral perfusion values, lung-brain arterial transit times, and the amount of time into the breath-hold when image acquisition begins. All these factors affect the concentration of HP ^{129}Xe dissolved in the brain at a particular moment in time. A recent study demonstrated that the utilization of a time-resolved initial depolarization pulse (TOF technique), reduces the variability of the HP ^{129}Xe signal by up to 2.4 times[72]. Utilization of an initial depolarization pulse, therefore, is highly beneficial for all further HP ^{129}Xe brain imaging studies. Despite achieving a significant reduction, however, the presence of an initial depolarization pulse did not completely eliminate the interbreath-hold signal variability issue. A contributing factor which cannot be eliminated originates from variations in blood flow in the cerebral arteries feeding the tissues, which directly affects the HP ^{129}Xe brain signal. The highest level of signal variability was observed to correspond to the brain region supplied by the posterior cerebral artery, whereas the lowest variability corresponded to the region supplied by the anterior cerebral artery[72].

In order to maximize the image SNR, data acquisition should be performed once the brain tissues are saturated with HP ^{129}Xe[72]. Based on the various HP ^{129}Xe brain uptake models previously developed[50,54], the concentration of HP ^{129}Xe in the brain reaches a maximum at approximately 15 s into the breath-hold for typical values of cerebral perfusion, arterial transit times, and T_1 relaxation times in the blood and brain tissues. In order to maximize the HP ^{129}Xe SNR, therefore, the image should be acquired at this moment in time. If a subject cannot hold their breath for this amount of time (e.g. subjects with pulmonary disorders or children), however, or if the imaging purpose is to acquire dynamic images over a breath-hold (e.g. to quantify HP ^{129}Xe uptake), the resulting image SNR can potentially be lower.

It is worth considering other breathing protocols. One that might be of interest for future studies, and which might overcome some of the issues mentioned above, is continuous breathing using HP ^{129}Xe premixed with oxygen. Continuous breathing protocols have been utilized for animal lung studies[85,86], and human lung studies with ^{3}He[87–89] and ^{129}Xe[90]. They might be beneficial for HP ^{129}Xe brain imaging since they can prolong the plateau of the maximum brain ^{129}Xe concentration period. This could allow the conductance of longer scans, signal averaging, and acquisition of HP ^{129}Xe brain images in subjects that are not capable of performing a long breath-hold.

Currently, the main advantages of ASL over HP ^{129}Xe cerebral perfusion imaging is the higher in-plane spatial resolution (typically 64 x 64), thinner slices, and commercially available software for image analysis. As shown in Table 2, the SNR values of HP ^{129}Xe perfusion images are comparable with clinically available pseudo-continuous ASL (pCASL) perfusion images. The recent implementation of a 3D GRE readout has further increased the SNR of HP ^{129}Xe brain images up to the level that is comparable with velocity-selective ASL (VSASL). The spatial

resolution of HP ^{129}Xe images, however, remains at least four times lower compared to ASL techniques. To bridge this gap, further improvements to the HP ^{129}Xe SNR, as discussed above, can be converted into increasing the acquisition matrix and reducing the slice thickness.

In addition, the further development of mathematical models for HP ^{129}Xe signal dynamics and its conversion into computer algorithms for HP ^{129}Xe cerebral perfusion image calculation can improve the accuracy of HP ^{129}Xe perfusion imaging. Additional experimental characterization of HP ^{129}Xe in the brain should accompany the optimization of mathematical models, as there still remain multiple fundamental physical properties of HP ^{129}Xe dissolved in cerebral blood and brain tissues that remain unknown. For example, accurate measurements of the T_1 relaxation times of each of the HP ^{129}Xe spectral components, as well as HP ^{129}Xe diffusion coefficients, are required. Without these experimental data, it will not be possible to quantify cerebral perfusion accurately.

In spite of these shortcomings, it is inspiring that HP ^{129}Xe brain imaging has already demonstrated its potential to image subjects with Alzheimer's Disease[56] and stroke[70]. Moreover, because the HP ^{129}Xe brain signal depends upon the cerebral perfusion, as well as the permeability of the blood-brain barrier (BBB), it might also be useful for the detection of other diseases associated with cerebral blood flow changes (e.g. Parkinson's disease[91], atherosclerosis[92], etc.) or those with associated BBB impairment (e.g. cerebral small vessel disease[93], multiple sclerosis[94], etc.). Additionally, due to the high lipophilicity of xenon, HP ^{129}Xe imaging may also be useful for brain cancer detection. Although there were two preliminary studies on this application[95,96], the validation of HP ^{129}Xe brain imaging for use in cancer detection will require further proof-of-concept studies.

In summary, HP ^{129}Xe brain imaging is a promising imaging modality that has been rapidly developing over the past several years. With further development, it has the potential to provide

rapid and direct imaging of perfusion with an SNR comparable to that of ASL perfusion imaging, even at low field. HP ^{129}Xe perfusion imaging has an extremely fast acquisition time (less than 20 s), has no endogenous background signal, and is much simpler in practice than other MRI techniques from the MR pulse sequence design point of view. The rapid acquisition times possible for HP ^{129}Xe perfusion images ensure its insensitivity to motion artifacts. In addition, due to xenon's ability to cross the BBB, assessment of BBB permeability can readily be performed using HP ^{129}Xe MRI[55,60]. HP ^{129}Xe perfusion imaging has the potential to become a valuable new perfusion imaging technique that eventually will take its place alongside of clinical ASL MRI and dynamic contrast-enhanced perfusion imaging.

Acknowledgements:

ǂYS and VG contributed equally to this work. This research was funded by the Ontario Research Fund (ORF RE 09 029), Northern Ontario Academic Medical Association (A-18-05), Mitacs Elevate (IT25574), and Natural Science and Engineering Research Council (NSERC) Discovery grant (RGPIN-2017-05359). JMW and MRR were funded by the Medical Research Council (MRC - MR/M008894/1). YS was supported by the Mitacs Elevate Postdoctoral Fellowship (IT25574). VG was supported by an Ontario Trillium Scholarship. MSA thanks Dilip Balamore for stimulating discussions on the topic of ^{129}Xe brain MR imaging. The authors are grateful to Vincent Knight for manuscript editing.

References:

1. Lauterbur PC. Image Formation by Induced Local Interactions: Examples Employing Nuclear Magnetic Resonance. *Nature*. 1973;242:190-191. doi:10.1038/242190a0

2. Couch MJ, Blasiak B, Tomanek B, Ouriadov A V., Fox MS, Dowhos KM, Albert MS. Hyperpolarized and Inert Gas MRI: The Future. *Molecular Imaging and Biology*. 2015;17(2):149-162. doi:10.1007/s11307-014-0788-2

3. Caravan P. Strategies for increasing the sensitivity of gadolinium based MRI contrast agents. *Chemical Society Reviews*. 2006;35(6):512-523. doi:10.1039/b510982p

4. Wahsner J, Gale EM, Rodríguez-Rodríguez A, Caravan P. Chemistry of MRI contrast agents: Current challenges and new frontiers. *Chemical Reviews*. 2019;119(2):957-1057. doi:10.1021/acs.chemrev.8b00363

5. Xiao YD, Paudel R, Liu J, Ma C, Zhang ZS, Zhou SK. MRI contrast agents: Classification and application (Review). *International Journal of Molecular Medicine*. 2016;38(5):1319-1326. doi:10.3892/ijmm.2016.2744

6. Caravan P. Strategies for increasing the sensitivity of gadolinium based MRI contrast agents. *Chemical Society Reviews*. 2006;35(6):512-523. doi:10.1039/b510982p

7. Buyuksarac B, Ozkan M. Utilization of MR angiography in perfusion imaging for identifying arterial input function. *Magnetic Resonance Materials in Physics, Biology and Medicine*. 2017;30(6):609-620. doi:10.1007/s10334-017-0643-y

8. Kim SH, Lee HHS, Kang BJ, Song BJ, Kim H Bin, Lee HHS, Jin MS, Lee A. Dynamic contrast-enhanced MRI perfusion parameters as imaging biomarkers of angiogenesis. *PLoS ONE*. 2016;11(12):e0168632. doi:10.1371/journal.pone.0168632

9. Albert MS, Cates GD, Driehuys B, Happer W, Saam B, Springer CS, Wishnia A. Biological Magnetic Resonance Imaging Using Laser-Polarized 129Xe. *Nature*. 1994;370(6486):199-201. doi:10.1038/370199a0

10. Kurhanewicz J, Vigneron DB, Ardenkjaer-Larsen JH, Bankson JA, Brindle K, Cunningham CH, Gallagher FA, Keshari KR, Kjaer A, Laustsen C, Mankoff DA, Merritt ME, Nelson SJ, Pauly JM, Lee P, Ronen S, Tyler DJ, Rajan SS, Spielman DM, Wald L, Zhang X, Malloy CR, Rizi R. Hyperpolarized 13C MRI: Path to Clinical Translation in Oncology. *Neoplasia (United States)*. 2019;21(1):1-16. doi:10.1016/j.neo.2018.09.006

11. Leary D, Svenningsen S, Guo F, Bhatawadekar S, Parraga G, Maksym GN. Hyperpolarized ^{3} He magnetic resonance imaging ventilation defects in asthma: relationship to airway mechanics. *Physiological Reports*. 2016;4(7):e12761. doi:10.14814/phy2.12761

12. Svenningsen S, Kirby M, Starr D, Leary D, Wheatley A, Maksym GN, McCormack DG, Parraga G. Hyperpolarized 3He and 129Xe MRI: Differences in asthma before bronchodilation. *Journal of Magnetic Resonance Imaging*. 2013;38(6):1521-1530. doi:10.1002/jmri.24111

13. Kruger SJ, Nagle SK, Couch MJ, Ohno Y, Albert M, Fain SB. Functional imaging of the lungs with gas agents. *Journal of Magnetic Resonance Imaging*. 2016;43(2):295-315. doi:10.1002/jmri.25002

14. Chang Y V. MOXE: A model of gas exchange for hyperpolarized 129Xe magnetic resonance of the lung. *Magnetic Resonance in Medicine*. 2013;69(3):884-890. doi:10.1002/mrm.24304

15. Chang Y V., Quirk JD, Ruset IC, Atkinson JJ, Hersman FW, Woods JC. Quantification of human lung structure and physiology using hyperpolarized 129Xe. *Magnetic Resonance in Medicine*. 2014;71(1):339-344. doi:10.1002/mrm.24992

16. Driehuys B, Cofer GP, Pollaro J, Mackel JB, Hedlund LW, Johnson GA. Imaging alveolar-capillary gas transfer using hyperpolarized 129Xe MRI. *Proceedings of the National Academy of Sciences*. 2006;103(48):18278-18283.

17. Stewart NJ, Horn FC, Norquay G, Collier GJ, Yates DP, Lawson R, Marshall H, Wild JM. Reproducibility of quantitative indices of lung function and microstructure from 129Xe chemical shift saturation recovery (CSSR) MR spectroscopy. *Magnetic Resonance in Medicine*. 2017;77(6):2107-2113.

18. Albert MS, Balamore D, Kacher DF, Venkatesh AK, Jolesz FA. Hyperpolarized 129XE T1 in oxygenated and deoxygenated blood. *NMR in Biomedicine*. 2000;13(7):407-414. doi:10.1002/1099-1492(200011)13:7<407::AID-NBM661>3.0.CO;2-1

19. Albert MS, Kacher DF, Balamore D, Venkatesh AK, Jolesz FA. T1 of 129 Xe in Blood and the Role of Oxygenation. *Journal of Magnetic Resonance*. 1999;140(1):264-273. doi:10.1006/jmre.1999.1836

20. Wolber J, Cherubini A, Dzik-Jurasz ASKK, Leach MO, Bifone A. Spin-lattice relaxation of laser-polarized xenon in human blood. *Proceedings of the National Academy of Sciences of the United States of America*. 1999;96(7):3664-3669. doi:10.1073/pnas.96.7.3664

21. Norquay G, Leung G, Stewart NJ, Wolber J, Wild JM. 129Xe Chemical Shift in Human Blood and Pulmonary Blood Oxygenation Measurement in Humans Using Hyperpolarized 129Xe NMR. *Magn Reson Med*. 2017;77:1399-1408. doi:10.1002/mrm.26225

22. Chacon-Caldera J, Maunder A, Rao M, Norquay G, Rodgers OI, Clemence M, Puddu C, Schad LR, Wild JM. Dissolved hyperpolarized xenon-129 MRI in human kidneys. *Magnetic Resonance in Medicine*. 2020;83:262-270. doi:https://doi.org/10.1002/mrm.27923

23. Albert MS, Balamore D. Development of hyperpolarized noble gas MRI. *Nuclear Instruments and Methods in Physics Research, Section A: Accelerators, Spectrometers, Detectors and Associated Equipment*. 1998;402(2-3):441-453. doi:10.1016/S0168-9002(97)00888-7

24. Ruppert K. Biomedical imaging with hyperpolarized noble gases. *Reports on Progress in Physics*. 2014;77(11):116701. doi:10.1088/0034-4885/77/11/116701

25. Cullen SC, Gross EG. The anesthetic properties of xenon in animals and human beings, with additional observations on krypton. *Science*. 1951;113(2942):580-582. doi:10.1126/science.113.2942.580

26. Bein B, Hanne P, Hanss R, Renner J, Weber B, Steinfath M, Scholz J, Tonner PH. Effect of xenon anaesthesia on accuracy of cardiac output measurement using partial CO2 rebreathing. *Anaesthesia*. 2004;59(11):1104-1110. doi:10.1111/j.1365-2044.2004.03897.x

27. Sanders RD, Franks NP, Maze M. Xenon: No stranger to anaesthesia. *British Journal of Anaesthesia*. 2003;91(5):709-717. doi:10.1093/bja/aeg232

28. Roehl AB, Goetzenich A, Rossaint R, Zoremba N, Hein M. A practical rule for optimal flows for xenon anaesthesia in a semi-closed anaesthesia circuit. *European Journal of Anaesthesiology*. 2010;27(7):660-665. doi:10.1097/EJA.0b013e328336ec3b

29. Martins CF, Neves LA, Chagas R, Ferreira LM, Coelhoso IM, Crespo JG. Removing CO2 from Xenon anaesthesia circuits using an amino-acid ionic liquid solution in a membrane contactor. *Separation and Purification Technology*. 2021;275:119190. doi:10.1016/j.seppur.2021.119190

30. Yonas H, Darby JM, Marks EC, Durham SR, Maxwell C. CBF Measured by Xe-CT: Approach to Analysis and Normal Values. *Journal of Cerebral Blood Flow & Metabolism*. 1991;11(5):716-725. doi:10.1038/jcbfm.1991.128

31. Van Roost D, Hartmann A, Quade G. Changes of cerebral blood flow following dexamethasone treatment in brain tumour patients. A Xe/CT study. *Acta neurochirurgica*. 2001;143:37-44. doi:10.1007/s007010170136

32. Sturnegk P, Mellergård P, Yonas H, Theodorsson A, Hillman J. Potential use of quantitative bedside CBF monitoring (Xe-CT) for decision making in neurosurgical intensive care. *British Journal of Neurosurgery*. 2007;21(4):332-339. doi:10.1080/02688690701411574

33. Swanson SD, Rosen MS, Agranoff BW, Coulter KP, Welsh RC, Chupp TE. Brain MRI with Laser-Polarized 129Xe. *MAGNETIC RESONANCE IN MEDICINE*. 1997;38(5):695-698. doi:10.1002/mrm.1910380503

34. Mugler JP, Driehuys B, Brookeman JR, Cates GD, Berr SS, Bryant RG, Daniel TM, De Lange EE, Downs JH, Erickson CJ, Happer W, Hinton DP, Kassel NF, Maier T, Phillips CD, Saam BT, Sauer KL, Wagshul ME. MR imaging and spectroscopy using hyperpolarized 129Xe gas: Preliminary human results. *Magnetic Resonance in Medicine*. 1997;37(6):809-815. doi:10.1002/mrm.1910370602

35. Swanson SD, Rosen MS, Coulter KP, Welsh RC, Chupp TE. Distribution and dynamics of laser-polarized129Xe magnetization in vivo. *Magnetic Resonance in Medicine*. 1999;42(6):1137-1145. doi:10.1002/(SICI)1522-2594(199912)42:6<1137::AID-MRM19>3.0.CO;2-4

36. Duhamel G, Choquet P, Leviel JL, Steibel J, Lamalle L, Julien C, Kober F, Grillon E, Derouard J, Décorps M, Ziegler A, Constantinesco A. In vivo 129 Xe NMR in rat brain

during intra-arterial injection of hyperpolarized 129 Xe dissolved in a lipid emulsion. *Comptes Rendus de l'Académie des Sciences - Series III - Sciences de la Vie*. 2000;323(6):529-536.

37. Wakai A, Nakamura K, Kershaw J, Kanno I. In vivo MR spectroscopy of hyperpolarized Xe-129 in rat brain. *International Congress Series*. 2004;1265(C):139-143. doi:10.1016/j.ics.2004.04.063

38. Nakamura K, Kondoh Y, Wakai A, Kershaw J, Wright D, Kanno I. 129Xe spectra from the heads of rats with and without ligation of the external carotid and pterygopalatine arteries. *Magnetic Resonance in Medicine*. 2005;53(3):528-534. doi:10.1002/mrm.20399

39. Kershaw J, Nakamura K, Kondoh Y, Wakai A, Suzuki N, Kanno I. Confirming the existence of five peaks in129Xe rat head spectra. *Magnetic Resonance in Medicine*. 2007;57(4):791-797. doi:10.1002/mrm.21186

40. Kilian W, Seifert F, Rinneberg H. Chemical Shift Imaging of Human Brain after Inhaling Hyperpolarized 129Xe-Gas. In: *Proc. Intl. Soc. Mag. Reson. Med 10*. ; 2002:758.

41. Kilian W, Seifert F. 2D Chemical Shift Imaging of hyperpolarized isotopically enriched 129 Xe within human brain. In: *Proc. Intl. Soc. Mag. Reson. Med 13*. ; 2005:1163.

42. Rao M, Stewart N, Norquay G, Griffiths P, Wild J. Imaging the human brain with dissolved xenon MRI at 1 . 5T. In: *Proc. Intl. Soc. Mag. Reson. Med 23*. ; 2015:1254.

43. Rao M, Stewart NJ, Norquay G, Griffiths PD, Wild JM. High resolution spectroscopy and chemical shift imaging of hyperpolarized 129Xe dissolved in the human brain in vivo at 1.5 tesla. *Magnetic Resonance in Medicine*. 2016;75(6):2227-2234. doi:10.1002/mrm.26241

44. Li H, Zhang Z, Zhong J, Ruan W, Han Y, Sun X, Ye C, Zhou X. Oxygen-dependent hyperpolarized 129Xe brain MR. *NMR in Biomedicine*. 2016;29(3):220-225. doi:10.1002/nbm.3465

45. Zhou X, Tzeng YS, Mansour JK, Mazzanti ML, Sun Y, Albert MS. Optimum Ventilation Mixture Ratio for Maximizing Hyperpolarized 129Xe MR Brain Signal. In: *Proc. Intl. Soc. Mag. Reson. Med 15*. ; 2007:1270.

46. Antonacci MA, Zhang L, Burant A, McCallister D, Branca RT. Simple and robust referencing system enables identification of dissolved-phase xenon spectral frequencies. *Magnetic Resonance in Medicine*. 2018;80(2):431-441. doi:10.1002/mrm.27042

47. Wilson GJ, Santyr GE, Anderson ME, Deluca PM. Longitudinal Relaxation Times of 129 Xe in Rat Tissue Homogenates at 9.4 T. *Magnetic Resonance in Medicine*. 1999;41(5):933-938. doi:10.1002/(sici)1522-2594(199905)41:5<933::aid-mrm12>3.0.co;2-z

48. Duhamel G, Choquet P, Grillon E, Leviel JL, Décorps M, Ziegler A, Constantinesco A. Global and regional cerebral blood flow measurements using NMR of injected hyperpolarized xenon-129. *Academic Radiology*. 2002;9(SUPPL. 2):S498-500. doi:10.1016/S1076-6332(03)80275-1

49. Duhamel G, Choquet P, Grillon E, Leviel JL, Décorps M, Ziegler A, Constantinesco A. Global and regional cerebral blood flow measurements using NMR of injected hyperpolarized xenon-129. *Academic Radiology*. 2002;9(SUPPL. 2):S498-500. doi:10.1016/S1076-6332(03)80275-1

50. Kilian W, Seifert F, Rinneberg H. Dynamic NMR Spectroscopy of Hyperpolarized 129Xe in Human Brain Analyzed by an Uptake Model. *Magnetic Resonance in Medicine*. 2004;51(4):843-847. doi:10.1002/mrm.10726

51. Wakai A, Nakamura K, Kershaw J, Kondoh Y, Wright D, Kanno I. A Method for Measuring the Decay Time of Hyperpolarized 129 Xe Magnetization in Rat Brain without Estimation of RF Flip Angles. *Magnetic Resonance in Medical Sciences*. 2005;4(1):19-25. doi:10.2463/mrms.4.19

52. Zhou X, Mazzanti ML, Chen JJ, Tzeng YS, Mansour JK, Gereige JD, Venkatesh AK, Sun Y, Mulkern R V., Albert MS. Reinvestigating hyperpolarized 129Xe longitudinal relaxation time in the rat brain with noise considerations. *NMR in Biomedicine*. 2008;21(3):217-225. doi:10.1002/nbm.1184

53. Mazzanti ML, Walvick RP, Zhou X, Sun Y, Shah N, Mansour J, Gereige J, Albert MS. Distribution of hyperpolarized xenon in the brain following sensory stimulation: Preliminary MRI findings. *PLoS ONE*. 2011;6(7):e21607. doi:10.1371/journal.pone.0021607

54. Shepelytskyi Y, Hane FT, Grynko V, Li T, Hassan A, Albert MS. Hyperpolarized 129Xe Time-of-Flight MR Imaging of Perfusion and Brain Function. *Diagnostics*. 2020;10:630. doi:10.3390/diagnostics10090630

55. Rao MR, Norquay G, Stewart NJ, Wild JM. Measuring 129Xe transfer across the blood-brain barrier using MR spectroscopy. *Magnetic Resonance in Medicine*. 2021;85(6):2939-2949. doi:10.1002/mrm.28646

56. Hane FT, Li T, Plata JA, Hassan A, Granberg K, Albert MS. Inhaled Xenon Washout as a Biomarker of Alzheimer's Disease. *Diagnostics*. 2018;8:41. doi:10.3390/diagnostics8020041

57. Choquet P, Hyacinthe JN, Duhamel G, Grillon E, Leviel JL, Constantinesco A, Ziegler A. Method to determine in vivo the relaxation time T1 of hyperpolarized xenon in rat brain. *Magnetic Resonance in Medicine*. 2003;49(6):1014-1018. doi:10.1002/mrm.10471

58. Nouls J, Cleveland Z, Freeman M, Moeller H, Hedlund L, Driehuys B. 3D MRI of the Hyperpolarized 129 Xe Distribution in the Rat Brain. In: *Proc. Intl. Soc. Mag. Reson. Med. 19*. ; 2011:879.

59. Friedlander Y, Zanette B, Couch M, Kassner A, Santyr G. Spiral-IDEAL for Time-Resolved Imaging of Hyperpolarized 129Xe Kinetics in the Rat Brain. In: *Proc. Intl. Soc. Mag. Reson. Med. 27*. ; 2019:4300.

60. Friedlander Y, Zanette B, Lindenmaier A, Li D, Kadlecek S, Santyr G, Kassner A. Hyperpolarized 129Xe MRI of the rat brain with chemical shift saturation recovery and spiral-IDEAL readout. *Magnetic Resonance in Medicine*. 2021;00:1-9. doi:10.1002/mrm.29105

61. Rao MR, Collier GJ, Norquay G, Schulte RF, Wild JM. 3D isotropic spectroscopic imaging of hyperpolarized 129Xe in the human brain. In: *Proc. Intl. Soc. Mag. Reson. Med. 29*. ; 2021:3567.

62. Grynko V, Shepelytskyi Y, Li T, Hassan A, Granberg K, Albert MS. Hyperpolarized 129Xe multi-slice imaging of the human brain using a 3D gradient echo pulse sequence. *Magnetic Resonance in Medicine*. 2021;86(6):3175-3181. doi:10.1002/mrm.28932 *(Included as Chapter 4 in the thesis.)*

63. Peled S, Jolesz FA, Tseng CH, Nascimben L, Albert MS, Walsworth RL. Determinants of Tissue Delivery for lZ9Xe Magnetic Resonance in Humans. *Magnetic Resonance in Medicine*. 1996;36(3):340-344.

64. Weathersby PK, Homer LD. Solubility of inert gases in biological fluids and tissues: a review. *Undersea Biomedical Research*. 1980;7(4):277-296.

65. Martin CC, Williams RF, Gao JH, Nickerson LDH, Xiong J, Fox PT. The Pharmacokinetics of Hyperpolarized Xenon: Implications for Cerebral MRI. *Journal of Magnetic Resonance Imaging*. 1997;7:848-854. doi:10.1002/jmri.1880070512

66. Kimura A, Imai H, Wakayama T, Fujiwara H. A simple method for quantitative measurement and analysis of hyperpolarized 129Xe uptake dynamics in mouse brain under controlled flow. *Magnetic Resonance in Medical Sciences*. 2008;7(4):179-185. doi:10.2463/mrms.7.179

67. Imai H, Kimura A, Akiyama K, Ota C, Okimoto K, Fujiwara H. Development of a fast method for quantitative measurement of hyperpolarized 129Xe dynamics in mouse brain. *NMR in Biomedicine*. 2012;25(2):210-217. doi:10.1002/nbm.1733

68. Rao M, Stewart N, Norquay G, Wild J. Quantification of perfusion and xenon-transport across the blood-brain barrier in humans with hyperpolarized 129Xe brain MR at 1.5T. In: *Proc. Intl. Soc. Mag. Reson. Med 23*. ; 2015:1445.

69. Rao M, Stewart N, Gri P, Norquay G, Wild J. Advances in imaging the human brain with inhaled hyperpolarized xenon-129 MRI at 1.5 T. In: *Proc. Intl. Soc. Mag. Reson. Med. 25*. ; 2017:4543.

70. Rao MR, Stewart NJ, Griffiths PD, Norquay G, Wild JM. Imaging human brain perfusion with inhaled hyperpolarized 129Xe MR imaging. *Radiology*. 2018;286(2):659-665. doi:10.1148/radiol.2017162881

71. Rao M, Norquay G, Wild J. Investigating gas-exchange and tissue perfusion in the human brain using a combination of proton and hyperpolarized xenon-129 MRI. In: *Proc. Intl. Soc. Mag. Reson. Med 27*. ; 2019:3095.

72. Shepelytskyi Y, Grynko V, Li T, Hassan A, Granberg K, Albert MS. The effects of an initial depolarization pulse on dissolved phase hyperpolarized 129Xe brain MRI. *Magnetic Resonance in Medicine*. 2021;86(6):3147-3155. doi:10.1002/mrm.28918

73. Zhou X, Sun Y, Mazzanti M, Henninger N, Mansour J, Fisher M, Albert M. MRI of stroke using hyperpolarized 129Xe. *NMR in Biomedicine*. 2011;24(2):170-175. doi:10.1002/nbm.1568

74. Rao MR, Norquay G, Stewart NJ, Hoggard N, Griffiths PD, Wild JM. Assessment of brain perfusion using hyperpolarized 129Xe MRI in a subject with established stroke. *Journal of Magnetic Resonance Imaging*. 2019;50(3):1002-1004. doi:10.1002/jmri.26686

75. Parra-Robles J, Cross AR, Santyr GE. Theoretical signal-to-noise ratio and spatial resolution dependence on the magnetic field strength for hyperpolarized noble gas magnetic resonance imaging of human lungs. *Medical Physics*. 2005;32(1):221-229. doi:10.1118/1.1833593

76. Middleton H, Black RD, Saam B, Cates GD, Cofer GP, Guenther R, Happer W, Hedlund LW, Alan Johnson G, Juvan K, Swartz J. MR Imaging with Hyperpolarized 3He Gas. *Magnetic Resonance in Medicine*. 1995;33(2):271-275. doi:10.1002/mrm.1910330219

77. Venkatesha AK, Zhang AX, Mansour J, Kubatina L, Oh CH, Blasche G, Selim Ünlü M, Balamore D, Jolesz FA, Goldberg BB, Albert MS. MRI of the lung gas-space at very low-field using hyperpolarized noble gases. *Magnetic Resonance Imaging*. 2003;21(7):773-776. doi:10.1016/S0730-725X(03)00178-4

78. Petersen ET, Zimine I, Ho YCL, Golay X. Non-invasive measurement of perfusion: A critical review of arterial spin labelling techniques. *British Journal of Radiology*. 2006;79(944):688-701. doi:10.1259/bjr/67705974

79. Amukotuwa SA, Yu C, Zaharchuk G. 3D Pseudocontinuous arterial spin labeling in routine clinical practice: A review of clinically significant artifacts. *Journal of Magnetic Resonance Imaging*. 2016;43(1):11-27. doi:10.1002/jmri.24873

80. Alsop DC, Detre JA, Golay X, G€ M, Hendrikse J, Hernandez-Garcia L, Lu H, Macintosh BJ, Parkes LM, Smits M, Van Osch MJP, Wang DJJ, Wong EC, Zaharchuk G. Recommended Implementation of Arterial Spin-Labeled Perfusion MRI for Clinical Applications: A Consensus of the ISMRM Perfusion Study Group and the European Consortium for ASL in Dementia. *Magn Reson Med*. 2015;73(1):102-116. doi:10.1002/mrm.25197

81. Norquay G, Parnell SR, Xu X, Parra-Robles J, Wild JM. Optimized production of hyperpolarized 129Xe at 2 bars for in vivo lung magnetic resonance imaging. *Journal of Applied Physics*. 2013;113(4):044908. doi:10.1063/1.4776763

82. Puddu C, Rao M, Rodgers O, Maunder A, Wild J. 6-channel RF array for hyperpolarized 129 Xe brain MRI at 3T. In: *Proc. Intl. Soc. Mag. Reson. Med. 28*. ; 2020:4099.

83. Shepelytskyi Y, Hane FT, Grynko V, Li T, Hassan A, Albert MS. Hyperpolarized 129 Xe functional brain mapping. In: *Proc. Intl. Soc. Mag. Reson. Med. 28*. ; 2020:0556.

84. Rao M, Norquay G, Wild J. Assessment of repeatability of imaging inhaled hyperpolarized xenon-129 in the human brain. In: *Proc. Intl. Soc. Mag. Reson. Med. 29*. ; 2019:3319.

85. Loza LA, Kadlecek SJ, Pourfathi M, Hamedani H, Duncan IF, Ruppert K, Rizi RR. Quantification of Ventilation and Gas Uptake in Free-Breathing Mice With Hyperpolarized

129Xe MRI. *IEEE transactions on medical imaging*. 2019;38(9):2081-2091. doi:10.1109/TMI.2019.2911293

86. Imai H, Matsumoto H, Miyakoshi E, Okumura S, Fujiwara H, Kimura A. Regional fractional ventilation mapping in spontaneously breathing mice using hyperpolarized 129Xe MRI. *NMR in Biomedicine*. 2015;28(1):24-29. doi:10.1002/nbm.3222

87. Hamedani H, Emami K, Kadlecek S, McAdams H, Xin Y, Mongkolwisetwara P, Miller GW, Rossman M, Ishii M, Rizi RR. Differences In Pulmonary Function Testing And Distribution Of Alveolar Oxygen Tension In Asymptomatic Smokers. In: *Am J Respir Crit Care Med 185*. ; 2012:A6046.

88. Hamedani H, Clapp JT, Kadlecek SJ, Emami K, Ishii M, Gefter WB, Xin Y, Cereda M, Shaghaghi H, Siddiqui S, Rossman MD, Rizi RR. Regional fractional ventilation by using multibreath wash-in 3He MR imaging. *Radiology*. 2016;279(3):917-924. doi:10.1148/radiol.2015150495

89. Hamedani H, Kadlecek S, Xin Y, Siddiqui S, Gatens H, Naji J, Ishii M, Cereda M, Rossman M, Rizi R. A hybrid multibreath wash-in wash-out lung function quantification scheme in human subjects using hyperpolarized 3He MRI for simultaneous assessment of specific ventilation, alveolar oxygen tension, oxygen uptake, and air trapping. *Magnetic Resonance in Medicine*. 2017;78(2):611-624. doi:10.1002/mrm.26401

90. Hamedani H, Bermudez F, Baron R, Kadlecek S, Ruppert K, Xin Y, Siddiqui S, Pourfathi M, Amzajerdian F, Loza L, Achekzai T, Duncan I, Cereda M, Sertic F, Rizi RR. A Comparison of Hyperpolarized Gas Imaging of Aeration and Fractional Ventilation. In: *Am J Respir Crit Care Med*. ; 2019:A5772. doi:10.1164/ajrccm-conference.2019.199.1_meetingabstracts.a5772

91. Melzer TR, Watts R, MacAskill MR, Pearson JF, Rueger S, Pitcher TL, Livingston L, Graham C, Keenan R, Shankaranarayanan A, Alsop DC, Dalrymple-Alford JC, Anderson TJ. Arterial spin labelling reveals an abnormal cerebral perfusion pattern in Parkinson's disease. *Brain*. 2011;134(3):845-855. doi:10.1093/brain/awq377

92. Sfyroeras GS, Karkos CD, Gerassimidis TS. Cerebral perfusion patterns in patients with extracranial carotid atherosclerosis and the impact of carotid stenting: A review. *Journal of Cardiovascular Surgery*. 2008;49(4):497-502.

93. Wong SM, Jansen JFA, Zhang CE, Hoff EI, Staals J, van Oostenbrugge RJ, Backes WH. Blood-brain barrier impairment and hypoperfusion are linked in cerebral small vessel disease. *Neurology*. 2019;92(15):e1669-e1677. doi:10.1212/WNL.0000000000007263

94. Leech S, Kirk J, Plumb J, McQuaid S. Persistent endothelial abnormalities and blood?brain barrier leak in primary and secondary progressive multiple sclerosis. *Neuropathology and Applied Neurobiology*. 2007;33(1):86-98. doi:10.1111/j.1365-2990.2006.00781.x

95. Wolber J, McIntyre DJO, Rodrigues LM, Carnochan P, Griffiths JR, Leach MO, Bifone A. In vivo hyperpolarized 129Xe NMR spectroscopy in tumors. *Magnetic Resonance in Medicine*. 2001;46(3):586-591. doi:10.1002/mrm.1231

96. Il'yasov A V., Mazitov RK, Enikeev KM, Panov AN, Il'yasov NA, Khasanov RZ. 129Xe NMR in study of tissues and plants. *Applied Magnetic Resonance*. 1999;17(1):77-84. doi:10.1007/BF03162070

Chapter 3: Effect of blood glycation on ^{129}Xe spectroscopic parameters

This topic has been elaborated in the following publication: Mikowska, L.; **Grynko, V**.; Shepelytskyi, Y.; Ruset, I.C.; Deschamps, J.; Aalto, H.; Targosz-Korecka, M.; Balamore, D.; Harańczyk, H.; Albert, M.S. "**Revealing a Third Dissolved-Phase Xenon-129 Resonance in Blood Caused by Hemoglobin Glycation**" published in *International Journal of Molecular Sciences,* volume 24. Issue 14, article number 11311 (2023). The publication text is listed below.

Revealing a Third Dissolved-Phase Xenon-129 Resonance in Blood Caused by Hemoglobin Glycation

Lutosława Mikowska [1,†], Vira Grynko [2,3,†], Yurii Shepelytskyi [3,4], Iullian C. Ruset [5], Joseph Deschamps [6], Hannah Aalto [6], Marta Targosz-Korecka [1], Dilip Balamore [7], Hubert Harańczyk [1] and Mitchell S. Albert [3,4,8,*]

1. Faculty of Physics, Astronomy, and Applied Computer Science, Jagiellonian University, 30-348 Krakow, Poland; lutoslawa.mikowska@doctoral.uj.edu.pl (L.M.); marta.targosz-korecka@uj.edu.pl (M.T.-K.); hubert.haranczyk@uj.edu.pl (H.H.)
2. Chemistry and Material Science Program, Lakehead University, Thunder Bay, ON P7B 5E1, Canada; vgrynko@lakeheadu.ca
3. Thunder Bay Regional Health Research Institute, Thunder Bay, ON P7B 7A5, Canada; yshepely@lakeheadu.ca
4. Chemistry Department, Lakehead University, Thunder Bay, ON P7B 5E1, Canada
5. Xemed LLC, Durham, NH 03824, USA; iulian@xemed.com
6. Applied Life Sciences Program, Lakehead University, Thunder Bay, ON P7B 5E1, Canada; jddescha@lakeheadu.ca (J.D.); haaalto@lakeheadu.ca (H.A.)
7. Department of Engineering/Physics/Technology, Nassau Community College, New York, NY 11530, USA
8. Northern Ontario School of Medicine University – West Campus, Thunder Bay, ON P3E 2C6, Canada; balamore@gmail.com

*Correspondence: malbert1@lakeheadu.ca; Tel.: +1-807-355-9191

†These authors contributed equally to this work.

Abstract:

Hyperpolarized (HP) xenon-129 (^{129}Xe), when dissolved in blood, has two NMR resonances: one in red blood cells (RBC) and one in plasma. The impact of numerous blood components on these resonances, however, has not yet been investigated. This study evaluates the effects of elevated glucose levels on the chemical shift (CS) and T_2^* relaxation times of HP ^{129}Xe dissolved in sterile citrated sheep blood for the first time. HP ^{129}Xe was mixed with sheep blood samples premixed with a stock glucose solution using a liquid–gas exchange module. Magnetic resonance spectroscopy was performed on a 3T clinical MRI scanner using a custom-built quadrature dual-tuned ^{129}Xe/^{1}H coil. We observed an additional resonance for the RBCs (^{129}Xe-RBC1) for the increased glucose levels. The CS of ^{129}Xe-RBC1 and ^{129}Xe-plasma peaks did not change with glucose levels, while the CS of ^{129}Xe-RBC2 (original RBC resonance) increased linearly at a rate of 0.015 ± 0.002 ppm/mM with glucose level. ^{129}Xe-RBC1 T_2^* values increased nonlinearly from 1.58 ± 0.24 ms to 2.67 ± 0.40 ms. As a result of the increased glucose levels in blood samples, the novel additional HP ^{129}Xe dissolved phase resonance was observed in blood and attributed to the ^{129}Xe bound to glycated hemoglobin (HbA_{1c}).

Keywords: hyperpolarized ^{129}Xe; magnetic resonance spectroscopy; glycation; glucose; hemoglobin

3-1. Introduction

Since its invention [1], hyperpolarized (HP) xenon-129 (^{129}Xe) MRI has been primarily used for the functional imaging of the human lungs and for studying pulmonary disorders [2–7]. Over the past decade, the feasibility of HP ^{129}Xe dissolved-phase imaging has been demonstrated for imaging pulmonary gas transfer [8–12], brain imaging [13–18], and kidney imaging [19,20].

HP ^{129}Xe dissolved-phase imaging relies on the sufficiently long T_1 relaxation time in blood (~3.4–7.8 s) [21–25] and the well-distinguished resonances of HP ^{129}Xe nuclei dissolved in blood and various tissue compartments. Therefore, the chemical composition of blood should have a critical effect on HP ^{129}Xe dissolved-phase imaging since it affects the T_1 and chemical shift (CS) of the dissolved ^{129}Xe resonances. A number of studies have previously evaluated the role of blood oxygenation and its effects on HP ^{129}Xe MR spectra [21,22,24,26]. However, there is another vital component of blood chemical composition that has yet to be explored—the glucose level.

A high glucose concentration in blood leads to excessive non-enzymatic chemical interactions between glucose and proteins in the blood [27]. Hemoglobin is the protein most affected by glycation. Structurally, hemoglobin has four subunits, consisting of two α and two β chains, each of which carry an iron-containing heme group responsible for oxygen binding [28]. During the glycation process, a non-enzymatic reaction occurs between glucose and the α-amino groups of valine residues at the N-terminus of the β-chains [29]. The most abundant form of glycated hemoglobin, which is widely used in clinical practice for the evaluation of glycemia in diabetes mellitus, is hemoglobin A1c (HbA1c) [30]. Glycated hemoglobin is naturally present in healthy individuals (~4%), whereas glycation levels up to 20% have been reported in patients diagnosed with diabetes [31]. Elevated HbA1c levels (>6.5%) are routinely used for the diagnosis of diabetes mellitus [32]. The standard HbA1c test is used for the diagnosis of type 2 diabetes and prediabetes. It shows the amount of glycated hemoglobin and reflects the average blood glucose level over the past three months [33].

Hemoglobin glycation induces the formation of oxygen-derived free radicals, which are responsible for causing oxidative stress in erythrocytes [34], leading to an increase in membrane lipid peroxidation [35] and membrane damage in diverse cell types. The glycation of iron-

containing heme proteins can cause the degradation of heme and further reactions with H_2O_2, leading to increased iron release, as well as ferryl myoglobin formation [27,36]. In addition, iron overload caused by high concentrations of glycated hemoglobin has been shown to be associated with changes in the structure of the red blood cells (RBCs) and increased thrombotic events [37]. Numerous studies have been conducted evaluating the effect of elevated levels of glycated hemoglobin on red blood cell distribution width (RDW); however, the data published has been inconclusive [38]. Some studies have also suggested that hyperglycemia may have some effect on erythropoiesis and RBC survival at concentrations of glucose higher than 40 mM [35,38].

It is known that the HP ^{129}Xe signal from blood originates from Xe in plasma and the RBCs [1]. ^{129}Xe binds to hemoglobin in hydrophobic cavities close to the external surface in both α and β chains [39]. Therefore, alternations in the structure of hemoglobin caused by glycation are expected to have a direct effect on the HP ^{129}Xe magnetic environment and its dipole–dipole interaction with hemoglobin, potentially resulting in CS changes. Furthermore, the overall increase in free radical levels can also be anticipated to cause an effect on HP ^{129}Xe CS. The destruction of heme groups accompanied by the release of iron would be expected to have potential effects on HP ^{129}Xe-RBC CS, as well as on the T_2^* relaxation process.

The present lung studies with HP ^{129}Xe exploit the measuring of the signal intensity of ^{129}Xe bound to tissue and RBC [2–4,7,8]. However, the elevated glucose level in blood may have a considerable impact on the ^{129}Xe spectroscopic properties and should be taken into account for patients with diabetes.

This work, for the first time, investigates the effect of glucose concentration in blood on the physical properties of dissolved HP ^{129}Xe, such as CS and on the effective spin–spin relaxation time T_2^*. Moreover, using non-linear curve fitting, we demonstrated that the spectrum of HP ^{129}Xe

in blood contains not two (as was conventionally thought) but three dissolved-phase resonances. We report the resonance frequencies, T_2^* relaxation times, and the CS dependance on glucose level of the three observed spectral components in sterile citrated sheep blood. In addition, we propose a potential mechanism for glycation-related changes in the physical parameters of the dissolved HP ^{129}Xe. This research suggests that for a comprehensive understanding of dissolved-phase imaging, glucose levels in the blood should also be taken into account along with blood oxygenation, since both play distinct roles.

3-2. Results

3-2.1. CS Analysis Using a Conventional Three-Peak Model (3PM)

The measurements of the CS of the ^{129}Xe dissolved in plasma (^{129}Xe-plasma) and ^{129}Xe dissolved in RBC (^{129}Xe-RBC) resonances were conducted for the glucose concentration range of 0–55 mM. The acquired MRS spectra were first fitted using the conventional three-peak model (3PM): gas peak, plasma peak, and RBC peak. Figure 3-1A,B show MRS acquired for 10 mM and 45 mM glucose concentrations in the blood, respectively. The increase in glucose concentration did not cause a significant change in the ^{129}Xe-plasma CS. Conversely, the ^{129}Xe-RBC resonance shifted from 217.86 ppm (10 mM of glucose) to 219.07 ppm (45 mM). Figure 3-1C shows three representative cumulative Lorentzian 3PM fits for 10 mM, 20 mM, and 45 mM glucose concentrations. The downfield shift of the HP ^{129}Xe-RBC resonance with respect to the gaseous ^{129}Xe resonance can be clearly observed with increasing glucose concentration. The observed CS increased linearly with the increased glucose concentration (Figure 3-1D). The fit of the CS dependence of the ^{129}Xe-RBC peak on glucose concentration revealed a (0.025 ± 0.004) ppm/mM ^{129}Xe-RBC change rate. A strong positive correlation (r = 0.91) was observed between the ^{129}Xe-RBC peak CS and the glucose concentration in the measured blood samples. It can be clearly seen

that the ^{129}Xe-plasma peak was completely unaffected by an increase in glucose concentration (r = 0.1 with a slope of the line equal to (0.001 ± 0.005) ppm/mM. The observed downfield shift of the HP ^{129}Xe-RBC resonance is similar to the HP ^{129}Xe-RBC resonance frequency change due to the increase in blood oxygenation, albeit with a total span of only ~1.25 ppm.

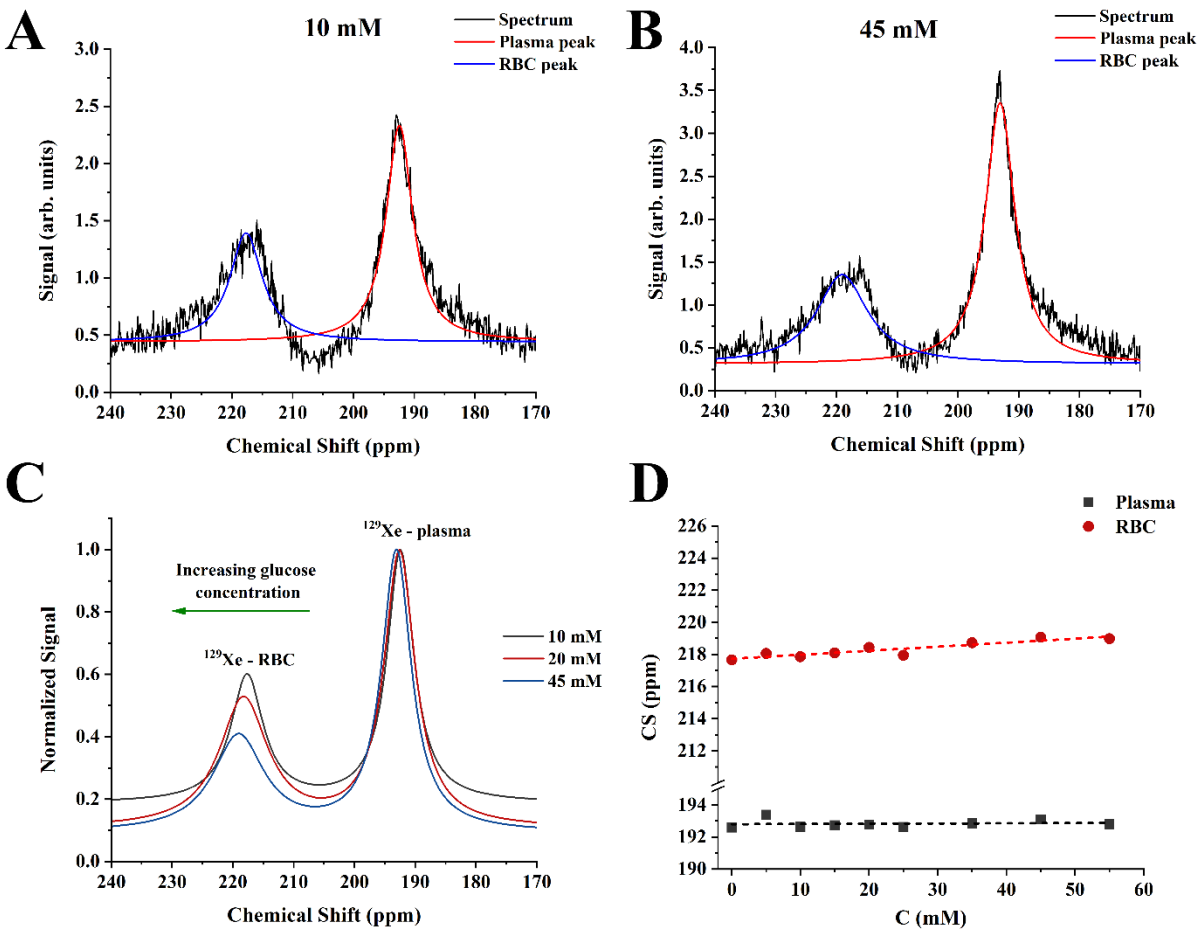

Figure 3-1 HP 129Xe MRS spectra of the 10 mM sample (A) and 45 mM sample (B) fitted to the conventional 3PM. The CS scale was selected to depict dissolved-phase resonances. The black line corresponds to the acquired HP 129Xe spectra. The red and blue lines are Lorentzian fits of the 129Xe-plasma and 129Xe-RBC peaks, respectively. (C) Three fitted HP 129Xe MRS spectra of 10 mM, 20 mM, and 45 mM samples demonstrate a noticeable downfield shift of the 129Xe-RBC resonance with a glucose concentration increase. The CS versus glucose concentration dependence of HP 129Xe-RBC peak appeared to be linear (D), whereas the CS of the HP 129Xe dissolved in plasma remained unaffected by blood glucose concentration.

3-2.2. T_2^* Relaxation Measurements

Following the measurements of CS, T_2^* relaxation was assessed based on Lorentzian fits of the measured spectra to 3PM. No significant change was observed in T_2^* values for HP ^{129}Xe dissolved in both RBC and plasma pools with an increase in glucose content (Figure 3-2). The mean T_2^* values were equal to (1.48 ± 0.09) ms and (0.87 ± 0.07) ms for HP ^{129}Xe dissolved in plasma and RBC, respectively.

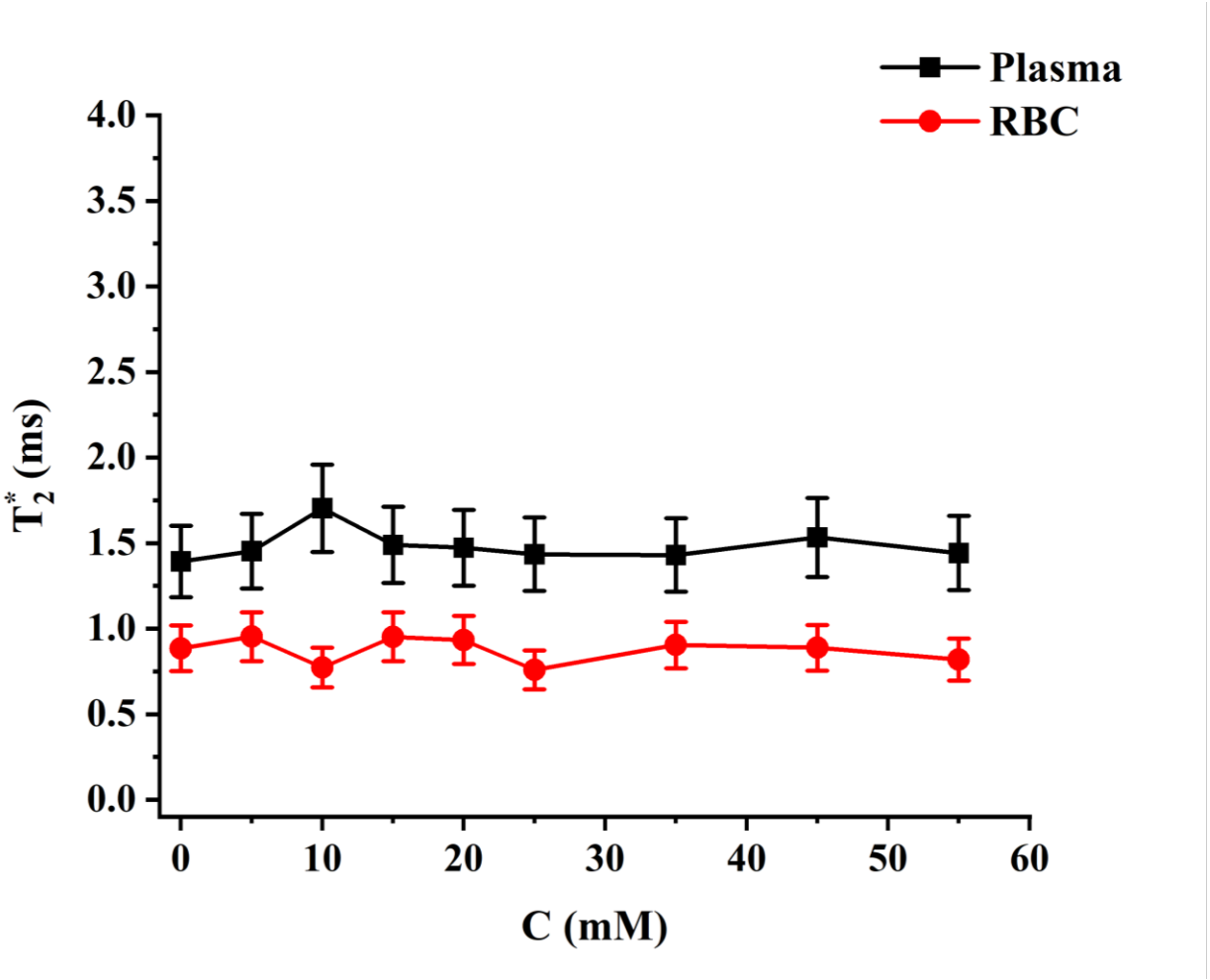

Figure 3-2 HP ^{129}Xe T_2^* relaxation dependance on blood glucose level for ^{129}Xe-plasma (black line) and ^{129}Xe-RBC (red line). T_2^* values were not affected by the blood glucose level.

3-2.3. Four-Peak Spectroscopic Model (4PM) Analysis

With the blood glucose level increase, the RBC resonance in the ^{129}Xe spectrum became more asymmetrical and its linewidth increased slightly (Figure 3-3). In addition, a small splitting of the RBC peak was noted for higher glucose concentrations (red arrow on Figure 3-3). Considering the glycation process in RBCs, the observed asymmetry and splitting in the RBC peak can be interpreted by a four-peak spectroscopic model (4PM). In general, structural and functional changes to hemoglobin occur as a result of glycation [27]. Therefore, we can subdivide the RBC pool into HP ^{129}Xe bound to non-glycated HbA_0 and HP ^{129}Xe bound to glycated HbA_{1c}. These two pools can be characterized by their own HP ^{129}Xe resonances. The suggested 4PM includes one gas phase resonance and three dissolved-phase resonances: ^{129}Xe-plasma, ^{129}Xe-RBC1, and ^{129}Xe-RBC2.

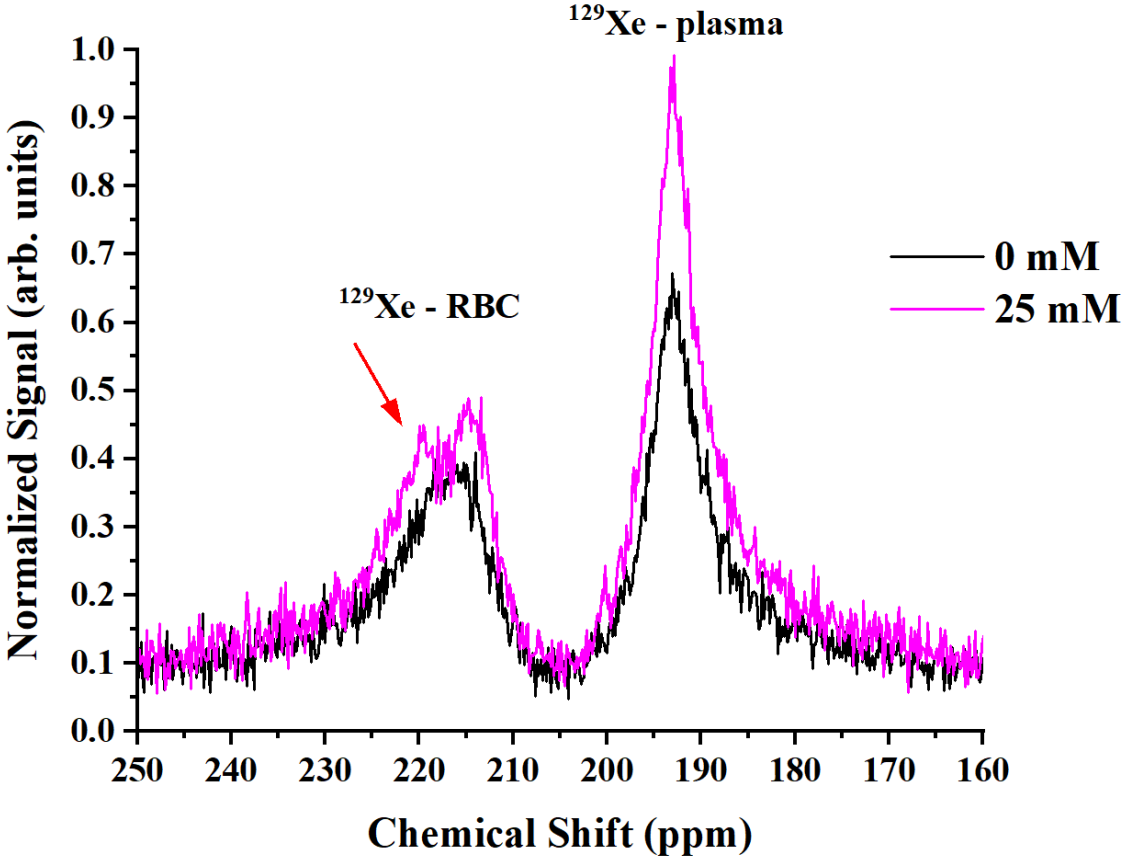

Figure 3-3 HP ^{129}Xe MRS spectra acquired for a pure blood sample (black line) and for a 25 mM blood glucose concentration (purple line). The RBC peak became asymmetrical and broader with the addition of glucose. A small splitting of the RBC peak can be seen (red arrow).

The suggested 4PM was used to fit the experimental data (Figure 3-4A,B). The application of the 4PM did not affect the plasma peak position. The position of the HP ^{129}Xe-RBC1 peak was barely affected by glucose: 216.08 ppm for the 10 mM solution and 215.92 ppm for the 45 mM solution. The ^{129}Xe-RBC2 peak, however, shifted downfield with increasing glucose concentrations: 220.32 ppm for the 10 mM solution and 220.78 ppm for the 45 mM. The residual error for the 3PM, once plotted, showed distinct peaks at 216, 218, and 222 ppm for the 10 mM sample and at 216 ppm and 219 ppm for the 45 mM sample (Figure 3-4C,D). Once the spectrum is fitted to the 4PM, however, the residual error becomes flat at the RBC resonance position

(between 210 ppm and 240 ppm). This indicates that 4PM fits the acquired HP ^{129}Xe blood spectra more accurately compared to the conventional 3PM.

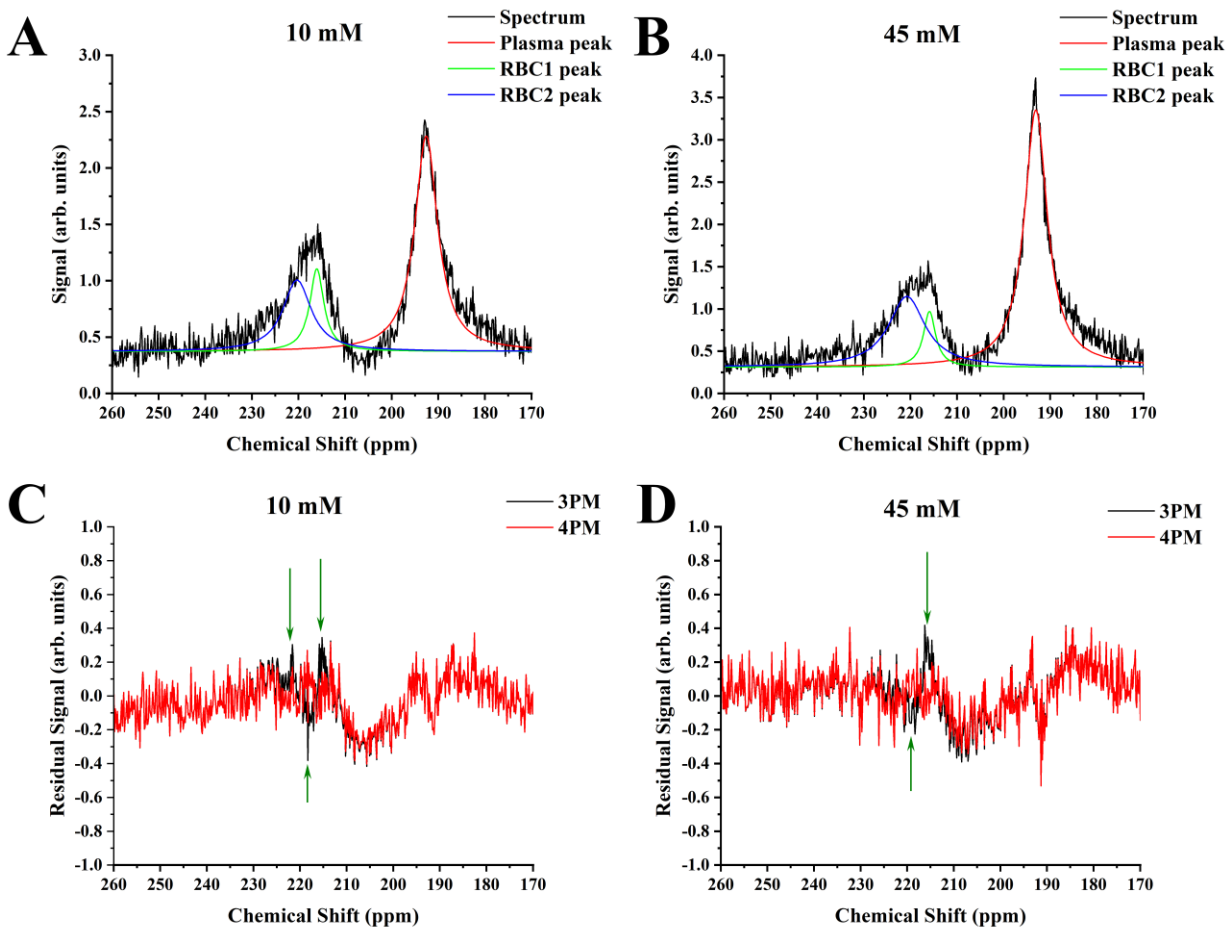

Figure 3-4 HP ^{129}Xe MRS spectra of the 10 mM sample (**A**) and 45 mM sample (**B**) fitted to the proposed 4PM. The CS scale was selected to depict dissolved-phase resonances. The black line corresponds to the acquired HP ^{129}Xe spectra. The red line corresponds to the Lorentzian fit of the plasma resonance. The green and blue lines represent the Lorentzian fit of the ^{129}Xe-RBC1 and ^{129}Xe-RBC2 peaks, respectively. The residuals of 3PM (black lines) and 4PM (red line) were plotted as a function of chemical shift for the 10 mM sample (**C**) and 45 mM sample (**D**). It can be clearly seen that the conventional 3PM shows some residual signal present (green arrows). The proposed 4PM, however, results in a flat baseline with almost no residual signal at the RBC resonance position (between 210 ppm and 240 ppm) indicating a better fit of the RBC signal. Therefore, the proposed 4PM better suits the acquired HP ^{129}Xe MRS spectra analysis compared to the conventional 3PM.

It should be noted that the 4PM fit worked better for glucose concentrations above 5 mM. This was indicated by slightly higher R^2 values. In addition, small alterations in the peak position for the RBC resonances did not affect R^2 significantly. Therefore, a lower accuracy of the recalculated spectral parameters can be anticipated for the pure blood and 5 mM samples compared to the samples with higher glucose levels. This is in accordance with our hypothesis that the second HP ^{129}Xe RBC peak originates from HbA1c. There is no naturally occurring HbA1c in the pure blood and the concentration is expected to be low in a 5 mM glucose sample.

The proposed 4PM did not affect the CS of the HP ^{129}Xe gas peak and ^{129}Xe-plasma peak. The HP ^{129}Xe-RBC1 CS change was not observed with a glucose level increase (Figure 3-5A). The HP ^{129}Xe-RBC2 resonance frequency, however, increased with a rate of (0.015 ± 0.002) ppm/mM. A strong Pearson correlation was observed between the HP ^{129}Xe-RBC2 peak position and the blood glucose level ($r = 0.95$). The T_2^* relaxation time for ^{129}Xe-plasma did not depend on the glucose concentration in the sample (Figure 3-5B). Conversely, the ^{129}Xe-RBC1 T_2^* time increased non-linearly from (1.58 ± 0.24) ms up to (2.67 ± 0.40) ms over the studied range of glucose concentrations. The ^{129}Xe-RBC2 T_2^* relaxation time increased from (0.66 ± 0.10) ms to (1.23 ± 0.19) ms over a 0–10 mM glucose concentration range and leveled out at approximately (0.91 ± 0.03) ms at higher glucose levels.

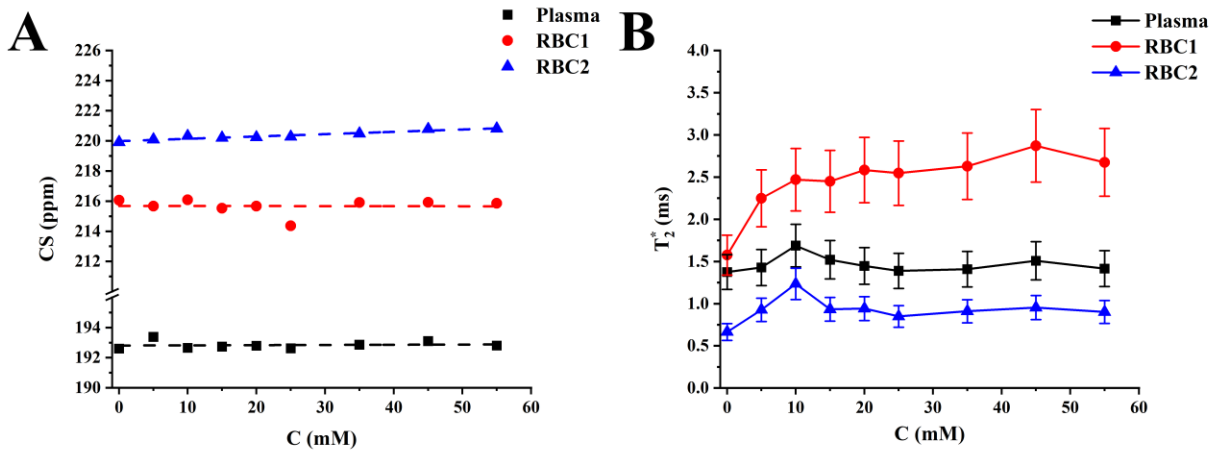

Figure 3-5 HP ^{129}Xe 4PM CS measurements and T_2^* relaxometry. (**A**) HP ^{129}Xe CS dependences for ^{129}Xe-plasma (black), ^{129}Xe-RBC1 (red), and ^{129}Xe-RBC2 (blue) as a function of blood glucose concentration. The dashed lines correspond to a linear fit of the measured CS dependances. A strong positive correlation can be observed between ^{129}Xe-RBC2 CS and glucose level, whereas the CS of HP ^{129}Xe-plasma and ^{129}Xe-RBC1 remains unaffected by blood glucose. (**B**) HP ^{129}Xe T_2^* relaxation dependence on blood glucose level for ^{129}Xe-plasma (black line), ^{129}Xe-RBC1 (red line), and ^{129}Xe-RBC2 (blue line). T_2^* values of HP ^{129}Xe in plasma were not affected by the blood glucose level, whereas the T_2^* relaxation time of ^{129}Xe-RBC1 increased non-linearly with a glucose concentration increase. T_2^* values of the ^{129}Xe-RBC2 peak increased slightly over the range of 0–10 mM and then leveled out.

3-3. Discussion

In normal physiological conditions, 95–98% of the hemoglobin in RBCs is present in the HbA_0 state [31]. Once glucose levels elevate in the blood, HbA_{1c} is generated as part of the glycation process [40]. In fact, the concentration of HbA_{1c} hemoglobin increases linearly with the glucose concentration [30]. Watala et al. demonstrated that there are three major sites where structural changes occur in HbA_{1c}: at the amino N-terminus of the β chain (~1/3 of the total amount of glucose binds to this site), α amino sites (~1/3 of the total glycation), and lysine residues (~40% of all glycation) [41]. Even if glucose is mostly linked to N-terminal valine, the glycation affects the spatial structure of the whole hemoglobin molecule. Ye at al. demonstrated that glycation transforms alpha-helices into beta-sheets, which results in conformation changes or the unfolding or even aggregation of hemoglobin [42]. Moreover, Sen at al. observed that the conformation

caused by glycation increased the exposure of the hydrophobic tryptophan residues, like Trp14 in alpha-chains, which created one of the xenon-binding sites [27]. These structural changes result in significant alterations in hemoglobin conformation [27,41]. Glycation-induced conformational changes in hemoglobin weaken the heme-globing linkage in HbA_{1c} and make it more thermolabile compared to HbA_0 [27]. Thus, the global changes in spatial hemoglobin's structure (tertiary and quaternary structure) may affect the shape of hydrophobic cavities or the binding sites of xenon, potentially resulting in a different chemical shift.

Savino et al. identified a total of twelve ^{129}Xe binding sites per Hb_4 tetramer: the α_1 chain contains four binding sites; the α_2 chain contains three; three more are located in the β_2 chain; and two can be found in the β_1 chain [43]. Considering the glycation-induced structural changes in HbA_{1c}, it is possible and fairly likely that the number, size, and/or spatial location of ^{129}Xe binding sites are different in HbA_{1c} compared with HbA_0. In addition, the glycation of hemoglobin results in the accumulation of free OH· radicals due to an iron-mediated Fenton's reaction [27]. Increasing OH· concentrations are anticipated to result in the deshielding of the HP ^{129}Xe nuclei. This hypothesis is supported by our experimental data, indicating the linear shift of the RBC HP ^{129}Xe resonance downfield with respect to the resonance frequency of the gaseous HP ^{129}Xe due to the increase in glucose concentration. The linear change in the HP ^{129}Xe CS as a function of glucose level is in agreement with a known linear increase in HbA_{1c} concentration caused by an increase in glucose concentration.

Considering our hypothesis that HP ^{129}Xe binding sites are affected by glycation and are different in HbA_{1c} compared to HbA_0, it is reasonable to assume the existence of two HP ^{129}Xe resonances—one from ^{129}Xe bound to HbA_0 and another originating from ^{129}Xe bound to HbA_{1c}. Therefore, instead of utilizing a conventional three peak model (gas phase resonance, plasma

resonance, and RBC resonance) for spectroscopic data analysis, a four-peak model (gas phase resonance, plasma resonance, and two RBC resonances) can be used, according to our hypothesis. Spectral data were analyzed using both models and the residual analyses better supported the hypothesis of the 4PM. After 4PM Lorentzian fits, the residual error was smooth and almost completely flat in the region between 213 and 235 ppm. On the contrary, several residual peaks were observed in the same region after 3PM Lorentzian fits, indicating the presence of certain spectral component that remained unaccounted for by the 3PM. The residual analysis findings were further supported by the visual observation of asymmetry of the RBC peak and the presence of a small peak splitting for higher glucose concentrations.

It should also be mentioned that the 4PM Lorentzian fits of the spectroscopy data acquired for higher glucose concentrations were much better compared to the 4PM Lorentzian fits for the low glucose levels. For the pure blood samples as well as for the 5 mM glucose concentration, perturbations in ^{129}Xe-RBC1 and ^{129}Xe-RBC2 peak positions did not affect R^2 significantly, if at all. Therefore, it can be concluded that the 4PM functions better for blood glucose levels above 5 mM. For concentration ranges between 0 mM and 5 mM, the 4PM can potentially result in some level of inaccuracy due to the four-peak fitting process. This can plausibly be explained by a low glycation level of the 0 mM and 5 mM samples.

The utilization of the 4PM demonstrated that the CS of one of HP ^{129}Xe-hemoglobin peaks (RBC1) is independent of glucose level, whereas the resonances of the RBC2 peak experience a downfield shift linearly with an increase in the glucose level, and thereby, an increase in HbA_{1c} concentration. Although the 4PM preserves the overall linear trend of the ^{129}Xe CS evolution, the net span of CS changes was reduced from ~1.25 ppm (for 3PM) down to ~0.9 ppm. The CS change in HP ^{129}Xe resonances due to the glycation of hemoglobin is much smaller than the previously

reported changes due to the blood oxygenation by Norquay et al. [24]. It should be mentioned that the actual physiological range of glucose levels in the blood has an upper limit of ~35 mM. Therefore, the net expected physiologically relevant change in HP ^{129}Xe RBC resonances due to HbA_{1c} formation is limited to ~ (0.53 ± 0.07) ppm, which is one order of magnitude smaller compared to the blood oxygenation CS changes. The plasma resonance position was unaffected by the elevation of the blood glucose level.

The analysis of the T_2^* relaxation times indicated that the HP ^{129}Xe-plasma resonance was unaffected by glucose level. Interestingly, the T_2^* values for the RBC1 peak increased non-linearly over the studied range of glucose concentrations. The T_2^* dynamics of the RBC2 peak were similar for glucose levels below 10 mM, albeit leveling out at higher concentrations.

Considering that the HP ^{129}Xe-plasma resonance was completely unaffected by alternations in glucose concentration, the detected changes of HP ^{129}Xe RBC relaxation should originate from internal alternations in RBCs' magnetic susceptibilities and/or from changes in HP ^{129}Xe spin–spin interactions with hemoglobin. There are two plausible mechanisms accounting for HP ^{129}Xe transverse relaxation changes within the RBC. It was previously suggested that glycation induces iron release from heme pockets of hemoglobin [27] and, therefore, should reduce the spin–spin interaction between HP ^{129}Xe enclosed in hemoglobin and the heme–iron atoms. Alternatively, conformational changes of HbA_{1c} may occur in a way that the heme pockets become spatially distanced from HP ^{129}Xe binding sites, thereby reducing the HP ^{129}Xe—namely iron spin–spin interactions. Considering that iron release and conformational changes occur during the glycation process itself, it is possible that both mechanisms contribute to the observed changes in the T_2^* relaxation of HP ^{129}Xe within the RBC.

Although a careful study of the position of the ^{129}Xe binding sites in HbA_{1c} is required for a proper explanation of the observed results, it is plausible that conformational changes in hemoglobin due to glycation occur in such a way that the dissociation constant of the HP ^{129}Xe-HbA_{1c} becomes substantially lower compared to the dissociation constant of the HP ^{129}Xe-HbA_0 complexes. Unfortunately, an accurate assessment of the relative changes in dipole–dipole interaction strength is not possible without knowledge of the location of ^{129}Xe atoms in HbA_{1c}.

Despite the fact that the knowledge of the ^{129}Xe-HbA_{1c} binding sites is of critical importance before attempting a quantitative description of the relaxation mechanisms responsible for the changes in HP ^{129}Xe relaxation and the alternations of the CS, it should be possible to hypothesize the origin of the ^{129}Xe-RBC1 and ^{129}Xe-RBC2 peaks by combining our experimental results with previous knowledge on the glycation process and HbA_{1c}. Due to the glycation process, iron is released from the heme pocket of hemoglobin [27]. In addition, hydrogen peroxide is produced by autoxidizing glucose, and its concentration builds up with time [44]. Hydrogen peroxide further initiates iron release from hemoglobin [45], affecting HbA_{1c} much faster compared to HbA_0 [27]. The iron released from heme pockets participates in an iron-dependent Fenton's reaction that becomes a source of free OH· radicals within RBCs [27]. The charge of free radicals deshields the HP ^{129}Xe nuclei, resulting in a downfield chemical shift detected via MRS. On the other hand, the release of iron may result in a decrease in the spin–spin interaction between the HP ^{129}Xe bound to the hemoglobin. Since the iron release is much higher for HbA_{1c}, it is plausible that the reduction in spin–spin interaction would be substantial for HP ^{129}Xe enclosed within HbA_{1c}. The T_2^* of HP ^{129}Xe bond to HbA_0 would be less affected due to the lower amount of iron released. Therefore, based on our results, we hypothesize that the RBC1 peak originates from HP ^{129}Xe-HbA_{1c}, while the RBC2 peak corresponds to the HP ^{129}Xe-HbA_0 signal. It is further

plausible that the CS of the HP ^{129}Xe-HbA1c signal is unaffected by the free OH· radical levels due to the conformational changes of the HbA1c and potential enclosure of HP ^{129}Xe within the protein structure. On the other hand, the HP ^{129}Xe-HbA_0 signal experiences a linear downfield CS change due to the interaction with free radicals. It is also possible that the small change in T_2^* of HP ^{129}Xe-HbA_0 is a result of substantially slower iron extraction from HbA_0.

Our study has several limitations. First, the initial incubation time of the blood samples with glucose solution was relatively short (only ~1 h). The glycation process is relatively slow, consisting of several steps and lasting a span of several days [44]. In the first step, the non-enzymatic Maillard early phase reaction takes place. This occurs after the binding of glucose transferred from the blood to the hemoglobin in RBCs and dictated by the interaction between the aldehyde group of the reducing glucose with the N-terminal amino base and ε-amino base of the lysine residue with the consequent formation of the Schiff base (almidine). This reaction is reversible—it is followed by an irreversible Amadori rearrangement, which results in the production of a stable form of HbA_{1c} (ketoamine) [46]. The Amadori rearrangement is considered to be the limiting reaction in the glycation process [47,48]. The amount of HbA_{1c} and synthetized H_2O_2, and therefore, the final concentration of free radicals, increases gradually over the glycation time course. Koga et al. used a 1 h incubation time in their study and confirmed the formation of the labile-glycated hemoglobin (aldimine); however, the formation of stable glycated hemoglobin (ketoamine) was not observed [46]. Thus, it is likely that we observed only the initial changes in the HP ^{129}Xe CS and T_2^* relaxation time. A longer incubation time period will result in more pronounced changes in CS and in T_2^* relaxation time for HP ^{129}Xe dissolved in RBCs. It should be noted that longer incubation times must be moderated by the fact that a small percentage of hemoglobin will be converted into methemoglobin in standing blood over time [49]. The formation

of methemoglobin from hemoglobin within the red blood cells is an ongoing oxidative process that can result from the exposure of blood to the atmosphere in long standing blood samples. Methemoglobin forms when hemoglobin is oxidized to contain iron in the ferric [Fe^{3+}] state rather than the normal ferrous [Fe^{2+}] state [49]. Since methemoglobin is paramagnetic, this itself will cause additional changes to the CS and T_2^* relaxation time [23]. Therefore, longer incubation times are a tradeoff between allowing the full glycation of the blood samples versus limiting the formation of methemoglobin. In addition, all experiments were conducted on sterile citrated sheep blood. While it is not clear how the presence of citric acid affects protein glycation, the reproduction of these experiments may be performed in other types of animal blood.

Our work is a pioneering proof-of-concept study that should be further expanded by performing experiments with purified human hemoglobin, which is very low in the glycated form and separated RBCs from healthy and hyperglycemic subjects. This will allow us to study the effects of glucose on human RBCs. Consequently, the present study can be translated to the utilization of human blood drawn from healthy participants and hyperglycemic participants to observe how glycose-related changes are affected by the presence of other biological moieties from human blood. Furthermore, glycation level measurements are vital for obtaining reliable conclusions regarding the glucose effect on the ^{129}Xe spectroscopic properties in blood. Additionally, no studies have yet been performed that investigate HP ^{129}Xe binding to the glycated form of hemoglobin, which can be assessed in future X-ray diffraction (XRD) studies.

3-4. Materials and Methods

3-4.1. Sample Preparation

A 500 mM solution of glucose was prepared by dissolving 3.6 g of D-glucose (Sigma-Aldrich, St. Louis, MO, USA) in 40 mL of phosphate-buffered saline (PBS) at pH 7.4 at room

temperature. The mixture was stirred for complete dissolution and used as a stock solution for the preparation of the blood samples. Various volumes of the glucose solution in PBS were mixed with 20 mL of fresh citrated sheep blood (Cedarlane, Burlington, CA, USA) to create the following set of concentrations: 5, 10, 15, 20, 25, 35, 45, and 55 mM. The volume of glucose solution added to the blood was at least one order of magnitude smaller than the volume of the blood, in order to minimize blood dilution effects. A total of 20 mL of the pure citrated sheep blood without any additives served as a control sample. All blood samples were allowed to equilibrate to room temperature for approximately 1 h. The reported incubation times for glycation in the literature vary between 30 min up to hundreds of hours, depending on the incubation protocol [50]. Moreover, the vast majority of studies were able to confirm hemoglobin glycation for all of the incubation time periods. Therefore, successful hemoglobin glycation is expected within our experimental time frame.

4.2. Magnetic Resonance Spectroscopy (MRS)

^{129}Xe gas was polarized up to 56% using a XeBox-10E polarizer (Xemed, Durham, NH, USA) and disposed into 1 L Tedlar bags. The experimental setup (Figure 3-6) used for mixing HP ^{129}Xe with blood was similar to that used by Norquay et al. [25]. Mixing was performed using an exchange module (Superphobic MicroModule 0.5 × 1 G680 Contactor; Membrana, Charlotte, NC, USA). A steady flow of HP ^{129}Xe was set through the exchange module with the help of a pressure chamber pressurized with a continuous flow of N_2 gas. The flow rate of N_2 into the pressure chamber was controlled by a ventilator. The solution of sheep blood in the 10 mL syringe was connected to an exchange module and placed in a custom-built dual ^{1}H/^{129}Xe quadrature MRI birdcage coil, while the other empty syringe was connected to the other side of the exchange module. The blood was pumped back and forth manually through the exchange module

perpendicular to the ^{129}Xe flow for ~6 s. This technique allowed a sufficient amount of HP ^{129}Xe to dissolve in the sheep blood and avoid the formation of gas bubbles in the blood.

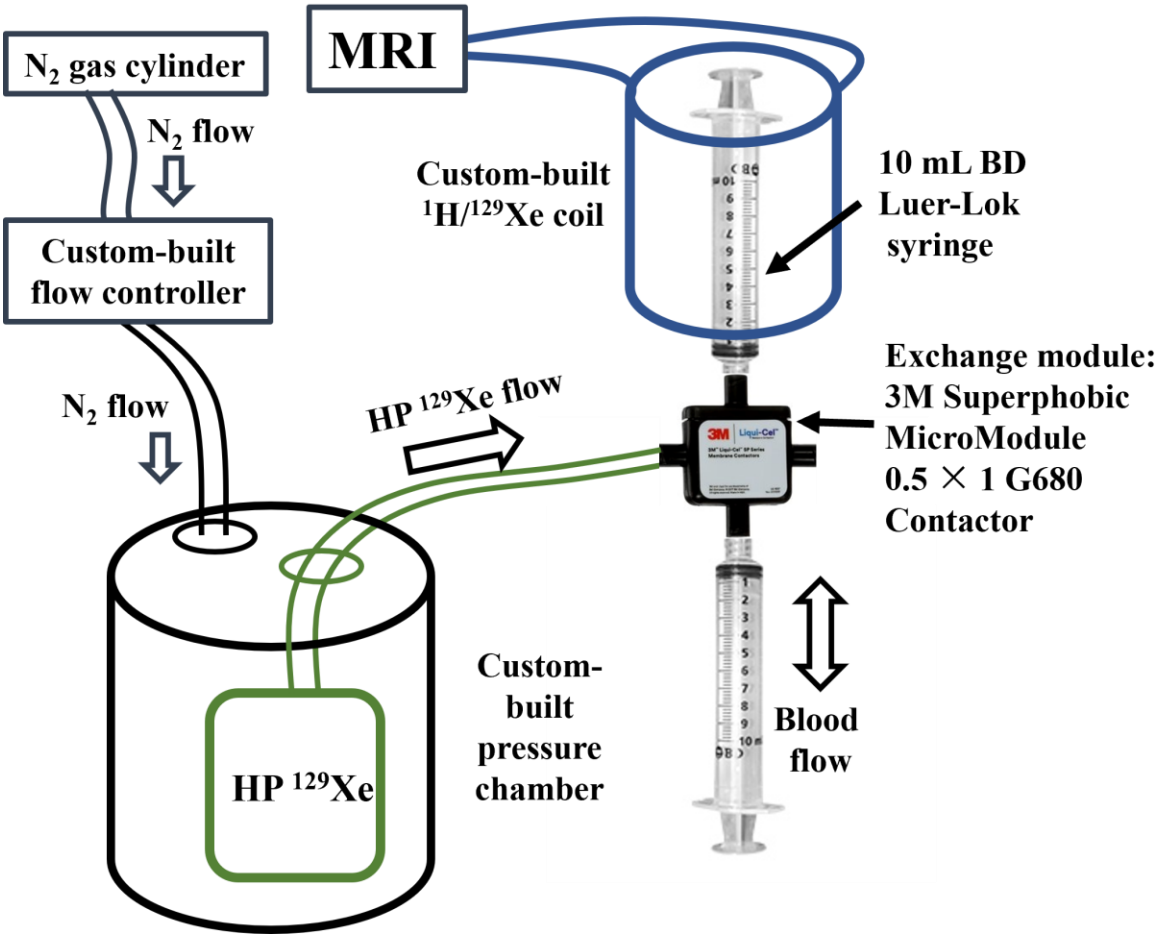

Figure 3-6 Setup used for mixing the blood with HP ^{129}Xe and further MR signal acquisition. A steady flow of HP ^{129}Xe from the 1L bag was regulated by the continuous flow of N_2 in the pressure chamber, forcing the HP ^{129}Xe through the exchange module. The mixing of blood and HP ^{129}Xe was performed by manually pumping the blood through the exchange module.

A clinical Philips Achieva 3.0 T MRI scanner (Philips, Andover, MA, USA) equipped with a custom-built dual ^{1}H/^{129}Xe quadrature MRI birdcage coil was used for all ^{129}Xe-blood spectroscopy acquisitions. The coil was tuned to 35.33 MHz, and the scanner was shimmed on the ^{1}H signal from blood to correct for B_1 inhomogeneities. Prior to taking any measurements, the coil was calibrated for the blood samples by applying a series of ten RF pulses with a 10° flip angle

centered on the gas peak position of HP ^{129}Xe resonance (for this, 1 mL syringes filled with HP ^{129}Xe were placed into the coil near the blood sample).

To measure the effect of glucose concentration on the CS of the ^{129}Xe dissolved in plasma (^{129}Xe-plasma) and in RBC (^{129}Xe-RBC) resonances, high-resolution single voxel spectroscopy was acquired for all samples. The receiver bandwidth was equal to 22 kHz and the number of samples was set to 4096, yielding a 0.15 ppm spectral resolution. A total of 0 ppm was set in between the peaks of ^{129}Xe dissolved in plasma and the RBCs. A 90° rectangular excitation pulse was utilized. An FID spectrum was acquired with a TR of 189.6ms and a TE of 0.25 ms. Measurements were repeated five times for each sample.

3-4.3. Data Reconstruction and Statistical Analysis

All data were initially analyzed using custom MatLab scripts in Matlab 2020b (Mathworks, Natick, MA, USA). The MRS spectra were postprocessed in Origin2021b (OriginLab, Northampton, MA, USA) for CS and T_2^* relaxation time assessment. HP ^{129}Xe MRS spectra were fitted to either three (gas resonance, ^{129}Xe-plasma resonance, and ^{129}Xe-RBC resonance) or four (gas resonance, ^{129}Xe-plasma resonance, and two ^{129}Xe-RBC resonances) Lorentzian curves. The quality of fit was accessed via R^2 value and through the residual fit error, which was automatically calculated at the end of the fitting algorithm. The comparison between the three and four peak model was performed based on the R^2 and the residuals.

The full width half maximum (FWHM) of Lorentzian curves was utilized for calculations of the T_2^* of ^{129}Xe dissolved in RBCs and plasma using the following equation [51]:

$$T_2^* = \frac{1}{\pi * FWHM}. \qquad [3-1]$$

To evaluate statistical significance of the acquired results, a paired two-tailed *t*-test was used with a statistical significance level of 0.05. Pearson's correlation coefficient was calculated between the CS changes of each HP ^{129}Xe dissolved phase resonance and the glucose concentration. All statistical analysis was conducted using Origin2021b v.9.8.5.212 software.

3-5. Conclusions

In this work, for the first time, we demonstrated glucose-induced changes in CS and T_2^* relaxation of HP ^{129}Xe dissolved in blood. By using a residual analysis, we observed the evidence for a third dissolved-phase resonance, which was attributed to HP ^{129}Xe bound to HbA_{1c} produced during HbA_0 glycation. Our four-peak model suggests that one dissolved ^{129}Xe resonance originates from plasma, whereas two other peaks originate from ^{129}Xe encapsulated by HbA_0 and HbA_{1c} (the fourth peak stems from the gas phase resonance). We observed a linear dependence of the ^{129}Xe-HbA_0 resonance CS on the blood glucose levels. The ^{129}Xe-HbA_{1c} T_2^* changed non-linearly with an increase in glucose level. The HP ^{129}Xe-plasma resonance was not affected by alternations in the glucose level.

Author Contributions: Conceptualization, L.M. and M.T.-K.; methodology, L.M., V.G., Y.S., M.S.A. and M.T.-K.; software, Y.S. and V.G.; validation, Y.S., M.S.A., I.C.R., M.T.-K. and H.H.; formal analysis, Y.S., V.G. and L.M.; investigation, L.M., V.G., Y.S., I.C.R., J.D., H.A. and M.S.A.; resources, M.S.A., L.M. and H.H.; data curation, M.S.A. and D.B.; writing—original draft preparation, V.G., L.M. and Y.S.; writing—review and editing, Y.S., V.G., L.M., M.S.A., H.H. and D.B.; visualization, V.G., Y.S. and L.M.; supervision, M.S.A., D.B., H.H. and M.T.-K.; project administration, Y.S., V.G. and M.S.A.; funding acquisition, L.M., V.G., Y.S. and M.S.A. All authors have read and agreed to the published version of the manuscript.

Funding: This research was funded by Natural Science and Engineering Research Council (NSERC) Discovery grant (RGPIN-2017-05359) and by the Priority Research Area SciMat under the program Excellence Initiative—Research University at the Jagiellonian University in Kraków (PSP: U1U/P05/NO/03.35). Y.S. was supported by the Mitacs Elevate Postdoctoral Fellowship (IT25574). V.G. was partially supported by an Ontario Trillium Scholarship and by Mitacs Accelerate Grant (IT31144). L.M. was supported by Jagiellonian Interdisciplinary PhD Program.

Institutional Review Board Statement: This study was approved by the local biosafety committee.

Informed Consent Statement: Not applicable.

Data Availability Statement: The data that support the findings of this study are available from the corresponding author upon reasonable request.

Conflicts of Interest: Author I.C.R. was employed by the company Xemed LLC, Durham, NH, USA. The remaining authors declare that the research was conducted in the absence of any commercial or financial relationships that could be construed as a potential conflict of interest.

References

1. Albert, M.S.; Cates, G.D.; Driehuys, B.; Happer, W.; Saam, B.; Springer, C.S.; Wishnia, A. Biological Magnetic Resonance Imaging Using Laser-Polarized ^{129}Xe. *Nature* **1994**, *370*, 199–201.
2. Kruger, S.J.; Nagle, S.K.; Couch, M.J.; Ohno, Y.; Albert, M.; Fain, S.B. Functional Imaging of the Lungs with Gas Agents. *J. Magn. Reson. Imaging* **2016**, *43*, 295–315.
3. Patz, S.; Muradyan, I.; Hrovat, M.I.; Dabaghyan, M.; Washko, G.R.; Hatabu, H.; Butler, J.P. Diffusion of Hyperpolarized ^{129}Xe in the Lung: A Simplified Model of ^{129}Xe Septal Uptake

and Experimental Results. *New J. Phys.* **2011**, *13*, 015009. https://doi.org/10.1088/1367-2630/13/1/015009.

4. Ruppert, K.; Mata, J.F.; Brookeman, J.R.; Hagspiel, K.D.; Mugler, J.P. Exploring Lung Function with Hyperpolarized ^{129}Xe Nuclear Magnetic Resonance. *Magn. Reason. Med.* **2004**, *51*, 676–687. https://doi.org/10.1002/mrm.10736.
5. Santyr, G.; Fox, M.; Thind, K.; Hegarty, E.; Ouriadov, A.; Jensen, M.; Scholl, T.J.; Van Dyk, J.; Wong, E. Anatomical, Functional and Metabolic Imaging of Radiation-Induced Lung Injury Using Hyperpolarized MRI. *NMR Biomed.* **2014**, *27*, 1515–1524. https://doi.org/10.1002/nbm.3180.
6. Svenningsen, S.; Kirby, M.; Starr, D.; Leary, D.; Wheatley, A.; Maksym, G.N.; McCormack, D.G.; Parraga, G. Hyperpolarized ^{3}He and ^{129}Xe MRI: Differences in Asthma before Bronchodilation. *J. Magn. Reson. Imaging* **2013**, *38*, 1521–1530. https://doi.org/10.1002/jmri.24111.
7. Matheson, A.M.; Mcintosh, M.J.; Kooner, H.K.; Lee, J.; Desaigoudar, V.; Bier, E.; Driehuys, B.; Svenningsen, S.; Santyr, G.E.; Kirby, M.; et al. Persistent ^{129}Xe MRI Pulmonary and CT Vascular Abnormalities in Symptomatic Individuals with Post-Acute COVID-19 Syndrome. *Radiology* **2022**, *305*, 466–476.
8. Rankine, L.J.; Wang, Z.; Wang, J.M.; He, M.; McAdams, H.P.; Mammarappallil, J.; Rackley, C.R.; Driehuys, B.; Tighe, R.M. ^{129}xenon Gas Exchange Magnetic Resonance Imaging as a Potential Prognostic Marker for Progression of Idiopathic Pulmonary Fibrosis. *Ann. Am. Thorac. Soc.* **2020**, *17*, 121–125.
9. Grist, J.T.; Chen, M.; Collier, G.J.; Raman, B.; Abueid, G.; McIntyre, A.; Matthews, V.; Fraser, E.; Ho, L.P.; Wild, J.M.; et al. Hyperpolarized ^{129}Xe MRI Abnormalities in Dyspneic Patients

3 Months after COVID-19 Pneumonia. *Radiology* **2021**, *301*, E353–E360. https://doi.org/10.1148/radiol.2021210033.

10. Wang, Z.; Robertson, S.H.; Wang, J.; He, M.; Virgincar, R.S.; Schrank, G.M.; Bier, E.A.; Rajagopal, S.; Huang, Y.C.; O'Riordan, T.G.; et al. Quantitative Analysis of Hyperpolarized ^{129}Xe Gas Transfer MRI. *Med. Phys.* **2017**, *44*, 2415–2428. https://doi.org/10.1002/mp.12264.
11. Willmering, M.M.; Cleveland, Z.I.; Walkup, L.L.; Woods, J.C. Removal of Off-Resonance Xenon Gas Artifacts in Pulmonary Gas-Transfer MRI. *Magn. Reason. Med.* **2021**, *86*, 907–915. https://doi.org/10.1002/mrm.28737.
12. Niedbalski, P.J.; Hall, C.S.; Castro, M.; Eddy, R.L.; Rayment, J.H.; Svenningsen, S.; Parraga, G.; Zanette, B.; Santyr, G.E.; Thomen, R.P.; et al. Protocols for Multi-Site Trials Using Hyperpolarized ^{129}Xe MRI for Imaging of Ventilation, Alveolar-Airspace Size, and Gas Exchange: A Position Paper from the ^{129}Xe MRI Clinical Trials Consortium. *Magn. Reason. Med.* **2021**, *86*, 2966–2986. https://doi.org/10.1002/mrm.28985.
13. Shepelytskyi, Y.; Grynko, V.; Rao, M.R.; Li, T.; Agostino, M.; Wild, J.M.; Albert, M.S. Hyperpolarized ^{129}Xe Imaging of the Brain: Achievements and Future Challenges. *Magn. Reason. Med.* **2022**, *88*, 83–105. https://doi.org/10.1002/MRM.29200. *(Included as Chapter 2 in the thesis)*
14. Grynko, V.; Shepelytskyi, Y.; Li, T.; Hassan, A.; Granberg, K.; Albert, M.S. Hyperpolarized ^{129}Xe Multi-Slice Imaging of the Human Brain Using a 3D Gradient Echo Pulse Sequence. *Magn. Reason. Med.* **2021**, *86*, 3175–3181. https://doi.org/10.1002/mrm.28932. *(Included as Chapter 4 in the thesis)*

15. Shepelytskyi, Y.; Grynko, V.; Li, T.; Hassan, A.; Granberg, K.; Albert, M.S. The Effects of an Initial Depolarization Pulse on Dissolved Phase Hyperpolarized ^{129}Xe Brain MRI. *Magn. Reason. Med.* **2021**, *86*, 3147–3155. https://doi.org/10.1002/mrm.28918.
16. Shepelytskyi, Y.; Hane, F.T.; Grynko, V.; Li, T.; Hassan, A.; Albert, M.S. Hyperpolarized ^{129}Xe Time-of-Flight MR Imaging of Perfusion and Brain Function. *Diagnostics* **2020**, *10*, 630. https://doi.org/10.3390/diagnostics10090630.
17. Rao, M.R.; Norquay, G.; Stewart, N.J.; Hoggard, N.; Griffiths, P.D.; Wild, J.M. Assessment of Brain Perfusion Using Hyperpolarized ^{129}Xe MRI in a Subject with Established Stroke. *J. Magn. Reson. Imaging* **2019**, *50*, 1002–1004. https://doi.org/10.1002/jmri.26686.
18. Rao, M.R.; Stewart, N.J.; Griffiths, P.D.; Norquay, G.; Wild, J.M. Imaging Human Brain Perfusion with Inhaled Hyperpolarized ^{129}Xe MR Imaging. *Radiology* **2018**, *286*, 659–665. https://doi.org/10.1148/radiol.2017162881.
19. Chacon-Caldera, J.; Maunder, A.; Rao, M.; Norquay, G.; Rodgers, O.I.; Clemence, M.; Puddu, C.; Schad, L.R.; Wild, J.M. Dissolved Hyperpolarized Xenon-129 MRI in Human Kidneys. *Magn. Reason. Med.* **2020**, *83*, 262–270. https://doi.org/10.1002/mrm.27923.
20. Loza, L.A.; Kadlecek, S.J.; Pourfathi, M.; Hamedani, H.; Duncan, I.F.; Ruppert, K.; Rizi, R.R. Quantification of Ventilation and Gas Uptake in Free-Breathing Mice With Hyperpolarized ^{129}Xe MRI. *IEEE Trans. Med. Imaging* **2019**, *38*, 2081–2091. https://doi.org/10.1109/TMI.2019.2911293.
21. Albert, M.S.; Balamore, D.; Kacher, D.F.; Venkatesh, A.K.; Jolesz, F.A. Hyperpolarized ^{129}XE T1 in Oxygenated and Deoxygenated Blood. *NMR Biomed.* **2000**, *13*, 407–414. https://doi.org/10.1002/1099-1492(200011)13:7<407::AID-NBM661>3.0.CO;2-1.

22. Albert, M.S.; Kacher, D.F.; Balamore, D.; Venkatesh, A.K.; Jolesz, F.A. T1 of ^{129}Xe in Blood and the Role of Oxygenation. *J. Magn. Reson.* **1999**, *140*, 264–273. https://doi.org/10.1006/jmre.1999.1836.

23. Wolber, J.; Cherubini, A.; Dzik-Jurasz, A.S.K.K.; Leach, M.O.; Bifone, A. Spin-Lattice Relaxation of Laser-Polarized Xenon in Human Blood. *Proc. Natl. Acad. Sci. USA* **1999**, *96*, 3664–3669. https://doi.org/10.1073/pnas.96.7.3664.

24. Norquay, G.; Leung, G.; Stewart, N.J.; Wolber, J.; Wild, J.M. ^{129}Xe Chemical Shift in Human Blood and Pulmonary Blood Oxygenation Measurement in Humans Using Hyperpolarized ^{129}Xe NMR. *Magn. Reason. Med.* **2017**, *77*, 1399–1408. https://doi.org/10.1002/mrm.26225.

25. Norquay, G.; Leung, G.; Stewart, N.J.; Tozer, G.M.; Wolber, J.; Wild, J.M. Relaxation and Exchange Dynamics of Hyperpolarized ^{129}Xe in Human Blood. *Magn. Reason. Med.* **2015**, *74*, 303–311. https://doi.org/10.1002/mrm.25417.

26. Wolber, J.; Cherubini, A.; Leach, M.O.; Bifone, A. On the Oxygenation-Dependent ^{129}Xe T 1 in Blood. *NMR Biomed.* **2000**, *13*, 234–237.

27. Sen, S.; Kar, M.; Roy, A.; Chakraborti, A.S. Effect of Nonenzymatic Glycation on Functional and Structural Properties of Hemoglobin. *Biophys. Chem.* **2005**, *113*, 289–298. https://doi.org/10.1016/j.bpc.2004.05.005.

28. Giulivi, C.; Hochstein, P.; Davies, K.J.A. Hydrogen Peroxide Production by Red Blood Cells. *Free Radic. Biol. Med.* **1994**, *16*, 123–129. https://doi.org/10.1016/0891-5849(94)90249-6.

29. De Rosa, M.C.; Sanna, M.T.; Messana, I.; Castagnola, M.; Galtieri, A.; Tellone, E.; Scatena, R.; Botta, B.; Botta, M.; Giardina, B. Glycated Human Hemoglobin HbA1c : Functional Characteristics and Molecular Modeling Studies. *Biophys. Chem.* **1998**, *72*, 323–335.

30. Sacks, D.B. Correlation between Hemoglobin A1c (HbA1c) and Average Blood Glucose: Can HbA1c Be Reported as Estimated Blood Glucose Concentration? *J. Diabetes Sci. Technol.* **2007**, *1*, 801–803. https://doi.org/10.1177/193229680700100602.
31. Coletta, M.; Amiconi, G.; Bellellil, A.; Carsky, J.; Castagnola, M.; Condb, S.; Brunori, M. Alteration of T-State Binding Properties of Naturally Glycated. *J. Mol. Biol.* **1988**, *203*, 233–239. https://doi.org/10.1016/0022-2836(88)90104-0.
32. Freeman, V.S. Glucose and Hemoglobin A1c. *Lab. Med.* **2014**, *45*, e21–e24. https://doi.org/10.1309/LMNSU432YJWCWZKX.
33. Penttilä, I.; Penttilä, K.; Holm, P.; Laitinen, H.; Ranta, P.; Törrönen, J.; Rauramaa, R. Methods, Units and Quality Requirements for the Analysis of Haemoglobin A 1c in Diabetes Mellitus . *World J. Methodol.* **2016**, *6*, 133. https://doi.org/10.5662/wjm.v6.i2.133.
34. Inouye, M.; Mio, T.; Sumino, K. Glycated Hemoglobin and Lipid Peroxidation in Erythrocytes of Diabetic Patients. *Metabolism* **1999**, *48*, 205–209. https://doi.org/10.1016/s0026-0495(99)90035-5.
35. Viskupicova, J.; Blaskovic, D.; Galiniak, S.; Soszyński, M.; Bartosz, G.; Horakova, L.; Sadowska-Bartosz, I. Effect of High Glucose Concentrations on Human Erythrocytes in Vitro. *Redox Biol.* **2015**, *5*, 381–387. https://doi.org/10.1016/j.redox.2015.06.011.
36. Kar, M.; Chakraborti, A.S. Effect of Glucosylation on Iron-Mediated Free Radical Reactions of Haemoglobin. *Curr. Sci.* **2001**, *80*, 770–773.
37. Buys, A.V.; Van Rooy, M.J.; Soma, P.; Van Papendorp, D.; Lipinski, B.; Pretorius, E. Changes in Red Blood Cell Membrane Structure in Type 2 Diabetes: A Scanning Electron and Atomic Force Microscopy Study. *Cardiovasc. Diabetol.* **2013**, *12*, 1–7. https://doi.org/10.1186/1475-2840-12-25.

38. Salvagno, G.L.; Sanchis-Gomar, F.; Picanza, A.; Lippi, G. Red Blood Cell Distribution Width: A Simple Parameter with Multiple Clinical Applications. *Crit. Rev. Clin. Lab. Sci.* **2015**, *52*, 86–105.

39. Schoenborn, B.P. Binding of Xenon to Horse Haemoglobin. *Nature* **1965**, *208*, 760–762. https://doi.org/10.1038/208760a0.

40. Peterson, K.P.; Pavlovich, J.G.; Goldstein, D.; Little, R.; England, J.; Peterson, C.M. What Is Hemoglobin A1c? An Analysis of Glycated Hemoglobins by Electrospray Ionization Mass Spectrometry Endocrinology and Metabolism. *Clin. Chem.* **1998**, *44*, 1951–1958.

41. Watala, C.; Gwozdzinski, K.; Malek', M. Direct Evidence for the Alterations in Protein Structure and Conformation upon In Vitro Nonenzymatic Glycosylation. *J. Biochem.* **1992**, *24*, 1295–1302. https://doi.org/10.1016/0020-711x(92)90204-e.

42. Ye, S.; Ruan, P.; Yong, J.; Shen, H.; Liao, Z.; Dong, X. The Impact of the HbA1c Level of Type 2 Diabetics on the Structure of Haemoglobin. *Sci. Rep.* **2016**, *6*, 33352. https://doi.org/10.1038/srep33352.

43. Savino, C.; Miele, A.E.; Draghi, F.; Johnson, K.A.; Sciara, G.; Brunori, M.; Vallone, B. Pattern of Cavities in Globins: The Case of Human Hemoglobin. *Biopolym. Pept. Sci. Sect.* **2009**, *91*, 1097–1107. https://doi.org/10.1002/bip.21201.

44. Wolff, S.P.; Jiang, Z.Y.; Huwr, J.V. Protein Glycation and Oxidative Stress in Diabetes Mellitus and Ageing. *Free Radic. Biol. Med.* **1991**, *10*, 339–352. https://doi.org/10.1016/0891-5849(91)90040-a.

45. Halliwell, B.; Gutteridge, J.M.C. Role of Free Radicals and Catalytic Metal Ions in Human Disease: An Overview. *Methods Enzymol.* **1990**, *186*, 1–85. https://doi.org/10.1016/0076-6879(90)86093-b.

46. Koga, M.; Inada, S.; Shimizu, S.; Hatazaki, M.; Umayahara, Y.; Nishihara, E. Aldimine Formation Reaction, the First Step of the Maillard Early-Phase Reaction, Might Be Enhanced in Variant Hemoglobin, Hb Himeji. *Ann. Clin. Lab. Sci.* **2015**, *45*, 643–649.
47. Kerber, R.C. The A1c Blood Test: An Illustration of Principles from General and Organic Chemistry. *J. Chem. Educ.* **2007**, *84*, 1541–1545. https://doi.org/10.1021/ed084p1541.
48. Lowrey, C.H.; Lyness, S.J.; Soeldner, J.S. The Effect of Hemoglobin Ligands on the Kinetics of Human Hemoglobin A(1c) Formation. *J. Biol. Chem.* **1985**, *260*, 11611–11618. https://doi.org/10.1016/s0021-9258(17)39075-0.
49. Umbreit, J. Methemoglobin—It's Not Just Blue: A Concise Review. *Am. J. Hematol.* **2007**, *82*, 134–144.
50. da Silva, M.V.B.; Alet, A.I.; Castellini, H.V.; Riquelme, B.D. Methods: A New Protocol for in Vitro Red Blood Cell Glycation. *Comp. Biochem. Physiol. Part A* **2022**, *264*, 111109.
51. Shepelytskyi, Y.; Li, T.; Grynko, V.; Newman, C.; Hane, F.T.; Albert, M.S. Evaluation of Fluorine-19 Magnetic Resonance Imaging of the Lungs Using Octafluorocyclobutane in a Rat Model. *Magn Reson Med* **2021**, *85*, 987–994, doi:10.1002/mrm.28473.

Disclaimer/Publisher's Note: The statements, opinions and data contained in all publications are solely those of the individual author(s) and contributor(s) and not of MDPI and/or the editor(s). MDPI and/or the editor(s) disclaim responsibility for any injury to people or property resulting from any ideas, methods, instructions or products referred to in the content.

Chapter 4: Multi-slice brain imaging with hyperpolarized ^{129}Xe

This topic has been elaborated in the following publication: **Grynko V.**, Shepelytskyi Y., Li T., Hassan A., Granberg K., Albert M.S "**Hyperpolarized 129Xe multi-slice imaging of the human brain using a 3D gradient echo pulse sequence**" published as a technical note in *Magnetic Resonance in Medicine*, volume 86, issue 6, pages: 3175-3186 (2021). The publication text is listed below.

Hyperpolarized 129Xe multi--slice imaging of the human brain using a 3D gradient echo pulse sequence

Vira Grynko[1,2], Yurii Shepelytskyi[2,3], Tao Li[3], Ayman Hassan[4,5], Karl Granberg[4], Mitchell S. Albert[2,3,5]

1. Chemistry and Materials Science Program, Lakehead University, Thunder Bay, ON, Canada
2. Thunder Bay Regional Health Research Institute, Thunder Bay, ON, Canada
3. Chemistry Department, Lakehead University, Thunder Bay, ON, Canada
4. Thunder Bay Regional Health Sciences Centre, Thunder Bay, ON, Canada
5. Northern Ontario School of Medicine, Thunder Bay, ON, Canada

Correspondence: M.S.A., Thunder Bay Regional Health Research Institute, 980 Oliver Road, Thunder Bay, Ontario P7B 6V4, Canada. E-mail: malbert1@lakeheadu.ca

Funding information: Ontario Research Foundation, Grant/Award Number: ORF RE 09 029; Northern Ontario Academic Medicine Association, Grant/Award Number: A--18--05; MITACS Elevate, Grant/Award Number: IT25574

Abstract

Purpose: To demonstrate the possibility of performing multi-slice *in-vivo* human brain magnetic resonance imaging (MRI) using hyperpolarized (HP) xenon-129 (^{129}Xe) in two different orientations and to calculate the signal-to-noise ratio (SNR).

Methods: Two healthy female participants were imaged during a single breath-hold of HP ^{129}Xe using a Philips Achieva 3.0T MRI scanner (Philips, Andover, MA). Each HP ^{129}Xe multi-slice brain image was acquired during separate HP ^{129}Xe breathholds using 3D gradient echo (GRE) imaging. The acquisition started 10 s after the inhalation of 1 L of HP ^{129}Xe. Overall, four sagittal and three axial images were acquired with five slices each (seven imaging sessions per participant). The SNR was calculated for each slice in both orientations.

Results: The first ever HP ^{129}Xe multi-slice images of the brain were acquired in axial and sagittal orientations. The HP ^{129}Xe signal distribution correlated well with the grey matter distribution. The highest SNR values were close in the axial and sagittal orientations (19.46±3.25 and 18.76±4.94 respectively). Additionally, anatomical features, such as the ventricles, were observed in both orientations.

Conclusion: The possibility of using multi-slice HP ^{129}Xe human brain magnetic resonance imaging was demonstrated for the first time. HP ^{129}Xe multi-slice MRI can be implemented for brain imaging to improve current diagnostic methods.

4-1. Introduction

Since the introduction of HP ^{129}Xe as an MRI imaging agent in 1994[1], the scope of its applications has grown tremendously. The imaging of various lung diseases such as asthma[2–4], chronic obstructive pulmonary disease (COPD)[4–6], idiopathic pulmonary fibrosis (IPF)[7,8], and

cystic fibrosis (CF)[9–12] has been investigated. HP ^{129}Xe MRI has been clinically approved in the United Kingdom[13] and has a promising role in the clinic. HP ^{129}Xe is not restricted to only the gas phase as it undergoes gas exchange in the lungs[14–16] and easily dissolves in the pulmonary blood[17–19]. Upon inhalation, the gas is distributed throughout human body via the blood flow and dissolves in highly perfused organs such as the kidneys[20,21] and brain[18,22-34].

Early imaging of the brain using HP ^{129}Xe was performed in animals using 2D Chemical shift imaging (CSI)[26–28] followed by axial rat brain imaging[29]. The first 3D multi-slice rat brain HP ^{129}Xe imaging was performed in 2011[30]. This achievement suggests the possibility of transitioning 3D HP ^{129}Xe imaging into human studies.

During the relatively short period of time from the first human brain imaging until present, advances in the application of HP ^{129}Xe have revealed its potential as a functional imaging modality for visualizing cerebral perfusion[22,25], hemodynamic response detection[22], stroke diagnosis[18] and detection of Alzheimer's disease[31]. Despite active progress in the field of HP ^{129}Xe human brain imaging, the studies to date were limited to only single slice imaging. This fact has limited the application of HP ^{129}Xe brain imaging due to the inaccurate anatomical localization of the HP ^{129}Xe signal in the brain. The necessity of acquiring a thick single slice images for HP ^{129}Xe brain imaging is due to the low concentration of HP ^{129}Xe dissolved in the brain tissues (~μM)[34], which results in a weak signal intensity. The further development of effective imaging pulse sequences can further improve the quality of HP ^{129}Xe human brain imaging. Utilization of 3D GRE pulse sequences allow fast and robust acquisition and better use of the hyperpolarization in the brain as the time required for conducting the full scan is much smaller than the T_1 relaxation times of the HP ^{129}Xe in the brain tissues[34]. Excitation of a thick slab and data readout into one 3D k-space, leads to the acquisition of isotropic voxels[32,33] and decreases motion and blood flow

artifacts[35]. In addition, isotropic 3D k-space acquisition eliminates potential cross-talk artifacts which are characteristic of 2D multi-slice acquisitions[36].

In this work, we have demonstrated for the first time, multi-slice HP ^{129}Xe 3D GRE imaging of the human brain. Five slices were acquired in the axial and sagittal orientations. Using a multi-slice 3D GRE imaging pulse sequence is an important step for the evolution of the development of HP ^{129}Xe brain imaging as it allows a relatively accurate spatial localization of the HP ^{129}Xe signals.

4-2. Methods

1. General information

This research study was approved by the research ethics boards (REB) at Lakehead University and the Thunder Bay Regional Health Sciences Centre (TBRHSC; REB file number RP-307), and conducted in accordance with the Tri-Council Policy Statement-2 (TCPS-2). Two healthy female volunteer participants (25 and 29 years) were recruited from the community and signed an informed consent form. All participants were cognitively normal and consented to the dissemination of data obtained from them in this report. A clinical Philips Achieva 3T MRI scanner (Philips, Andover, MA) was equipped with a dual-tuned ^{1}H/^{129}Xe quadrature head coil (Clinical MR Solution, LLC, Brookfield, WI, USA).

2. ^{1}H MRI imaging

Participants were placed into a dual-tuned ^{1}H/^{129}Xe head coil. A ^{1}H GRE imaging localizer scan was acquired first using the following parameters: FOV = 250×250 mm^2; TR/TE = 11 ms/4.6 ms; acquisition matrix = 256×128; BW = 142 Hz/pixel; slice thickness = 10 mm; gap = 5 mm; number of slices = 15 (5 axial, 5 coronal, and 5 sagittal), NSA = 1, flip angle (FA) = 15º. Following the localizer scan, high-resolution ^{1}H T_2-weighted (T_2W) anatomical scans were acquired using a

fast spin echo (FSE) imaging pulse sequence with the following parameters: FOV = 250×250 mm^2; TR/TE = 3s/80ms; acquisition matrix = 256×256; BW = 298 Hz/pixel; slice thickness = 20 mm; number of slices = 5; gap =0; NSA =1; FA = 90º.

The high-resolution T_2W proton images were acquired in the sagittal and axial orientations. Sagittal slices were aligned in such a way that the centre of the middle slice matched the midbrain line in the axial view (Figure 4-1a). In order to align the high-resolution axial scans, the border between the second and third slices was aligned with the line between the anterior and posterior commissures on the mid-sagittal slice (Figure 4-1b).

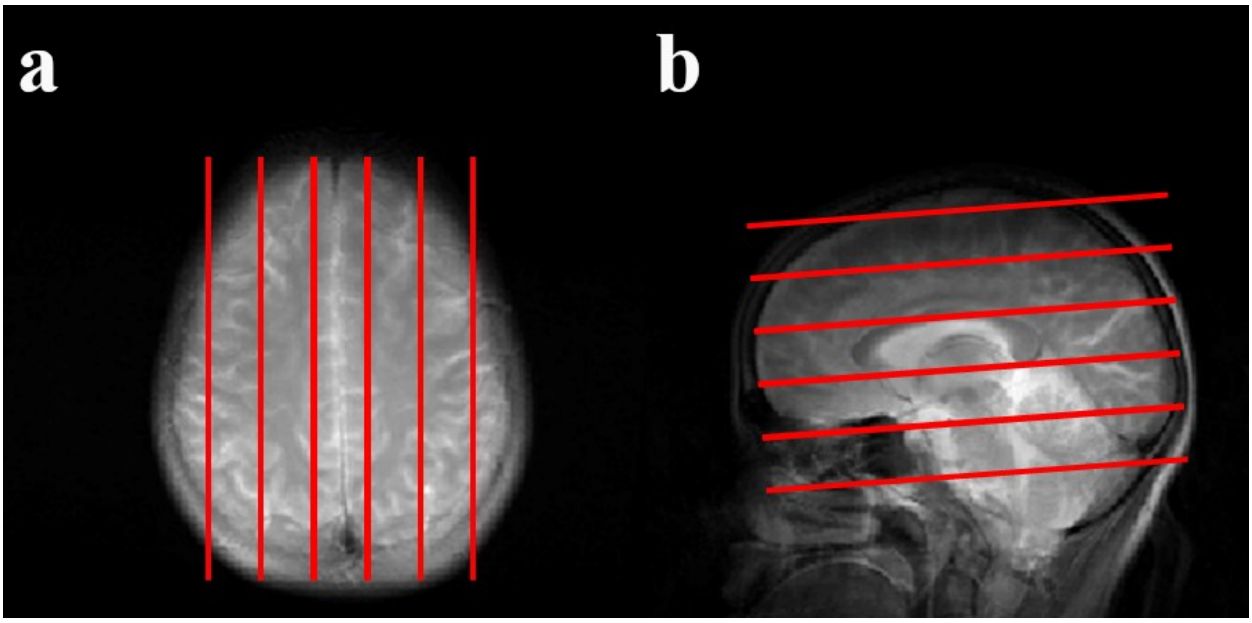

Figure 4-1 Slice orientation for high-resolution T_2W proton and 3D HP ^{129}Xe images in (a) sagittal and (b) axial views.

3. HP ^{129}Xe MRI imaging

A commercial polarizer (Xemed LLC, NH, USA) was used to polarize enriched (83%) ^{129}Xe gas up to a ~50% polarization level. HP ^{129}Xe was dispensed into four 1 L Tedlar bags. Following anatomical localization, the participants inhaled 1 L of HP ^{129}Xe gas and held their breath for a period of 20 s. HP ^{129}Xe 3D multi-slice (GRE) MRI with a Cartesian readout was

performed in both the axial and sagittal orientations: FOV = 250×250 mm^2; TR /TE = 6.2 ms/1.45 ms, FA = 12.5°, BW = 150 Hz/pixel, acquisition matrix = 32×32, slice thickness = 20 mm, number of slices = 5. The acquisition duration was optimal for the chosen bandwidth and matrix size because the T_2* of grey matter is 8.8 ms[37]. In addition, a Cartesian method was used for readout with centric k-space ordering. Overall, 6 phase encodes were performed in the slice selection direction. The total scan time was 0.88 s. The acquisition started 10 s after the breath-hold initialization. The HP ^{129}Xe images have the same orientation as the high-resolution ^{1}H T_2W images. During each scan session, we acquired four axial and three sagittal HP ^{129}Xe 3D multi-slice images; one acquisition was performed per one breath hold. Overall, each participant inhaled seven 1L batches of HP ^{129}Xe.

4. Image reconstruction and data analysis

All MRI images were reconstructed and analyzed using custom MATLAB scripts using MATLAB R2016b (MathWorks, Inc, Natick, MA). No zero padding was performed. The image signal-to noise ratio (SNR) was calculated for each slice as the ratio of the mean signal value in a rectangular region of interest (ROI) (marked as green rectangles on Figure 2 and Figure 3) in a posterior region of the brain, divided by the standard deviation of noise in a similar ROI located in the background. The mean SNR was calculated as the average value for eight images in the axial orientation and for six images in the sagittal view. The standard deviation (STD) of the SNR was calculated and taken into account as SNR uncertainty. Segmentation of the high-resolution ^{1}H T_2W image was performed using the SPM12 software according to the procedure previously described [38] using MATLAB R2018b (The Mathworks, Inc, Natick, MA). HP ^{129}Xe images were thresholded with the level of 40 for slices #1-4 and threshold of 15 for slice #5. Thresholded HP ^{129}Xe images were overlayed on top of 1H T_2W anatomical images.

4-3. Results

The oxygen saturation (SpO_2) level of the participants did not fall below 97% during the experiments. The second participant reported mild light-headedness and mild finger numbness after each xenon breath-hold, which was reversed within a few seconds of free breathing. No additional adverse effects were observed.

Five axial slices for HP ^{129}Xe dissolved in the human brain are shown in Figure 4-2E. For comparison of the anatomical structures in each slice, T_2W ^{1}H anatomical images of the slices corresponding to the HP ^{129}Xe slices are shown in Figure 4-2A. Segmented from T_2W ^{1}H anatomical gray matter image, white matter and SCF images are shown in Figures 4-2B, 4-2C, and 4-2D respectively. Figure 4-2F shows HP ^{129}Xe images superimposed on top of ^{1}H anatomical T_2W images. The mean SNR value of the HP ^{129}Xe images increased in the second slice: from 17.18 ± 3.85 in the first slice to 18.76 ± 4.95 in the second slice; this was the highest SNR value observed in the axial orientation. The SNR values, however, gradually diminished over the remaining slices. The SNR values for the third, fourth and fifth slices were 14.16 ± 3.64, 8.63 ± 2.17 and 3.21 ± 0.53, respectively.

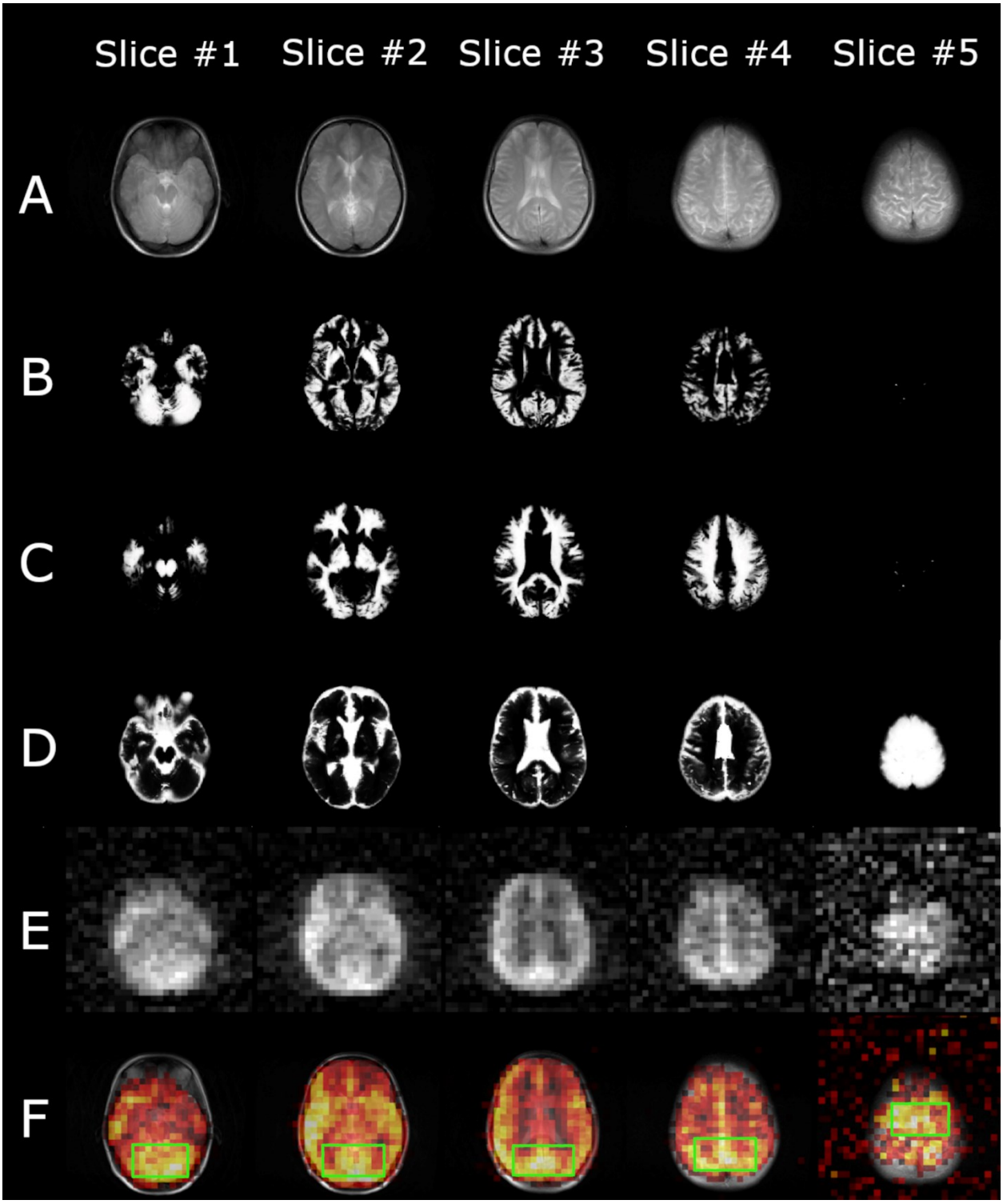

Figure 4-2 1H T2W anatomical axial turbo spin-echo (TSE) images of a representative healthy volunteer, (B-D) Axial anatomical images of grey matter (B), white matter (C), and cerebrospinal fluid (CSF) (D) segmented using high-resolution TSE 1H T2W images of a representative healthy volunteer. (E) 3D GRE HP 129Xe axial brain slices acquired 10 s into the breath-hold. (F) Thresholded HP 129Xe axial

brain slice images superimposed on top of the corresponding 1H anatomical images from row (A). It can be seen, that the HP 129Xe signal corresponds well to the grey matter distribution in the brain. In addition, a partial correlation has been observed between the white matter images and the HP 129Xe images. Green rectangles illustrate the ROIs used for SNR calculations

Figure 4-3B illustrates HP ^{129}Xe MR images from five sagittal slices. The highest SNR values were observed from the three middle slices and were approximately the same: 19.47 ± 3.25, 19.28 ± 3.32 and 19.28 ± 4.02 in the second, third and fourth slices respectively. It should be noted that the SNR values decayed symmetrically in both hemispheres towards the sides of the brain. The first and fifth edge slices also had similar SNR values of 14.08 ± 2.76 and 16.03 ± 3.32, respectively. T_2W ^{1}H anatomical images of the same slices are shown in Figure 4-3A. Figure 4-3C shows HP ^{129}Xe MR images overlaid onto the proton images. ^{129}Xe signal hypointensity was observed from the brain ventricles.

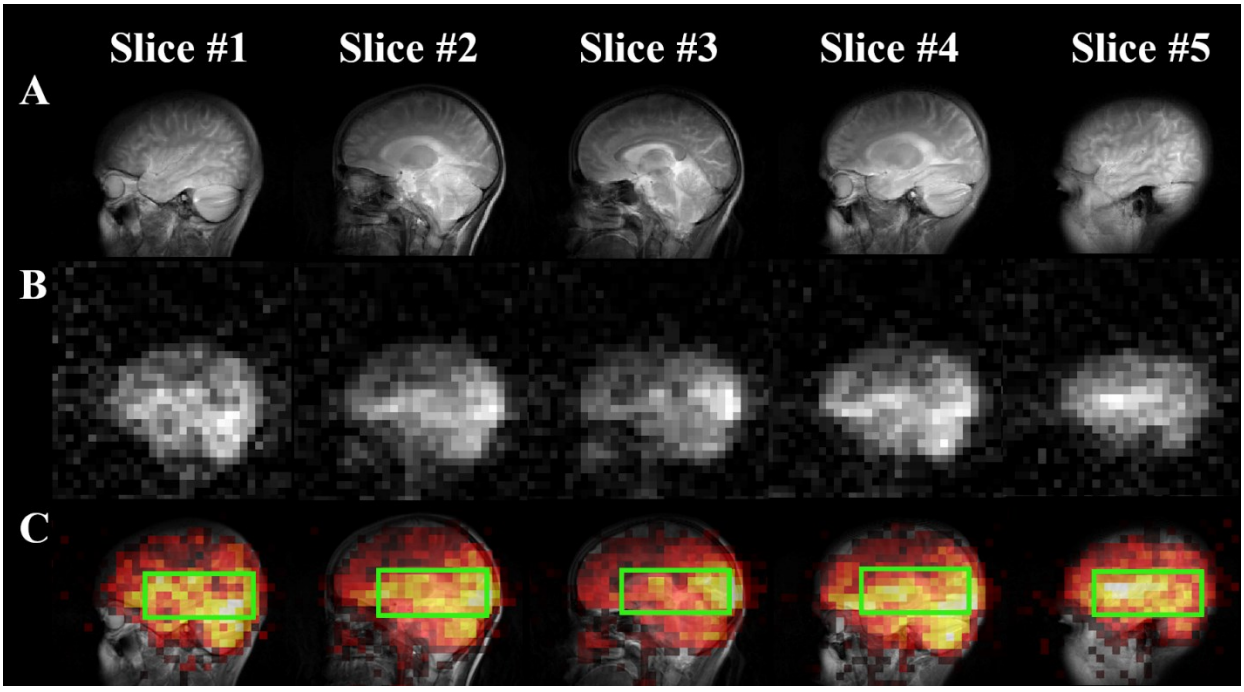

Figure 4-3 1H T2W anatomical sagittal TSE images of a representative healthy volunteer. (B) HP 129Xe sagittal brain slice images of a representative healthy volunteer acquired using 3D GRE imaging 10

s into the breath-hold. (C)Thresholded HP 129Xe sagittal brain slice images superimposed on top of the corresponding 1H anatomical images. Green rectangles illustrate the ROIs used for SNR calculations.

The mean SNR and STD values calculated for each slice in the axial and sagittal orientations are shown in Figure 4-4. The SNR values of the second slice in the axial view (18.76 ± 4.95) and the middle slices in sagittal view (19.47 ± 3.25, 19.28 ± 3.32 and 19.28 ± 4.02) were relatively similar. The SNR dependence on slice number for the sagittal scans was relatively symmetrical. The SNR values of the axial slices decreased towards the top of the brain.

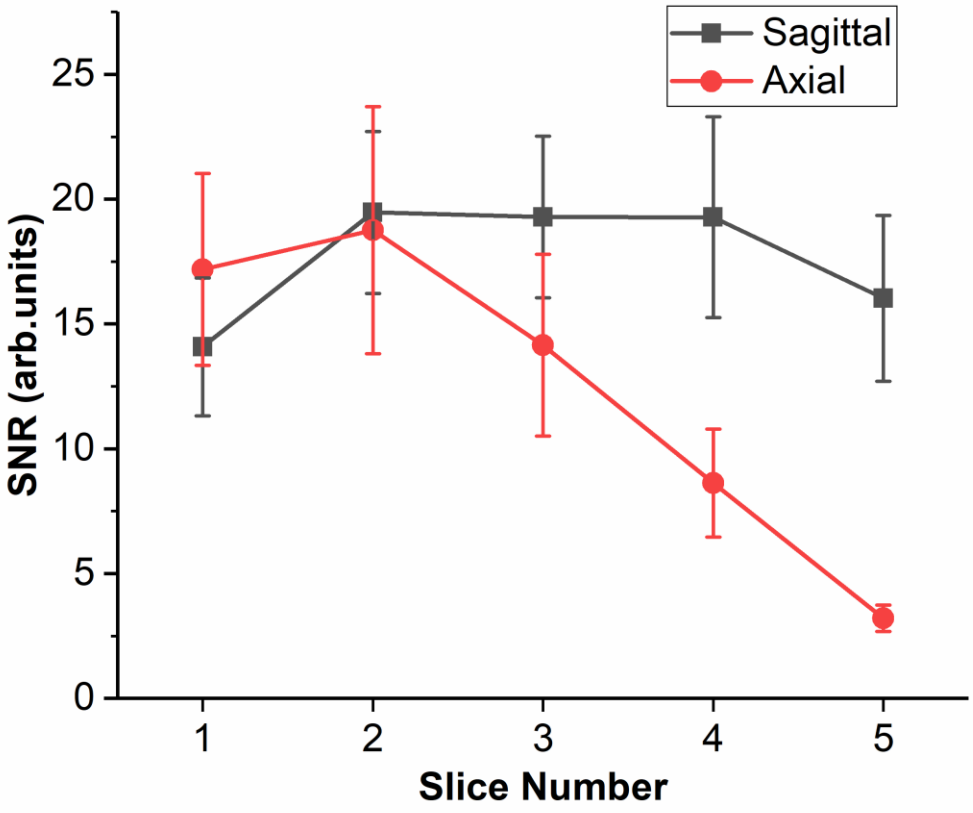

Figure 4-4 Calculated mean SNR values with standard deviation in the axial and sagittal orientations for each slice.

4-4. Discussion

Even though HP ^{129}Xe MRI of the human brain is a relatively new imaging modality, its potential has been previously demonstrated for the detection of perfusion related diseases such as stroke[18] and Alzheimer's disease[31]. Additionally, its use has been proposed for functional brain mapping and detection of a hemodynamic response[22]. Previous HP ^{129}Xe human brain images were acquired as a single 50 mm slice with a voxel volume of 2.36 cm^3, [18,25] and in the present work we demonstrate the first acquisition of multi-slice HP ^{129}Xe images of the human brain with voxel volume of 1.22cm^3. In addition, two 25 mm thick slices acquired using 2D GRE were presented by Rao et al. at the Annual meeting of the International Society for Magnetic Resonance in Medicine in 2019.

The main problem associated with HP ^{129}Xe brain imaging is the low concentration of HP ^{129}Xe in the brain tissue. To transfer this technique from single slice to multi-slice imaging, a high enough HP ^{129}Xe signal level has to be attained. Therefore, the future of HP ^{129}Xe dissolved phase imaging consists of increasing the signal intensity. There are several different approaches for boosting the SNR. The first is to increase the polarization of HP ^{129}Xe, and the second to the use of more highly enriched gas. The polarization level achieved in this study was ~50% and is currently the highest achievable among commercially available polarizers. The enrichment level of the ^{129}Xe gas utilized was 83%. To maximize the image SNR further, we employed a 3D GRE pulse sequence instead of a 2D sequence. According to the basic principles of MRI[32], the SNR increases as the square root of the number of phase encodes[39] and, therefore, performing phase encoding in the third dimension provides an additional SNR boost that can be used for multi-slice image acquisition. Finally, the center lines of k-space were acquired first, followed by the outer

lines of k-space. This approach allows for an additional SNR increase since the low spatial frequencies in k-space are responsible for the overall image signal level.

On the contrary, increasing of the number of slices can potentially cause some additional T_1-associated signal loss issues. The total scan time of one HP ^{129}Xe 3D multi-slice GRE was equal to 0.88 s. The net scan time was short enough to neglect the potential SNR differences between the acquired slices caused by any T_1 relaxation of HP ^{129}Xe. However, if the scan time is sufficiently long, an SNR decrease with slice number may be observed. This issue can be resolved at the image reconstruction stage by correcting the k-space lines with respect to HP ^{129}Xe T_1 relaxation. On the other hand, the short TR makes destruction of ^{129}Xe hyperpolarization due to RF excitation pulses dominant. Although the inflow of fresh HP ^{129}Xe into the imaged region with utilization of longer TR may boost the SNR, the increase of TR should be carefully considered, taking into account the T_1 of the HP ^{129}Xe in the alveoli (*ca.* 16 sec)[43] and blood (*ca*. 6.4 sec)[43], so that the gains from increasing TR are not negated by the losses due to spin-lattice relaxation. Additionally, a sufficiently long TR would not permit the acquisition of a larger number of slices within a tolerable breathhold period.

Five slices of HP ^{129}Xe in the human brain were acquired in the axial and sagittal orientations. Some anatomical features such as the ventricles can be clearly observed on the middle slices in both orientations (slices 2, 3 and 4 in Figure 4-2E and 4-3C). A high local correlation between the gray matter tissue distribution segmented from T_2W ^{1}H brain images and HP ^{129}Xe signal intensity was clearly observed on the first four slices (Figures 4-2B and 4-2E slices #1-4). In addition, there was a moderate correlation between the white matter and HP ^{129}Xe signal observed (Figures 4-2C and 4-2E). This can be explained by a higher perfusion of the grey matter compared to the white matter (68±10 ml·min^{-1}·(100 ml tissue)$^{-1}$ and 25±5 ml·min^{-1}·(100 ml tissue)$^{-}$

[1] respectively)[40]. Albeit solubility of Xe in grey matter is lower (HP ^{129}Xe Ostwald solubility coefficients are 0.135 for gray matter and 0.224 for white matter)[34,41]. A weak local correlation was observed between the CSF distribution and the HP ^{129}Xe signal on the first four slices; the signal origin on the fifth slice is inconclusive due to a relatively weak HP ^{129}Xe signal. Overall, it can be concluded that a much higher HP ^{129}Xe signal originated from the grey matter compared to the HP ^{129}Xe in the white matter.

The second slice in the axial orientation had the highest SNR value out of all image slices (Figure 4-4, axial); the observed SNR gradually decreased in the top brain slices. Similar to the axial slices, the sagittal slices had similar SNR changes where the highest value was observed in the three centre slices and is close to the values of the adjacent slices (Figure 4-4, sagittal). It should be noted that the maximum SNR values were similar for the axial and sagittal views.

In this study, we acquired the first multi-slice HP ^{129}Xe human brain imaging using a 3D GRE pulse sequence with a Cartesian readout. This achievement is beneficial for all currently developed methodologies using HP ^{129}Xe, including cerebral perfusion imaging, functional brain imaging with HP ^{129}Xe MRI, and disease detection such as Alzheimer's disease and stroke. Hopefully, this research will open the door to a new era for 3D multi-slice HP ^{129}Xe brain imaging. The ability to produce multiple slices will allow the accurate and precise anatomical localization of HP ^{129}Xe in brain images. Further, accurate spatial localization will be extremely beneficial for HP ^{129}Xe hemodynamic response detection and quantitative cerebral perfusion measurements.

Acknowledgments

This research was funded by the Ontario Research Fund (ORF RE 09 029) and the Northern Ontario Academic Medical Association (A-18-05). The authors would like to thank Lakehead University and the Thunder Bay Regional Health Research Institute for partial support of this work

and access to their facilities. Yurii Shepelytskyi was partially supported by an Ontario Graduate Fellowship. Vira Grynko is supported by an Ontario Trillium Scholarship. The authors would like to thank the numerous administrative and technical staff that assisted in conducting these experiments, including Martina Agostino, Kendra Rhys, Sue Wright, Lori-Ann Moon, Kim Bunt Raynak, Jordan Zanatta, and Shawna Mamos. This project would not have been possible without the diligent assistance of these individuals. The authors also would like to thank Martina Agostino for contributing to manuscript editing.

References

1. Albert MS, Cates GD, Driehuys B, et al. Biological magnetic resonance imaging using laser-polarized 129Xe. *Nature*. 1994;370(6486):199-201. doi:10.1038/370199a0
2. Ebner L, He M, Virgincar RS, et al. Hyperpolarized 129 Xenon MRI to Quantify Regional Ventilation Differences in Mild to Moderate Asthma: A Prospective Comparison between Semi-Automated Ventilation Defect Percentage Calculation and Pulmonary Function Tests HHS Public Access. *Invest Radiol*. 2017;52(2):120-127. doi:10.1097/RLI.0000000000000322
3. Safavi S, Zanette B, Munidasa S, et al. Correlation of Hyperpolarised Xenon-129 Magnetic Resonance Imaging (129Xe-MRI) of the Lung with Multi-Breath Washout (MBW) in Children with Severe Asthma. *Eur Respir J*. 2020;56(64):4339. doi:10.1183/13993003.congress-2020.4339
4. Qing K, Mugler JP, Altes TA, et al. Assessment of lung function in asthma and COPD using hyperpolarized 129Xe chemical shift saturation recovery spectroscopy and dissolved-phase MRI. *NMR Biomed*. 2014;27(12):1490-1501. doi:10.1002/nbm.3179

5. Driehuys B, Martinez-Jimenez S, Cleveland ZI, et al. Chronic Obstructive Pulmonary Disease: Safety and Tolerability of Hyperpolarized 129 Xe MR Imaging in Healthy Volunteers and Patients 1. *Radiology*. 262. doi:10.1148/radiol.11102172/-/DC1

6. Doganay O, Matin T, Chen M, et al. Time-series hyperpolarized xenon-129 MRI of lobar lung ventilation of COPD in comparison to V/Q-SPECT/CT and CT. *Eur Radiol*. 2019;29(8):4058-4067. doi:10.1007/s00330-018-5888-y

7. Mammarappallil JG, Rankine L, Chan H-F, Weatherley N, Wild J, Driehuys B. New developments in imaging Idiopathic Pulmonary Fibrosis with hyperpolarized Xenon MRI. *J Thorac Imaging*. 2019;34(2):136-150. doi:10.1097/RTI.0000000000000392

8. Wang JM, Robertson SH, Wang Z, et al. Using hyperpolarized 129Xe MRI to quantify regional gas transfer in idiopathic pulmonary fibrosis. *Thorax*. 2018;73(1):21-28. doi:10.1136/thoraxjnl-2017-210070

9. Santyr G, Kanhere N, Morgado F, Rayment JH, Ratjen F, Couch MJ. Hyperpolarized Gas Magnetic Resonance Imaging of Pediatric Cystic Fibrosis Lung Disease. *Acad Radiol*. 2019;26(3):344-354. doi:10.1016/j.acra.2018.04.024

10. Couch MJ, Munidasa S, Rayment JH, et al. Comparison of Functional Free-Breathing Pulmonary 1H and Hyperpolarized 129Xe Magnetic Resonance Imaging in Pediatric Cystic Fibrosis. *Acad Radiol*. 2020:1-10. doi:10.1016/j.acra.2020.05.008

11. McCallister A, Chung SH, Antonacci M, et al. Comparison of single breath hyperpolarized ^{129} Xe MRI with dynamic ^{19} F MRI in cystic fibrosis lung disease. *Magn Reson Med*. 2021;85(2):1028-1038. doi:10.1002/mrm.28457

12. Thomen RP, Walkup LL, Roach DJ, Cleveland ZI, Clancy JP, Woods JC. Hyperpolarized 129 Xe for investigation of mild cystic fibrosis lung disease in pediatric patients. *J Cyst Fibros*. 2017;16:275-282. doi:10.1016/j.jcf.2016.07.008

13. Hyperpolarized Gas Lung Imaging. *GE Signapulse*. 2019. https://www.gesignapulse.com/signapulse/spring_2019/MobilePagedArticle.action?articleId=1488828#articleId1488828.

14. Chang Y V. MOXE: A model of gas exchange for hyperpolarized 129Xe magnetic resonance of the lung. *Magn Reson Med*. 2013;69(3):884-890. doi:10.1002/mrm.24304

15. Chang Y V., Quirk JD, Ruset IC, Atkinson JJ, Hersman FW, Woods JC. Quantification of human lung structure and physiology using hyperpolarized 129Xe. *Magn Reson Med*. 2014;71(1):339-344. doi:10.1002/mrm.24992

16. Driehuys B, Cofer GP, Pollaro J, Mackel JB, Hedlund LW, Johnson GA. Imaging alveolar-capillary gas transfer using hyperpolarized 129Xe MRI. *Proc Natl Acad Sci*. 2006;103(48):18278-18283. doi: 10.1073/pnas.0608458103.

17. Kruger SJ, Nagle SK, Couch MJ, Ohno Y, Albert M, Fain SB. Functional imaging of the lungs with gas agents. *J Magn Reson Imaging*. 2016;43(2):295-315. doi:10.1002/jmri.25002

18. Rao MR, Norquay G, Stewart NJ, Hoggard N, Griffiths PD, Wild JM. Assessment of brain perfusion using hyperpolarized 129Xe MRI in a subject with established stroke. *J Magn Reson Imaging*. 2019;50(3):1002-1004. doi:10.1002/jmri.26686

19. Stewart NJ, Horn FC, Norquay G, et al. Reproducibility of quantitative indices of lung function and microstructure from 129Xe chemical shift saturation recovery (CSSR) MR spectroscopy. *Magn Reson Med*. 2017;77(6):2107-2113. doi: 10.1002/mrm.26310.

20. Ruppert K. Biomedical imaging with hyperpolarized noble gases. *Reports Prog Phys*. 2014;77(11):116701. doi:10.1088/0034-4885/77/11/116701

21. Loza LA, Kadlecek SJ, Pourfathi M, et al. Quantification of Ventilation and Gas Uptake in Free-Breathing Mice With Hyperpolarized 129Xe MRI. *IEEE Trans Med Imaging*. 2019;38(9):2081-2091. doi:10.1109/TMI.2019.2911293

22. Shepelytskyi Y, Hane FT, Grynko V, Li T, Hassan A, Albert MS. Hyperpolarized 129Xe Time-of-Flight MR Imaging of Perfusion and Brain Function. *Diagnostics*. 2020;10(9):630. doi:10.3390/diagnostics10090630

23. Albert MS, Balamore D. Development of hyperpolarized noble gas MRI. *Nucl Instruments Methods Phys Res Sect A Accel Spectrometers, Detect Assoc Equip*. 1998;402(2-3):441-453. doi:10.1016/S0168-9002(97)00888-7

24. Rao MR, Norquay G, Stewart NJ, Wild JM. Measuring 129Xe transfer across the blood-brain barrier using MR spectroscopy. *Magn Reson Med*. 2021;(00):1-11. doi:10.1002/mrm.28646

25. Rao MR, Stewart NJ, Griffiths PD, Norquay G, Wild JM. Imaging human brain perfusion with inhaled hyperpolarized 129Xe MR imaging. *Radiology*. 2018;286(2):659-665. doi:10.1148/radiol.2017162881

26. Swanson SD, Rosen MS, Agranoff BW, Coulter KP, Welsh RC, Chupp TE. Brain MRI with Laser-Polarized 129Xe. *Magn Reson Med*. 1997;38(5):695-698. doi:10.1002/mrm.1910380503

27. Swanson SD, Rosen MS, Coulter KP, Welsh RC, Chupp TE. Distribution and dynamics of laser-polarized129Xe magnetization in vivo. *Magn Reson Med*. 1999;42(6):1137-1145. doi:10.1002/(SICI)1522-2594(199912)42:6<1137::AID-MRM19>3.0.CO;2-4

28. Duhamel G, Choquet P, Leviel J-L, et al. In vivo 129 Xe NMR in rat brain during intra-arterial injection of hyperpolarized 129 Xe dissolved in a lipid emulsion. *Comptes Rendus l'Académie des Sci - Ser III - Sci la Vie*. 2000;323(6):529-536. doi: 10.1016/s0764-4469(00)00147-5.

29. Duhamel G, Choquet P, Grillon E, et al. Xenon-129 MR Imaging and Spectroscopy of Rat Brain Using Arterial Delivery of Hyperpolarized Xenon in a Lipid Emulsion. *Magn Reson Med*. 2001;46(2):208-212. doi: 10.1002/mrm.1180.

30. Nouls J, Cleveland Z, Freeman M, Moeller H, Hedlund L, Driehuys B. 3D MRI of the Hyperpolarized 129 Xe Distribution in the Rat Brain. *Int Soc Magn Reson Med Annu Meet*. 2011;695(1997):879. doi: 10.1371/journal.pone.0021607.

31. Hane F, Li T, Plata J-A, Hassan A, Granberg K, Albert M. Inhaled Xenon Washout as a Biomarker of Alzheimer's Disease. *Diagnostics*. 2018;8(2):41. doi:10.3390/diagnostics8020041

32. Wild JM, Woodhouse N, Paley MNJ, et al. Comparison between 2D and 3D gradient-echo sequences for MRI of human lung ventilation with hyperpolarized 3He. *Magn Reson Med*. 2004;52(3):673-678. doi:10.1002/mrm.20164

33. He M, Robertson SH, Sivaram Kaushik S, et al. Original contributions Dose and pulse sequence considerations for hyperpolarized 129 Xe ventilation MRI ☆. *Magn Reson Imaging*. 2015;33:877-885. doi:10.1016/j.mri.2015.04.005

34. Kilian W, Seifert F, Rinneberg H. Dynamic NMR Spectroscopy of Hyperpolarized 129Xe in Human Brain Analyzed by an Uptake Model. *Magn Reson Med*. 2004;51(4):843-847. doi:10.1002/mrm.10726

35. Ozturk A, Aygun N, Smith SA, Caffo B, Calabresi PA, Reich DS. Axial 3D gradient-echo imaging for improved multiple sclerosis lesion detection in the cervical spinal cord at 3T. *Neuroradiology*. 2013;55(4):431-439. doi:10.1007/s00234-012-1118-5

36. Zhuo J, Gullapalli RP. MR Artifacts, Safety, and Quality Control. *RadioGraphics*. 2006;26(1):275-297. doi:10.1148/rg.261055134

37. Rao M, Stewart NJ, Norquay G, Griffiths PD, Wild JM. High resolution spectroscopy and chemical shift imaging of hyperpolarized 129Xe dissolved in the human brain in vivo at 1.5 tesla. *Magn Reson Med*. 2016;75(6):2227-2234. doi:10.1002/mrm.26241

38. Wellcome Trust Centre for Neuroimaging. *SPM (Statistical Parametric Mapping)*.; 2014.

39. Runge VM, Wood ML, Kaufman DM, Traill MR, Nelson KL. The straight and narrow path to good head and spine MRI. *Radiographics*. 1988;8(3):507-531. doi:10.1148/radiographics.8.3.3380992

40. Parkes LM, Rashid W, Chard DT, Tofts PS. Normal Cerebral Perfusion Measurements Using Arterial Spin Labeling: Reproducibility, Stability, and Age and Gender Effects. *Magn Reson Med*. 2004;51(4):736-743. doi:10.1002/mrm.20023

41. Lavini C, Payne GS, Leach MO, Bifone A. Intravenous delivery of hyperpolarized 129Xe: A compartmental model. *NMR Biomed*. 2000;13(4):238-244. doi:10.1002/1099-1492(200006)13:4<238::AID-NBM633>3.0.CO;2-5

Chapter 5: Optimization of Hyperpolarized Chemical Exchange Saturation Transfer Performance

This topic has been elaborated in the following publication: **Grynko, V**.; Shepelytskyi, Y.; Batarchuk, V., Aalto, H.; Li, T., Ruset, I.C.; DeBoef, B., Albert, M.S. "Cucurbit[6]uril Hyperpolarized Chemical Exchange Saturation Transfer Pulse Sequence Parameter Optimization and Detectability Limit Assessment at 3.0T" published in *ChemPhysChem,* article number e202300346 (2023). The publication text is listed below.

Cucurbit[6]uril Hyperpolarized Chemical Exchange Saturation Transfer Pulse Sequence Parameter Optimization and Detectability Limit Assessment at 3.0T

Vira Grynko*[a,b], Yurii Shepelytskyi[a,c], Viktoriia Batarchuk[a,c], Hannah Aalto[d], Tao Li[c], Iulian C. Ruset[e], Brenton DeBoef[f], Mitchell S. Albert[a,c,g]

[a] V. Grynko, Dr. Y. Shepelytskyi, Dr. V. Batarchuk, Prof. Dr. M.S. Albert

Thunder Bay Regional Health Research Institute, 1040 Oliver Rd, Thunder Bay, ON P7B 7A5, Canada E-mail: malbert1@lakeheadu.ca

[b] V. Grynko

Chemistry and Materials Science Program, Lakehead University, 955 Oliver Rd, Thunder Bay, ON P7B 5E1, Canada

[c] Dr. Y. Shepelytskyi, Dr. V. Batarchuk, T. Li, Prof. Dr. M.S. Albert

Chemistry Department, Lakehead University, 955 Oliver Rd, Thunder Bay, ON P7B 5E1, Canada

[d] H. Aalto

Applied Life Science Program, Lakehead University, 955 Oliver Rd, Thunder Bay, ON P7B 5E1, Canada

[e] Dr. I.C. Ruset

Xemed LCC, 16 Strafford Ave, Durham, NH 03824, United States

[f] Prof. Dr. B. DeBoef

Chemistry Department, University of Rhode Island, 45 Upper College Rd, Kingston, RI 02881, United States

[g] Prof. Dr. M.S. Albert

Northern Ontario School of Medicine, 955 Oliver Rd, Thunder Bay, ON P7B 5E1, Canada

Abstract:

Molecular imaging is the future of personalized medicine; however, it requires effective contrast agents. Hyperpolarized chemical exchange saturation transfer (HyperCEST) can boost the signal of Hyperpolarized ^{129}Xe MRI and render it a molecular imaging modality of high efficiency. Cucurbit[6]uril (CB6) has been successfully employed in vivo as a contrast agent for HyperCEST MRI, however its performance in a clinical MRI scanner has yet to be optimized.

In this study, MRI pulse sequence parameter optimization was first performed in CB6 solutions in phosphate-buffered saline (PBS), and subsequently in whole sterile citrated bovine blood. The performance of four different depolarization pulse shapes (sinusoidal, 3-lobe sinc (3LS), rectangular (block), and hyperbolic secant (hypsec) was optimized. The detectability limits of CB6 in a clinical 3.0T MRI scanner were assessed using the optimized pulse sequences. The 3LS depolarization pulses performed best and demonstrated 24% depletion in a 25μM solution of CB6 in PBS. It performed similarly in blood. The CB6 detectability limit was found to be 100μM in citrated bovine blood with a correspondent HyperCEST depletion of 30% ± 9%. For the first time, the HP ^{129}Xe HyperCEST effect was observed in red blood cells (RBC) and had a similar strength as HyperCEST in plasma.

5-1. Introduction

Hyperpolarized (HP) xenon-129 (^{129}Xe) magnetic resonance imaging (MRI) is a powerful imaging modality utilized for imaging of the lungs[1–7] and brain[8–14]. Hyperpolarization multiplies the nuclear polarization of ^{129}Xe by a factor of 10^5, substantially increasing its MRI signal[1]. Further amplification of the HP ^{129}Xe signal by several orders of magnitude is possible via utilization of HP chemical exchange saturation transfer (HyperCEST)[15]. The HyperCEST effect relies on constant chemical exchange between the dissolved HP ^{129}Xe in the pool and a supramolecular cage

that can effectively encapsulate HP ^{129}Xe atoms. If a radiofrequency (RF) pulse is applied at the specific resonance frequency of HP ^{129}Xe that corresponds to ^{129}Xe residing withing the macrocycle, the ^{129}Xe atoms become depolarized within the supramolecular agent. Due to chemical exchange, the depolarized atoms enter the liquid pool next, depleting the HP ^{129}Xe signal in it. The HyperCEST effect renders HP ^{129}Xe MRI as a molecular imaging modality that can potentially detect, localize, and characterize lesions within the body without the need for invasive biopsies.

Currently, numerous HyperCEST agents such as cryptophanes[15–17], cucurbit[6]urils[18–21], cyclodextrin-based pseudorotaxanes[22], pillar[5]arenes[23,24], metal-organic capsules[25], and microbubbles[26] have been investigated in vitro. Despite this technique being invented in 2006 [15], it took more than a decade to move from in vitro to in vivo imaging. Currently, cucurbit[6]uril (CB6) is the only HyperCEST agent studied in vivo because of its biocompatibility[27] and commercial availability. The biodistribution of CB6 was first imaged in living rats at 3.0T[21] and, recently, in a living mice at 9.4T [28]. Although McHugh et. al. performed a breathing protocol optimization for in vivo HyperCEST MRI in the most recent work[28], none of the studies previously conducted have optimized HyperCEST MRI and MR spectroscopy (MRS) pulse sequences in order to maximize the performance of the agent. Furthermore, none of the studies have performed a comparison of the performance of different RF pulse shapes during HyperCEST experiments.

In the current study, we conducted a thorough optimization of HyperCEST saturation RF pulses. We investigated four different pulse shapes including a (3-lobe sinc (3LS), sinusoidal, rectangular, and hyperbolic secant (hypsec)), and their performances during HyperCEST MR spectroscopy experiments at 3.0T. In addition, we have measured, for the first time, the detectability limits of CB6 in aqueous solution in a clinical whole body 3.0T MRI scanner.

5-2. Methods

Sample Preparation

Samples in PBS:

A 1mM solution of CB6 was made by dissolving 9.968mg of CB6 hydrate (Sigma-Aldrich, St. Louis, MO, USA) in 10mL of PBS at a pH of 7.4 at room temperature. The mixture was shaken gently until full dissolution of CB6 was achieved. A portion of the original 1mM solution of CB6 was diluted with PBS to create 0.5mM, 0.25mM, 0.1mM, 25μM, and 10μM solutions of CB6 in PBS. Samples of 2.5mL of the various CB6 solutions were drawn into the frit phantom vessel and placed inside a custom-built quadrature dual-tuned $^{1}H/^{129}Xe$ MRI coil within a clinical Philips Achieva 3.0T MRI scanner (Philips, Andover, MA).

Samples in citrated bovine blood:

Citrated sterile bovine blood was purchased from Cedarlane, Burlington, CA, USA. Samples of CB6 (1mM, 0.5mM, 0.25mM, 0.1mM, 50μM, 25μM, and 10μM) were prepared by adding a constant volume (1.33mL) of CB6 in PBS to blood (8.67mL) in order to achieve 10mL samples. The citrated bovine blood was chosen for its stability in the liquid state since citrate acts as anticoagulant and prevents blood clotting[29]. The concentrations of CB6 in PBS stock solutions were 7.5mM, 3.75mM, 1.875mM, 0.750mM, 0.347mM, 0.188mM, 0.075mM, which maintained a constant dilution of the blood. Samples were drawn into the 10mL syringe and pumped through the exchange module into a second 10mL syringe which was placed into the RF coil.

^{129}Xe Magnetic Resonance Spectroscopy

Samples in PBS:

Naturally abundant ^{129}Xe gas (~ 26% of the ^{129}Xe isotope) was polarized up to 56% via spin-exchange optical pumping (SEOP) using a XeBox-10E commercial polarizer (Xemed LLC,

Durham, NH, USA). A 1L volume of HP ^{129}Xe was dispensed into a TedLar bag which was immediately transferred into a pressurized chamber withing the bore of the MRI scanner. The pressure within the chamber was maintained between 20-45kPa above atmospheric pressure using a pressure sensitive ventilation device connected to a nitrogen (N_2) source to facilitate the flow of HP ^{129}Xe gas from Tedlar bag. The pressure chamber was connected to the glass-fritted cell containing the CB6 solution to create a constant HP ^{129}Xe flow through the sample. While passing through the fritted disc, the HP ^{129}Xe produced microbubbles which aided in its dissolution into the solution.

As HP ^{129}Xe gas continually flowed through the sample, ^{129}Xe MRS data was simultaneously obtained. The MRI scanner software was configured to allow automated dynamic measurements of HyperCEST depletion spectra. To depolarize HP ^{129}Xe encapsulated within the CB6 macrocycles, an RF pulse train was applied with a net duration of 480ms, ensuring the same depolarization time for each HyperCEST experiment. Four different depolarization pulse shapes were investigated: 3LS, block, sinusoidal, and hypsec. In the cases of the 3LS, block, and sinusoidal RF depolarization pulses, the depolarization train contained 16x30ms subsequent RF pulses. The duration of 30ms resulted in 106.0Hz (3ppm at 3T), 4.6Hz (0.13ppm at 3T), and 3.9Hz (0.11ppm at 3T) spectral bandwidths (BW) for the 3LS pulses, block pulses, and sinusoidal pulses, respectively. The hypsec RF pulse train consisted of 12x40ms pulses, resulting in a 388.6Hz (11ppm at 3T) depolarization BW. The BW of the studied pulses was obtained from Philips Sequence Development Tool on our R5.3 MRI system.

During the HyperCEST experiments, 3LS pulses were applied in a range from -149 to 50ppm with a step of 3ppm. The sinusoidal and block RF depolarization pulses were applied with a step of 2ppm starting at -150ppm. The adiabatic hypsec pulses were applied using a 12ppm step,

starting at -144ppm. Numerous flip angles (FA) of the depolarization pulses were studied: 90°, 180°, 270°, 330°, 400°, 540°, 800°, 990°, 1200°, 1530°, and 1800°. The effect of the FA for the 3LS pulses was evaluated only up to 1200º since higher FAs were not allowed by the scanner software for the given pulse duration, due to governance of the specific absorption rate (SAR).

Dynamic HyperCEST MRS was performed using the following parameters: TR/TE = 10s/0.25ms; receiving BW = 32kHz; 90° excitation block pulse; 2048 sampling data point. One free induction decay (FID) spectrum was acquired per one depolarization pre-pulse train. The spectral resolution in the experiments was equal to 0.44ppm.

Samples in citrated bovine blood:

The experimental set-up used for mixing HP ^{129}Xe with blood was similar to that used by Norquay et al[30]. Mixing was performed using an exchange module (Superphobic MicroModule 0.5×1 G680 Contactor; Membrana, North Carolina, USA). A steady flow of HP ^{129}Xe was sent through the exchange module with the aid of a pressurized chamber that was pressurized with a continuous flow of N_2 gas. The flow rate of N_2 into the pressurized chamber was controlled by a ventilator. A 10mL syringe containing blood was connected to an exchange module and placed into a custom-built dual ^{1}H/^{129}Xe quadrature MRI birdcage coil. The blood was pumped back and forth through the exchange module perpendicular to the ^{129}Xe flow for ~6s.

MRS spectra for the 1mM solution of CB6 in blood were acquired after each “pump” cycle using the same parameters as for CB6 in the PBS solutions. 0ppm was assigned to be at the midpoint between the ^{129}Xe-RBC and ^{129}Xe-plasma resonances. The depolarization pulses had the same parameters, however, the FA used were the maximum for each pulse (1800° for sine, block and hypsec and 1200° for 3LS).

The HyperCEST effect in blood at CB6 concentrations other than 1mM was measured using the following approach. The "off-resonance" spectrum was acquired following the application of the depolarization pulse train at +80ppm. The "on-resonance" FID spectrum was acquired following depolarization pulses applied at -83ppm. The "on-resonance" and "off-resonance" FID spectra were acquired four times for each concentration.

MRS data analysis

All the acquired HP ^{129}Xe spectra were initially analyzed using a custom-built MatLab script in MATLAB 2020b (The Mathworks, Inc, Natick, MA). The acquired spectra for CB6 solutions in blood were averaged (NSA = 4). The intensities of peaks which could not be distinguished from noise, for the samples in bovine blood, were considered to be 0. The signal-to-noise ratio (SNR) of the dissolved ^{129}Xe peak was calculated as the ratio of peak intensity to the standard deviation (SD) of the noise region. The HyperCEST depletion value was calculated as previously described by Fernando et. all[23]. The spectral data were further postprocessed using OriginPro 2021b (OriginLab Corp, USA).

5-3. Results and Discussion

Even though CB6 is one of the most well studied molecular cages for ^{129}Xe HyperCEST[18,19,21,31–35], there were no studies performed to date to maximize its performance as a HyperCEST agent via pulse sequence development. We began the evaluation of four different depolarization pulse trains (3-lobe sinc, sine, block, and hypsec) with CB6 dissolved in PBS and subsequently proceeded to the solutions of CB6 in citrated bovine blood. The overall depolarization pre-pulse train duration was set the same for all the RF pulse shapes investigated and was equal to 480ms (which is the closest value to the maximum duration of 500ms allowed by default on a clinical Philips Achieva 3T scanner). The number of pulses within the

depolarization pulse train was the same for the block, sine and 3LS pulses and was equal to 16. The hypsec pulses had a longer pulse duration of 40ms, which resulted in 12 RF pulses within the depolarization train.

Four representative depletion spectra acquired using the sinusoidal depolarization pre-pulses of 540°, 800°, 900°, and 1200° from the 1mM CB6 solution in PBS illustrate the effect of FA values on the HyperCEST effect in Fig 5-1A. The HyperCEST effect increased with an increase in the depolarization FA up to 95% for a FA of 1200°. The observed HyperCEST effect dynamics can be easily explained by an increase in overall RF power transmitted to the encapsulated HP ^{129}Xe with an increase in pulse FA. Indeed, having the constant pulse duration, the increase of the FA resulted in a linear increase in the maximum RF B_1 field and root mean square (rms) B_1 field as shown in Fig 5-1C and 5-1D respectively. The effect of different shapes of depolarization pulses is illustrated in Fig 5-1B. Fig 5-1B shows the HyperCEST depletion spectra acquired with the sinusoidal, block, hypersecant and 3LS depolarization pulse trains of 1200° FA. The 3LS, block, and sinusoidal pulses demonstrated similar HyperCEST depletion of ~ 95%, whereas hypsec pulses showed a slightly smaller depletion of 91%. This could be explained by a smaller number of hypsec pulses within the depolarization pre-pulse train resulting in a somehow weaker depolarization of CB6-encapsulated HP ^{129}Xe nuclei.

It should be noted that an increase in the transmitted RF power resulted in an increase in off-resonance saturation effects that ultimately caused the lower depletion values in a range between -20ppm and -55ppm (Fig 5-1A, 5-1B). Despite this, both dissolved phase HP ^{129}Xe and encapsulated ^{129}Xe resonances were well distinguished. Further implementation of the pre-pulse trains with higher power remains promising and should have no negative effect on the resulting HyperCEST image quality during in vivo imaging.

In spite of having a higher B_1 field and, thereby, higher peak power compared to the sine and block pulse shapes (Fig 5-1C), an adiabatic hypsec RF pulse train demonstrated much lower off-resonance saturation effects. In addition, the average transmitted power (which is proportional to the square of rms B_1) of the hyperbolic secant pulse was similar to the mean power of the sinusoidal pulse and slightly exceeded the average power of the block pulse. Thereby, the substantially lower HyperCEST depletion of hypersec saturation pulses can be attributed to the lower number of pulses in the saturation pre-pulse train.

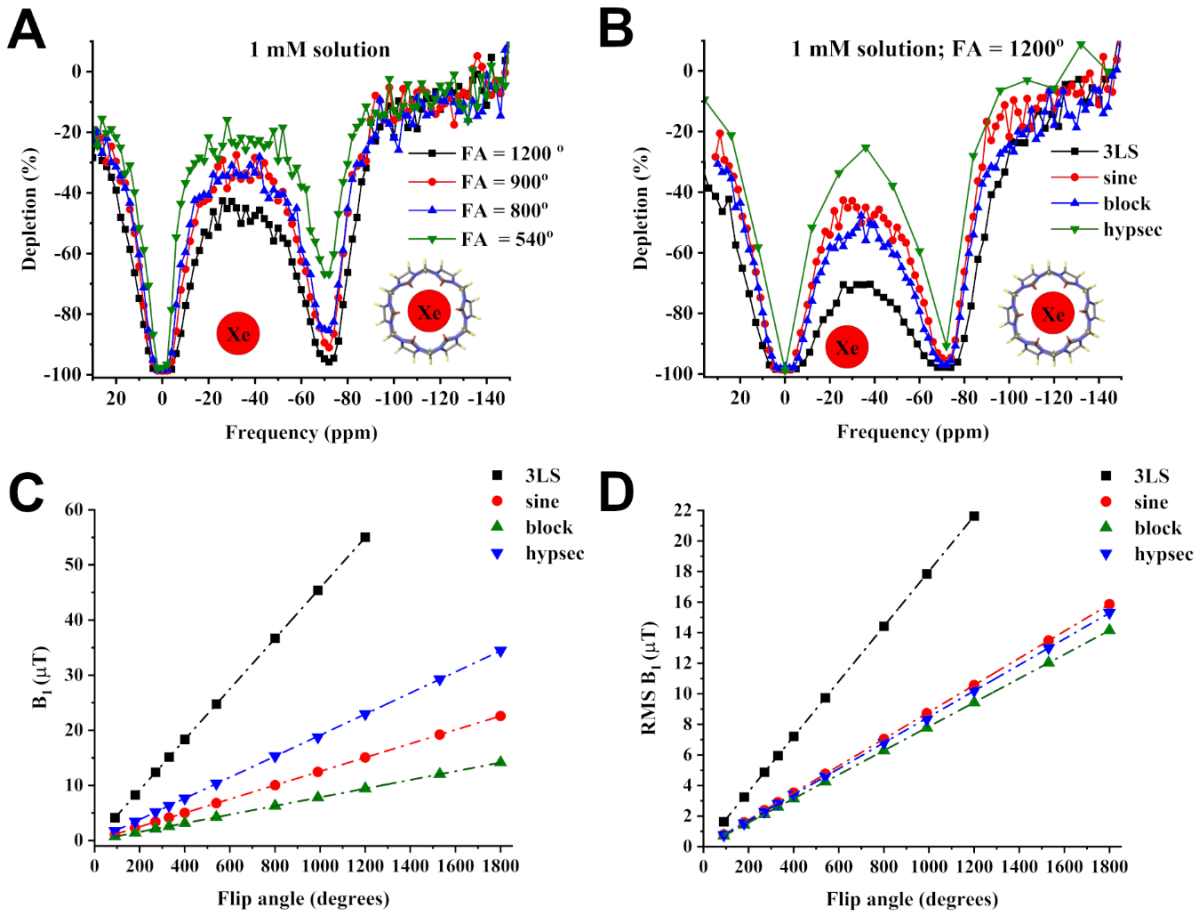

Figure 5-1 HyperCEST depletion spectra of a 1mM CB6 solution in PBS using A) sinusoidal depolarization pulses with 540°, 800°, 900°, 1200° flip angles B) 3 lobe-sinc, sinusoidal, block, and hypsec depolarization pulses with a flip angle of 1200°. C) peak B_1 field values for different flip angles of 3 lobe-sinc, sinusoidal, block, and hypsec depolarization pulses. D) rms B_1 field values for different flip angles of 3 lobe-sinc, sinusoidal, block, and hypsec depolarization pulses

The effect of the depolarization train flip angle on the HyperCEST effect is shown for all pulse shapes that were investigated in Fig. 5-2A. The representative MRS spectra of 1mM CB6 in PBS after application of each depolarization pulse of the highest FA are presented in Supporting Information (S1-4). Depletion increased with FA growth for the sine, block and hypsec pulses and reached a maximum of 95% at FA higher than 1530°. This depletion increase occurred with a similar rate for the sinusoidal and block pulses. The adiabatic pulse train exhibited a somewhat slower HyperCEST increase rate. Similar HyperCEST behavior was observed for the 3-lobe sinc depolarization pulse train; the increase in depletion, however, was much more rapid and the maximum depletion (96%) was observed at a lower FA of 800°. Unfortunately, FA higher than 1200° were not possible to achieve for 3LS depolarization pulses due to SAR limitations on our MRI scanner. Due to the smaller number of depolarization pulses in the pre-pulse train, the adiabatic hypsec pulse shape demonstrated the weakest HyperCEST performance. Sinusoidal and rectangular pulses demonstrated quite similar performances, which was expected due to the similarity in their BW. Finally, the 3LS completely outperformed the other three pulse shapes due to its highest transmitting power and relatively broad (3ppm) rectangularly-shaped BW, allowing better depolarization of HP ^{129}Xe nuclei within the supramolecular host.

Further dilution of the 1mM CB6 solution in PBS and depletion measurements allowed the determination of the detectability limits for each pulse train (Fig 5-2B). The same FA of 1200° was used for all depolarization pulses to compare their performance for different CB6 concentrations. The detectability limit of CB6 in PBS was 25μM for all pulse shapes; the depletion values were 24%, 17%, 12% and 7% for the 3LS, sine, block and hypsec pulses respectively. The difference in detectability limit for different pulses originates from the cumulative effect of the following factors: a) transmitted RF power, b) number of pulses in the pulse train. Indeed, sine and block

pulses had an average transmitted power approximately two times smaller compared to 3LS pulse (Fig. 5-1D) which is in good agreement with depletion values drop at the detectability limit for these pulses. On the contrary, hypsec depletion at the detectability limit was three times smaller compared to achieved with 3LS pulses. This can be attributed to a smaller number of saturation pulses as well as smaller transmitted RF power.

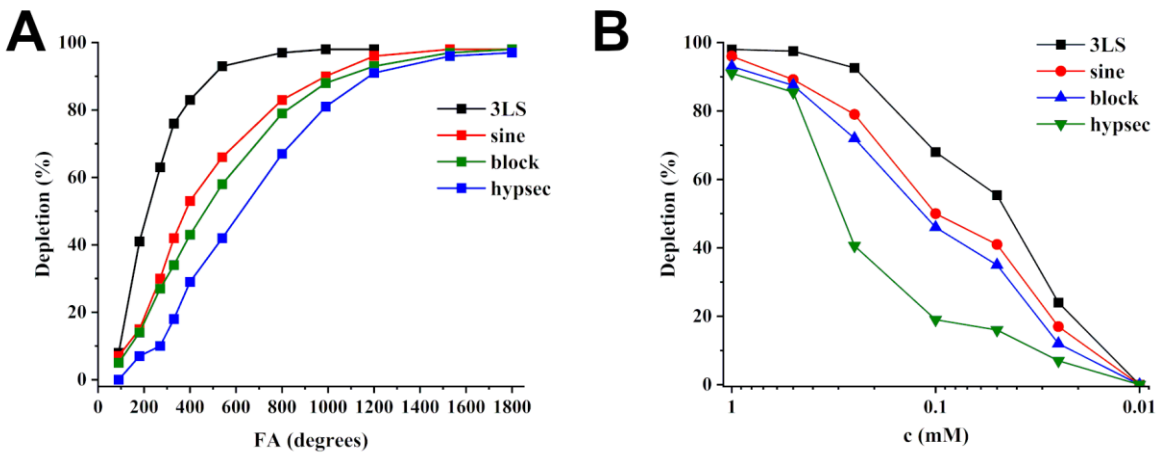

Figure 5-2 HyperCEST depletion of the CB6 solution in PBS as a function of A) applied FA for depolarization pulses and B) CB6 concentration for 3-lobe sinc, sinusoidal, block, and hypsec depolarization pulses.

Once we optimized all the parameters and determined the most promising depolarization pulse for the maximum CB6 performance as a molecular agent in PBS, we decided to investigate biological media. The FAs that demonstrated the best HyperCEST performance in PBS were used during in vitro blood experiments. Citrated sterile bovine blood was chosen for its similarity to human blood. Unfortunately, the continuous flow set-up for HP ^{129}Xe bubbling through the solution was not suitable for these experiments with blood due to rapid contamination of the glass-fritted cell membrane. Hence, another experimental set-up was adopted from Norquay et al[30] and altered for our experiments, which allowed gas exchange between the HP ^{129}Xe flow and the blood

pool without creating ^{129}Xe bubbles within the solution and thereby avoiding creation of blood foam.

Full depletion z-spectra were acquired for the 1mM solution of CB6 in bovine blood using sinusoidal (Fig 5-3A), block (Fig 5-3B) and hyperbolic secant pulses (Fig 5-3D) with FA equal to 1800° and a 3-lobe sinc pulse of 1200° (Fig 5-3C). The depletion values were calculated separately for the resonances of HP ^{129}Xe dissolved in the plasma pool and ^{129}Xe bound to the RBC. The strong HyperCEST depletion peaks (HyperCEST effect ~ 100%) were observed for both ^{129}Xe-plasma and the ^{129}Xe-RBC pools (representative on- and off- resonance MRS spectra are provided in Supporting Information S5-8). In fact, to the best of our knowledge, ^{129}Xe HyperCEST was observed in the RBC pool for the first time. Observation of this phenomenon was allowed by maximization of the HyperCEST effect for CB6 and by employing the alternative experimental setup for measuring the HyperCEST effect compared to previous studies. There was a previous study of the HyperCEST effect of CB6 in the whole bovine blood performed by Hane at al[18], however, that study had several experimental drawbacks. The blood was almost twice diluted with the solution of CB6 in PBS for the highest concentration and the dilutions were different for the lower concentrations. In our study, we specifically maintained a constant dilution of blood (it was only 15%) to minimize the effect of different amounts of blood cells within the sample. Additionally, in the previous study, the mixing of blood with HP ^{129}Xe was performed manually by shaking the syringe of blood with ^{129}Xe, which resulted in unequal dissolution of ^{129}Xe within each sample. Furthermore, it created ^{129}Xe bubbles, which could also affect the HyperCEST results by potentially increasing the ^{129}Xe signal by further exchange between the ^{129}Xe gas in the bubbles and in solution. In present work, we used the set-up similar to that utilised by Norquay et al[30], which allowed us to minimize the experimental error associated with uneven amounts of dissolved

^{129}Xe, since ^{129}Xe was constantly exchanged through the membrane while blood was pumped in the perpendicular direction through the membrane with the same speed and time for each sample. The present set-up, however, has its own drawbacks since the extraction of the depolarized ^{129}Xe from the blood sample between two subsequent pump cycles is somewhat complicated and the complete replenishment of depolarized ^{129}Xe with fresh HP ^{129}Xe cannot be guarantied. We believe that in the future, the set-up for testing molecular agents in blood should allow continuous flow of HP ^{129}Xe through the blood to allow the substitution of depolarized ^{129}Xe with fresh HP ^{129}Xe.

Although the sinusoidal, rectangular, and 3LS pulse shapes resulted in an approximately 100% HyperCEST effect in bovine blood, the adiabatic hypsec pre-pulse train demonstrated a limited performance. The HyperCEST depletion values of ^{129}Xe-RBC was 44.5% and ^{129}Xe dissolved in plasma was 70.6% after hypsec pulse application. (Fig 5-3D).

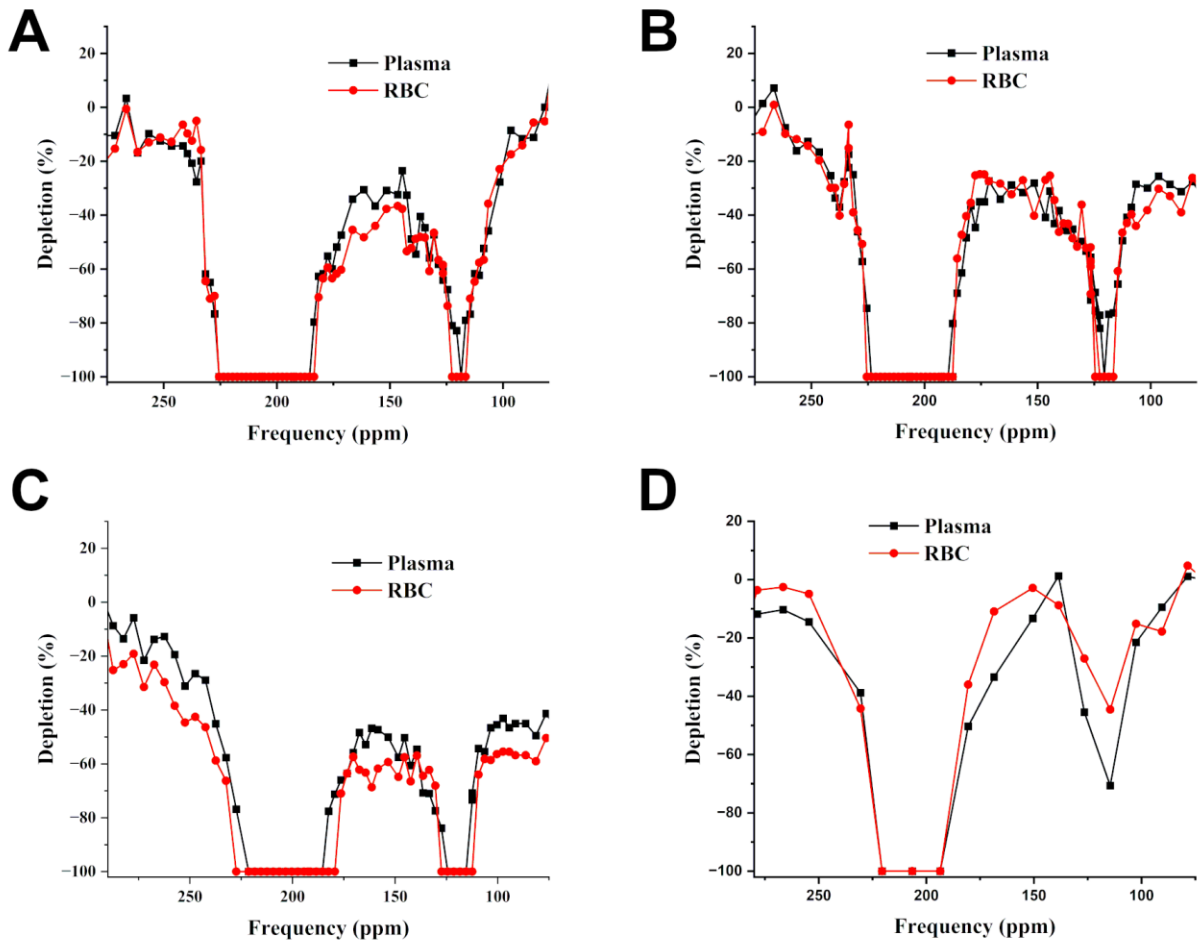

Figure 5-3 HyperCEST depletion spectra of 1 mM CB6 in whole citrated bovine blood after application of A) sine and B) block depolarization pulses 1800° FA; c) 3LS 1200° FA pulse and D) hypsec pulse with 1800° FA.

The next step of the present project was to quantitatively evaluate the detectability limit of CB6 in the sterile citrated bovine blood using the optimized pulse sequence parameters. The CB6 detectability limit was assessed based on both HP ^{129}Xe-plasma and ^{129}Xe-RBC depletions (Fig. 5-4). The HyperCEST values decreased with a decrease of CB6 concentrations for both plasma and RBC resonances, albeit the measured RBC HyperCEST values demonstrated larger variability compared to the plasma HyperCEST values. Larger variability of the RBC HyperCEST values may be explained by the lower ^{129}Xe-RBC peak intensity compared to the plasma resonance.

Moreover, oxygenation of the blood could potentially vary throughout the experiment as well as the possibility of partial coagulation occurring. Finally, there exists a large array of additional molecules present in biological fluids such as blood which may limit the mobility of ^{129}Xe within the solution and which may take part in non-specific competitive binding with the CB6 molecule.

The CB6 detectability limit was set as 2 standard deviations (SD) of the HyperCEST depletion value and was found to be equal to 100uM in citrated bovine blood for the 3LS and sinusoidal depolarization pulses. The observed HyperCEST effect strength varied between the different RF pulse shapes. Application of 3LS pulses resulted in ~30% ± 9% HyperCEST effect in plasma and only ~ 4%± 7% for the RBC (Fig. 5-4C). The HyperCEST depletion of the HP ^{129}Xe-plasma resonances was similar for the sine and hypsec pulse shapes and was approximately equal to 15% for the 100μM CB6 concentration (Fig. 5-4A, D), however, for the block pulse it was only ~6% ± 8% (Fig. 5-4B). On the contrary, the ^{129}Xe-RBC HyperCEST demonstrated larger variations between the pulses. The strongest ^{129}Xe-RBC HyperCEST effect was observed after application of the sinusoidal pulse shapes (~ 28% ± 9%), whereas the adiabatic hyperbolic secant depolarization pulses resulted in only ~ 16% ± 13%. The detectability limit was much lower for CB6 concentration than was observed by Hane et al. in the previous study using bovine blood[18]. Hane et al. observed a 14% depletion at 0.25mM using the 3LS pulses with 330° FA, while we observed a 41% HyperCEST effect in plasma at the same concentration with the same pulse shape but using a larger FA. The observed 2.5 improvement in sensitivity compared to the previous study resulted from the proper pulse sequence optimization performed in our present study.

Lower HyperCEST effect values are expected when transitioning to in vivo studies since the in vivo milieu is much more complex than sterile bovine blood. More biological molecules could potentially bind to CB6 and ^{129}Xe in vivo, reducing their ability to interact. The large values

of HyperCEST observed at the 0.1mM CB6 concentration in bovine blood, however, give a basis to predict a similar detectability limit within a living organism.

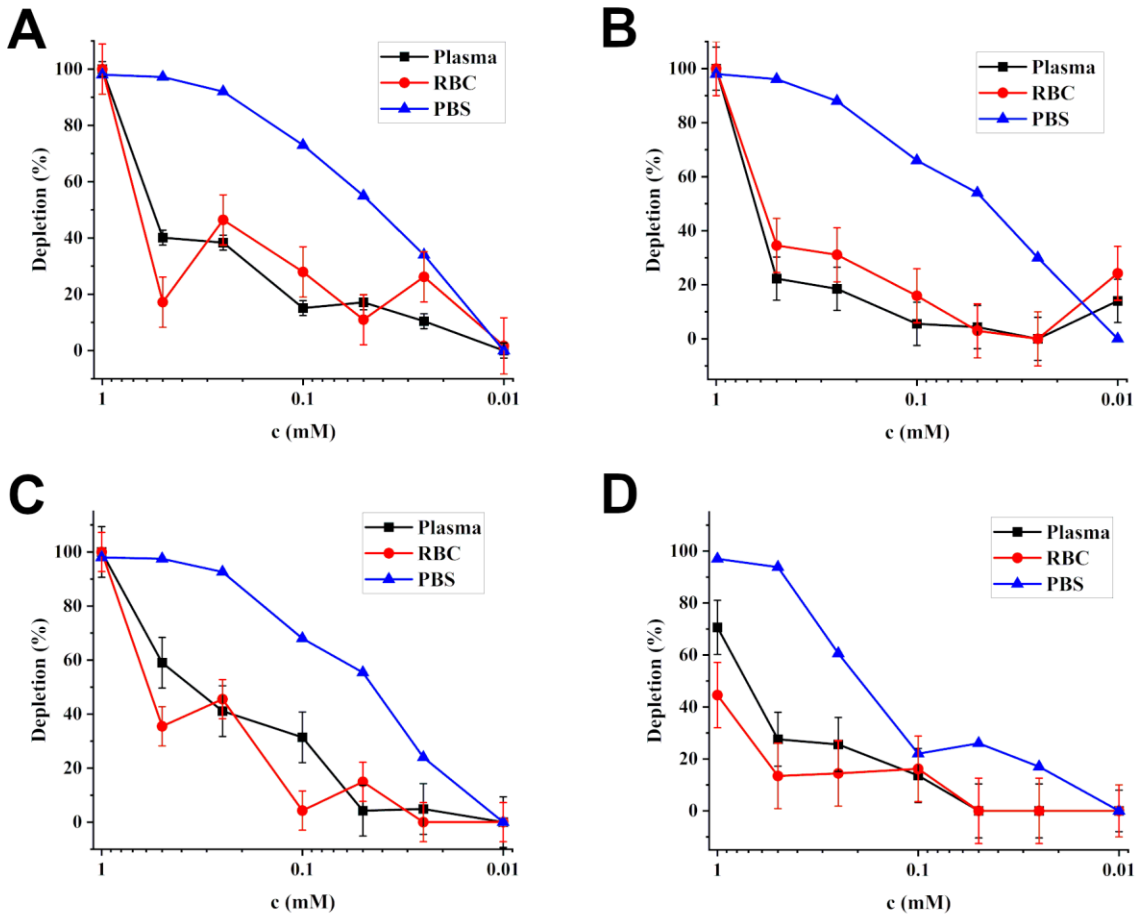

Figure 5-4 HyperCEST depletion dependence on the CB6 concentration in citrated sterile whole bovine blood after application of A) sinusoidal (1800° FA), B) block (1800° FA), C) 3-lobe sinc (1200° FA), and D) hyperbolic secant (1800° FA) depolarization pre-pulse trains.

In the current study, we evaluated the HyperCEST performance of four different depolarization pre-pulse trains: sinusoidal, block, 3LS and hyperbolic secant. Each of these pulses has its own advantages and disadvantages for further practical implementation. We kept the duration of the pulse trains the same (480ms) to maintain the same net magnetization so that the results would be comparable. Sinusoidal and block pulse shapes are commonly employed in NMR spectroscopy and the block pulse shape is usually available on clinical MRI scanners. Both pulse

shapes have a very narrow bandwidth and transfer high energy at the specific frequency. The duration of both pulses in this study was 30ms which was equal to a 0.1ppm bandwidth. This BW value is very selective and extremally useful for in vitro evaluation of unknown HyperCEST agents since high selectivity allows accurate probing of the entire spectral region. Such high spectral selectivity, however, may cause some issues during further translation to preclinical and clinical studies since the frequency of ^{129}Xe within the CB6 cage may change within living tissues and may cause a mismatch of the pulse and ^{129}Xe frequencies; this will result in lower HyperCEST performance, ultimately resulting in much lower sensitivity. The performances of the sine and block pulses were similar, however, the sine pulse resulted in a somewhat higher variability of the HyperCEST effect. This possibly could be explained by an off-resonance saturation of the HP ^{129}Xe dissolved phase caused by the block pulses.

The most promising depolarization pre-pulse train is the 3LS. It has a rectangular spectrum and a relatively wide BW (~ 3ppm in the present study), allowing depolarization of a larger ^{129}Xe frequency region. Although it may not be the best choice for in vitro studies, it is useful for in vivo HyperCEST imaging since it is much less sensitive to a potential mismatch of frequencies. In addition, the 3LS has the highest amount of power transmitted for each pulse, resulting in the most optimal performance in our study. The relatively wide BW of the 3LS pulses, however, can also cause unwanted off-resonance saturation if the cage peak is close to the dissolved phase HP ^{129}Xe resonance.

The hyperbolic secant depolarization pulse demonstrated the worst performance among all the pulses, albeit further implementation of this pulse shape may be attractive for in vivo HyperCEST imaging. The poor performance of the hypsec pulse can be explained by a smaller number of pulses (12) in the 480ms pre-pulse train. which was caused by limitations on our clinical

MRI scanner. Hypsec pulses have a bell-shaped spectrum with a large BW (~ 12ppm). This resulted in a lower amount of depolarization energy transmitted, compared to the other pulses. Despite its underperformance, the hypsec pulse has one considerable benefit over all other pulses – its performance is independent of B_1 field inhomogeneities due to its adiabatic nature. This makes its further investigation highly worthy for future use for in vivo imaging and further translation to human studies.

There are several avenues for further improvement of the effectiveness of the depolarization pulses, such as increasing the number of pulses within the saturation pulse train and hence increasing its length. This, however, will increase the SAR, which is not desirable. An increase in SAR can be mitigated by either introducing time spacing between the depolarization pulses or increasing the scan TR. Time delays between depolarization pulses, however, likely will not be beneficial due to the short T_1 relaxation of HP ^{129}Xe in blood. On the other hand, increases in TR may allow for higher HP ^{129}Xe signal to accumulate due to a larger amount of ^{129}Xe being washed into the field of view (FOV) with blood flow, albeit prolonging the scan duration. While considering further prolongation of the depolarization pulse train, we should keep in mind the software and hardware limitations that different MRI scanners have. For example, the depolarization duration time can be increased on our clinical MRI by employing pulse programming. This may not be a straightforward option, however, for sites that desire to implement HyperCEST imaging on their MRI machines for preclinical and clinical imaging in the future.

5-4. Conclusion

In the present study we tested different depolarization pre-pulse trains and identified the best parameters for maximization of the ^{129}Xe HyperCEST effect for the CB6 molecule. In addition, we determined the detectability limit of CB6 in whole citrated sterile bovine blood, which

should allow us to minimize the concentration of CB6 injected in future studies. This study is a stepping stone for the further investigation of potential CB6 applications for molecular imaging.

Acknowledgements

The authors would like to thank Dr. Guillaume Gilbert for the insights in pulse sequence development and RF pulse parameters calculation.

This research was supported by a Natural Science Engineering Research Council Discovery grant (RGPIN-2017-05359) and an Ontario Research Fund (ORF RE 09 029). Yurii Shepelytskyi was supported by a MITACS Elevate postdoctoral fellowship (IT25574). Vira Grynko was partially supported by an Ontario Trillium Scholarship and by a MITACS Accelerate grant (IT31144). Viktoriia Batarchuk was supported by a MITACS Accelerate grant (IT31144).

Keywords: Cucurbit[6]uril • HyperCEST • Hyperpolarized ^{129}Xe • Molecular Imaging • Magnetic Resonance Imaging

References:

1. Albert MS, Cates GD, Driehuys B, et al. Biological Magnetic Resonance Imaging Using Laser-Polarized 129Xe. *Nature*. 1994;370(6486):199-201. doi:10.1038/370199a0
2. Couch MJ, Munidasa S, Rayment JH, et al. Comparison of Functional Free-Breathing Pulmonary 1H and Hyperpolarized 129Xe Magnetic Resonance Imaging in Pediatric Cystic Fibrosis. *Acad Radiol*. 2021;Aug; 28(8):e209-e218. doi:10.1016/j.acra.2020.05.008
3. Rankine LJ, Wang Z, Wang JM, et al. 129xenon gas exchange magnetic resonance imaging as a potential prognostic marker for progression of idiopathic pulmonary fibrosis. *Ann Am Thorac Soc*. 2020;17(1):121-125. doi:10.1513/AnnalsATS.201905-413RL

4. Grist JT, Chen M, Collier GJ, et al. Hyperpolarized 129Xe MRI abnormalities in dyspneic patients 3 months after COVID-19 Pneumonia. *Radiology*. 2021;301(1):E353-E360. doi:10.1148/radiol.2021210033

5. Evans A, McCormack DG, Santyr G, Parraga G. Mapping and quantifying hyperpolarized 3He magnetic resonance imaging apparent diffusion coefficient gradients. *J Appl Physiol*. 2008;105(2):693-699. doi:10.1152/JAPPLPHYSIOL.00178.2008/ASSET/IMAGES/LARGE/ZDG008088068000 5.JPEG

6. Li H, Zhao X, Wang Y, et al. Damaged lung gas exchange function of discharged COVID-19 patients detected by hyperpolarized 129Xe MRI. *Sci Adv*. 2021;7(1):1-9. doi:10.1126/sciadv.abc8180

7. Matheson Bsc AM, Mcintosh Bsc MJ, Kooner Bsc HK, et al. Persistent 129 Xe MRI Pulmonary and CT Vascular Abnormalities in Symptomatic Individuals with Post-Acute COVID-19 Syndrome. *Radiology* . 2022;305(2):466-476. https://apilab.ca/our_code.html

8. Rao MR, Norquay G, Stewart NJ, Hoggard N, Griffiths PD, Wild JM. Assessment of brain perfusion using hyperpolarized 129Xe MRI in a subject with established stroke. *Journal of Magnetic Resonance Imaging*. 2019;50(3):1002-1004. doi:10.1002/jmri.26686

9. Shepelytskyi Y, Grynko V, Li T, Hassan A, Granberg K, Albert MS. The effects of an initial depolarization pulse on dissolved phase hyperpolarized 129Xe brain MRI. *Magn Reson Med*. 2021;86(6):3147-3155. doi:10.1002/mrm.28918

10. Shepelytskyi Y, Hane FT, Grynko V, Li T, Hassan A, Albert MS. Hyperpolarized 129Xe Time-of-Flight MR Imaging of Perfusion and Brain Function. *Diagnostics*. 2020;10:630. doi:10.3390/diagnostics10090630

11. Grynko V, Shepelytskyi Y, Li T, Hassan A, Granberg K, Albert MS. Hyperpolarized 129Xe multi-slice imaging of the human brain using a 3D gradient echo pulse sequence. *Magn Reson Med*. 2021;86(6):3175-3181. doi:10.1002/mrm.28932 *(Included as Chapter 4 in the thesis)*

12. Friedlander Y, Zanette B, Lindenmaier A, et al. Hyperpolarized 129Xe MRI of the rat brain with chemical shift saturation recovery and spiral-IDEAL readout. *Magn Reson Med*. 2022;Apr; 87(4):1971-1979. doi:10.1002/mrm.29105

13. Rao MR, Stewart NJ, Griffiths PD, Norquay G, Wild JM. Imaging human brain perfusion with inhaled hyperpolarized 129Xe MR imaging. *Radiology*. 2018;286(2):659-665. doi:10.1148/radiol.2017162881

14. Shepelytskyi Y, Grynko V, Rao MR, et al. Hyperpolarized 129Xe imaging of the brain: Achievements and future challenges. *Magn Reson Med*. 2022;88(1):83-105. doi:10.1002/MRM.29200 *(Included as Chapter 2 in the thesis)*

15. Schroder L, Lowery TJ, Hilty C, Wemmer DE, Pines A. Molecular Imaging Using a Targeted Magnetic Resonance Hyperpolarized Biosensor. *Science (1979)*. 2006;314(5798):446-449. doi:10.1126/science.1131847

16. Stevens TK, Palaniappan KK, Ramirez RM, Francis MB, Wemmer DE, Pines A. HyperCEST detection of a 129Xe-based contrast agent composed of cryptophane-A molecular cages on a bacteriophage scaffold. *Magn Reson Med*. 2013;69(5):1245-1252. doi:10.1002/mrm.24371

17. Bai Y, Hill PA, Dmochowski IJ. Utilizing a Water-Soluble Cryptophane with Fast Xenon Exchange Rates for Picomolar Sensitivity NMR Measurements. *Anal Chem*. 2012;84:46. doi:10.1021/ac302347y

18. Hane FT, Smylie PS, Li T, et al. HyperCEST detection of cucurbit[6]uril in whole blood using an ultrashort saturation Pre-pulse train. *Contrast Media Mol Imaging*. 2016;11(4):285-290. doi:10.1002/cmmi.1690

19. Wang Y, Dmochowski IJ. Cucurbit[6]uril is an ultrasensitive129Xe NMR contrast agent. *Chemical Communications*. 2015;51:8982-8985. doi:10.1039/c5cc01826a

20. Wang Y, Dmochowski IJ. An Expanded Palette of Xenon-129 NMR Biosensors. *Acc Chem Res*. 2016;49(10):2179-2187. doi:10.1021/acs.accounts.6b00309

21. Hane FT, Li T, Smylie P, et al. In vivo detection of cucurbit[6]uril, a hyperpolarized xenon contrast agent for a xenon magnetic resonance imaging biosensor. *Sci Rep*. 2017;(3):41027. doi:10.1038/srep41027

22. Hane FT, Fernando A, Prete BRJ, et al. Cyclodextrin-Based Pseudorotaxanes: Easily Conjugatable Scaffolds for Synthesizing Hyperpolarized Xenon-129 Magnetic Resonance Imaging Agents. *ACS Omega*. 2018;3(1):677-681. doi:10.1021/acsomega.7b01744

23. Fernando PUAI, Shepelytskyi Y, Cesana PT, et al. Decacationic pillar[5]arene: A new scaffold for the development of 129Xe MRI imaging agents. *ACS Omega*. 2020;5(43):27783-27788. doi:10.1021/acsomega.0c02565

24. Schnurr M, Joseph R, Naugolny-Keisar A, et al. High Exchange Rate Complexes of 129 Xe with Water-Soluble Pillar[5]arenes for Adjustable Magnetization Transfer MRI. *ChemPhysChem*. 2018;20(2):246-251. doi:10.1002/cphc.201800618

25. Du K, Zemerov SD, Hurtado Parra S, Kikkawa JM, Dmochowski IJ. Paramagnetic Organocobalt Capsule Revealing Xenon Host-Guest Chemistry. *Inorg Chem*. 2020;59(19):13831-13844. doi:10.1021/acs.inorgchem.9b03634

26. McHugh CT, Durham PG, Atalla S, et al. Low-boiling point perfluorocarbon nanodroplets as dual-phase dual-modality MR/US contrast agent. *ChemPhysChem*. 2022;23:e20220043. doi:10.1002/cphc.202200438

27. Walker S, Kaur R, Mcinnes FJ, Wheate NJ. Synthesis, Processing and Solid State Excipient Interactions of Cucurbit[6]uril and Its Formulation into Tablets for Oral Drug Delivery. *Mol Pharmaceutics*. 2010;7(6):2166-2172. doi:10.1021/mp100191b

28. McHugh CT, Kelley M, Bryden NJ, Branca RT. In vivo hyperCEST imaging: Experimental considerations for a reliable contrast. *Magn Reson Med*. 2022;87(3):1480-1489. doi:10.1002/mrm.29032

29. Mollison PI. The introduction of citrate as an anticoagulant for transfusion and of glucose as a red cell preservative. *Br J Haematol*. 2000;108(1):13-18. doi:10.1046/j.1365-2141.2000.01827.x

30. Norquay G, Leung G, Stewart NJ, Tozer GM, Wolber J, Wild JM. Relaxation and exchange dynamics of hyperpolarized 129Xe in human blood. *Magn Reson Med*. 2015;74(2):303-311. doi:10.1002/mrm.25417

31. Kim BS, Ko YH, Kim Y, et al. Water soluble cucurbit[6]uril derivative as a potential Xe carrier for 129Xe NMR-based biosensors. *Chemical Communications*. 2008;(24):2756-2758. doi:10.1039/b805724a

32. Finbloom JA, Slack CC, Bruns CJ, et al. Rotaxane-mediated suppression and activation of cucurbit[6]uril for molecular detection by 129Xe hyperCEST NMR. *Chemical Communications*. 2016;52(15):3119-3122. doi:10.1039/c5cc10410f

33. Prete BRJ, Robinson D, Fernando A, et al. Benzene-Appended Cucurbit[6]uril as a Potential Biosensor Scaffold for Hyperpolarized 129Xe MRI Molecular Contrast Agents Benzene-

Appended Cucurbit[6]uril as a Potential Biosensor Scaaold for Hyperpolarized 129Xe MRI Molecular Contrast Agents. In: *Proc. Intl. Soc. Mag. Reson. Med. 26*. ; 2018:3034.

34. Newman C, Shepelytskyi Y, Campbell M, Grynko V. Evaluation of Cucurbit [6] uril Diffusion Across an Artificial Blood-Brain Barrier. In: *Proc. Intl. Soc. Mag. Reson. Med. 28*. ; 2020:3079.
35. Korchak S, Riemer T, Kilian W, Mitschang L. Quantitative Assessment of Xenon Exchange Kinetics with Cucurbit[6]uril in Physiological Saline. *ChemPhysChem*. 2018;19:1859-1865. doi:10.1002/cphc.201800048
36. Mikowska L, Grynko V, Shepelytskyi Y, et al. Revealing a Third Dissolved-Phase Xenon-129 Resonance in Blood Caused by Hemoglobin Glycation. *Int J Mol Sci*. 2023;24(14):11311. doi:10.3390/ijms241411311 *(Included as Chapter 3 in the thesis)*

Hyperpolarized ^{129}Xe Spectra in Phosphate-Buffered Saline and Whole Bovine Blood

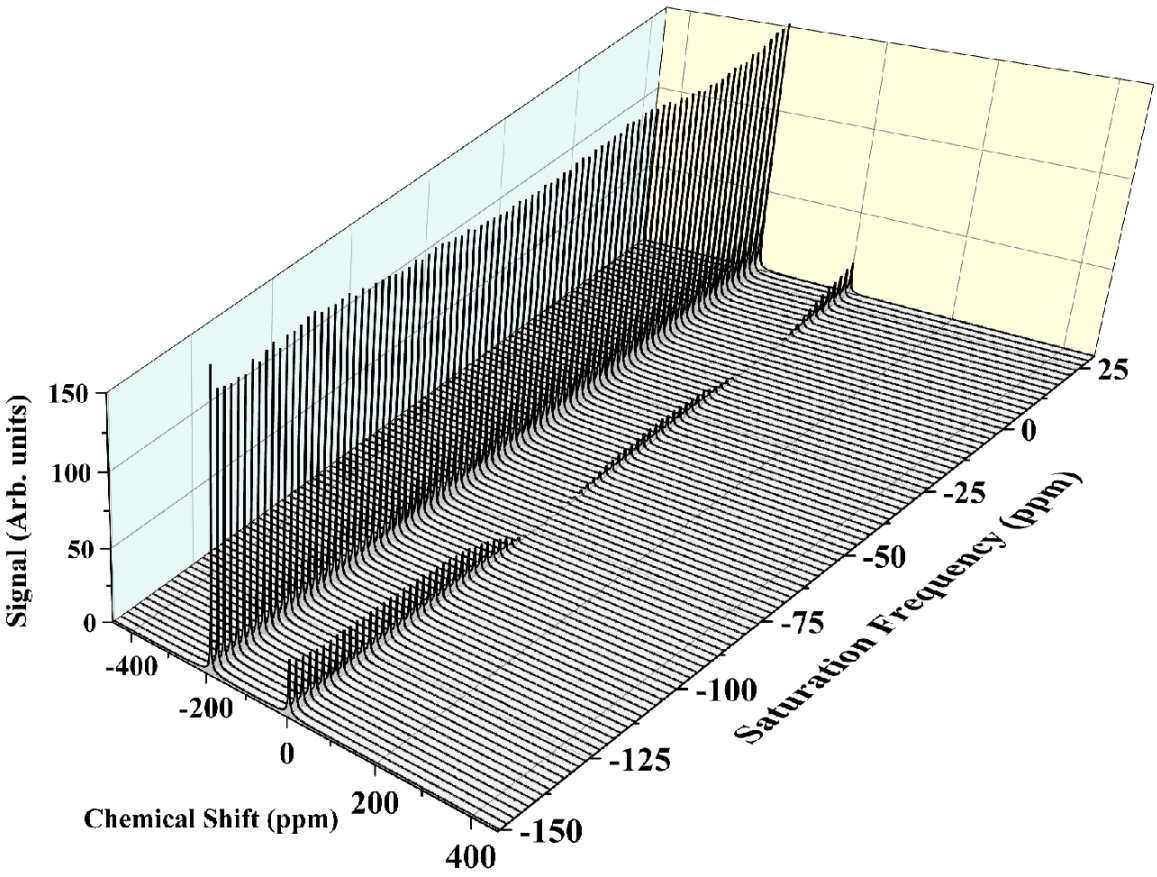

Figure 5-S1 MRS spectra of 1mM CB6 in PBS after application of sinusoidal saturation pulse at different frequencies. 0 ppm was set on the dissolved phase.

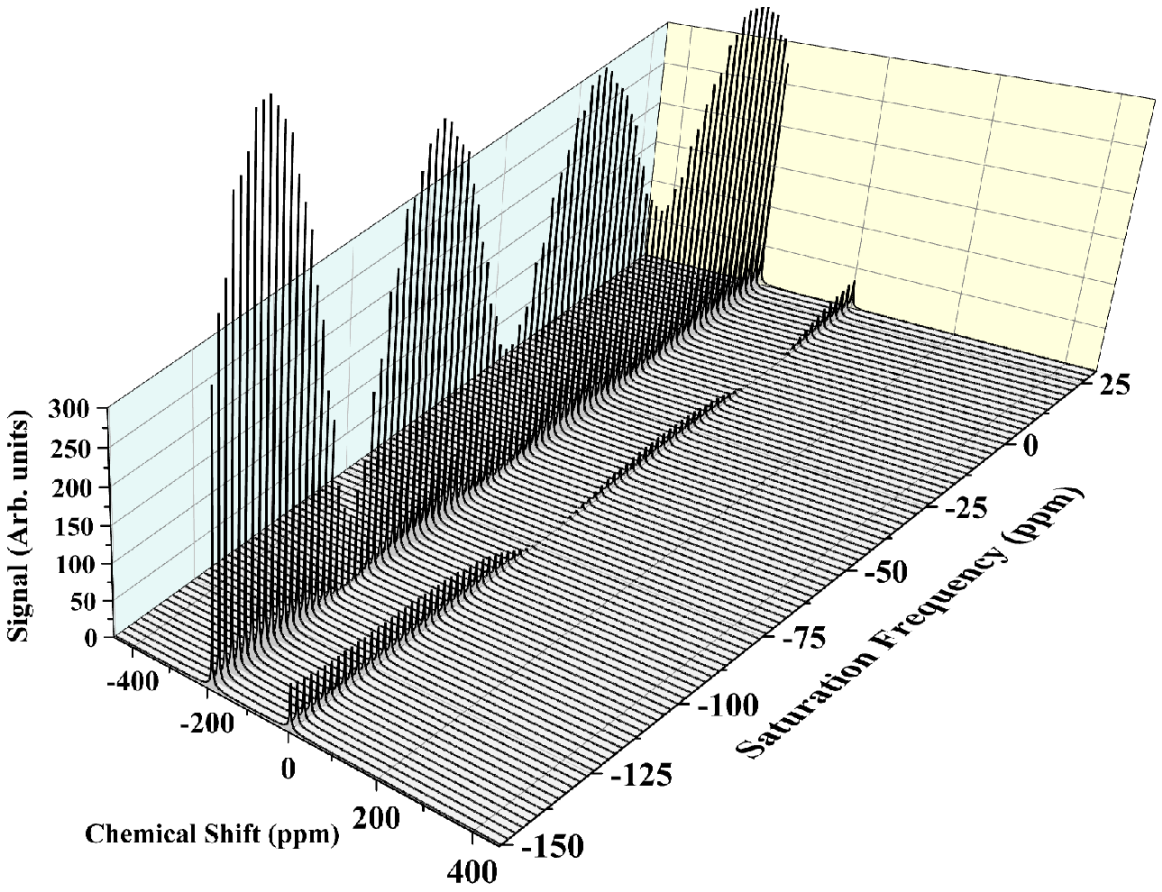

Figure 5-S2 MRS spectra of 1mM CB6 in PBS after application of block saturation pulse at different frequencies. 0 ppm was set on the dissolved phase.

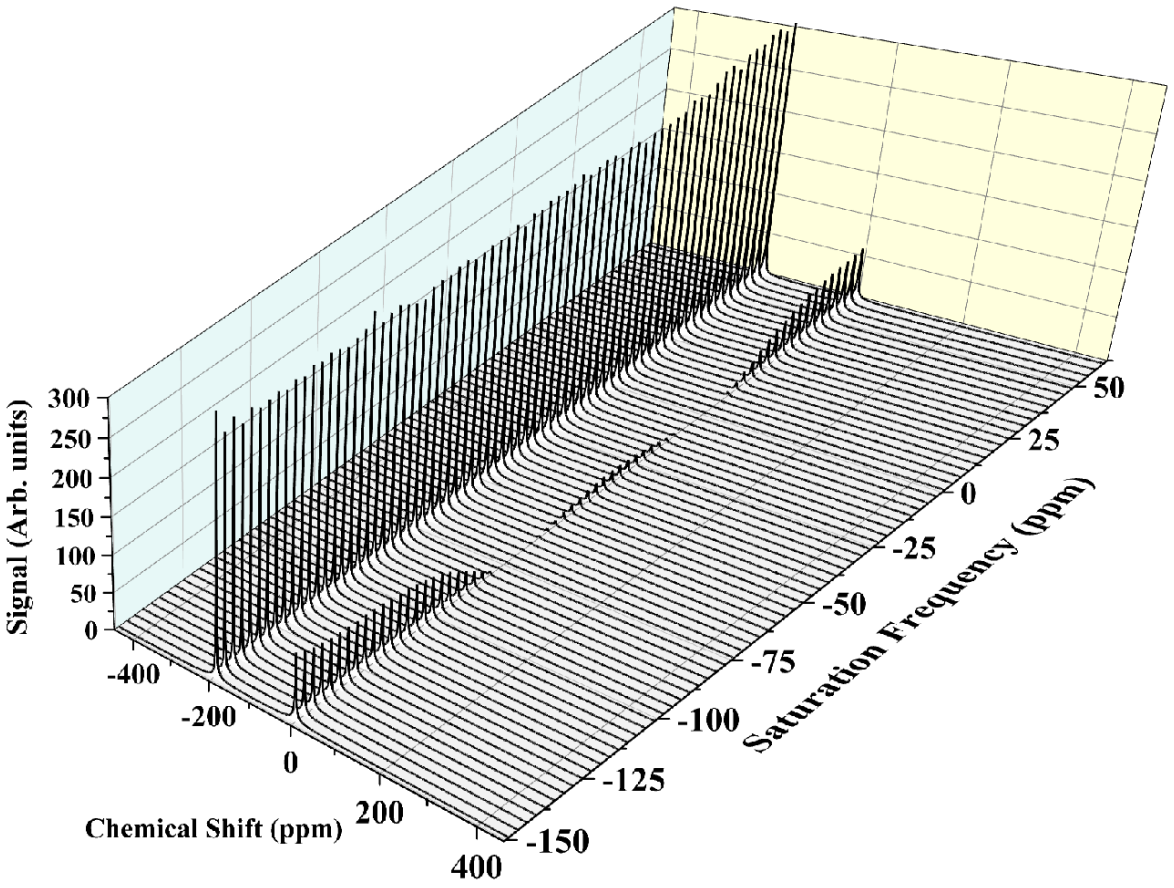

Figure 5-S3 MRS spectra of 1mM CB6 in PBS after application of 3-lobe sinc saturation pulse at different frequencies. 0 ppm was set on the dissolved phase.

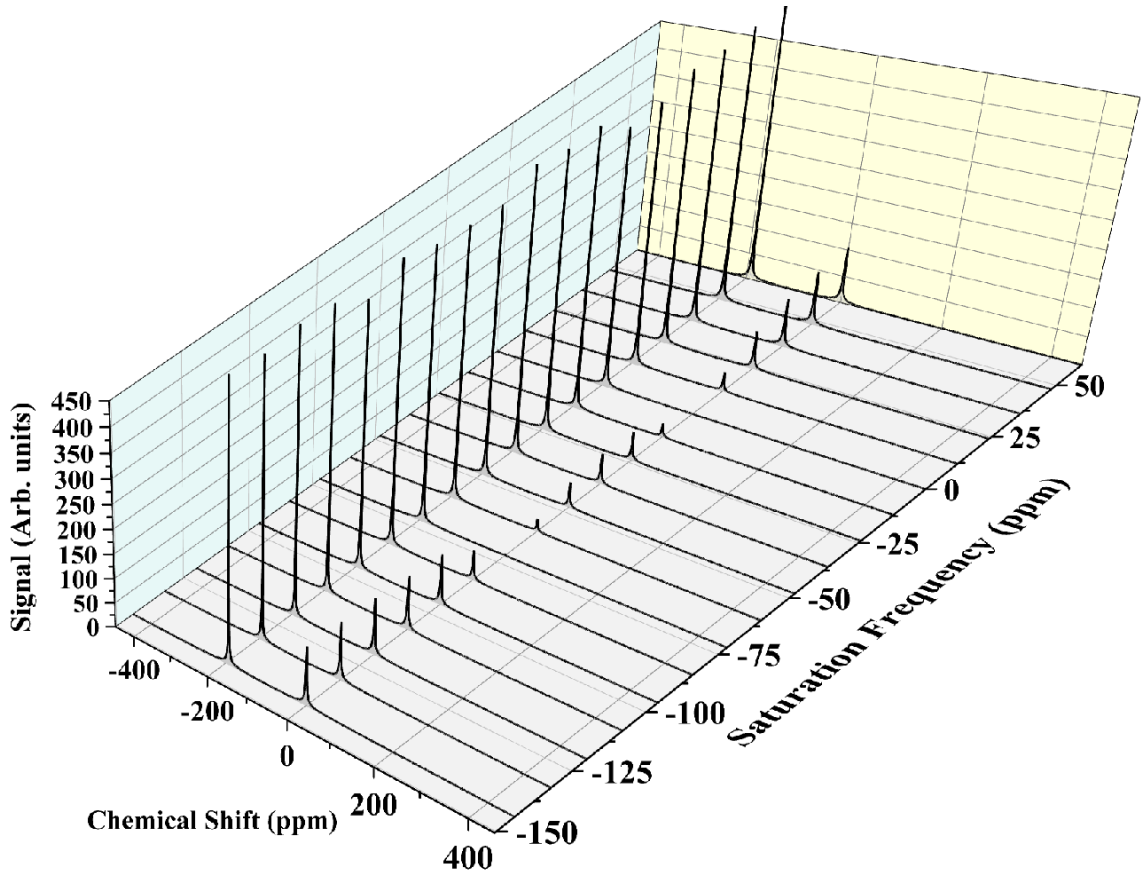

Figure 5-S4 MRS spectra of 1mM CB6 in PBS after application of hyperbolic secant saturation pulse at different frequencies. 0 ppm was set on the dissolved phase.

The peak at -192ppm observed on Figs. S1 to S4 originates from the ^{129}Xe gas phase which accumulates in the free space above the solution in the glass frit used for dissolution of HP ^{129}Xe. The set-up used for the CB6 in PBS solutions is the same as was used by Prete at al[33].

Unfortunately, the set-up used for CB6 in PBS solution is not suitable for CB6 solution in blood due excessive foam creation once put in a frit phantom under constant flow of Xe. Hence, the new set-up utilized previously by Mikowska et al[36] was used for mixing of HP ^{129}Xe and blood. The ^{129}Xe gas phase peak was not observed with utilization of this set-up.

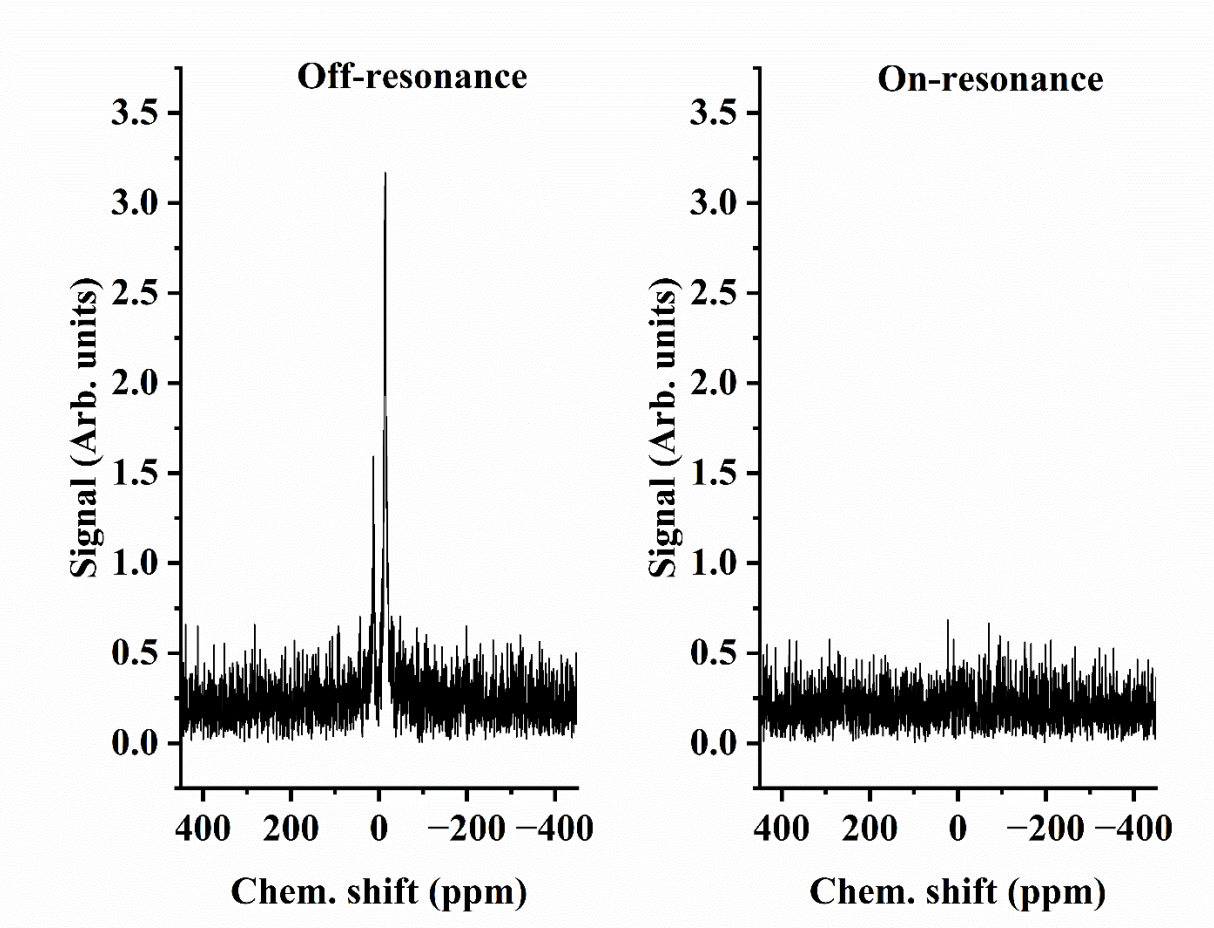

Figure 5-S5 MRS spectra of 1mM CB6 in sterile citrated bovine blood after application of sinusoidal depolarization pulse train 1800° FA at A) 80 ppm (off-resonance) and B) -83 ppm (on-resonance). 0 ppm was set in between ^{129}Xe-RBC and ^{129}Xe plasma.

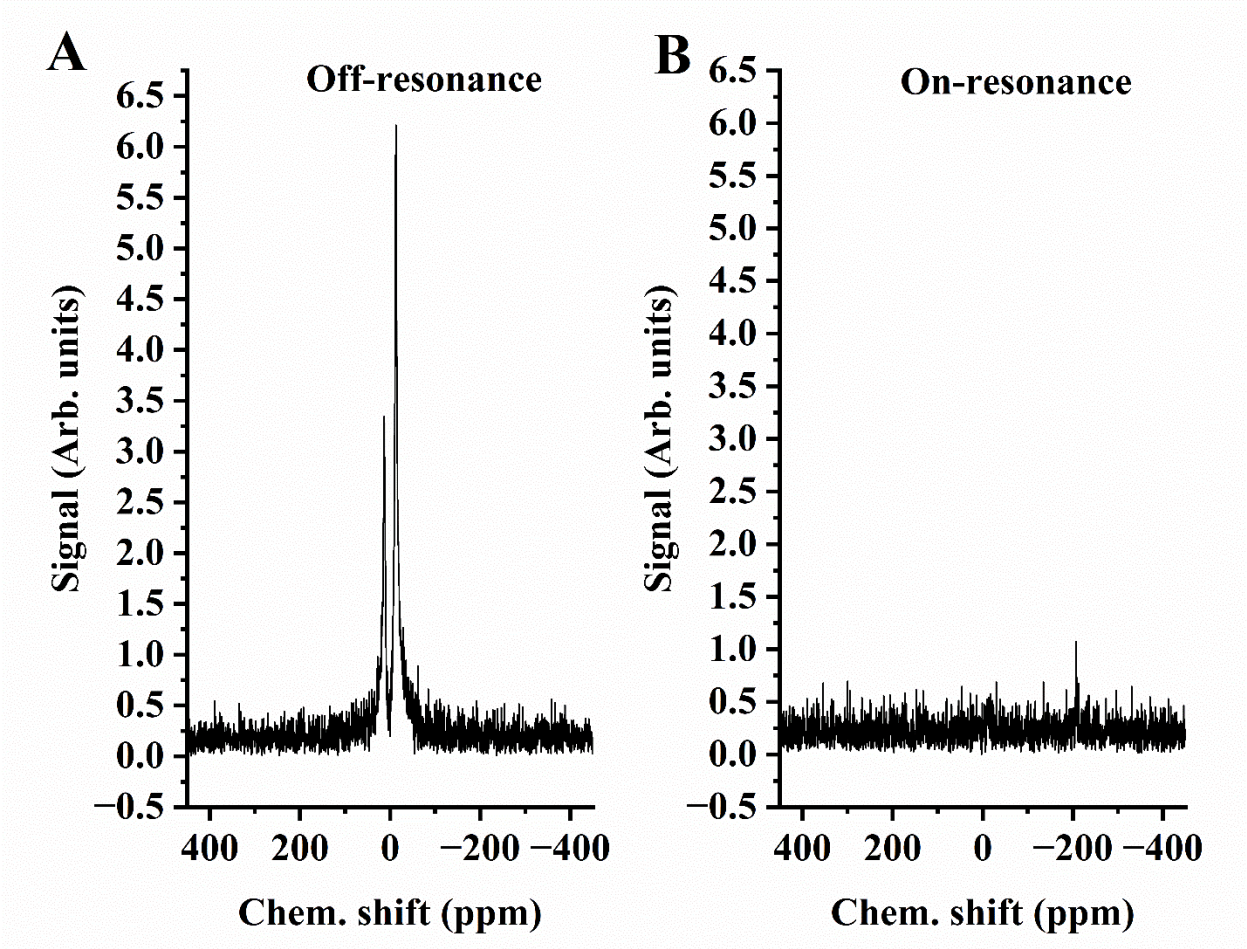

Figure 5-S6 MRS spectra of 1mM CB6 in sterile citrated bovine blood after application of block depolarization pulse train 1800° FA at A) 80 ppm (off-resonance) and B) -83 ppm (on-resonance). 0 ppm was set in between ^{129}Xe-RBC and ^{129}Xe plasma.

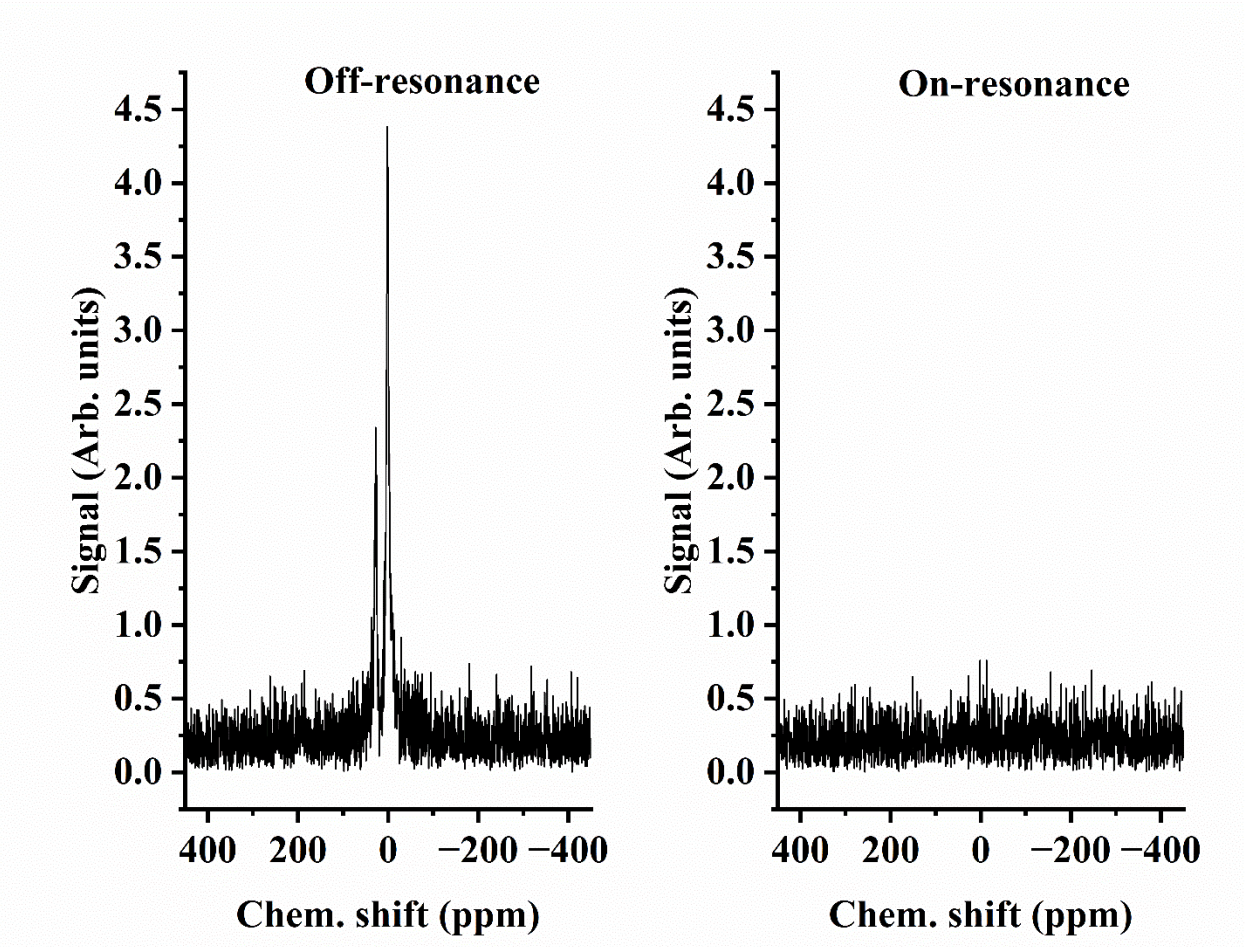

Figure 5-S7 MRS spectra of 1mM CB6 in sterile citrated bovine blood after application of 3-lobe sinc depolarization pulse train 1800° FA at A) 80 ppm (off-resonance) and B) -83 ppm (on-resonance). 0 ppm was set in between ^{129}Xe-RBC and ^{129}Xe plasma.

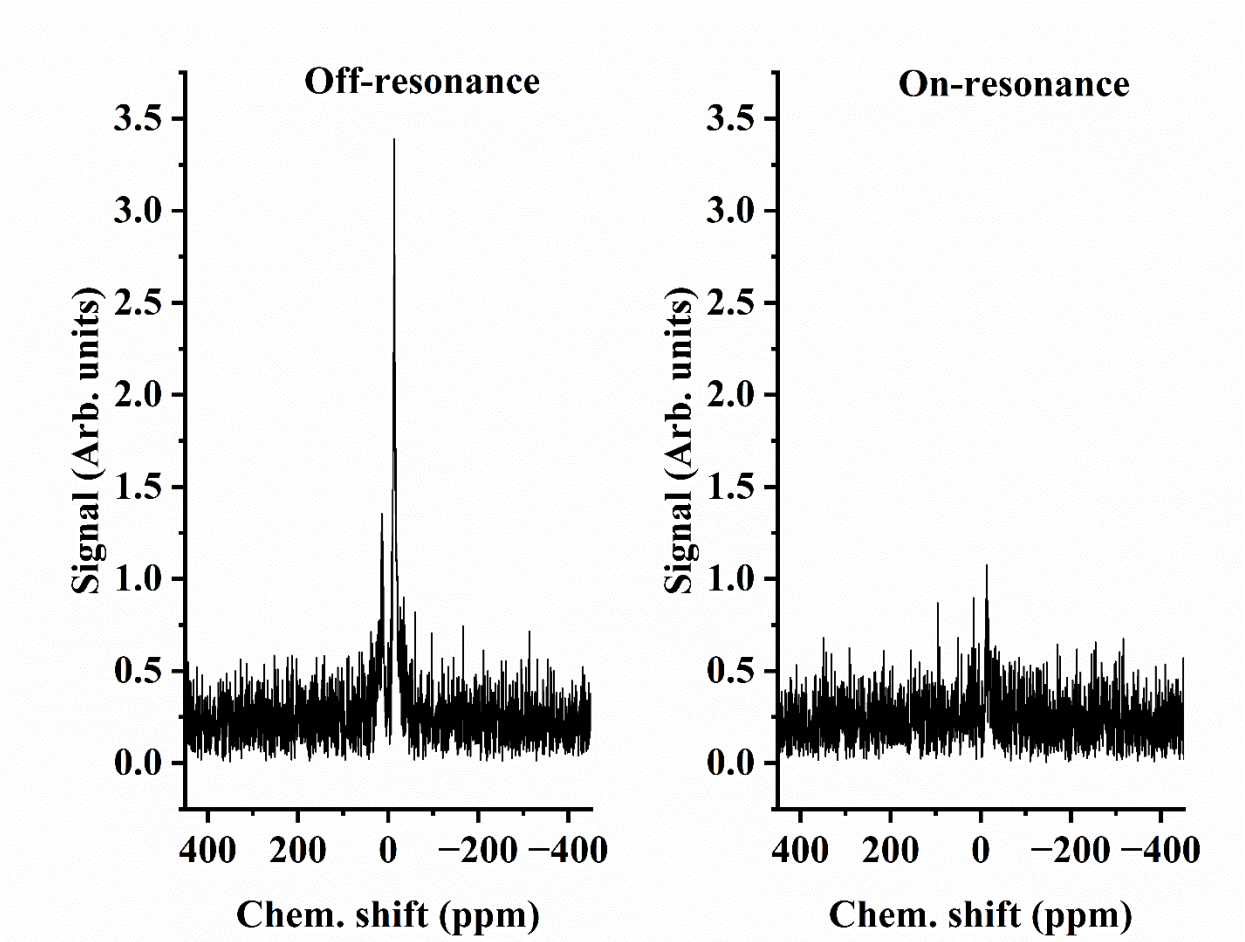

Figure 5-S8 MRS spectra of 1mM CB6 in sterile citrated bovine blood after application of hyperbolic secant depolarization pulse train 1800° FA at A) 80 ppm (off-resonance) and B) -83 ppm (on-resonance). 0 ppm was set in between ^{129}Xe-RBC and ^{129}Xe plasma.

References:

1. Prete BRJ, Robinson D, Fernando A, et al. Benzene-Appended Cucurbit[6]uril as a Potential Biosensor Scaffold for Hyperpolarized 129Xe MRI Molecular Contrast Agents Benzene-Appended Cucurbit[6]uril as a Potential Biosensor Scaaold for Hyperpolarized 129Xe MRI Molecular Contrast Agents. In: *Proc. Intl. Soc. Mag. Reson. Med. 26*. ; 2018:3034.

2. Mikowska L, Grynko V, Shepelytskyi Y, et al. Revealing a Third Dissolved-Phase Xenon-129 Resonance in Blood Caused by Hemoglobin Glycation. *Int J Mol Sci*. 2023;24(14):11311. doi:10.3390/ijms241411311

Chapter 6: Conclusion and Future Work

6.1 Summary

Non-Proton MRI gained a lot of attention during the last two decades. Its ability to solve various imaging problems, and fill the gaps in diagnostics needs, makes it even more promising in the future. We are entering the era of personalized medicine when conventional imaging modalities do not provide enough information for proper individual treatment guidance. The need for precise detection and visualization of the disease sites is crucial and the quantitative functional analysis is vital. HP ^{129}Xe MRI has already proven its efficiency for the detection, imaging, and treatment monitoring of lung diseases and abnormalities. HP ^{129}Xe is a perfect exogenous contrast agent that can transfer to the blood flow and travel to the highly perfused organs. It gives the ability to use it for brain imaging. However, despite extensive development of the imaging techniques with HP ^{129}Xe, there are multiple fundamental questions that haven't been explored and several stepping stones are vitally necessary for further progression. Therefore, this work was focused on the two most promising and least developed areas of HP ^{129}Xe MRI application: molecular imaging, and brain imaging.

HP ^{129}Xe has specific NMR characteristics such as chemical shift and relaxation times in biological fluids and is highly sensitive to the chemical environment. These HP ^{129}Xe physical parameters may be affected by physiological factors such as blood oxidation and glycation. Knowledge of HP ^{129}Xe chemical shift and relaxation times is crucial for molecular imaging utilizing the HyperCEST contrast mechanism as well as for cerebral perfusion evaluation in different tissues. The accurate pulse application at the precise frequency guarantees a successful experiment. Despite the paramount importance of the understanding how chemical composition of

blood affects HP ^{129}Xe, there was a limited number of studies dedicated to this issue and all of them focused on blood oxygenation.

This work studied the impact of the glucose concentration on the chemical shift and transverse relaxation in the whole citrated sheep blood. It was found that increasing glucose concentration causes HP ^{129}Xe to have an additional peak which was attributed to the glycated haemoglobin. Spin-lattice relaxation time also increased nonlinearly. These findings may be used for parameter corrections in patients with hyperglycemia.

Perfusion imaging in the brain may provide valuable information about its function and any structural abnormalities at the early stages of its development. HP ^{129}Xe was previously shown as a promising agent for perfusion imaging. Multiple imaging techniques were developed for accurate perfusion imaging with HP ^{129}Xe. However, up to now, all brain imaging done with HP ^{129}Xe was performed for the whole-brain projection, which subsequently limited accurate localization of the signal.

This work demonstrated, for the first time, the multi-slice HP ^{129}Xe brain imaging by using the commercially available 3D GRE pulse sequence. Overall, five slices of the brain were acquired and the HP ^{129}Xe signal was correlated with the segmented ^{1}H conventional MRI images.

Another advanced technique that allows molecular imaging with HP ^{129}Xe is HyperCEST. Currently, various supramolecular hosts have been explored for effective HyperCEST performance. Typically, only a 3-lobe sinc saturation pulse shape has been used for imaging of HyperCEST agents, but the optimization and comparison of different pulse shapes' performance has never been done. Cucurbit[6]uril is the only supramolecular cage whose performance was proven in-vivo in living rodents, which makes it a promising molecular imaging agents for further explorations.

The optimization of the cucurbit[6]uril HyperCEST performance was done for four different saturation pulses sinusoidal, block, sinc, and hyperbolic secant. The highest HyperCEST depletion values were observed for sinusoidal and sinc pulses at the highest flip angles. Additionally, the detectability limit of cucurbit[6]uril was studied in phosphate-buffered saline and whole bovine blood. The values obtained with optimized saturation pulses were significantly lower than previously observed.

6.2 Future Work

6.2.1 Hardware development

Unfortunately, HP ^{129}Xe SNR in the brain and bloodstream is significantly limited by ^{129}Xe concentration. This SNR limitation directly translates into the spatial resolution and the slice thickness of acquired HP ^{129}Xe brain images. Therefore, in order to further progress in the multi-slice brain imaging with HP ^{129}Xe, the acquired SNR should be considerably higher.

RF coil is one of the main hardware aspects that determines image SNR. Only quadrature single-channel coils are widely available for HP ^{129}Xe imaging. Unfortunately, the development of the multichannel phased array coils for multinuclear MRI, which can significantly increase captured SNR and decrease scan time, is rather slow. Recently, a four-channel RF receive coil was custom built for HP ^{129}Xe brain imaging and used for assessment of perfusion[1] and establishment of stroke[2]. The same coil was also used in brain MRSI to describe brain tissue uptake[3]. Additionally, a 6-channel RF array was reported for ^{129}Xe brain imaging at 3T, however, only phantom studies were performed with it[4]. Multi-channel RF receivers are also developed for lung imaging with HP ^{129}Xe. Eight-channel receive-only RF coil has been demonstrated for lung imaging in 1.5T[5]. Moreover, a 32-channel phased-array surface coil was designed for the improvement of lung imaging[6].

The implementation of a multi-channel coil for multi-slice ^{129}Xe brain imaging will be highly beneficial for the resolution and will allow the acquisition higher number of thinner slices. This will lead to better signal localization and a more accurate correlation of the ^{129}Xe signal with brain tissues.

6.2.2 Pulse sequences improvement

Pulse sequences utilized for imaging are the major contributors to the HP ^{129}Xe image quality.

The multi-slice HP ^{129}Xe brain imaging in this work was performed using conventional and widely available GRE pulse sequence with Cartesian readout. Moreover, a couple of approaches for SNR boost were utilized in the present work. Centric k-space ordering was used for higher SNR acquisition in the k-space low spatial frequencies. To maximize the image SNR 3D GRE sequence was used as it gives additional increase to the SNR. However, the acquisition of multiple slices significantly increased the scan time which made SNR susceptible to the T_1-associated signal loss. This issue may be resolved at the image reconstruction stage with the correction of k-space lines with respect to T_1 relaxation. An additional approach that may be used for shortening the scan time is the utilization of non-cartesian k-space trajectories such as stack-of-spirals and FLORET[7]. However, this may result in undesired SNR loss and image blurriness due to k-space undersampling. In addition, the effect of HP ^{129}Xe signal decay over time may be corrected with flip-angle maps generation from 2D spiral images acquired in addition to 3D GRE images. This approach was used for HP ^{129}Xe lung imaging[8].

It would be very beneficial to acquire separate multi-slice images of HP ^{129}Xe in grey matter, white matter, and cerebrospinal fluid. This will allow to measure ^{129}Xe uptake by each brain tissue which can be used for brain abnormalities assessment. This may be achieved through

the utilization of phase separation methodologies. The most promising one is iterative decomposition with echo asymmetry and least squares estimation (IDEAL)[9–11].

The combination of multi-slice HP ^{129}Xe imaging approach with perfusion imaging will result in accurate spatial localization of perfusion values. This will take perfusion imaging with HP ^{129}Xe on the same level with clinically used perfusion assessment techniques such as ASL and DCE imaging.

6.2.3 Translation to the in-vivo imaging

The assessment of the glucose effect on HP ^{129}Xe chemical shift and optimization of the HyperCEST pulse sequence were performed in-vitro. The evaluation of the glucose concentration effect on HP ^{129}Xe spectroscopic parameters was done in sterile citrated sheep blood. This is a decent media for initial assessment; yet, the evaluation of the glucose effect should be also done in the different blood types. Additionally, the important parameter such as blood oxygenation was not taken into account. The complex study for evaluation of glucose effect on the HP ^{129}Xe chemical shift and relaxation time should be performed in the whole human blood along with measurements of oxygenation level changes. This will allow the transfer to the in-vivo experiments with living animals.

Optimization of the cucurbit[6]uril HyperCEST performance was done *in-vitro* in phosphate-buffered saline, which is the best solution for blood mimicking without an abundance of biological molecules. The *in vitro* experiments were performed with whole sterile citrated bovine blood utilizing the saturation pulse's flip angles which previously demonstrated the best results. The project's subsequent phase will involve in-vivo HyperCEST performance evaluation using the optimized saturation pulse parameters.

It should be noted, that cucurbit[6]uril is the only supramolecular host that is now suitable for utilization as a molecular biosensor. Henceforth, it should be functionalized with affinity tags, which will have high affinity. Alternatively, cucurbit[6]uril may be modified to have chemical or biological activation at the disease site. Unfortunately, it is almost impossible to attach affinity tags directly to the cucurbit[6]uril molecule due to its spherical symmetry, however, there is another potential approach which involves the creation of the cucurbit[6]uril-based rotaxanes. The activation of cucurbit[6]uril may happen with the cleavage of the internal molecular axle of rotaxane, which may happen under various conditions. The performed optimization of the saturation pulses for HyperCEST maximization will also allow to gain more prominent results from molecular imaging with rotaxanes.

In addition to all the aforementioned, the optimization of HyperCEST performance should be done for all HP ^{129}Xe molecular hosts to maximize their performance. This will allow to decrease the injection volume of the molecular agents that have toxicity considerations.

6.3 Conclusion

While HP ^{129}Xe MRI holds immense promise for clinical applications, its full potential is hindered by the absence of crucial foundational elements. Presently, the primary focus of HP ^{129}Xe MRI development centers on lung imaging. Nevertheless, the scope of HP ^{129}Xe MRI applications extends far beyond this, encompassing molecular imaging with its remarkable sensitivity levels and offering a viable alternative to conventional clinical methods in the realm of perfusion imaging.

This thesis demonstrates the multiple advances to the HP ^{129}Xe MRI, specifically HP ^{129}Xe brain imaging and HyperCEST molecular imaging. In addition, it answers the fundamental question of blood composition effects on the HP ^{129}Xe spectral characteristics.

Every project within this study was designed to tackle one or more of the obstacles that have been encountered in the field of HP ^{129}Xe MRI imaging. These challenges have historically impeded the widespread application of this promising technology in clinical settings. Furthermore, each of these projects plays a pivotal role in laying down the essential building blocks required to bridge the gap between cutting-edge HP ^{129}Xe imaging techniques and their practical use in clinical environments. In doing so, they contribute significantly to the realization of the potential benefits that HP ^{129}Xe MRI can offer within healthcare.

6.4 References

1. Rao MR, Stewart NJ, Griffiths PD, Norquay G, Wild JM. Imaging human brain perfusion with inhaled hyperpolarized 129Xe MR imaging. *Radiology*. 2018;286(2):659-665. doi:10.1148/radiol.2017162881

2. Rao MR, Norquay G, Stewart NJ, Hoggard N, Griffiths PD, Wild JM. Assessment of brain perfusion using hyperpolarized 129Xe MRI in a subject with established stroke. *Journal of Magnetic Resonance Imaging*. 2019;50(3):1002-1004. doi:10.1002/jmri.26686

3. Collier GJ, Schulte RF, Rao M, Norquay G, Ball J, Wild JM. Imaging gas-exchange lung function and brain tissue uptake of hyperpolarized <scp> ^{129} Xe </scp> using sampling density-weighted MRSI. *Magn Reson Med*. Published online February 6, 2023. doi:10.1002/mrm.29602

4. Puddu C, Rao M, Rodgers O, Maunder A, Wild J. 6-channel RF array for hyperpolarized 129 Xe brain MRI at 3T. In: *Proc. Intl. Soc. Mag. Reson. Med. 28*. ; 2020:4099.

5. Puddu C, Rao M, Xu X, Deppe MH, Collier G, Maunder A, Chan HF, De Zanche N, Robb F, Wild JM. An asymmetrical whole-body birdcage RF coil without RF shield for hyperpolarized 129Xe lung MR imaging at 1.5 T. *Magn Reson Med*. 2021;86(6):3373-3381. doi:10.1002/mrm.28915

6. Dregely I, Ruset IC, Wiggins G, Mareyam A, Mugler JP, Altes TA, Meyer C, Ruppert K, Wald LL, Hersman FW. 32-channel phased-array receive with asymmetric birdcage transmit coil for hyperpolarized xenon-129 lung imaging. *Magn Reson Med*. 2013;70(2):576-583. doi:10.1002/mrm.24482

7. Willmering MM, Robison RK, Wang H, Pipe JG, Woods JC. Implementation of the FLORET UTE sequence for lung imaging. *Magn Reson Med*. 2019;82(3):1091-1100. doi:10.1002/mrm.27800

8. Bdaiwi AS, Costa ML, Plummer JW, Willmering MM, Walkup LL, Cleveland ZI. B1 and magnetization decay correction for hyperpolarized 129Xe lung imaging using sequential 2D spiral acquisitions. *Magn Reson Med*. 2023;90(2):473-482. doi:10.1002/mrm.29655

9. Friedlander Y, Zanette B, Couch M, Kassner A, Santyr G. Spiral-IDEAL for Time-Resolved Imaging of Hyperpolarized 129Xe Kinetics in the Rat Brain. In: *Proc. Intl. Soc. Mag. Reson. Med. 27*. ; 2019:4300.

10. Friedlander Y, Zanette B, Lindenmaier A, Li D, Kadlecek S, Santyr G, Kassner A. Hyperpolarized 129Xe MRI of the rat brain with chemical shift saturation recovery and spiral-IDEAL readout. *Magn Reson Med*. 2022;Apr; 87(4):1971-1979. doi:10.1002/mrm.29105

11. Reeder SB, Pineda AR, Wen Z, Shimakawa A, Yu H, Brittain JH, Gold GE, Beaulieu CH, Pelc NT. Iterative decomposition of water and fat with echo asymmetry and least-squares estimation (IDEAL): Application with fast spin-echo imaging. *Magn Reson Med*. 2005;54(3):636-644. doi:10.1002/mrm.20624

Appendix A: Research Ethics Board Approval

Lakehead UNIVERSITY myEmail

Martina Agostino <magosti1@lakeheadu.ca>

Approval of Human Ethics Renewal, Romeo #1465072
1 message

research.ethics@lakeheadu.ca <research.ethics@lakeheadu.ca> 25 February 2021 at 13:58
To: "Albert Mitchell S.(Primary Investigator)" <malbert1@lakeheadu.ca>
Cc: "Agostino Martina(Project Staff/Research Assistant)" <magosti1@lakeheadu.ca>, "Forsyth Crystal(Project Staff/Research Assistant)" <forsythc@tbh.net>, "Granberg Karl(Co-Investigator)" <karlerik.granberg@gmail.com>, "Grynko Vira(Project Staff/Research Assistant)" <vgrynko@lakeheadu.ca>, "Hassan Ayman(Co-Investigator)" <hassana@tbh.net>, "Li Tao(Project Staff/Research Assistant)" <tli@lakeheadu.ca>, "Lod Elizabeth(Project Staff/Research Assistant)" <lode@tbh.net>, "McNabb James(Project Staff/Research Assistant)" <mcnabbj@tbh.net>, "Mikowska Lutoslawa(Student)" <lmikowsk@lakeheadu.ca>, "Shepelytskyi Yurii(Project Staff/Research Assistant)" <yshepely@lakeheadu.ca>, research.ethics@lakeheadu.ca

Date: February 25, 2021

To: Dr. Mitchell S. Albert, Primary Investigator

From: Dr. Kristin Burnett, Chair, Research Ethics Board

Subject: Renewal of REB Romeo #1465072

On behalf of the Research Ethics Board, I am pleased to grant *renewal of ethical approval* to your research project titled, "Hyperpolarized Xenon-129 Functional Magnetic Resonance Imaging of Healthy Volunteers and Participants with Alzheimer's Disease".

Ethics approval is valid for one year. A Request for Renewal can be applied for through the Romeo Research Portal. A Final Report must be submitted promptly upon completion of the project, also available through the Romeo Research Portal.

During the course of the study, any modifications to the protocol or forms must not be initiated without prior approval from the REB. You must also promptly notify the REB of any adverse events that may occur.

If you have any questions, please contact Sue Wright, Research Ethics & Administrative Officer.

Best wishes for continued success with your research project.

/lb

Lakehead UNIVERSITY myEmail

Martina Agostino <magosti1@lakeheadu.ca>

Approval of Human Ethics Renewal, Romeo #1465072 "Hyperpolarized Xenon-129 Functional Magnetic Resonance Imaging of Healthy Volunteers and Participants with Alzheimer's Disease"

1 message

swright@lakeheadu.ca <swright@lakeheadu.ca> 11 February 2022 at 09:55
To: "Albert Mitchell S.(Primary Investigator)" <malbert1@lakeheadu.ca>
Cc: "Agostino Martina(Project Staff/Research Assistant)" <magosti1@lakeheadu.ca>, "Forsyth Crystal(Project Staff/Research Assistant)" <forsythc@tbh.net>, "Granberg Karl(Co-Investigator)" <karlerik.granberg@gmail.com>, "Grynko Vira(Project Staff/Research Assistant)" <vgrynko@lakeheadu.ca>, "Hassan Ayman(Co-Investigator)" <hassana@tbh.net>, "Li Tao(Project Staff/Research Assistant)" <tli@lakeheadu.ca>, "Lod Elizabeth(Project Staff/Research Assistant)" <lode@tbh.net>, "McNabb James(Project Staff/Research Assistant)" <mcnabbj@tbh.net>, "Mikowska Lutoslawa(Student)" <lmikowsk@lakeheadu.ca>, "Shepelytskyi Yurii(Project Staff/Research Assistant)" <yshepely@lakeheadu.ca>, swright@lakeheadu.ca

Date: February 11, 2022

To: Dr. Mitchell S. Albert, Primary Investigator

From: Dr. Kristin Burnett, Chair, Research Ethics Board

Subject: Renewal of REB Romeo #1465072

On behalf of the Research Ethics Board, I am pleased to grant *renewal of ethical approval* to your research project titled, "Hyperpolarized Xenon-129 Functional Magnetic Resonance Imaging of Healthy Volunteers and Participants with Alzheimer's Disease".

Ethics approval is valid for one year. A Request for Renewal can be applied for through the Romeo Research Portal. A Final Report must be submitted promptly upon completion of the project, also available through the Romeo Research Portal.

During the course of the study, any modifications to the protocol or forms must not be initiated without prior approval from the REB. You must also promptly notify the REB of any adverse events that may occur.

If you have any questions, please contact Sue Wright, Manager, Research Ethics & Contracts at swright@lakeheadu.ca.

Best wishes for continued success with your research project.

/sw

Thunder Bay Regional Health Sciences Centre

RESEARCH ETHICS BOARD
Re-approval Application Form

Thunder Bay Regional Health Sciences Centre
DEC 16 2019
Research Ethics Board

Please complete, sign and submit this form to the Research Ethics Office
If you require any assistance, please contact: TBR_REO@tbh.net

Research Ethics Office Use Only

Re-approval Granted on: 27-Jan-2020 [ ] Delegated Approval
[X] Full Board Meeting approval

Starting on: 28-Jan-2020 Expiring on: 28-Jan-2021

Recorded at REB Full Board meeting date: 27-Jan-2020

Signature of Chair: [signature]

Date: 27-Jan-2020

TBRHSC REB # 2015144 Current expiry date: January 28, 2020

Principal Investigator: Dr. Mitchell Albert

Full Study Title: Hyperpolarized Xenon-129 Functional Magnetic Resonance Imaging of Healthy Volunteers and Participants with Alzheimer's Disease

1.	Study Status	Yes	No
	Enrollment Closed/Completed	☐	☒
	All Assessments/Intervention Completed	☐	☒
	Follow-up Completed	☐	☒
	Data verification/Data analyses Completed	☐	☒

FOR STUDIES INVOLVING CHART REVIEWS		
Study Status	Yes	No
Review of all charts completed	☐	☐

2.	**Number of local study participants** (since study initiation)		
	Enrolled in Study	A	40
	In active intervention phase of study	B	0
	In follow-up phase of study	C	26
	Completed study	D	14
	Withdrew from study	E	0

All participants need to be accounted for

A = B + C + D + E + F

Comments, if needed: 4 Alzheimer's participants; 35 Healthy participants, 1 Quality Control participant

	Deceased, lost-to-follow up, transferred	F	0	

3.	Reports/Updates of Research Study	Yes	No	Check if attachment
a.	Has an interim data analysis been done? → If Yes, attach a summary.	☒	☐	☒
b.	Have articles been published or presentations given using results of the study? → If Yes, submit a copy of the abstract(s) or a list of references	☒	☐	☒
c.	Have all serious adverse events been reported? [☒] not applicable → If No, include with this report.	☐	☐	☐
d.	Has new literature changed your assessment of risk/benefits for participants?	☐	☒	☐
	→ If Yes, have participants been informed? → If No, attach an explanation of how & when participants will be informed	☐	☐	☐
e.	Have there been any changes in investigators since the last approval?	☒	☐	☐
	→ If Yes, has the REB been notified? → If No, submit an amendment with this application	☒	☐	☐
f.	Is there new evidence from other studies that impact your study? → If Yes, attached summary	☐	☒	☐
g.	Have there been any changes to the local study protocol or consent form? → If Yes, submit an amendment form with this application.	☐	☒	☐
h.	Are study results available? → If Yes, attach a brief summary of study results to date.	☐	☒	☐

Principal Investigator's Signature:
(print, sign and deliver hardcopy to REO)

Mitchell Albert

Print Name: Dr. Mitchell Albert

Date: [month day, year] December 11, 2019

Thunder Bay Regional Health Sciences Centre

RESEARCH ETHICS BOARD

Re-approval Application Form

Thunder Bay Regional Health Sciences Centre
26-Jan-2021
Research Ethics Board

Please complete, sign and submit this form to the Research Ethics Office
If you require any assistance, please contact: TBR_REO@tbh.net

Research Ethics Office Use Only

Re-approval Granted on: 22-Feb-2021 [ ] Delegated Approval
[X] Full Board Meeting approval

Starting on: 22-Feb-2021 Expiring on: 28-Jan-2022

Recorded at REB Full Board meeting date: 22-Feb-2021

Signature of Chair:

Date: 22-Feb-2021

TBRHSC REB # 2015144 Current expiry date: February 22, 2021

Principal Investigator: Dr. Mitchell Albert

Full Study Title: Hyperpolarized Xenon-129 Functional Magnetic Resonance Imaging of Healthy Volunteers and Participants with Alzheimer's Disease

1.	Study Status	Yes	No
	Enrollment Closed/Completed	☐	☒
	All Assessments/Intervention Completed	☐	☒
	Follow-up Completed	☐	☒
	Data verification/Data analyses Completed	☐	☒

FOR STUDIES INVOLVING CHART REVIEWS		
Study Status	Yes	No
Review of all charts completed	☐	☐

2.	**Number of local study participants** (since study initiation)		
	Enrolled in Study	A	49
	In active intervention phase of study	B	0
	In follow-up phase of study	C	47
	Completed study	D	2
	Withdrew from study	E	0

All participants need to be accounted for

A = B + C + D + E + F

Comments, if needed: 5 Alzheimer's participants; 43 Healthy participants, 1 Quality Control participant

	Deceased, lost-to-follow up, transferred	F	0	

3.	Reports/Updates of Research Study	Yes	No	Check if attachment
a.	Has an interim data analysis been done? → If Yes, attach a summary.	☒	☐	☒
b.	Have articles been published or presentations given using results of the study? → If Yes, submit a copy of the abstract(s) or a list of references	☒	☐	☒
c.	Have all serious adverse events been reported? [☒] not applicable → If No, include with this report.	☐	☐	☐
d.	Has new literature changed your assessment of risk/benefits for participants?	☐	☒	☐
	→ If Yes, have participants been informed? → If No, attach an explanation of how & when participants will be informed	☐	☐	☐
e.	Have there been any changes in investigators since the last approval?	☐	☒	☐
	→ If Yes, has the REB been notified? → If No, submit an amendment with this application	☐	☐	☐
f.	Is there new evidence from other studies that impact your study? → If Yes, attached summary	☐	☒	☐
g.	Have there been any changes to the local study protocol or consent form? → If Yes, submit an amendment form with this application.	☐	☒	☐
h.	Are study results available? → If Yes, attach a brief summary of study results to date.	☐	☒	☐

Principal Investigator's Signature:
(print, sign and deliver hardcopy to REO)

Mitchell Albert

Print Name: Dr. Mitchell Albert

Date: [month day, year] January 26, 2021